Gravitational Lensing and Telescope Aberrations

by

Rebecca S Levinson

Submitted to the Department of Physics
in partial fulfillment of the requirements for the degree of

Doctor of Philosophy

at the

MASSACHUSETTS INSTITUTE OF TECHNOLOGY

September 2014

Author .....
Department of Physics
August 28, 2014

Certified by .....
Paul L. Schechter
Professor of Astrophysics
Thesis Supervisor

Accepted by .....
Krishna Rajagopal
Associate Department Head for Education, Department of Physics

Gravitational Lensing and Telescope Aberrations

by

Rebecca S Levinson

Submitted to the Department of Physics
on August 28, 2014, in partial fulfillment of the
requirements for the degree of
Doctor of Philosophy

Abstract

This is a work in three parts, each of which addresses challenges to weak gravitational lensing flexion measurements. Part one is a derivation and analysis of the aberration shapes and patterns imparted onto images by misaligned telescopes. As telescope aberrations will generally interfere with lensing measurements, it is important to be able to quantify and ultimately minimize them. The conclusions of this first part are (1) misaligned telescopes produce the same aberration shapes, but different field patterns, as aligned telescopes, (2) these misalignment patterns are generic for on-axis telescopes and can be modeled with relatively few parameters, and (3) with well-placed wavefront sensors, telescopes can be kept near enough to alignment so that any remaining aberrations are benign.

The second part of this work explores the effect of any un-removed telescope aberrations on images of flexed galaxies. Telescope astigmatism, coma, and trefoil distort stellar images in much the same way that gravitational shear and flexion distort galaxy images. In this chapter, I derive simple models for lensed galaxies and for aberrated PSFs, and convolve the two models to determine the analytic form for the gravitationally lensed and optically distorted galaxy shapes that one might expect to see in actual telescope images. Given this representation of the galaxy image, one can analytically disentangle the gravitational signal from the other distortions.

The final chapter is an observational study of weak gravitational lensing flexion in Abell 1689. Using the analytic models for images of lensed and aberrated galaxies that I derived in the preceding section, I attempt to measure galaxy halo truncation from galaxy-galaxy lensing flexion in Abell 1689. While I am able to successfully measure flexed and distorted galaxy shapes and extract the de-aberrated flexion signal, the measurement of galaxy-galaxy gravitational flexion is ultimately thwarted by inherent shape noise in Abell 1689's background source galaxy population. I characterize this shape noise, concluding that it is much larger than previously reported. I further analyze the other hindrances to the lensing flexion measurement and conclude with a recipe for perhaps succeeding in the future.

Thesis Supervisor: Paul L. Schechter

Title: Professor of Astrophysics

Acknowledgments

Thank you to my husband, Josh, for his godlike patience with me during my 6 years at MIT. I owe you.

Thanks also to my family for their unwavering confidence in me, and to my advisor, Paul, for his guidance, encouragement, and support.

Contents

List of Figures

List of Tables

Introduction

> "A few years ago the city council of Monza, Italy, barred pet owners from keeping goldfish in curved bowls. The measure's sponsor explained the measure in part by saying that it is cruel to keep a fish in a bowl with curved sides because, gazing out, the fish would have a distorted view of reality. But how do we know we have the true, undistorted picture of reality?" –Stephen Hawking & Leonard Mlodinow, *The Grand Design*, 2010

Images portray a distorted version of reality. I am not being allegorical. Myopia, hyperopia, and astigmatism distort images created by the eye, at least for the more unfortunate of us. Telescopes and cameras are subject to defocus, spherical aberration, coma, astigmatism, curvature of field, trefoil, and more, all which lead to distorted images. And light traveling through the cosmos must bend and deflect as it encounters gravitational wells along its path, so that when it reaches its destination, the image it creates is a displaced and disfigured version of the source that generated it. This last distortion is known as gravitational lensing.

This thesis is a work in three parts, bound together by two overarching themes (1) addressing challenges to weak gravitational lensing flexion measurements and (2) extracting information from distorted images. Each section is written to be self-contained, and has its own introduction, bibliography, and appendices. Chapters 1 and 2 have been published as individual works by *PASP* on July 2011 and December 2013 respectively. An shortened version of chapter 3 will also be published as an individual work.

0.1 Synopsis of chapter 1: Generic misalignment aberration patterns in wide field telescopes

Chapter 1 of this thesis is a derivation and analysis of the aberration shapes and patterns imparted onto images by misaligned telescopes. Despite the subject being telescopes, this section is motivated by the stringent constraints on image quality demanded by gravitational lensing studies. Recently constructed experiments such as the Dark Energy Survey (DES), ground based projects which are in various stages of construction such as the Large Synoptic Survey Telescope (LSST) and the Kilo-Degree Survey (KIDS), and space based experiments such as the Wide-Field InfraRed Survey Telescope (WFIRST) and Euclid all propose to use weak lensing as a tool to constrain cosmology and galaxy formation. However, in order to achieve these scientific goals, these projects must understand and control their point spread functions (PSFs). As an example of the stringent constraints weak lensing science goals place on image quality for these experiments, the LSST weak lensing goals require PSF systematics affecting astigmatism to be controlled to better than a few parts in a thousand.

In an effort to shed further light on the nature of aberrations that will affect these experiments and how they might be characterized and controlled, Paul Schechter and I set out to examine the aberrations that affect modern, multiple mirror telescopes. Our particular focus was on misalignment aberrations, those aberrations and patterns that manifest when the optics of a telescope are laterally offset or tilted with respect to one another. These misalignments and tilts must be corrected in the initial construction and alignment of a telescope, and also during science observations as the mirrors are subject to the varying gravitational stresses associated with different pointings, and as the optical elements expand and contract with thermal conditions.

Empirical tests and ray-tracing had shown that misalignments in many types of telescopes cause the same basic patterns of aberrations. McLeod (1996) even uses the misalignment coma patterns to align Cassegrain telescopes. However, before I undertook this present work, the only existing constructs with which to model misalignment aberrations were designed primarily to ease the programming of ray-

tracing software on (ancient) computers, and were therefore somewhat conceptually cumbersome. In chapter 1, I expand on the work of Schroeder (1987) to develop a more intuitive, fully generic, first principles framework to describe the magnitudes, patterns, and shapes of misalignment aberrations. The equations derived herein are based on simple geometric arguments, and might equally well have been derived a century ago had there been a need for them. Only recently, with the proposal of large, wide-field, multiple-mirror telescopes, has there been a need for a schema with which to understand misalignment aberrations.

The idea to undertake this work was Paul Schechter's and therefore he is first author on the published paper in *PASP*, 07/2011. However, I take credit for deriving the generic patterns and for much of the writing, which is why I include the work here, with Schechter's permission.

0.2 Synopsis of chapter 2: Analytic PSF corrections for gravitational flexion measurements

For my prepared question in the third part of my general exam, Paul Schechter 'suggested' that I examine the similarities between telescope aberrations, and those distortions caused by weak gravitational lensing. Result: they are the same. And since they are the same, telescope aberrations can mimic gravitational lensing signals.

The second chapter of my thesis builds on this question and explores the effect of atmospheric smearing and telescope aberrations on the images of galaxies which have been weakly gravitationally lensed. The idea behind this work is very straightforward: make a simple model for a lensed galaxy, make a simple model for an aberrated PSF, and convolve the two to show the effects of atmospheric smearing and telescope distortions on a lensed galaxy image. Since the analytic form for telescope distortions (coma, astigmatism, and trefoil) are very similar to the analytic form for the highest order effects of lensing on galaxies (F-flexion, shear, and G-flexion) one would expect coma, astigmatism, and trefoil to imitate F-flexion, shear, and G-flexion respectively

in telescope images.

What started as a short letter to show how telescope aberrations affect measurements of flexion using the Analytic Image Method (henceforward, AIM), has since turned into a 46 page treatise on minimal acceptable models for flexed galaxies, minimal models for an atmospherically aberrated and possibly asymmetric PSFs, and the various distortions that mimic the gravitational flexion signal but are NOT gravitational flexion. These impostors include the telescope distortions we had initially surmised, but also include mixing between galaxy elongation and flexion, and mixing between telescope aberrations and the galaxy shape. This work establishes an analytic form for gravitationally lensed, atmospherically smeared, and asymmetrically aberrated galaxies, so that one can extract the gravitational contribution from telescope images.

This work has been previously published in *PASP*, 12/2013. As I am the sole author of this work, I include it here for completeness.

0.3 Synopsis of chapter 3: A failure to measure galaxy-galaxy flexion in Abell 1689, and the role of shape noise at $z \sim 1$

The first two chapters of this work are theory based; they establish telescope aberrations as a hurdle in making a gravitational flexion measurement, and set down a method by which one can extract gravitational flexion from data in spite of those aberrations. In contrast, this third chapter is experimentally based; it is a detailed account of the steps I took to measure gravitational galaxy-galaxy flexion in the cluster Abell 1689.

My initial goal was to measure galaxy halo truncation for galaxies in Abell 1689, possibly verifying the prediction that galaxies nearer to the cluster center would have more truncated halos than their counterparts at the edge of the cluster. I was not able to make this measurement with my data, and so this last section of my thesis is

an inquest of sorts: why did this measurement fail?

I am able to successfully measure flexed and distorted galaxy shapes in my images using DoPHOT. I am also able to account for telescope aberrations and extract a de-aberrated flexion signal using the methods outlined in chapter 2. What I did not predict and could not control was the large inherent shape noise in the background source galaxies behind Abell 1689. I perform a thorough analysis of this shape noise, both at low and high redshift, and find that the shape noise at $z \sim 1$ is much larger than some of the values previously reported in the literature. I examine why these previously reported measurements of shape noise may be artificially low. I additionally analyze the shortcomings in the depth of my images and in the selection and redshift determination of source galaxies that hinders my flexion measurement. These observational and analysis shortcomings, combined with the inherent galaxy shape noise, ultimately prohibit any possible measurement of halo-truncation or galaxy-galaxy lensing flexion with my data. I conclude with a recipe for making a galaxy-galaxy flexion measurement in the future with deeper, redder, and possibly space-based data.

Chapter 1

Generic Misalignment Aberration Patterns in Wide-Field Telescopes

Published 07/2011 by Publications of the Astronomical Society of the Pacific
Volume 123, issue 905, pp.812-832
http://www.jstor.org/stable/pdfplus/10.1086/661111.pdf?acceptTC=true

1.1 Abstract

Axially symmetric telescopes produce well known "Seidel" off-axis third-order aberration patterns: coma, astigmatism, curvature of field and distortion. When axial symmetry is broken by the small misalignments of optical elements, additional third-order aberration patterns arise: one each for coma, astigmatism and curvature of field and two for distortion. Each of these misalignment patterns is characterized by an associated two-dimensional vector, each of which in turn is a linear combination of the tilt and decenter vectors of the individual optical elements. For an N-mirror telescope, $2(N-1)$ patterns must be measured to keep the telescope aligned. Alignment of the focal plane may require two additional patterns. For $N = 3$, as in a three mirror anastigmat, there is a two-dimensional "subspace of benign misalignment" over which the misalignment patterns for third-order coma, astigmatism and curvature of field are identically zero. One would need to measure at least one of

the two distortion patterns to keep the telescope aligned. Alternatively, one might measure one of the fifth-order misalignment patterns, which are derived herein. But the fifth-order patterns are rather insensitive to misalignments, even with moderately wide fields, rendering them of relatively little use in telescope alignment. Another alternative would be to use telescope pointing as part of the alignment solution.

1.2 Introduction

1.2.1 new telescopes, stringent constraints

The designs for several large telescopes that may get built in the next decade are driven largely by the need for superb and stable image quality over wide fields [5, 14]. Perhaps the most demanding of the scientific programs that in turn drive these requirements is that of cosmological weak lensing, using galaxy images to measure gravitational shape distortions as small as as one part in ten thousand.

Of particular concern for ground-based telescopes are the rigid body motions of the optical elements due to gravitational and thermal stresses on the telescope structure.[1] The positions of the optical elements can be controlled only to the extent that they can be measured, putting a premium on the accurate characterization of the aberrations generated by telescope misalignments.

On the assumption that at least some of these aberrations are best measured with wavefront sensors, several questions immediately arise. How many aberrations must be measured? Which ones? At how many field positions must the measurements be made? Where?

One can always, as a last resort, attempt to answer these questions by simulation. But we argue here that the answers to these questions hinge on the identification of generic field aberration patterns that emerge in a wide variety of circumstances. A relatively small number of such patterns suffices to efficiently diagnose and correct misalignments. And only a small number of field points must be sampled to measure

[1] Such telescopes are *also* subject to deformations of the optical elements, but on longer timescales than the rigid body motions.

these patterns. Moreover two of the patterns may in some cases be determined directly from science data.

1.2.2 literature

The practical astronomical literature on the alignment of wide field telescopes is very limited. McLeod's [1996] paper describing the use of coma and astigmatism patterns to align the Whipple Observatory 1.2-m telescope anchors the recent literature. Wilson & Delabre [27] discuss the alignment of the ESO NTT. Gitton & Noethe [1] describe the alignment of the ESO VLTs, and Noethe & Guisard [12] give a more general description of the astigmatism patterns expected from two-mirror telescopes. Lee et al. [4] give a general treatment of third-order misalignment distortions and then discuss coma and astigmatism and curvature of field in their case studies. Palunas et al. [13] describe the alignment of the Magellan Nasmyth telescopes using coma, astigmatism and curvature of field.

Maréchal [8] derives the third-order misalignment aberration patterns for coma, astigmatism, curvature of field and distortion.

Thompson and collaborators [20, 24, 25] develop a formalism for analyzing telescope misalignments using a vector notation that is elegant and relatively transparent. It isolates generic misalignment patterns associated with third-order aberrations – coma, astigmatism, curvature of field and distortion – and beyond that, generic misalignment patterns associated with fifth-order aberrations.

In an unpublished M.S. thesis, Tessieres [22] used ray tracing software to determine amplitudes for Thompson's misalignment patterns, which at that time had only appeared in Thompson's Ph.D. thesis [1980]. Hvisc & Burge [3] build on Tessieres' work in modeling a four mirror corrector for the Hobby-Ebberly Telescope. They identify the linear combinations of orthogonal aberration patterns (integrated over the field) that are most sensitive to the tilts and decenters of the mirrors.

1.2.3 outline

In the following sections we rederive these same misalignment aberration patterns, using the Thompson et al. vector notation but following instead the development of Schroeder [18]. The present paper is quite similar in spirit to Tessieres': identify those aberration patterns of potential interest and ascertain which are of greatest value in aligning a telescope. However our approach differs in that, in the interest of efficiency, we ignore patterns that are non-linear in the tilts and decenters of the mirrors. This simplification is appropriate for small misalignments of an otherwise rotationally symmetric telescope. We also give greater consideration to the role of distortion, curvature of field and spherical aberration than did Tessieres.

In §1.3 we discuss the misalignment patterns produced by two-mirror telescopes, proceeding from the better known generic coma and astigmatism misalignment patterns, through the almost trivial curvature of field misalignment pattern, to the two distortion misalignment patterns. We then retrace our steps using a more general approach that shows how the misalignment patterns produced by an optic derive from the surface of that optic. In §1.4 we discuss the alignment of three-mirror telescopes.

In §1.5 we use the same methods used in §1.3 to deduce the misalignment patterns associated with fifth-order aberrations. In the course of this we attempt to systematize the somewhat ragged nomenclature associated with the fifth-order aberrations. We additionally examine the relative magnitudes of the fifth-order aberrations, which cast some doubt on their practical utility for telescope alignment. In §1.6 we discuss the number and placement of wavefront sensors needed to align a three mirror telescope. In §1.7 we address a variety of complicating factors: mirror deformations, transmitting correctors, central obscurations and focal plane tilts. In §1.8 we discuss several ways in which the misalignment aberration patterns might be used, and why one might ultimately choose to forego their use.

1.3 Generic patterns and two-mirror telescopes

1.3.1 coma

McLeod's [1996] paper shows how an astigmatic misalignment pattern can be used in conjunction with coma to align a telescope. McLeod's first step is to center the secondary so as to zero the coma. He does not explicitly refer to a coma "pattern," but it is widely appreciated that decentering the secondary of a Ritchey-Chretien telescope produces coma that is to first order constant across the field. For the present purposes we take this to be a pattern, albeit a boring one. McLeod does identify an astigmatism pattern, which he then renders symmetric by rotating the secondary about its coma-free pivot.

Schroeder [18] calculates the coma patterns that arise in a two mirror telescope, allowing for tilting and decentering the secondary. The comatic wavefront G^{coma} is a function of position on the pupil $\vec{\rho}$, with polar coordinates ρ and ϕ, and field angle $\vec{\sigma}$, with polar coordinates σ and θ:

$$G^{coma} = G^{coma}_{Seidel}\sigma\rho^3\cos(\phi-\theta) + G^{coma}_{decenter}\ell\rho^3\cos(\phi-\phi_\ell) + G^{coma}_{tilt}\alpha\rho^3\cos(\phi-\phi_\alpha) \quad (1.1)$$

where $\vec{\ell}$ is the decenter of the secondary which projects to angle ϕ_ℓ on the pupil, and $\vec{\alpha}$ is the vector tilt of the secondary which projects to angle ϕ_α on the pupil. The first term on the right hand side gives the symmetric "Seidel" coma typical of an aligned two mirror telescope. The next two terms give the constant coma pattern typical of a decentering or tilt of the secondary. The coefficients G^{coma}_{Seidel}, $G^{coma}_{decenter}$, and G^{coma}_{tilt} depend upon the radii of curvature, R_i, and conic constants, K_i, of the two mirrors, the indices of refraction of the material (air) preceding the mirrors, n_i, the positions, s_i, and magnifications, m_i of the object for each mirror, and the distance from the primary mirror to the secondary, W. In a Ritchey-Chretien telescope the G^{coma}_{Seidel} term is identically zero, giving no coma when aligned. The notation here is different from that of Schroeder; the conversion from Schroeder's to the present notation is given in

appendix A.

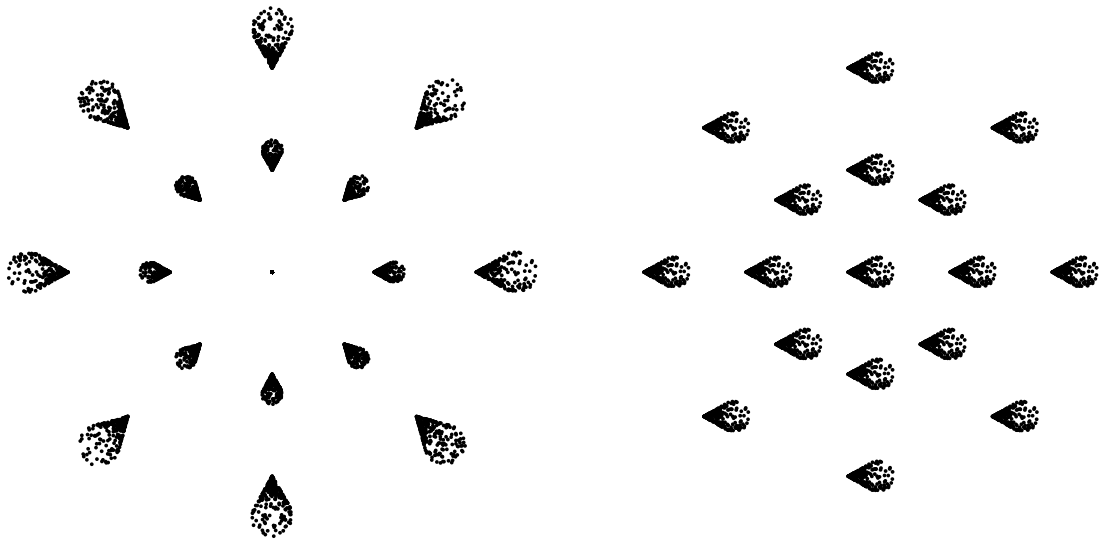

Figure 1-1 Comatic field patterns. (a) Seidel coma field pattern typical of an aligned telescope. (b) Constant coma indicating a tilt and (or) decentering of the secondary along the x axis.

The Seidel term varies linearly as field angle σ and as $\rho^3 \cos\phi$ and (or) $\rho^3 \sin\phi$ on the pupil. The tilt and decenter terms are constant over the field, but have the same functional dependence on pupil coordinates as the first term. We shall somewhat loosely refer to any aberration that has the same dependence upon pupil coordinates as "coma," even when it does not have the Seidel coma dependence on field angle σ. Figure 1-1a shows the point spread function at various points in the field for the first term in equation (1.1). Figure 1-1b shows the point spread function pattern typical of either of the last two terms in equation (1.1).

In practice, the constant coma pattern shown in Figure 1-1b will be superimposed on the Seidel pattern if one is present. We here plot the two patterns separately as the patterns have different physical motivations and thus provide different information about the telescope. The Seidel pattern is a result of the telescope design, and fitting for that pattern provides no information about tilts or decenterings of the mirrors. In contrast, the magnitude and orientation of the constant coma pattern *will* provide information about a telescope's alignment.

1.3.2 astigmatism

Following Schroeder's (1987) example for coma, McLeod [10] calculated the corresponding astigmatism pattern for the case of a nulled field constant coma pattern. He finds an astigmatic wavefront, G^{astig}, given by:

$$G^{astig} = G^{astig}_{sym}\sigma^2\rho^2\cos 2(\phi-\theta)+G^{astig}_{decenter}\sigma\ell\rho^2\cos(2\phi-\theta-\phi_\ell)+G^{astig}_{tilt}\sigma\alpha\rho^2\cos(2\phi-\theta-\phi_\alpha) \tag{1.2}$$

The first term on the right gives the symmetric astigmatism typical of an aligned two mirror telescope. The next two terms give the astigmatism pattern typical of a decentering or tilt of the secondary. The coefficients G^{astig}_{sym}, $G^{astig}_{decenter}$ and G^{astig}_{tilt} again depend upon the radii of curvature, R_i and conic constants, K_i of the two mirrors, the indices of refraction of the air preceding the mirrors, n_i, the positions, s_i and magnifications, m_i of the object for each mirror, and the distance from the primary mirror to the secondary, W. The details of the conversion from McLeod's notation to the above are given in appendix B.

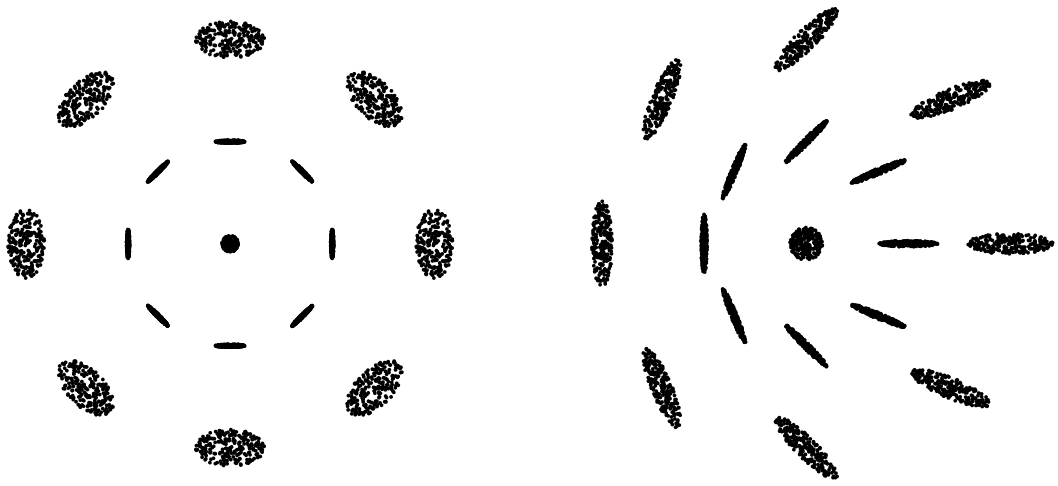

Figure 1-2 Astigmatic field patterns. (a) Seidel astigmatism field pattern typical of an aligned telescope. A constant defocus has been added to show the orientation of the astigmatism. (b) Astigmatic field pattern indicating a tilt and (or) decentering of the secondary along the x axis.

The symmetric term varies as the square of the field radius σ and varies as $\rho^2 \cos 2\phi$ and (or) $\rho^2 \sin 2\phi$ on the pupil. This is almost, but not quite the variation associated with third-order, Seidel astigmatism.[2] It is readily decomposed into terms that vary as $\rho^2 \cos^2 \phi$ (Seidel astigmatism) and $\rho^2 \cos^0 \phi$ (Seidel curvature of field). The tilt and decenter terms have the same functional dependence on pupil coordinates as the symmetric term, but vary linearly with distance from the center of the field σ, and vary as the cosine and (or) sine of the field angle θ. We shall again refer loosely to any aberration that has the same dependence upon pupil coordinates as astigmatism, even when it does not have the Seidel dependence on field position. Figure 1-2a shows the point spread function at various points in the field for the symmetric term in equation (1.2). Figure 1-2b shows the point spread function pattern characteristic of either the tilt or decenter terms in equation (1.2).[3]

As with the comatic aberrations, the astigmatic field pattern shown in Figure 1-2b will in general be superimposed on the Seidel pattern if one is present. Some previous treatments have referred to this superposition of field patterns as a single misalignment pattern; McLeod [10] describes a single astigmatism pattern, which he symmetrizes in the course of aligning his telescope; Thompson [24] refers to a binodal astigmatism pattern which results from misalignments. In this paper we decompose the astigmatism into two patterns, a symmetric one characteristic of an aligned telescope and an asymmetric one introduced by misalignments. The asymmetric pattern described by McLeod [10] and the binodal pattern plotted by Thompson [24] are produced by superimposing the symmetric and asymmetric patterns in Figures 1-2a and 1-2b. The nodes are simply field positions where the symmetric Seidel and

[2]By convention "Seidel" astigmatism is taken to vary as $\rho^2 \cos^2 \phi$ on the pupil. By contrast "Zernike" astigmatism is almost always taken to vary as $\rho^2 \cos 2\phi$. The Seidel definition emerges naturally from the derivation of aberration patterns. The Zernike definition makes for more symmetric wavefronts and orthogonality among the different aberrations. A similar ambiguity arises in the definition of trefoil.

[3]The "dreamcatcher" plot of Figure 2b makes cameo appearances in a number of contexts. It can be seen in a map of image elongations at the prime focus of the LBT [16] and in the point spread function map, Figure 4.14, in version 12.0 of the Chandra Proposer's Observatory Guide [28]. The first such plot of which the authors are aware is in the paper by Shack & Thompson [20]. Maréchal [8] comes close plotting the magnitude and orientation of the misalignment astigmatism pattern but suppressing the sign.

asymmetric misalignment patterns have cancelled.[4]

Both for coma and for astigmatism (and in the cases of the additional aberrations considered below) the misalignment pattern varies as one power of field radius less rapidly than the corresponding symmetric pattern.

1.3.3 curvature of field

Coma and astigmatism are just two of the five third-order Seidel aberrations. Curvature of field (henceforth COF) manifests itself as a defocus that varies as the square of the distance from the center of an assumed flat focal plane. McLeod might in principal have used curvature of field (rather than astigmatism) to align the Whipple 1.2-m, but there is a potential degeneracy with a tilted instrument. Following Schroeder and McLeod, we find an associated wavefront,

$$G^{COF} = G^{COF}_{Seidel}\sigma^2\rho^2 + G^{COF}_{decenter}\sigma\ell\rho^2\cos(\theta - \phi_\ell) + G^{COF}_{tilt}\sigma\alpha\rho^2\cos(\theta - \phi_\alpha). \qquad (1.3)$$

The first term on the right hand side gives the symmetric Seidel curvature of field typical of an aligned two mirror telescope, and the next two give the defocus patterns typical of a decenter or tilt of the secondary. The coefficients G^{COF}_{Seidel}, $G^{COF}_{decenter}$, and G^{COF}_{tilt} again depend upon the radii of curvature, R_i and conic constants, K_i of the two mirrors, the indices of refraction of the air preceding the mirrors, n_i, the positions, s_i and magnifications, m_i of the object for each mirror, and the distance from the primary mirror to the secondary, W. The details of the derivation of the above are given in appendix C.

The Seidel term varies as the square of the field radius σ and varies as ρ^2 on the pupil. But the dependence on pupil position is exactly the same as that of defocus, which is a first-order aberration. Anticipating the nomenclature introduced in §1.5

[4]Terms that are nonlinear in the misalignments also contribute to the positions of the nodes. Most interestingly, the inclusion of a non-linear term may rotate the orientation of the nodes by 90°. However, the inclusion of terms that are nonlinear in the misalignment has no effect on the underlying Seidel or linear patterns.

below, curvature of field might equally well be called "third-order defocus," but we bow to convention. The tilt and decenter terms vary linearly with distance from a line passing through the center of the field, but have the same functional dependence on pupil coordinates. This is precisely what one would expect for a tilted focal plane. Figure 1-3a shows the point spread function at various points in the field for the Seidel term in equation (1.3). Figure 1-3b shows the point spread function pattern introduced by either the tilt or decenter terms in equation (1.3).

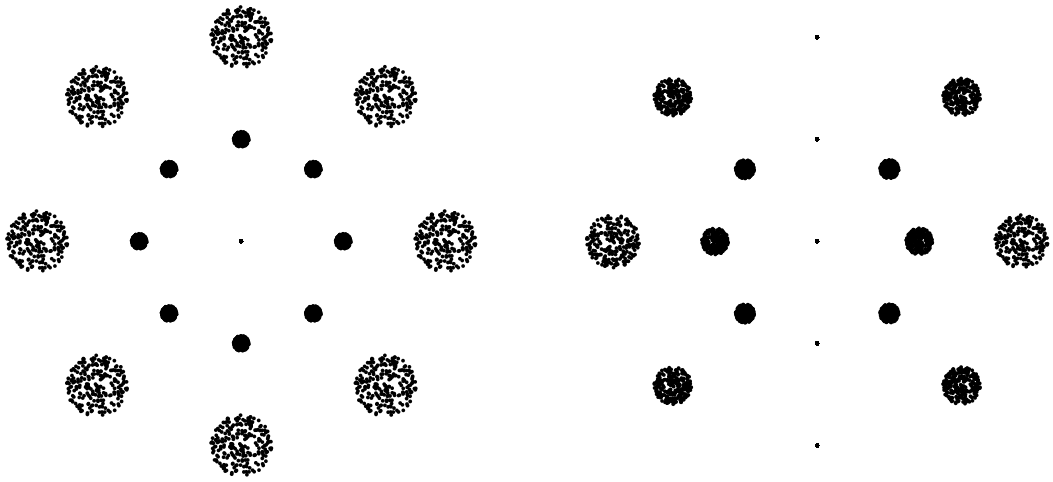

Figure 1-3 Curvature of field patterns. (a) Seidel COF typical of an aligned telescope. (b) COF field indicating a tilt and (or) decenter of the secondary along the x axis.

1.3.4 distortion

While distortion is one of the five Seidel aberrations, for many purposes it can be neglected, since it does not degrade image quality. Distortion does, however alter the positions of images in the field, and of particular interest for the measurements of weak gravitational lensing, it changes the shapes of extended objects. And most importantly for the present discussion it may be of some use in aligning a telescope.

Following the conventions of Schroeder and McLeod, we find the associated wavefront delay for a misaligned two mirror telescope:

$$
\begin{aligned}
G^{distortion} &= G^{distortion}_{Seidel}\sigma^3\rho\cos(\phi-\theta) \\
&+ G^{distortion}_{decenter,\sigma}\sigma^2\ell\cos(\theta-\phi_\ell)\rho\cos(\phi-\theta) + G^{distortion}_{decenter,\rho}\sigma^2\ell\rho\cos(\phi-\phi_\ell) \\
&+ G^{distortion}_{tilt,\sigma}\sigma^2\alpha\cos(\theta-\phi_\alpha)\rho\cos(\phi-\theta) + G^{distortion}_{tilt,\rho}\sigma^2\alpha\rho\cos(\phi-\phi_\alpha)
\end{aligned}
\tag{1.4}
$$

The Seidel term on the right varies as the cube of field angle σ and as $\rho\cos\phi$ and (or) $\rho\sin\phi$ on the pupil. Distortion differs from coma, astigmatism and curvature of field in having two distinct misalignment aberration patterns rather than only one. We will encounter several similar pairs of misalignment aberration patterns when we consider fifth-order misalignment patterns in §4. The two terms are distinguished by whether the direction of the tilt, $\vec{\alpha}$ or decenter, $\vec{\ell}$ enters in a dot product with the field position, $\vec{\sigma}$ or the pupil position, $\vec{\rho}$. We use "σ" and "ρ" to label the two alternatives.

The σ terms have the same functional dependence on pupil coordinates as the Seidel term, but are proportional to the square of the field angle σ and the cosine of its polar coordinate, θ. These produce a field distortion pattern directed radially outward, but with a magnitude that depends on the product of the field angle and its projection onto the decenter or tilt.

The ρ terms also have the same functional dependence on pupil coordinates as the first, but vary only as the square field angle σ. The direction of the distortion is that of the decenter or tilt, but its magnitude increases outward as the square of the distance from the center of the field.

The three distortion patterns are shown in figure 1-4. Details of the derivation of the coefficients are given in appendix D.

Each of the two distinct misalignment distortion patterns is characterized by a two-vector. Were one able to measure those vectors with the same accuracy as the two-vectors that characterize coma and astigmatism one might in principle use *only* distortion measurements to align a two mirror telescope.

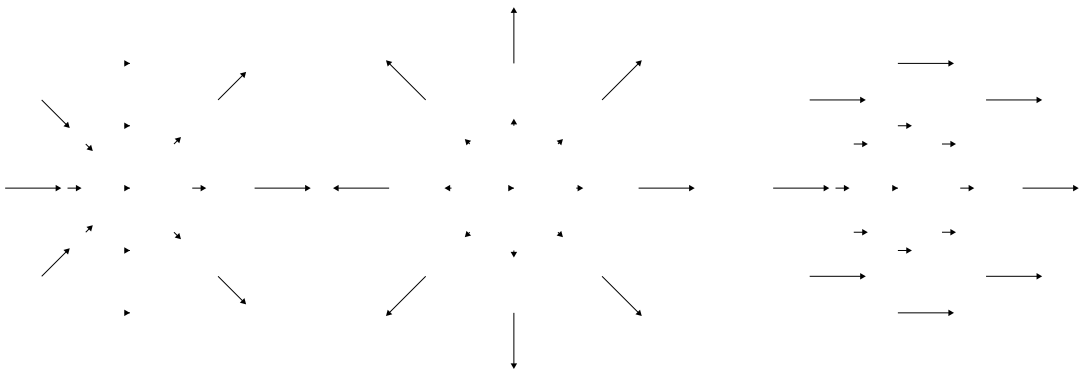

Figure 1-4 Distortion field patterns. (a) The "σ" distortion pattern indicating a tilt and (or) decentering of the secondary along the x axis. (b) Seidel distortion typical of an aligned telescope. (c) The "ρ" distortion pattern indicating a tilt and (or) decentering of the secondary along the x axis.

1.3.5 spherical aberration

Spherical aberration is the fifth of the Seidel aberrations and is constant across the field. Tilts and decenters do not produce asymmetric spherical aberration patterns.

1.3.6 generalization

In the preceding subsections the third-order aberrations were cast so as to display explicitly the azimuthal dependence upon pupil position, $\vec{\rho}$ and field angle, $\vec{\sigma}$. These can be recast more compactly and transparently in vector form. For example the Seidel distortion term above varies as $(\vec{\sigma} \cdot \vec{\sigma})(\vec{\sigma} \cdot \vec{\rho})$.

Suppose a single mirror i serves as its own pupil. The wavefront delay G^{3rd} for a ray that intercepts the mirror at position $\vec{\varpi}$ and that makes an angle $\vec{\psi}$ with the axis of the mirror is given by[5]

[5]We reserve $\vec{\rho}$ for the position on the pupil when the optic is despaced from the pupil.

Table 1.1. Aberration coefficient values for the optic-centered pupil.

W_{040}	W_{131}	W_{222}	W_{220}
$\frac{nR}{4}((\frac{R}{s}-1)^2+K)$	$-nR(\frac{R}{s}-1)$	nR	0

$$
\begin{aligned}
G^{3rd} = {} & W_{040}(\frac{\vec{\varpi}}{R}\cdot\frac{\vec{\varpi}}{R})(\frac{\vec{\varpi}}{R}\cdot\frac{\vec{\varpi}}{R}) + W_{131}(\vec{\psi}\cdot\frac{\vec{\varpi}}{R})(\frac{\vec{\varpi}}{R}\cdot\frac{\vec{\varpi}}{R}) \\
& + W_{222}(\vec{\psi}\cdot\frac{\vec{\varpi}}{R})(\vec{\psi}\cdot\frac{\vec{\varpi}}{R}) + W_{220}(\vec{\psi}\cdot\vec{\psi})(\frac{\vec{\varpi}}{R}\cdot\frac{\vec{\varpi}}{R}) \\
& + W_{311}(\vec{\psi}\cdot\vec{\psi})(\vec{\psi}\cdot\frac{\vec{\varpi}}{R})
\end{aligned}
\tag{1.5}
$$

where W_{040} is the spherical aberration coefficient, W_{131} is the coma coefficient, W_{222} is the astigmatism coefficient, W_{220} is the curvature of field coefficient, and W_{311} is the distortion coefficient. These aberration coefficients depend only on the curvature of the mirror, R, the conic constant of the mirror, K, the magnification of the mirror, m, the position of the object for the mirror, s, and the index of refraction immediately preceding the mirror, n[6]. In §5.1 of his book Schroeder [18] shows that the aberrations which vary linearly with ray height on the optic must be zero for conic section optics which serve as their own pupils. We therefore set W_{311} to zero and ignore it in the following discussion. The values for the other coefficients are given in Table 1.1.

Following Schroeder [18], one finds that if the pupil is offset by W along the axis of the mirror, the position at which a ray lands on the mirror, $\vec{\varpi}$ depends upon its position on the pupil, $\vec{\rho}$ and the angle the chief ray makes to the pupil normal, $\vec{\sigma}$ (which is defined to be the field angle), and upon W. The angle that the ray makes with the axis of the mirror, $\vec{\psi}$ depends upon field angle $\vec{\sigma}$ and the pupil offset, W.

If the mirror is tilted by angle $\vec{\alpha}$, it changes the angle $\vec{\psi}$ that a ray makes with

[6]We adopt the convention of Schroeder [18] whereby rays traveling in opposite directions encounter oppositely signed indices of refraction; a ray incident on the primary mirror through air ($n = 1$) will encounter a negative index of refraction ($n = -1$) once reflected and traveling towards the secondary. Therefore, although this discussion deals primarily with mirrors and thin lenses, the index of the refraction of the material surrounding the optics cannot be entirely ignored.

the mirror's axis. And if the mirror is decentered from the optical axis (which is perpendicular to and centered on the pupil) by $\vec{\ell}$, it changes both the position at which a ray lands on the mirror, ϖ and the angle $\vec{\psi}$ that the ray makes with respect to the mirror's axis.

The net effect of a pupil offset or a misalignment of the mirror relative to the pupil is to shift the position $\vec{\varpi}$ at which a given ray strikes the mirror and to change the angle $\vec{\psi}$ that the ray makes with the axis of the mirror. The transformations from pupil coordinates, $\vec{\rho}$ and field angle, $\vec{\sigma}$ to mirror coordinates and mirror angle for a mirror despaced by an amount W and decentered and tilted by $\vec{l}$ and $\vec{\alpha}$ are then[7]

$$\vec{\psi} = (1 - \frac{W}{s})\vec{\sigma} - (\vec{\alpha} + \frac{\vec{l}}{s}) \tag{1.6}$$

$$\vec{\varpi} = (\vec{\rho} - W\vec{\sigma}) - \vec{l}. \tag{1.7}$$

An offset of the pupil from the mirror by an amount W causes what was Seidel spherical aberration to manifest itself as a combination of spherical aberration, coma, astigmatism, curvature of field and distortion, all of which have the symmetric Seidel field dependence. Likewise what was coma manifests itself as a combination of coma, astigmatism, curvature of field and distortion. This cascade downward from spherical to coma to astigmatism and curvature of field and finally to distortion is embodied in the "stop shift" formulae (e.g. Wilson 26).

Decenterings and tilts of the mirror relative to the pupil also produce cascades.

[7]In deriving equations (1.6) and (1.7) we assume that all of the effects of the curvature of an optic on aberrations are embodied in equation (1.5), and we subsequently treat displacements, W, decenters, $\vec{\ell}$ and tilts, $\vec{\alpha}$ of an optic as displacements, decenters, and tilts of the flat surface defined by the plane containing the vertex of that optic. This is equivalent to using a first order approximation of pupil and field coordinates. While this assumption reproduces the stop shift formulae given in Schroeder [18] and Wilson [26], it is not strictly correct in the cases of large or very curved mirrors, large fields, or cases where the stop is quite close to the optic. In particular, when a telescope's primary mirror is the aperture stop, the computed aberrations are only correct when W for the primary mirror is set equal to zero, even though the physical aperture is defined by the edge of the optic, which may actually be a finite distance from the optic's vertex. Setting W equal to zero in this special case is natural, as equation (1.5) completely describes the aberrations introduced by an optic that is its own pupil, without any need for modification. However, this inconsistency would seem to indicate that the assumptions that predicate equations (1.6) and (1.7) may need to be modified in order to compute higher order aberrations.

For an axially symmetric telescope we may assume that these tilts and decenters are small and ignore terms that are quadratic and higher in either or both. In the aberration patterns associated with the surviving linear terms, a field angle vector $\vec{\sigma}$ is replaced by either a tilt, $\vec{\alpha}$ or a decenter, $\vec{\ell}/R$. The field angle exponents for the misalignment aberration patterns are therefore smaller by one than those of the corresponding Seidel aberrations.

Table 1.2 gives aberration patterns that arise when a mirror is offset by W with respect to its pupil, and decentered and tilted by small amounts.

The different signs for odd and even numbered mirrors arise from the fact that the chief ray for a given optic may be traveling in the opposite angular direction than the chief ray on the pupil for the primary mirror, which here determines the field angle $\vec{\sigma}$. Put otherwise, the sign accounts for the fact that preceding mirrors flipped the images. It does not account for the changing indices of refraction which are contained in the W_{klm} coefficients. The σ-type distortion patterns have factors $\vec{\sigma} \cdot \frac{\vec{l}}{R}$ or $\vec{\sigma} \cdot \vec{\alpha}$. The ρ-type distortion patterns have factors $\vec{\rho} \cdot \frac{\vec{l}}{R}$ or $\vec{\rho} \cdot \vec{\alpha}$.

1.3.7 application to 2-mirror telescopes and 2.5-mirror telescopes

Table 1.2 of the previous subsection gives the third-order aberrations for a single mirror with a pupil offset by W along the optical axis. The aberrations for a 2-mirror telescope are found by computing the elements of two such tables, one for the primary and one for the secondary, and adding.

Before one can use Table 1.2 to compute aberrations, one must first know the location of the center of the field as it is defined by the pointing of the pupil. If the center of pointing is unknown then one must add an additional vector variable to the table, $\vec{m}$, which maps the true field coordinate, $\vec{\sigma}$ to that adopted for measurement, $\vec{\sigma'}$ via the relation $\vec{\sigma} \rightarrow \vec{\sigma'} - \vec{m}$. This focal plane decenter will mathematically map Seidel terms to misalignment terms, but it will not physically aberrate the images. For the sake of simplicity, we here assume that the center of pointing is known and

Table 1.2. Symmetric and asymmetric aberration patterns for mirrors offset, decentered and tilted with respect to the pupil.

aberration	pupil offset W	decenter $\vec{\ell}$	tilt $\vec{\alpha}$
spherical	$(\frac{\vec{\rho}}{R}\cdot\frac{\vec{\rho}}{R})(\frac{\vec{\rho}}{R}\cdot\frac{\vec{\rho}}{R})\times W_{040}$		
coma	$(\frac{\vec{\rho}}{R}\cdot\frac{\vec{\rho}}{R})(\frac{\vec{\rho}}{R}\cdot\vec{\sigma})\times\mp[$[a] $\left(\frac{W}{s}-1\right)W_{131}$ $+4\frac{W}{R}W_{040}\quad]$	$(\frac{\vec{\rho}}{R}\cdot\frac{\vec{\rho}}{R})(\frac{\vec{\rho}}{R}\cdot\frac{\vec{l}}{R})\times[$ $-\left(\frac{R}{s}\right)W_{131}$ $-4W_{040}\quad]$	$(\frac{\vec{\rho}}{R}\cdot\frac{\vec{\rho}}{R})(\frac{\vec{\rho}}{R}\cdot\vec{\alpha})\times[$ $-W_{131}$ $]$
astigmatism	$(\frac{\vec{\rho}}{R}\cdot\vec{\sigma})(\frac{\vec{\rho}}{R}\cdot\vec{\sigma})\times[$ $\left(\frac{W}{s}-1\right)^2W_{222}$ $+2\frac{W}{R}\left(\frac{W}{s}-1\right)W_{131}$ $+4\frac{W^2}{R^2}W_{040}\quad]$	$(\frac{\vec{\rho}}{R}\cdot\vec{\sigma})(\frac{\vec{\rho}}{R}\cdot\frac{\vec{l}}{R})\times\pm[$[a] $2\left(\frac{R}{s}\right)\left(\frac{W}{s}-1\right)W_{222}$ $+2\left(\frac{2W}{s}-1\right)W_{131}$ $+8\frac{W}{R}W_{040}\quad]$	$(\frac{\vec{\rho}}{R}\cdot\vec{\sigma})(\frac{\vec{\rho}}{R}\cdot\vec{\alpha})\times\pm[$[a] $2\left(\frac{W}{s}-1\right)W_{222}$ $+2\frac{W}{R}W_{131}$ $]$
COF	$(\frac{\vec{\rho}}{R}\cdot\frac{\vec{\rho}}{R})(\vec{\sigma}\cdot\vec{\sigma})\times[$ $\left(\frac{W}{s}-1\right)^2W_{220}$ $+\frac{W}{R}\left(\frac{W}{s}-1\right)W_{131}$ $+2\frac{W^2}{R^2}W_{040}\quad]$	$(\frac{\vec{\rho}}{R}\cdot\frac{\vec{\rho}}{R})(\vec{\sigma}\cdot\frac{\vec{l}}{R})\times\pm[$[a] $2\left(\frac{R}{s}\right)\left(\frac{W}{s}-1\right)W_{220}$ $+\left(\frac{2W}{s}-1\right)W_{131}$ $+4\frac{W}{R}W_{040}\quad]$	$(\frac{\vec{\rho}}{R}\cdot\frac{\vec{\rho}}{R})(\vec{\sigma}\cdot\vec{\alpha})\times\pm[$[a] $2\left(\frac{W}{s}-1\right)W_{220}$ $+\frac{W}{R}W_{131}$ $]$
distortion	$(\frac{\vec{\rho}}{R}\cdot\vec{\sigma})(\vec{\sigma}\cdot\vec{\sigma})\times\mp[$[a, b] $2\frac{W}{R}\left(\frac{W}{s}-1\right)^2W_{220}$ $+2\frac{W}{R}\left(\frac{W}{s}-1\right)^2W_{222}$ $+3\frac{W^2}{R^2}\left(\frac{W}{s}-1\right)W_{131}$ $+4\frac{W^3}{R^3}W_{040}\quad]$	$(\frac{\vec{\rho}}{R}\cdot\frac{\vec{l}}{R})(\vec{\sigma}\cdot\vec{\sigma})\times[$ $-2\left(\frac{W}{s}-1\right)^2W_{220}$ $-2\left(\frac{W}{s}\right)\left(\frac{W}{s}-1\right)W_{222}$ $-2\frac{W}{R}\left(\frac{3W}{2s}-1\right)W_{131}$ $-4\frac{W^2}{R^2}W_{040}\quad]$	$(\frac{\vec{\rho}}{R}\cdot\vec{\alpha})(\vec{\sigma}\cdot\vec{\sigma})\times[$ $-2\frac{W}{R}\left(\frac{W}{s}-1\right)W_{222}$ $-\frac{W^2}{R^2}W_{131}$ $]$
		$(\frac{\vec{\rho}}{R}\cdot\vec{\sigma})(\vec{\sigma}\cdot\frac{\vec{l}}{R})\times[$ $-4\left(\frac{W}{s}\right)\left(\frac{W}{s}-1\right)W_{220}$ $-2\left(\frac{W}{s}-1\right)\left(\frac{2W}{s}-1\right)W_{222}$ $-4\frac{W}{R}\left(\frac{3W}{2s}-1\right)W_{131}$ $-8\frac{W^2}{R^2}W_{040}\quad]$	$(\frac{\vec{\rho}}{R}\cdot\vec{\sigma})(\vec{\sigma}\cdot\vec{\alpha})\times[$ $-4\frac{W}{R}\left(\frac{W}{s}-1\right)W_{220}$ $-2\frac{W}{R}\left(\frac{W}{s}-1\right)W_{222}$ $-2\frac{W^2}{R^2}W_{131}$ $]$

[a]The upper sign is for a primary, tertiary, or other odd numbered mirror. The lower sign is for a secondary or even numbered mirror.

[b]The W_{311} term has been omitted as it is equal to zero.

treat a decentered focal plane as a 'complication' in §1.7.

For many two-mirror telescopes the pupil is coincident with the primary. If one also takes the primary to define the pointing of the telescope, one can take the pupil offset, W_1, the mirror decenter, $\vec{\ell}_1$ and the mirror tilt, $\vec{\alpha}_1$ all to be zero. The misalignment patterns are then due entirely to the decenter, $\vec{\ell}_2$ and tilt, $\vec{\alpha}_2$ of the secondary. One need only measure two of the five misalignment patterns in Table 1.2 to align the telescope. If the aperture stop (and consequently the pointing) instead coincide with the secondary mirror as in Noethe & Guisard [12], the misalignments of the secondary mirror may be treated as identically zero and only the misalignments of the primary mirror relative to its pupil need to be considered. In this case as well, one need only measure two of the five misalignment patterns in Table 1.2 to align the telescope. There is a third case where the aperture stop is independent from either of the mirrors. In this case we would treat the aperture stop as a third optical element and analyze this telescope configuration as a three mirror telescope.

McLeod [10] measures coma and astigmatism in his two mirror telescope. He might in principle have used the two distortion patterns, but these would require a high precision astrometric catalog (perhaps using galaxy positions to avoid the effects of stellar proper motions). Moreover as the misalignment distortion patterns vary as a higher powers of field angle than the misalignment astigmatism and coma patterns, they might be expected to have smaller amplitudes. McLeod might also have used curvature of field, although here there is the danger that the detector might be tilted with respect to the primary. Or, had he been feeling particularly masochistic, he might have measured all five patterns, for the sake of redundancy.

With their folding flats, the Magellan telescopes in their Nasmyth configuration qualify as 2.5-mirror telescopes. One need not worry about the decentering of the tertiary but one must measure and correct for its tilt, $\vec{\alpha}_3$. The alignment procedure described by Palunas et al. [13] adds the curvature of field misalignment pattern (equivalent to a focal plane tilt) to those of coma and astigmatism.

1.4 Aligning 3-mirror telescopes using distortion patterns

Calculating the aberration patterns for a 3-mirror telescope (say a three mirror anastigmat, henceforth a TMA) is not quite twice as difficult as for a 2-mirror telescope. One applies Table 1.2 to the tertiary and finds misalignment patterns that depend upon the decenter $\vec{\ell}_3$ and tilt $\vec{\alpha}_3$ of the tertiary. If the stop is coincident with the primary, only the secondary and tertiary contribute to the five third-order misalignment patterns in Table 1.2. The patterns are linear in the decenter and tilt vectors, so that the combined wavefront gives the same five patterns, each characterized by a new pattern 2-vector. Each pattern 2-vector, $\vec{\mu}$, is a linear combination of the four misalignment 2-vectors, the tilts $\vec{\alpha}_2$ and $\vec{\alpha}_3$, and the decenterings $\vec{\ell}_2$ and $\vec{\ell}_3$. Likewise if the stop is coincident with the secondary or tertiary mirrors, only tilts and decenters of the other two mirrors contribute.

If coma, astigmatism and curvature of field are the only aberrations that adversely affect science, there is a two-dimensional "subspace of benign misalignment" for which the coma, astigmatism and curvature of field misalignment patterns are all zero in the limit of small misalignments. But if one does not bring additional information to bear, one runs the risk of drifting increasingly far from perfect alignment. This would produce large misalignment distortion, and ultimately, fifth-order misalignment patterns and third-order patterns that depend quadratically on the mirror tilts and decenters.

To measure the misalignment distortion patterns one would need either overlapping fields of images [21] or pre-existing astrometry. If one uses overlapping fields, one risks changing the misalignment between pointings, thus rendering distortion of limited use for measuring alignment at a given pointing. If one relies on pre-existing astrometry, the accuracy with which the distortion patterns could be measured would then be limited by the accuracy of the astrometric catalog. Moreover, regardless the technique used to measure the aberrations, the misalignment distortion patterns might be expected to have smaller amplitudes than misalignment astigmatism and

coma as the misalignment distortion patterns vary as a higher power of field angle. This raises the question of whether one might use fifth-order aberration patterns to keep the telescope aligned.

1.5 Generic fifth-order aberration patterns

1.5.1 fifth-order aberrations for a single mirror

In §1.3.6 we considered the third-order aberrations produced by a single mirror with a stop at the mirror. The generalization to fifth-order is straightforward. The fifth-order wavefront delay, G^{5th} for a ray that hits the mirror at position $\vec{\varpi}$ and that makes an angle $\vec{\psi}$ with the axis of the mirror is given by

$$\begin{aligned} G^{5th} = & W_{060}(\frac{\vec{\varpi}}{R}\cdot\frac{\vec{\varpi}}{R})(\frac{\vec{\varpi}}{R}\cdot\frac{\vec{\varpi}}{R})(\frac{\vec{\varpi}}{R}\cdot\frac{\vec{\varpi}}{R}) + W_{151}(\frac{\vec{\varpi}}{R}\cdot\frac{\vec{\varpi}}{R})(\frac{\vec{\varpi}}{R}\cdot\frac{\vec{\varpi}}{R})(\frac{\vec{\varpi}}{R}\cdot\vec{\psi}) \\ & + W_{242}(\frac{\vec{\varpi}}{R}\cdot\frac{\vec{\varpi}}{R})(\frac{\vec{\varpi}}{R}\cdot\vec{\psi})(\frac{\vec{\varpi}}{R}\cdot\vec{\psi}) + W_{240}(\frac{\vec{\varpi}}{R}\cdot\frac{\vec{\varpi}}{R})(\frac{\vec{\varpi}}{R}\cdot\frac{\vec{\varpi}}{R})(\vec{\psi}\cdot\vec{\psi}) \\ & + W_{333}(\frac{\vec{\varpi}}{R}\cdot\vec{\psi})(\frac{\vec{\varpi}}{R}\cdot\vec{\psi})(\frac{\vec{\varpi}}{R}\cdot\vec{\psi}) + W_{331}(\frac{\vec{\varpi}}{R}\cdot\frac{\vec{\varpi}}{R})(\frac{\vec{\varpi}}{R}\cdot\vec{\psi})(\vec{\psi}\cdot\vec{\psi}) \\ & + W_{422}(\frac{\vec{\varpi}}{R}\cdot\vec{\psi})(\frac{\vec{\varpi}}{R}\cdot\vec{\psi})(\vec{\psi}\cdot\vec{\psi}) + W_{420}(\frac{\vec{\varpi}}{R}\cdot\frac{\vec{\varpi}}{R})(\vec{\psi}\cdot\vec{\psi})(\vec{\psi}\cdot\vec{\psi}) \\ & + W_{511}(\frac{\vec{\varpi}}{R}\cdot\vec{\psi})(\vec{\psi}\cdot\vec{\psi})(\vec{\psi}\cdot\vec{\psi}) \end{aligned} \tag{1.8}$$

Since the pupil is coincident with the mirror, we might equally well have written the same equations but with position on the mirror $\vec{\varpi}$ replaced by position on the pupil $\vec{\rho}$ and the angle that a ray makes with the axis of the mirror, $\vec{\psi}$ replaced by the field angle $\vec{\sigma}$. For the remainder of this subsection we shall take $\vec{\rho} = \vec{\varpi}$ and $\vec{\sigma} = \vec{\psi}$.

W_{511}: fifth-order distortion

The W_{511} term has the same variation on the pupil as distortion, but varies as field angle to the fifth. We shall refer to this as "fifth-order distortion."[8]

[8]Our nomenclature is driven primarily by the functional form of the aberration on the pupil. Thus an aberration that varies as $\rho^3\cos\phi$ is referred to as coma. In this scheme third-order (Seidel) coma

W_{420}: fifth-order defocus

The W_{420} term has the same variation on the pupil as defocus, and produces a point spread function indistinguishable from that of Seidel curvature of field . But as this term varies as the fourth power of field angle rather than quadratically, we call this term "fifth-order defocus."

W_{422}: fifth-order astigmatism

The W_{422} term has the same variation on the pupil as third-order astigmatism, and produces a point spread function indistinguishable from it. But as this term varies as the fourth power of field angle rather than quadratically, we call this term "fifth-order astigmatism." Again as with third-order astigmatism, this term varies on the pupil as $\rho^2 \cos^2 \phi$. It can be decomposed into a term that varies as Zernike astigmatism, $\rho^2 \cos 2\phi$, and a second that varies as defocus, $\rho^2 \cos^0 \phi$,

W_{331}: fifth-order coma

The W_{331} term has the same variation on the pupil as coma, but varies as field angle cubed. We call this "fifth-order coma."

W_{333}: trefoil

The W_{333} term varies as $\rho^3 \cos^3 \phi$ on the pupil and as field angle cubed. None of the third-order aberrations has this behavior on the pupil; here we call it trefoil. This term can be decomposed into a term that varies as Zernike trefoil, $\rho^3 \cos 3\phi$, and a second that varies as coma, $\rho^3 \cos \phi$. Figure 1-5 shows the point spread function due to Zernike trefoil with varying amounts of an aberration that varies as ρ^3 added to it.

varies linearly with field angle and fifth-order coma varies as the cube of field angle. By contrast, the term that varies as $\rho^5 \cos \phi$ on the pupil is referred to here as second coma or coma-II. Hopkins [2] calls this term fifth-order coma, but from our pupil oriented perspective this term, albeit one of fifth-order, cannot be called coma, which can only vary as $\rho^3 \cos \phi$. Curiously, we agree with Hopkins in calling the term that varies as $\rho^2 \cos^2 \phi$ fifth-order astigmatism and in calling the term that varies as $\rho \cos \phi$ fifth-order distortion. We reserve the term "Zernike" aberrations for the orthogonalized linear combinations of aberrations described here.

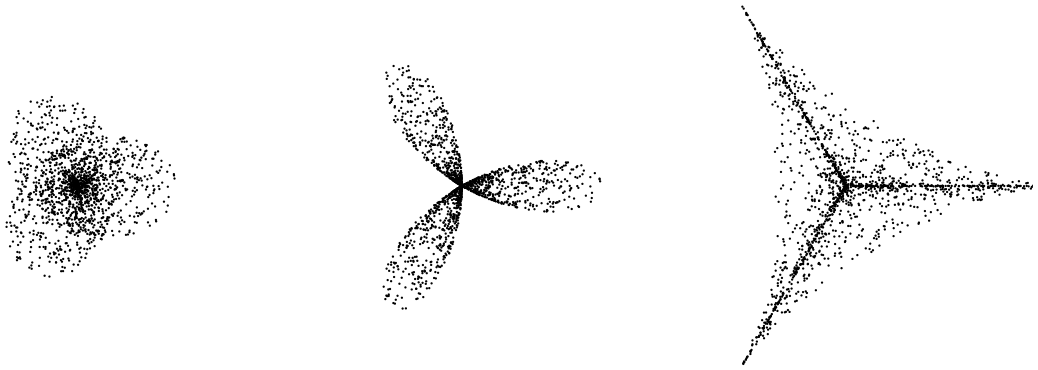

Figure 1-5 Point spread functions due to trefoil with $G^{tref} = \rho^3 \cos 3\phi$. Increasing amounts of a symmetric wavefront $G^{sym} = \rho^3$ have been added to bring out the three-fold symmetry of the wavefront. (a) $+\frac{2}{5}G^{sym}$ (b) $+G^{sym}$ (c) $+2G^{sym}$

W_{240}: fifth-order spherical

The W_{240} has the same variation on the pupil as spherical aberration, but varies as field angle squared. We shall refer to this as this "fifth-order spherical."

W_{242}: second astigmatism

Figure 1-6 Point spread functions for ordinary astigmatism, $G^{astig-I} = \rho^2 cos2\phi$ and second astigmatism, $G^{astig-II} = \rho^4 cos2\phi$. (a) Ordinary astigmatism $+\frac{1}{4}G^{defocus}$. (b) Pure ordinary astigmatism. (c) Pure second astigmatism.

The W_{242} term varies as $\rho^4 \cos^2 \phi$ on the pupil. The angular dependence is that of astigmatism but the radial dependence is quartic not quadratic. We shall call this "second astigmatism" or "astigmatism-II." Figure 1-6 shows the PSF for second

astigmatism next to those for ordinary astigmatism.

W_{151}: second coma

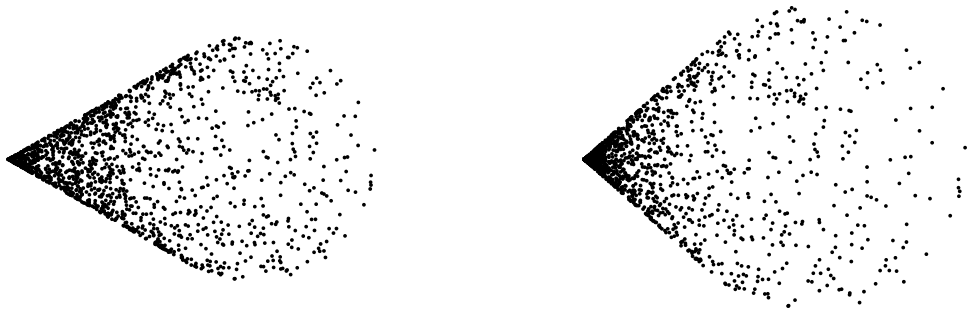

Figure 1-7 (a) Off axis (ordinary) coma PSF for the third-order and fifth-order coma patterns. The sine of the apex half angle is 1/2, giving an apex angle of 60°. (b) Off axis second coma PSF. The sine of the apex half angle is 2/3, giving an apex angle of 83.6°.

The W_{151} term varies as $\rho^5 \cos\phi$ on the pupil. The azimuthal dependence is that of coma but the radial dependence is quintic not cubic. We shall refer to this as "second coma" or "coma-II." Figure 1-7 shows a PSF produced by second coma alongside one produced by ordinary (first) coma.

W_{060}: second spherical

We shall call the W_{060} term "second spherical" or "spherical-II." Were we strictly consistent we would have called spherical aberration "second defocus" and would have called this "third defocus" but as Emerson says, a foolish consistency is the hobgoblin of a small mind.

Table 1.3. Fifth-order aberration patterns

aberration	symmetric	misalignment
2nd spherical	$(\vec{\rho}\cdot\vec{\rho})(\vec{\rho}\cdot\vec{\rho})(\vec{\rho}\cdot\vec{\rho})$	
2nd coma	$(\vec{\rho}\cdot\vec{\rho})(\vec{\rho}\cdot\vec{\rho})(\vec{\rho}\cdot\vec{\sigma})$	$(\vec{\rho}\cdot\vec{\rho})(\vec{\rho}\cdot\vec{\rho})(\vec{\rho}\cdot\vec{\mu}_{cII})$
2nd astigmatism	$(\vec{\rho}\cdot\vec{\rho})(\vec{\rho}\cdot\vec{\sigma})(\vec{\rho}\cdot\vec{\sigma})$	$(\vec{\rho}\cdot\vec{\rho})(\vec{\rho}\cdot\vec{\sigma})(\vec{\rho}\cdot\vec{\mu}_{aII})$
fifth-order spherical	$(\vec{\rho}\cdot\vec{\rho})(\vec{\rho}\cdot\vec{\rho})(\vec{\sigma}\cdot\vec{\sigma})$	$(\vec{\rho}\cdot\vec{\rho})(\vec{\rho}\cdot\vec{\rho})(\vec{\sigma}\cdot\vec{\mu}_{5s})$
trefoil	$(\vec{\rho}\cdot\vec{\sigma})(\vec{\rho}\cdot\vec{\sigma})(\vec{\rho}\cdot\vec{\sigma})$	$(\vec{\rho}\cdot\vec{\sigma})(\vec{\rho}\cdot\vec{\sigma})(\vec{\rho}\cdot\vec{\mu}_{t})$
fifth-order coma	$(\vec{\rho}\cdot\vec{\rho})(\vec{\rho}\cdot\vec{\sigma})(\vec{\sigma}\cdot\vec{\sigma})$	$(\vec{\rho}\cdot\vec{\rho})(\vec{\rho}\cdot\vec{\sigma})(\vec{\sigma}\cdot\vec{\mu}_{5c\sigma})$
		$(\vec{\rho}\cdot\vec{\rho})(\vec{\sigma}\cdot\vec{\sigma})(\vec{\rho}\cdot\vec{\mu}_{5c\rho})$
fifth-order astigmatism	$(\vec{\rho}\cdot\vec{\sigma})(\vec{\rho}\cdot\vec{\sigma})(\vec{\sigma}\cdot\vec{\sigma})$	$(\vec{\rho}\cdot\vec{\sigma})(\vec{\rho}\cdot\vec{\sigma})(\vec{\sigma}\cdot\vec{\mu}_{5a\sigma})$
		$(\vec{\rho}\cdot\vec{\sigma})(\vec{\sigma}\cdot\vec{\sigma})(\vec{\rho}\cdot\vec{\mu}_{5a\rho})$
fifth-order defocus	$(\vec{\rho}\cdot\vec{\rho})(\vec{\sigma}\cdot\vec{\sigma})(\vec{\sigma}\cdot\vec{\sigma})$	$(\vec{\rho}\cdot\vec{\rho})(\vec{\sigma}\cdot\vec{\sigma})(\vec{\sigma}\cdot\vec{\mu}_{5f})$
fifth-order distortion	$(\vec{\rho}\cdot\vec{\sigma})(\vec{\sigma}\cdot\vec{\sigma})(\vec{\sigma}\cdot\vec{\sigma})$	$(\vec{\rho}\cdot\vec{\sigma})(\vec{\sigma}\cdot\vec{\sigma})(\vec{\sigma}\cdot\vec{\mu}_{5d\sigma})$
		$(\vec{\sigma}\cdot\vec{\sigma})(\vec{\sigma}\cdot\vec{\sigma})(\vec{\rho}\cdot\vec{\mu}_{5d\rho})$

1.5.2 fifth-order aberrations for misaligned systems

Tilts and decenterings of mirrors produce misalignment patterns in a manner entirely analogous to those of third-order aberrations. The dependence upon field and pupil position and the first order dependence on misalignments are given in Table 1.3. Equations (1.6) and (1.7) are used to transform from the positions and angles with respect to the optic, $\vec{\varpi}$ and $\vec{\psi}$ of equation (1.8) to positions and angles with respect the pupil, $\vec{\rho}$ and $\vec{\sigma}$.[9] Terms with the same dependence on both of the latter are then added. The vectors $\vec{\mu}$ indicate linear combinations of misalignment angle $\vec{\alpha}$ and decenter $\vec{\ell}$.

In Table 1.3 we give only the dependence upon pupil position and field angle for the symmetric fifth-order aberration patterns and their associated misalignment patterns. For the third-order aberrations, there was one misalignment pattern each associated with coma, astigmatism and curvature of field, with two misalignment

[9]Third-order aberrations produced by an optic (equation (1.5)) may also contribute to the fifth-order aberrations on the pupil when the pupil and the optic do not coincide. As noted in §§1.3.6 equations (1.6) and (1.7) are truncated at first order in pupil and field coordinates. Analogous equations for (1.6) and (1.7) that have been expanded to third order can map third-order aberrations on the optic to fifth-order aberrations on the pupil. Other such approximations may also need to be relaxed in order to compute the magnitudes of the fifth-order aberrations.

patterns associated with distortion. There are again distinct σ and ρ misalignment patterns for fifth-order distortion, and now also for fifth-order astigmatism and fifth-order coma.

1.5.3 fifth-order aberration patterns and alignment

The amplitudes of aberration patterns implicit in Table 1.3 provide, at least in principle, additional information for use in aligning telescopes. But in all cases there are similarities between the fifth-order misalignment aberration patterns and their third-order counterparts. The ability to distinguish between the two depends, for the first group described below, upon the sampling of the wavefront, and, for the second group, upon the sampling of the field.

second coma: misalignment

The misalignment aberration pattern for second coma, shown in Figure 1-8 is identical to that for ordinary (first) coma (see Figure 1-1). The point spread functions for second coma and ordinary (first) coma have the same azimuthal dependence on pupil position but different radial dependence. The ability to distinguish between the coma-II misalignment pattern and the coma-I misalignment pattern therefore depends critically upon the sampling of the wavefront.

second astigmatism: misalignment

As with second coma, the misalignment aberration pattern for second astigmatism, shown in Figure 1-9 is identical to that for ordinary (first) astigmatism (see Figure 1-2). The point spread functions for second astigmatism and ordinary (first) astigmatism have the same angular dependence on pupil position but different radial dependence. The ability to distinguish between the astigmatism-II misalignment pattern and the astigmatism-I misalignment pattern again depends critically upon the sampling of the wavefront.

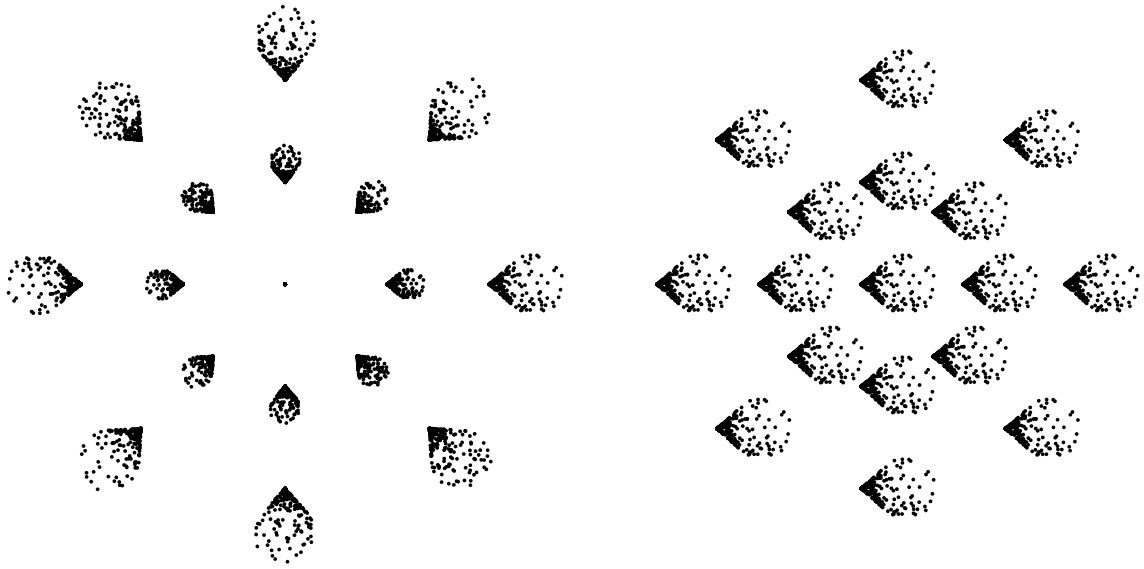

Figure 1-8 Second coma field patterns. (a) Second coma pattern typical of an aligned telescope. (b) Second coma pattern indicating a tilt and (or) decenter of a mirror along the x axis.

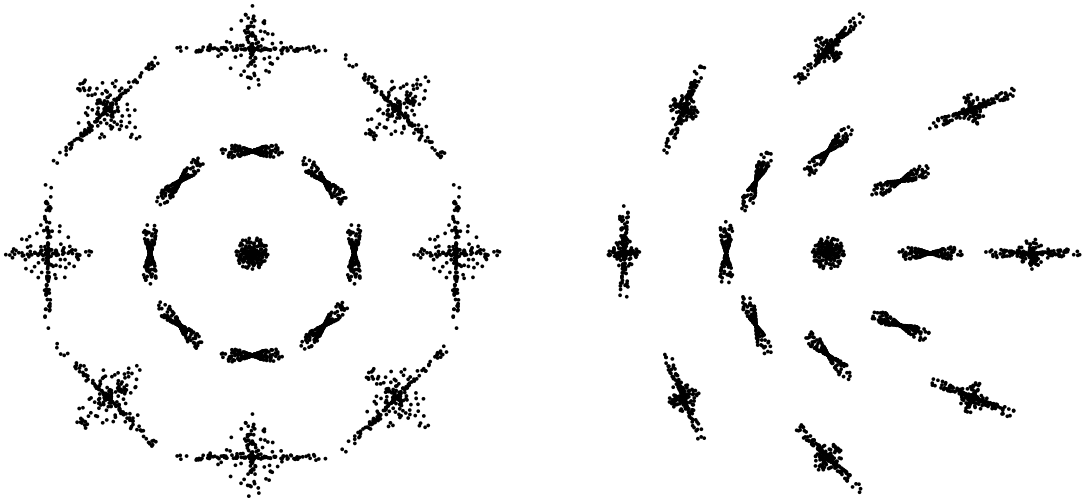

Figure 1-9 Second astigmatism field patterns. (a) Second astigmatism pattern typical of an aligned telescope. (b) Second astigmatism pattern indicating a tilt and (or) decentering of a mirror along the x axis. Spherical aberration has been added to bring out the asymmetry of the pattern.

fifth-order spherical: misalignment

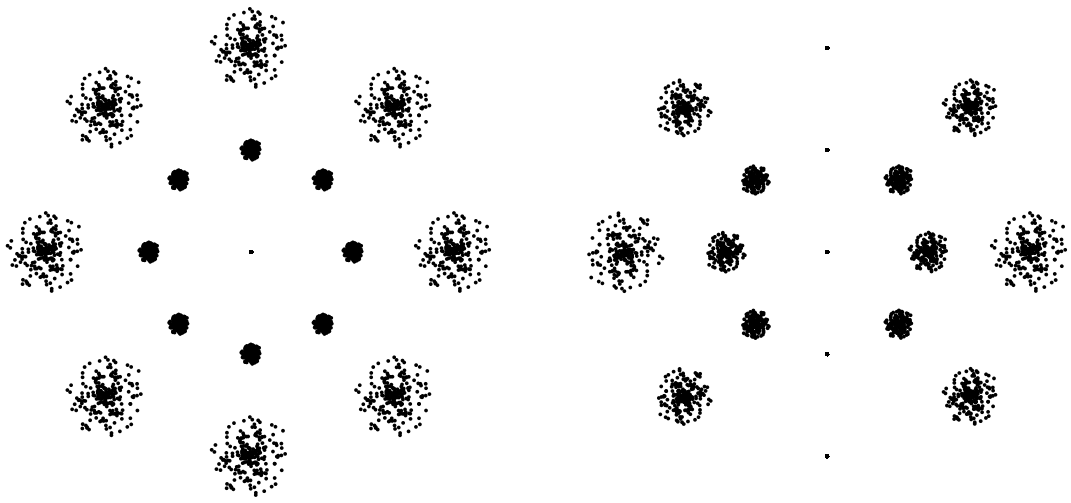

Figure 1-10 Fifth-order spherical field patterns. (a) Spherical aberration pattern typical of an aligned telescope. (b) Spherical aberration indicating a tilt and (or) decenter of a mirror along the x axis.

The aberration patterns for fifth-order spherical, shown in Figure 1-10 are identical to those for those of curvature of field. However the point spread functions are identical to spherical aberration, which itself has the same angular dependence on the pupil as defocus and COF, but a different radial dependence. The ability to distinguish between the fifth-order spherical and curvature of field misalignment pattern once again depends critically upon the sampling of the wavefront. The ability to distinguish between fifth-order spherical and ordinary spherical depends on the sampling of the field.

trefoil: misalignment

The PSF for trefoil is quite different from that of any of the Seidel third-order aberrations, as is its misalignment pattern, shown in Figure 1-11.

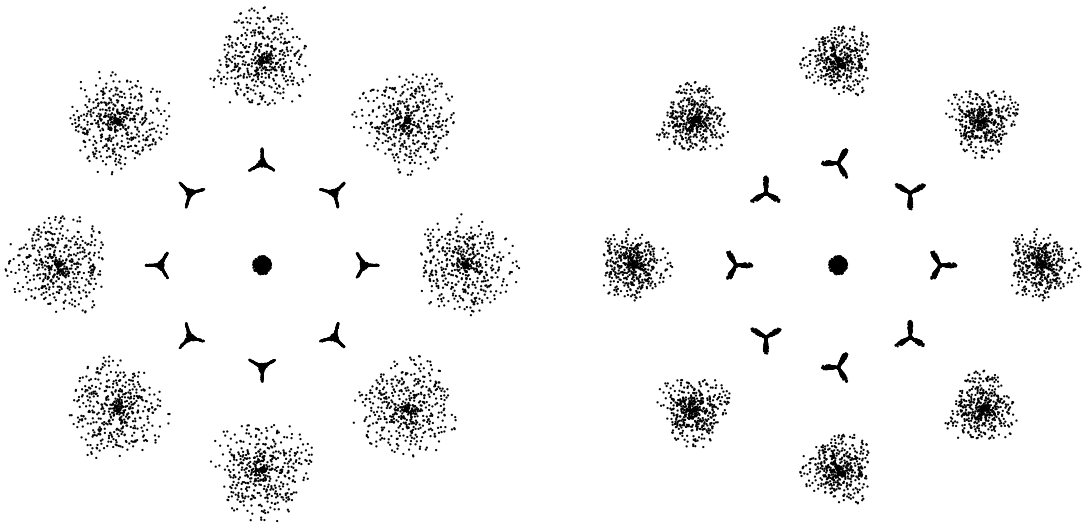

Figure 1-11 Trefoil field patterns. (a) Trefoil pattern characteristic of an aligned telescope. (b) Trefoil indicating a tilt and (or) decenter of a mirror along the x axis. In both cases a constant wavefront varying as ρ^3 has been added to bring out the orientation of the aberration.

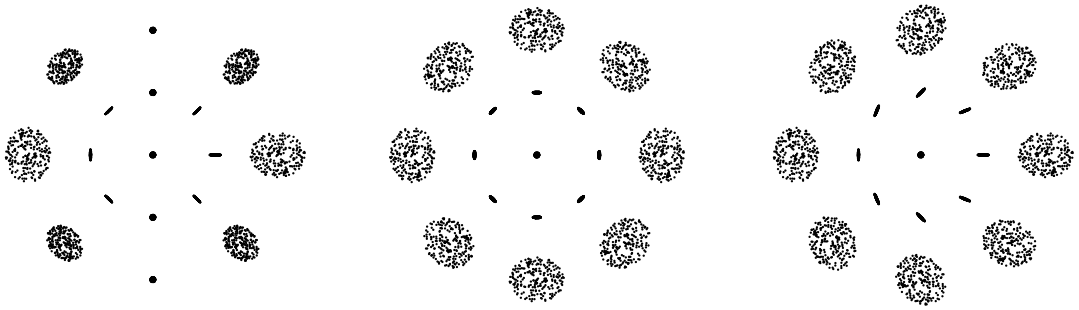

Figure 1-12 Fifth-order astigmatism field patterns. (a) The "σ" astigmatism pattern indicating a tilt and (or) decentering of a mirror along the x axis. Note that the astigmatism is radially aligned. (b) Astigmatism pattern typical of an aligned telescope. (c) The "ρ" astigmatism pattern indicating a tilt and (or) decentering of a mirror along the x axis. Note that the azimuthal dependence on field angle is identical to that for third-order misalignment astigmatism. A constant defocus has been added to all three panels to show the orientations of the aberrations.

fifth-order astigmatism: misalignment

The PSF for fifth-order astigmatism is identical to that of Seidel, third-order astigmatism. But the two misalignment aberration patterns shown in Figure 1-12 are unlike third-order misalignment astigmatism (see Figure 1-2). The ρ misalignment pattern has the same azimuthal field dependence as for third-order astigmatism, but has a different radial dependence. The σ misalignment pattern has a different azimuthal field dependence and a different radial dependence. The ability to distinguish between the two fifth-order astigmatism misalignment patterns and the third-order astigmatism misalignment pattern therefore depends critically upon the sampling of the field rather than the wavefront.

fifth-order coma: misalignment

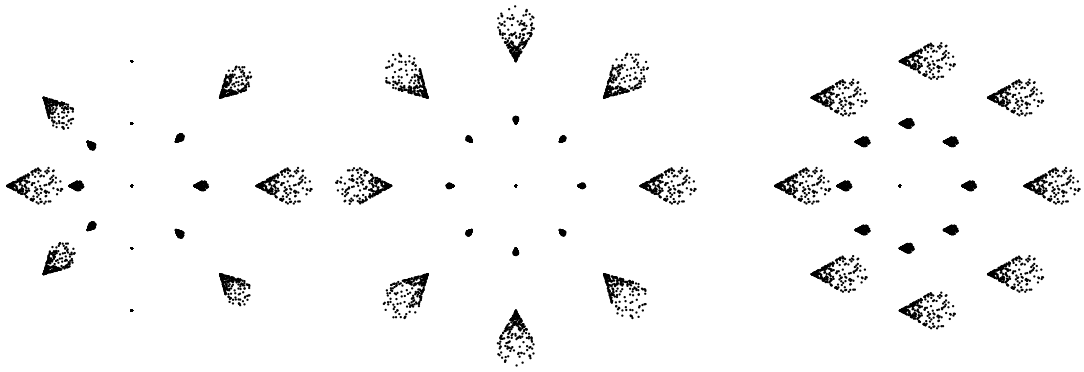

Figure 1-13 Fifth-order coma field patterns. (a) The "σ" coma pattern indicating a tilt and (or) decentering of a mirror along the x axis. Note that the coma is radially aligned. (b) Fifth-order coma characteristic of an aligned telescope (c) The "ρ" coma pattern indicating a tilt and (or) decentering of a mirror along the x axis. Note that the azimuthal dependence on field angle is identical to that for third-order misalignment coma.

As with fifth-order astigmatism, the PSF for fifth-order coma is identical to that of Seidel, third-order coma. But the two misalignment aberration patterns shown in Figure 1-13 are unlike third-order misalignment coma (see Figure 1-1). The ρ misalignment pattern has the same azimuthal field dependence as for third-order coma, but different radial dependence. The σ misalignment pattern has a different

azimuthal field dependence and a different radial dependence. As with fifth-order astigmatism, the ability to distinguish between the two fifth-order coma misalignment patterns and the third-order coma misalignment pattern therefore depends critically upon the sampling of the field rather than the wavefront.

fifth-order defocus: misalignment

As with fifth-order astigmatism and coma, the PSF for fifth-order defocus is identical to that of curvature of field (which might equally well be called third-order defocus). But the misalignment aberration patterns are not identical. They have the same angular dependence, but exhibit a different radial dependence. Once again, the ability to distinguish between the fifth-order defocus misalignment pattern and the curvature of field misalignment pattern depends critically upon the sampling of the field rather than the wavefront.

1.5.4 discussion of fifth-order misalignment aberration patterns

The literature on fifth-order aberrations is limited for several reasons. First, by their very nature, they tend to be smaller than the third-order (Seidel) aberrations. Second, they are rather cumbersome. As a matter of course, ray tracing programs handle them correctly, so as a matter of practice, they receive little attention.

But as we have seen in the previous section, fifth-order aberrations may be needed to keep a three-mirror telescope aligned, and would almost certainly be needed to keep a four-mirror telescope aligned. Conversely, if one uses only the more commonly measured third-order aberrations, coma, astigmatism, and COF, to keep a telescope aligned, there are degenerate telescope configurations that zero out these third-order misalignment aberrations and yet produce distortion and fifth-order misalignment aberrations. It is therefore of some interest to estimate which of these might be more or less substantial.

An order of magnitude argument can be made by noting that the entries in Table

1.3 are homogeneous and of sixth order in the sum of the exponents of the pupil radius and the field angle. Both of these are rendered dimensionless by the focal lengths. We would argue that it is the focal ratio of the fastest element that matters most in such considerations. Modern fast, wide field telescopes have primary f-ratios approaching unity, while the field angles are rarely greater than a tenth of a radian. By this argument the terms at the top of Table 1.3 would be larger than those at the bottom. Third- and fifth-order aberrations for three specific optical systems: the LSST, HET corrector, and a Magellan-like telescope, are analyzed in the following subsections.

1.5.5 Tessieres' models for the LSST

The approach advocated here is quite similar to that adopted by Regis Tessieres in an unpublished M.S. thesis [2003] carried out at the University of Arizona. Tessieres analyzed the off-axis aberrations for two telescopes in terms of patterns derived in Thompson's unpublished [1980] PhD thesis. But instead of computing the amplitudes of the patterns according to the principles set forth by Thompson, he used ray-tracing software to produce wavefronts across the field for various misalignments. He then fit these wavefronts to the expected patterns.

Of particular relevance for the present work, he analyzed an early version of the Large Synoptic Survey Telescope (Seppala 19; henceforth LSST) in which the tertiary and primary were independent (rather than fabricated from a single monolith, as with the ultimate design). He applied decenters and tilts to the secondary and tertiary (and to the corrector assembly) and decomposed the computed wavefronts into the third- and fifth-order aberration patterns. Results of those calculations are given in Table 1.4, which show the effects of tilts in the secondary and tertiary.[10] Each entry gives the amplitude of the aberration at the edge of the field and at the edge of the pupil, in microns, for one degree of tilt. Up to factors of order unity the rms spot size

[10]Tessieres' nomenclature is similar to Hopkins', but each aberration is preceded by its field angle dependence. Thus what we would called third-order misalignment astigmatism he calls field-linear astigmatism.

will be proportional to these.

The first impression one gets is that the third-order aberrations are factors of 30-300 larger than the fifth-order aberrations. A consequence of this disparity is that, to the extent that the fifth-order and third-order aberration patterns are correlated, a small relative error in a measurement of a third-order aberration pattern will produce a large relative error in the corresponding fifth-order aberration pattern. This bodes ill for using fifth-order aberrations for telescope alignment. Tessieres' calculations are themselves not entirely immune from such errors, but Tessieres had the luxury of measuring the wavefront with high precision at a large number of points in the field.

There are several patterns for which Tessieres did not report amplitudes – fifth-order astigmatism-σ and the ρ patterns for fifth-order coma and astigmatism for the secondary mirror. One suspects that the amplitudes for these were so small as to be in the noise, but Tessieres is not explicit on this point.

Tessieres *did* fit several patterns that vary quadratically with tilt and decenter. We suspect that the coefficients for these would approach zero for successively smaller tilts and decenters. Assuming iterative alignment correction these will play no role once the misalignments are small, and we have not included them in our discussion.

Tessieres did not measure the misalignment patterns for either spherical aberration or curvature of field (defocus). These surely contributed to his figure of merit, and his alignment experiments might have converged more rapidly had he measured them.

Finally Tessieres did not measure distortion, which might in principle be used to align a telescope.

1.5.6 Manuel's models for the HET corrector

In another unpublished Ph.D. thesis, Anastacia Manuel [2009], working at the University of Arizona, carried out a ray-tracing misalignment analysis of a four-element corrector for the Hobby-Ebberly telescope.

The emphasis was on identifying the combinations of motions of the four elements that produced the largest aberrations using singular value decomposition. These modes sometimes involved more than one of the patterns considered here. Several

Table 1.4. Amplitude of misalignment patterns at edge of the field for an early version of the LSST (in microns) for tilts of 1°.

here	Tessieres	M2	M3
third-order coma	constant coma	178	186
third-order astigmatism	linear astigmatism	114	36
coma-II	constant fifth-order coma	2.4	4.3
astigmatism-II	linear oblique spherical	0.58	0.17
trefoil	quadratic elliptical coma	0.41	0.49
fifth-order coma-σ	quadratic coma#2	0.90	2.09
fifth-order coma-ρ	quadratic coma#1	[a]	3.5
fifth-order astigmatism-ρ	cubic astigmatism#1	[a]	1.72

[a]no value given

of the larger modes were associated with despacing and manifested themselves in symmetric aberration patterns.

But of the misalignment patterns, the three largest were the misalignments associated coma, curvature of field, and astigmatism, all of which are third-order. Next after that came linear combinations of second coma and second astigmatism misalignment patterns. These modes produced a figure of merit (which we take to be proportional to the wavefront error) a factor of 10^4 smaller than those for coma-I and a factor of 30 smaller than those for astigmatism-I. This would again suggest that measurements of fifth-order aberrations may not contribute much to aligning the system in question.

1.5.7 modeled aberrations for a Magellan-like telescope

In order to explore the feasibility of using distortion or the fifth-order aberrations for telescope alignment, we used Zemax® to measure the third- and fifth-order aberrations of a Gregorian telescope adapted from the Magellan Baade and Clay telescopes. The model telescope consists of three optical elements and a detector: a 6.4784m diameter aperture stop which sits 0.32512m in front of the primary mirror, a primary mirror with radius of curvature of -16.2553m and conic constant -1.00001, and a sec-

Table 1.5. Design specifications of the Magellan-like telescope.

Surface	Radius of Curvature (m)	Diameter[a](m)	Conic Constant	Distance (m) to Next Surface
object plane	-	-	-	infinity
aperture stop	-	6.4784	-	0.32512000
primary mirror	-16.2553	6.4805	-1.00001	-9.72205034
secondary mirror	2.86282	1.6134	-0.63286	14.00230590
image plane	-	-	-	-

[a]Diameter of the optic is larger than the diameter of the beam at the optic.

ondary mirror 9.72205m in front of the primary with radius of curvature 2.86282m and conic constant -0.63286. The focal plane sits 4.28026m behind the primary mirror. We analyzed two telescope configurations: one with a 1mm decentered secondary mirror and one with a $1/4^\circ$ tilted secondary mirror. The telescope specs appear in table 1.5.

For each telescope configuration, the Zemax® analysis tool *Fringe Zernike* was used to compute the Zernike wavefront aberrations at the edge of the pupil for a total of 21 field points spanning the x and y axes of the field. For the points along each telescope axis, the Zernikes corresponding to the pupil variations given in tables 1.2 and 1.3 were then fit to the field patterns using a simple least squares algorithm. Measurement of the wavefront delay along two field axes was necessary to distinguish the effects of ρ and σ fifth-order astigmatism and also ρ and σ fifth-order coma. For the other aberrations the second field axis provided a redundancy with which to verify the results. All of those third-order patterns fitted redundantly are self-consistent to within 0.2%. The fifth-order patterns are self-consistent to within 2% with the exception of second coma for the tilted telescope and misalignment trefoil for the decentered telescope. The former is likely corrupted by higher order effects which will be discussed later, and the latter is consistent with zero.

We also used the Zemax® analysis tool *Grid Distortion* to analyze third- and fifth-order distortion for both telescope configurations. As with fifth-order coma and

Table 1.6. Amplitudes of aberration patterns for a Magellan-like telescope.

Aberration	Symmetric	Misalignment (ρ,σ) Decentered 1mm	Misalignment (ρ,σ) Tilted 1/4°
Third-order			
spherical	-0.005		
coma	-29.161	-15.600	108.527
astigmatism	129.592	-0.479	51.848
COF	-591.745	7.631	-72.386
distortion[a]	-7.908	0.079	-1.363
		0.098	-0.619
Fifth-order			
spherical-II	0.000		
coma-II	0.013	0.587	-4.087
astigmatism-II	1.005	-0.014	0.031
fifth-order spherical	-0.592	0.039	-0.248
trefoil	0.261	-0.001	0.263
fifth-order coma	3.641	-0.037	-0.375
		-0.055	0.286
fifth-order astigmatism	-0.031	0.001	-0.143
		-0.003	0.280
fifth-order defocus	0.102	0.002	-0.168
fifth-order distortion[a]	0.010	0.000	-0.003
		0.024	0.027
Analytic third-order			
spherical	-0.005		
coma	-29.180	-15.625	108.702
astigmatism	129.731	-0.425	51.485

fifth-order astigmatism, we fit the distortion and fifth-order distortion patterns along two separate field axes in order to distinguish between the effects of the ρ and σ misalignment patterns.

The fitted aberrations for third- and fifth-order and the corresponding analytically computed aberrations for third-order appear in table 1.6. The coefficients are given in microns of wavefront delay at the edge of the pupil for an image at the edge of a 1° field, with the exception of distortion and fifth-order distortion which are given in arcseconds of image displacement at the edge of the field.

Table 1.6 (cont'd)

Aberration	Symmetric	Misalignment (ρ,σ) Decentered 1mm	Misalignment (ρ,σ) Tilted 1/4°
COF	-591.864	7.660	-29.027
distortion[a]	-7.787	0.078	-1.369
		0.112	-0.875

[a]Distortion and fifth-distortion are reported in arcseconds of displacement at the edge of a 1° field. All other values are reported in microns of wavefront delay at the edge of the pupil.

While the magnitude of misalignment aberrations are specific to telescope design, for the Magellan-type telescope modeled here, the fifth-order misalignment aberrations are never more than 4% of the magnitude of the third-order misalignment coma aberration (and more often than not, less than 1% of misalignment coma). While the misalignment distortion terms are also small, $-1\farcs363$ and $-0\farcs619$ for ρ and σ distortion respectively in the tilted telescope, they are significant compared to the reported RMS error of the SDSS astrometric catalog, $0\farcs045 - 0\farcs075$ and $0\farcs100$ for stars with magnitudes up to 20 and 22 [15]. If the wavefront sensors on this hypothetical telescope sample the pupil well, second coma is the most easily measured fifth-order aberration with which to align the secondary. If field sampling is preferable to pupil sampling and either a catalog exists for the field or one is willing to dither on the field [21], distortion could be used for alignment.

In general, there is good agreement between the magnitudes of the third-order aberrations computed analytically using the formulae presented here and by Zemax®. By far the most significant discrepancy between the analytically computed aberrations and those measured by Zemax® is for misalignment curvature of field for the tilted mirror. This discrepancy could be due to an inadvertent focal plane tilt with the mirror tilt. Zemax®, however, reports that the focal plane is aligned with the primary mirror.

Interestingly, seventh-order effects become important for the measurement of the spherical and fifth spherical, second coma, and second spherical aberrations. For

each of these aberrations, the next order aberration intrinsic to the aligned telescope (seventh-order spherical, seventh-order second coma, and seventh-order second spherical) is of a similar magnitude or greater than the symmetric fifth-order aberration. Fortunately for telescope alignment, the corresponding seventh-order misalignment aberrations are smaller than the fifth-order misalignment aberrations.

1.6 Wavefront Sensors: How Many, Where and to What Order?

1.6.1 General considerations

In §1.3 and §1.5 we showed that telescope misalignments produce a finite and relatively small set of distinct aberration patterns, each of which is characterized by a two-vector. The degrees of freedom that produce these patterns are likewise finite and small in number.

Suppose that we have an N-mirror telescope with n wavefront sensors distributed throughout the field each capable of measuring m aberrations. We take the position and pointing of the telescope to be defined by one of the mirrors. There remain $N-1$ tilts and $N-1$ decenters, each of which is described by a two-vector, that can produce our misalignment aberration patterns. If the aberration patterns are linearly independent, one would need to measure and correct $2(N-1)$ misalignment patterns to keep the telescope aligned.

1.6.2 A naive approach to the 3-mirror telescope using trefoil

For a 3-mirror telescope one would certainly measure the coma, astigmatism, and curvature of field patterns, since these produce the largest aberrations. The choice of a fourth pattern is much less obvious, but for the sake of the present exposition, we choose trefoil (despite its relatively small amplitude compared to several other fifth order aberrations).

Coma, astigmatism and trefoil each have two independent components on the pupil: one that varies as $\cos\phi$, $\cos 2\phi$ and $\cos 3\phi$ respectively and another that varies as $\sin\phi$, $\sin 2\phi$ and $\sin 3\phi$ respectively. Thus, if the Seidel patterns and effects of despace errors and mirror deformations are well-constrained, one wavefront sensor alone will suffice to measure the two-vectors for the misalignment aberration patterns associated with these.

By contrast, defocus is radially symmetric on the pupil, and each wavefront sensor produces only one number. Two wavefront sensors suffice to measure the curvature of field pattern, provided that they are not diametrically opposed.

The situation is complicated by despace (piston) errors which produce the symmetric aberration patterns characteristic of aligned but incompletely corrected telescopes. One would certainly want to measure and correct the first-order defocus that this produces, but this demands a third wavefront sensor to distinguish between simple (uniform) defocus and curvature of field.

One possible arrangement of these three wavefront sensors would be to space the wavefront sensors around the periphery of the field, where the effects of the misalignments are largest. An alternative would be to have one wavefront sensor at the center of the field and two at the periphery, but not co-linear.

As there are two degrees of freedom for despace errors, one must measure a second field-symmetric pattern in addition to defocus. The three candidate patterns are coma, astigmatism and spherical aberration. Only two wavefront sensors are needed to distinguish between the third-order misalignment coma and the symmetric coma pattern characteristic of a telescope with despace errors. The same holds true for astigmatism. The three wavefront sensors needed to distinguish uniform defocus and curvature of field therefore provide information about both despace errors. In addition, one would obtain three measurements of spherical aberration, which at third order is constant across the field.

Our naive scheme has one major strength and one major weakness. The strength is that the aberrations are low order on the pupil. Wavefront sensors work by subdividing the pupil and making measurements on those elements. The more finely one

subdivides the pupil, the more light is needed. Moreover, high-order aberrations are likely to be small, so there is little danger of our low order aberrations being corrupted by covariances with higher order aberrations. Finally, for the case of wavefront sensors based on out-of-focus images, image overlap is less of a problem if one can work with images that are more nearly in focus, which this method allows.

The substantial weakness in our scheme is the use of trefoil, which, as we have noted, would appear to produce a substantially smaller signal than some of the other fifth-order misalignment aberrations.

1.6.3 alternatives to trefoil: second coma, astigmatism and spherical

Tessieres' results, shown in Table 3, would suggest second coma as an alternative to trefoil. But as is evident if Figure 7, the point spread functions for second coma and ordinary (third order) coma are quite similar to each other. And the misalignment patterns, shown in Figures 2 and 8, are identical. So one would need to sample the pupil well in order to distinguish between the two.

Coma and second coma vary, respectively, as $\rho^3 \cos\phi$ and $\rho^5 \cos\phi$. We let

$$C = \frac{\int_{r_i}^{r_o} (\rho^5)(\rho^3)\rho d\rho}{\left[\int_{r_i}^{r_o} (\rho^5)(\rho^5)\rho d\rho \int_{r_i}^{r_o} (\rho^3)(\rho^3)\rho d\rho\right]^{\frac{1}{2}}} \tag{1.9}$$

be a measure of the correlation of the two wavefronts, where we have suppressed the azimuthal dependence and assumed that the center of the pupil is obstructed out to some fraction r_i of its total radius. Taking $r_i = 0.5$ and $r_o = 1.0$ gives $C = 0.981$, indicating a very strong correlation. By contrast C is identically zero for any two of defocus, coma, astigmatism and trefoil.

As a consequence of this strong correlation, one needs very accurate wavefront sensing to keep the large third-order coma signal from corrupting the weaker second-coma signal.

The problem is exacerbated by the large central obscurations associated with

wide-field telescopes. One must obtain at least two radial samples in the range $0.5 < \rho < 1.0$. For a Shack-Hartmann sensor, this would mean at least 8 lenslets across the diameter of the pupil. For out-of-focus wavefront sensing this would mean defocussing by at least 8 seeing disks.

The same argument holds for discriminating between ordinary (third order) astigmatism and second astigmatism, but with a slightly smaller correlation, $C = 0.978$. And it holds again for discriminating between curvature of field and second spherical aberration, again with with $C = 0.978$.

1.6.4 alternatives to trefoil: fifth-order coma and astigmatism

The PSFs produced by the σ and ρ fifth-order misalignment coma are indistinguishable from those produced by third-order misalignment coma, but each of these produces substantially different field patterns. One can therefore hope to distinguish among them using additional wavefront sensors.

Since each of these patterns is characterized by a two-vector, and since each wavefront sensor gives only two numbers associated with the coma at that point, a bare minimum of three wavefront sensors are needed to distinguish among the three misalignment coma patterns.

Of the two alternative arrangements described in our naive approach, the one with all three wavefront sensors on the periphery fails to discriminate between the fifth-order ρ-coma pattern and the third-order misalignment coma pattern. By contrast the arrangement with one at the center and two non-colinear on the periphery *does* successfully discriminate among all three patterns.

One can still use only peripheral wavefront sensors as long as one was careful to include the contributions of misalignments to both the third-order coma pattern and fifth-order ρ-pattern. In solving for the misalignments, one might iterate, ignoring ρ-coma on the first iteration and then subtracting it off on subsequent iterations. But this would preclude counting ρ-coma as one of the $2(N-1)$ needed patterns.

The same arguments hold for the three misalignment astigmatism patterns as well. A strictly peripheral arrangement of wavefront cannot distinguish between the third-order misalignment astigmatism pattern and the fifth-order ρ pattern.

1.6.5 alternatives to fifth-order: pointing and distortion

One could alternately choose to neglect fifth-order aberrations and instead use pointing or distortion to maintain alignment in a three mirror telescope.

Tilt (or pointing) is one of only two first-order aberrations. As its name implies, pointing uniformly shifts the location of every object in the field. It does not alter an image's point spread function and so it cannot be measured with a wavefront sensor unless the position of that wavefront sensor in the image plane is accurately known. In a paper on the Advanced Solar Telescope, Manuel & Burge [7] suggest that one might use pointing to constrain telescope alignment. This method would require accurate measurement of the position of the detector with respect to one of the mirrors.

In the same way that spherical aberration might equally well have been called "second defocus" – the two have same dependence upon pupil azimuth – distortion might equally well have been called "second tilt." For a field with a pre-existing astrometric catalog, misalignment distortion can be measured directly from the science data or using two wavefront sensors whose positions are accurately determined. In the absence of a pre-existing catalog, one might also solve for the misalignment distortion patterns by comparing overlapping fields, as suggested by Sudol [21]. The distortion terms would then constrain four degrees of freedom of telescope misalignments.

1.6.6 An improved approach to the 3-mirror telescope

Both wavefront sensor arrangements adopted for our naive approach to the 3-mirror telescope suffice to keep it aligned, but not for the same reasons. For the arrangement with three peripheral wavefront sensors, either the σ-coma and σ-astigmatism is likely to give a stronger alignment signal than the trefoil pattern.

Alternatively, for the arrangement with one wavefront sensor at the center and two non-colinear sensors on the periphery, the ρ-coma and ρ-astigmatism can also be used. This would seem to give sufficient information to keep a 4-mirror telescope aligned, or a 3-mirror telescope with a corrector.

It should be noted, however, that if one measures all three misalignment coma patterns, one must add a fourth wavefront sensor if one also wants to measure the symmetric coma pattern due to despace errors. The same holds true for astigmatism.

Table 1.7 is a summary of misalignment and piston errors, and the number of wavefront sensors required to constrain them. The aberrations are divided into those measurable with very low order wavefront sensing, and those which require greater sampling of the pupil. Patterns that are degenerate in a single wavefront sensor and therefore require separate wavefront sensors to distinguish among them are grouped together. The P's and M's show the patterns one would measure with a minimal system of three wavefront sensors all at the same radius on the periphery: P denotes those patterns which can be used to constrain piston; M misalignments. Six independent misalignment patterns are measured, more than sufficient for a three mirror telescope and barely sufficient for a four mirror telescope.

1.7 Complications

1.7.1 mirror deformation

We have until now treated the mirrors of a telescope as rigid bodies. But under the influence of changing gravitational and thermal stresses, the mirror surfaces deform and influence the wavefront. Deformations of the mirrors can be expanded in terms of Zernike polynomials, but it is more efficient to expand them in terms of their elastic bending modes [11, 9, 17].

If the stop is coincident with one of the mirrors, then the deformations of that mirror have the same effect on the wavefront at every point in the field. But if not, deformations of a mirror will project onto different parts of the pupil at different points

Table 1.7. Wavefront sensing summary.

VERY LOW ORDER WAVEFRONT SENSING	
first-order symmetric defocus	P
third-order symmetric defocus (COF)	
third-order misalignment defocus (COF)	M[a]
third-order symmetric astigmatism	P
third order misalignment astigmatism	M
fifth-order misalignment astigmatism-σ	M
fifth-order misalignment astigmatism-ρ	[b]
third-order symmetric coma	P
third order misalignment coma	M
fifth-order misalignment coma-σ	M
fifth-order misalignment coma-ρ	[b]
fifth-order misalignment trefoil	M

HIGHER ORDER WAVEFRONT SENSING
third-order symmetric spherical
fifth-order misalignment second-astigmatism
fifth-order misalignment second-coma
fifth-order misalignment spherical

[a]Third-order misalignment defocus alone requires two wavefront sensors to fully constrain, even in the absence of first- or third-order symmetric defocus.

[b]If only three wavefront sensors are used, the four astigmatism patterns and the four coma patterns are degenerate. But if the misalignment can be determined from the remaining patterns, one of these can be computed from the alignment solution. For rho-coma this degeneracy is broken by placing a wavefront sensor at the center of the field. However, the astigmatism degeneracy cannot be broken this way.

in the field. Applying the same mirror deformation pattern to different mirrors will produce aberrated wavefronts that are offset with respect to each other. One must therefore sample the wavefront at relatively high density to ascertain which element is deformed.

Among the fifth-order aberrations, second-coma, second-astigmatism and fifth-order spherical likewise require good sampling of the pupil to distinguish their misalignment patterns from those of third order aberrations. The accuracy with which one might determine these fifth-order aberrations is diminished by the need to use the same information to determine the mirror deformations.

This would argue for using two kinds of wavefront sensors: low-order sensors, using only coma, astigmatism and defocus to correct the rigid body motions, and high-order sensors to correct for mirror deformations. These latter sensors might be run at lower cadence than the former, except perhaps immediately following a large change in telescope pointing.

In such a scheme one might still measure fifth-order misalignment coma and fifth-order misalignment astigmatism with the low-order wavefront sensors, provided that there are a sufficient number of such sensors. If the telescope is then properly aligned the second-coma and second-astigmatism misalignment patterns will be zeroed out on the high-order wavefront sensors, giving a cleaner measurement of the mirror deformations in the high-order sensors.

1.7.2 central obscuration

Many wide field telescope designs have a large central obscuration. As mentioned in §1.6, this would make it more difficult to distinguish between second coma and second astigmatism on the one hand and ordinary coma and astigmatism on the other, which in third-order have the same field pattern. The smaller range of pupil radii would increase correlated errors.

1.7.3 focal plane misalignments

We have until this point avoided the question of how one knows the position of one's wavefront sensors or one's field with respect to one or another of a telescope's mirrors. As noted in the discussion of pointing in the previous subsection, the position and tilt of the focal plane or wavefront sensors might be determined mechanically or interferometrically. But if not, and if one wishes to correct for focal plane misalignments, one must measure two additional aberration patterns, one for the tilt of the focal plane, and one for the decenter.

A tilted detector produces a field pattern identical to misalignment curvature of field. However, if that pattern is used to correct the detector tilt, it cannot also be used to keep the mirrors aligned.

A decentered focal plane creates no aberrations of its own, but as is discussed in §§1.3.7, it can cause Seidel or fifth-order aligned aberrations to masquerade as misalignment aberrations. Measuring telescope aberrations relative to an incorrect field center will produce spurious misalignment aberrations even if the telescope is otherwise aligned.

One can choose to fit for this focal plane decenter by measuring an additional field pattern. If it is not feasible to measure an additional field pattern and one assumes that the center of the detector is the center of pointing, he can still completely null the measured misalignment coma, astigmatism and curvature of field by tilting and decentering one of the mirrors and tilting the focal plane. Compensating for the detector decenter with mirror misalignments can put the telescope into a state of 'benign misalignment', where only the smaller aberrations patterns: misalignment distortion, the fifth-order misalignment aberrations, and the aberrations which vary as the square of misalignments are present.

1.7.4 transmitting correctors

In his treatment of the LSST, Tessieres [22] studies the effects of tilts and decenters on a focal plane assembly consisting of a multi-element corrector and the focal plane

array. Two additional patterns are needed to keep this assembly aligned. Interestingly, the fifth-order aberration patterns produced by these tilts and decenters are larger, compared to the third-order aberration patterns, than for the secondary and tertiary mirrors.

1.8 Using and not using misalignment aberration patterns

At least three of the generic misalignment aberration patterns described in the previous sections are currently used to align wide-field telescopes, and there may soon be reason to use more of them. Ignoring for the present, the question of whether or not to use distortion[11] we imagine here an N-mirror telescope with n wavefront sensors distributed throughout the field each capable of measuring m aberrations. One must determine $N-1$ tilts and $N-1$ decenters, each of which is described by a two-vector.

1.8.1 independent analysis of the wavefront sensors

The most straightforward and transparent approach is to analyze each wavefront sensor separately, determining the coefficients of the aberrations at each of m points in the field. One then fits the these coefficients to a linear combinations of the misalignment aberration patterns described in the previous section and finally fits the amplitudes of the misalignment patterns (assuming one has measured more patterns than one actually needs).[12]

A complication of this approach is that at each step the quantities for which one is fitting may be correlated with each other. Aberration coefficients will be correlated, pattern amplitudes will be correlated and tilts and decenters will be correlated. Under such circumstances one must be careful to fit for all correlated quantities; otherwise one runs the risk of introducing systematic errors in the quantities for which one does

[11] We take the view what can be measured can hurt you.

[12] It would not be surprising if two or more patterns were produced by the same, or nearly the same combination of tilts and decenters.

fit.

1.8.2 simultaneous fit of all wavefront sensors for pattern amplitudes

Instead of measuring the aberrations at each point in the field, one might fit the data for all n wavefront sensors simultaneously to determine the amplitudes of the misalignment aberration patterns. This has the advantage of eliminating the problem of correlated aberrations at each point, but unmodelled aberrations may then lead to systematic errors.

1.8.3 simultaneous fit of all wavefront sensors for tilts and decenters

One might also fit directly for the tilts and decenters, short-circuiting the misalignment aberration patterns except for using them to turn tilts and decenters into predicted wavefronts that are then compared with observed wavefronts. This reduces the number of parameters for which one fits and implicitly accounts for the correlations of aberration pattern amplitudes. Rather than fitting for poorly determined amplitudes of fifth-order aberration patterns, all of the fifth-order dependence is attributed to a smaller number of tilts and decenters, which are strongly constrained by the third-order aberration patterns.

1.8.4 forget about misalignment patterns

Finally one might dispense entirely with the decomposition of the wavefront into specific aberrations and instead use ray tracing to determine how it varies at each measured point. While this obviates the need for misalignment patterns, it sacrifices all understanding of why one might need n wavefront sensors with enough resolution to measure m aberrations.

1.9 Summary

We have derived and illustrated the generic third-order aberration patterns that arise when the axial symmetry of a telescope is broken by small misalignments of optical elements. There are five patterns: one each for coma, astigmatism and curvature of field and two for distortion. Each of these misalignment patterns is characterized by an associated two-dimensional vector. These two-vectors are in turn linear combinations of the tilt and decenter vectors of the individual optical elements.

For an N-mirror telescope, $2(N-1)$ patterns must be measured to keep the telescope aligned. For $N = 3$, as in a three mirror anastigmat, there is a two-dimensional "subspace of benign misalignment" over which the misalignment patterns for third-order coma, astigmatism and curvature of field are identically zero. If pre-existing astrometry is available, one or both of the distortion patterns may be used to keep the telescope aligned. Alternatively, one might measure one of the fifth-order misalignment patterns.

We have illustrated the generic fifth-order misalignment patterns that arise from small misalignments. These are relatively insensitive to misalignments and may be of little use in telescope alignment. One would appear to be driven back to using distortion, or alternatively, pointing.

Acknowledgements: We gratefully acknowledge helpful and thought provoking conversations and communications with Michael Jarvis, Don Phillion, Lothar Noethe, Stephen Shectman and Tony Tyson. We also thank the referee, Brian McLeod, for his extensive comments. This work was supported by the National Science Foundation through a Graduate Research Fellowship to Rebecca Sobel Levinson

Bibliography

[1] Gitton, P., & Noethe, L. 1998, The Messenger, 92, 15

[2] Hopkins, H. H. 1950, Clarendon Press, Oxford.

[3] Hvisc, A. M., & Burge, J. H. 2008, Proc. SPIE, 7018,

[4] Lee, H., Dalton, G., Tosh, I.A.J,, & Kim, S.-W. 2008, Opt. Exp., 16, 10992.

[5] Ma, Z., Bernstein, G., Weinstein, A., & Sholl, M. 2008, PASP, 120, 1307

[6] Manuel, A. 2009, Ph.D. dissertation, University of Arizona, Tucson, Arizona.

[7] Manuel, A. M., & Burge, J. H. 2009, Proc. SPIE, 7433

[8] Maréchal, A., 1950, Rev. Opt., 29, 1

[9] Martin, H. M., et al. 1998, Proc. SPIE, 3352, 412

[10] McLeod, B. A. 1996, PASP, 108, 217

[11] Noethe, L. 1991, J. Mod. Opt., Vol. 38, No. 6, p. 1043 - 1066, 38, 1043

[12] Noethe, L., & Guisard, S. 2000, Proc. SPIE, 4003, 382

[13] Palunas, P., et al. 2010, Proc. SPIE, 0, 0000

[14] Phillion, D. W., Olivier, S. S., Baker, K., Seppala, L., & Hvisc, S. 2006, Proc. SPIE, 6272

[15] Pier, J. R., Munn, J. A., Hindsley, R. B., Hennessy, G. S., Kent, S. M., Lupton, R. H., & Ivezić, Ž. 2003, AJ, 125, 1559

[16] Romano, A., et al. 2010, A&A, 514, A88

[17] Schechter, P. L., et al. 2003, Proc. SPIE, 4837, 619

[18] Schroeder, D. J. 1987, San Diego, CA, Academic Press, Inc, 363 p.

[19] Seppala, L. G. 2002, Proc. SPIE, 4836, 111

[20] Shack, R. V., & Thompson, K. 1980, Proc. SPIE, 251, 146

[21] Sudol, J. 2011, private communications

[22] Tessieres, R. 2003, M.S. thesis, University of Arizona, Tucson, Arizona.

[23] Thompson, K. 1980, Ph.D. dissertation, University of Arizona, Tucson, Arizona.

[24] Thompson, K. 2005, J. Opt. Soc. Am. A, 22, 1389

[25] Thompson, K., et al. 2009, J. Opt. Soc. Am. A, 26, 1503

[26] Wilson, R. N. 1996, Springer-Verlag Berlin Heidelberg New York, 543 p.

[27] Wilson, R. N., & Delabre, B. 1997, PASP, 109, 53

[28] *Chandra* X-ray Center 2009, *The Chandra Proposer's Observatory Guide, Version 12*. Retrieved from `http://cxc.harvard.edu/proposer/POG/`

1.10 Appendix A: Coma

Schroeder [18], calculates the the coma pattern cause by tilting and decentering the secondary of a two mirror telescope by amounts α and ℓ.

$$
\begin{aligned}
G &= B_2 \rho^3 \sin\phi \\
B_2 &= B_2(cen) + \frac{1}{R_2^2}\left[\frac{l}{R_2}\left[K_2 - \left(\frac{m_2+1}{m_2-1}\right)\right] - \alpha\left(\frac{m_2+1}{m_2-1}\right)\right] \\
B_2(cen) &= \frac{\theta}{R_1^2} - \frac{W\theta}{R_2^2}\left[\left(\frac{m_2+1}{m_2-1}\right)\left(\frac{1}{W} - \frac{1}{R_2}\right) + \frac{K_2}{R_2}\right]
\end{aligned}
\tag{1.10}
$$

where ρ and ϕ are the radial and angular coordinates on the pupil and θ is the radial coordinate of the image in the field. The quantities R_i, K_i and m_i are all mirror properties: the radius of curvature, conic constant, and magnification of a mirror, where the subscript denotes which mirror is being addressed. The index of refraction has been set equal to 1 for the primary mirror and -1 for the secondary mirror. Finally, W is the distance from the primary mirror to the secondary.

$B_2(cen)$ is the coma of an aligned two mirror telescope. For the sake of simplicity the tilt and decenter of the secondary from the primary, and the object displacement from the optical axis have been taken lie along the y axis in Schroeder's analysis.

Schroeder's equations can be generalized for an object displaced from the optical axis in an arbitrary direction. The chief ray for the object is given by $\vec{\sigma}$ with radial and angular components σ and θ. The equations can be further generalized to allow decentering and tilting of the secondary mirror in arbitrary directions $\vec{\ell}$ and $\vec{\alpha}$ with radial components ℓ and α and angular components ϕ_ℓ and ϕ_α. The equations become:

$$
G = B_{2x}\rho^3 \cos\phi + B_{2y}\rho^3 \sin\phi \tag{1.11}
$$

where the field dependences are given by

$$
\begin{aligned}
B_{2x} &= G^{coma}_{Seidel}\sigma\cos\theta + G^{coma}_{decenter}\ell\cos\phi_\ell + G^{coma}_{tilt}\alpha\cos\phi_\alpha \qquad (1.12)\\
B_{2y} &= G^{coma}_{Seidel}\sigma\sin\theta + G^{coma}_{decenter}\ell\sin\phi_\ell + G^{coma}_{tilt}\alpha\sin\phi_\alpha\\
G^{coma}_{Seidel} &= \frac{1}{R_1^2} - \frac{W}{R_2^2}\left[\left(\frac{m_2+1}{m_2-1}\right)\left(\frac{1}{W}-\frac{1}{R_2}\right)+\frac{K_2}{R_2}\right]\\
G^{coma}_{decenter} &= \frac{1}{R_2^3}\left[K_2 - \left(\frac{m+1}{m-1}\right)\right]\\
G^{coma}_{tilt} &= -\frac{1}{R_2^3}\left(\frac{m+1}{m-1}\right)
\end{aligned}
$$

Consolidating the above equations yields

$$G^{coma} = G^{coma}_{decenter}\sigma\rho^3\cos(\phi-\theta)+G^{coma}_{decenter}\ell\rho^3\cos(\phi-\phi_\ell)+G^{coma}_{tilt}\alpha\rho^3\cos(\phi-\phi_\alpha) \quad (1.13)$$

which is the form for the coma aberration given in §1.3

1.11 Appendix B: Astigmatism

McLeod [10] follows the notation of Schroeder and calculates the astigmatism pattern for a two mirror telescope for which the secondary mirror has been aligned (decentered) to null the field constant coma pattern. McLeod gives the form of the remaining astigmatism patterns as

$$
\begin{aligned}
W &= Z_4\rho^2\cos 2\phi + Z_5\rho^2\sin 2\phi \qquad (1.14)\\
Z_4 &= B_0(\theta_x^2-\theta_y^2) + B_1(\theta_x\alpha_x-\theta_y\alpha_y) + B_2(\alpha_x^2-\alpha_y^2)\\
Z_5 &= 2B_0(\theta_x\theta_y) + B_1(\theta_x\alpha_y+\theta_y\alpha_x) + 2B_2(\alpha_x\alpha_y)\\
B_0 &= A_0^p r_p^2 - A_0^s r_s^2\\
B_1 &= -r_s^2\left[2A_0^s + (W+d_n)A_1^s\right]\\
B_2 &= -r_s^2\left[A_0^s + (W+d_n)A_1^s + (W+d_n)^2A_2^s\right]\\
A_0 &= \frac{W^2}{2R}\left[\frac{K}{R^2} + \left(\frac{1}{W}-\frac{1}{R}\right)^2\right]\\
A_1 &= \frac{W}{R^2}\left[\frac{1}{W} - \frac{K+1}{R}\right]\\
A_2 &= \frac{K+1}{2R^3}
\end{aligned}
$$

where ρ and ϕ are the (normalized) radial and angular coordinates on the pupil and θ_x and θ_y are the cartesian coordinates of the image in the field. The quantities R_i, K_i and m_i are again all mirror properties: the radius of curvature, conic constant, and magnification of a mirror, where the subscript denotes which mirror is being addressed, the primary p, or the secondary s. W is the distance from the primary mirror to the secondary, and α_x and α_y are the tilts of the secondary mirror with respect to the primary mirror. The indices of refraction preceding the primary and secondary mirrors have been set to 1 and -1 respectively.

McLeod additionally uses two constants that are not present in Schroeder's analysis of the coma pattern: r_i, which is the marginal ray height at the optic, and d_n, which denotes the position of the coma free point. As McLeod nulled the misalignment coma prior to analyzing the astigmatism, the decenter of the system $\vec{\ell}$ is given by $\vec{\ell} = d_n\vec{\alpha}$. McLeod chose to express the astigmatism only in terms of the tilt of the secondary mirror, though he could have equivalently expressed the astigmatism only in terms of the decenter or as a combination of the two terms. For greater transparency of the field patterns caused by both decenters and tilts, we here decouple the

decenter and tilt terms in McLeod's equations, removing the variable d_n. We also de-normalize the pupil coordinates and remove the terms which vary as the square of the misalignment.

$$
\begin{aligned}
W &= Z_4\rho^2\cos 2\phi + Z_5\rho^2\sin 2\phi \qquad (1.15)\\
Z_4 &= B_0(\theta_x^2-\theta_y^2) + B_{1decenter}(\theta_x\ell_x-\theta_y\ell_y) + B_{1tilt}(\theta_x\alpha_x-\theta_y\alpha_y)\\
Z_5 &= 2B_0(\theta_x\theta_y) + B_{1decenter}(\theta_x\ell_y+\theta_y\ell_x) + B_{1tilt}(\theta_x\alpha_y+\theta_y\alpha_x)\\
B_0 &= A_0^p r_p^2 - A_0^s r_s^2\\
B_{1decenter} &= 2A_0^s + WA_1^s\\
B_{1tilt} &= A_1^s\\
A_0 &= \frac{W^2}{2R}\left[\frac{K}{R^2}+\left(\frac{1}{W}-\frac{1}{R}\right)^2\right]\\
A_1 &= \frac{W}{R^2}\left[\frac{1}{W}-\frac{K+1}{R}\right]
\end{aligned}
$$

By converting the field variables to polar coordinates σ and ϕ_σ and similarly converting the misalignment variables to polar form ℓ, ϕ_ℓ, α, ϕ_α, the expression for the wavefront delay yields the form given in §1.3,

$$G^{astig} = G^{astig}_{Seidel}\sigma^2\rho^2\cos 2(\phi-\theta) + G^{astig}_{decenter}\sigma\ell\rho^2\cos(2\phi-\theta-\phi_\ell) + G^{astig}_{tilt}\sigma\alpha\rho^2\cos(2\phi-\theta-\phi_\alpha) \qquad (1.16)$$

where B_0, $B_{1decenter}$ and B_{1tilt} are equal to G^{astig}_{Seidel}, $G^{astig}_{decenter}$ and G^{astig}_{tilt}. [13]

1.12 Appendix C: Curvature of Field

The misalignment patterns for curvature of field are less well-explored in the literature. Thompson [24] presents forms for the patterns, and we re-derive them here

[13] The form of the astigmatism field pattern holds even for telescopes which have not been aligned to null the misalignment coma pattern. The expanded coefficients for the wavefront delay of a randomly misaligned telescope can be found in Table 1.2.

from the despaces and misalignments of a single mirror from the pupil.

As stated in §1.3.6, the contribution of a single mirror to the wavefront delay of the ray which strikes the mirror at position $\vec{\varpi}$ and makes an angle $\vec{\psi}$ with the axis of the mirror is given by:

$$\begin{aligned} G^{3rd} = & W_{040}(\frac{\vec{\varpi}}{R} \cdot \frac{\vec{\varpi}}{R})(\frac{\vec{\varpi}}{R} \cdot \frac{\vec{\varpi}}{R}) + W_{131}(\vec{\psi} \cdot \frac{\vec{\varpi}}{R})(\frac{\vec{\varpi}}{R} \cdot \frac{\vec{\varpi}}{R}) \\ & + W_{222}(\vec{\psi} \cdot \frac{\vec{\varpi}}{R})(\vec{\psi} \cdot \frac{\vec{\varpi}}{R}) + W_{220}(\vec{\psi} \cdot \vec{\psi})(\frac{\vec{\varpi}}{R} \cdot \frac{\vec{\varpi}}{R}) \\ & + W_{311}(\vec{\psi} \cdot \vec{\psi})(\vec{\psi} \cdot \frac{\vec{\varpi}}{R}) \end{aligned} \tag{1.17}$$

where W_{040} is the spherical aberration coefficient, W_{131} is the coma coefficient, W_{222} is the astigmatism coefficient, W_{220} is the curvature of field coefficient, and W_{311} is the distortion coefficient. These aberration coefficients depend only on the curvature of the mirror, R, the conic constant of the mirror, K, the magnification of the mirror, m, the index of refraction of the air preceding the mirror, n and the position of the object for the mirror, s.

The transformations from pupil coordinates $\vec{\rho}$ and $\vec{\sigma}$ to mirror coordinates for a mirror despaced by an amount W and decentered and tilted by $\vec{l}$ and $\vec{\alpha}$ are

$$\vec{\psi} = (1 - \frac{W}{s})\vec{\sigma} - (\vec{\alpha} + \frac{\vec{l}}{s}) \tag{1.18}$$

$$\vec{\varpi} = (\vec{\rho} - W\vec{\psi}) - \vec{l}. \tag{1.19}$$

Expanding the wavefront delay caused by a single mirror in terms of the pupil coordinates and keeping only those terms which vary as ρ^2 on the pupil[14] and vary linearly with the misalignments or less, we find an expression for the curvature of field wavefront delay added by a single offset mirror.

[14]The astigmatic component of the wavefront additionally has terms which vary as ρ^2 on the pupil. We exclude these astigmatic terms in the analysis of COF

$$G_i^{COF} = \left[\frac{1}{2}\left(\frac{W}{s}-1\right)^2 W_{220} + \frac{W}{R}\left(\frac{W}{s}-1\right)W_{131} + 2\frac{W^2}{R^2}W_{040}\right](\frac{\vec{\rho}}{R}\cdot\frac{\vec{\rho}}{R})(\vec{\sigma}\cdot\vec{\sigma}) \tag{1.20}$$
$$+\left[2\left(\frac{R}{s}\right)\left(\frac{W}{s}+1\right)W_{220} + \left(\frac{2W}{s}+1\right)W_{131} + 4\frac{W}{R}W_{040}\right](\frac{\vec{\rho}}{R}\cdot\frac{\vec{\rho}}{R})(\vec{\sigma}\cdot\frac{\vec{l}}{R})$$
$$+\left[2\left(\frac{W}{s}+1\right)W_{220} + \frac{W}{R}W_{131}\right](\frac{\vec{\rho}}{R}\cdot\frac{\vec{\rho}}{R})(\vec{\sigma}\cdot\vec{\alpha})$$

For a two mirror telescope, the primary and the secondary both contribute to the wavefront delay. As the primary is neither despaced nor misaligned from the pupil, the form of its contribution to the wavefront delay is simplified; notably, the primary mirror only contributes to the Seidel aberration. The secondary mirror is despaced and possibly misaligned from its pupil and therefore contributes to the decenter and tilt terms as well as the Seidel pattern. Combining the effects of the primary and secondary mirror yields:

$$G^{COF} = G^{COF}_{Seidel}(\vec{\sigma}\cdot\vec{\sigma})(\vec{\rho}\cdot\vec{\rho}) + G^{COF}_{decenter}(\vec{\sigma}\cdot\vec{\ell})(\vec{\rho}\cdot\vec{\rho}) + G^{COF}_{tilt}(\vec{\sigma}\cdot\vec{\alpha})(\vec{\rho}\cdot\vec{\rho}) \tag{1.21}$$
$$G^{COF}_{Seidel} = R_1^2 W_{220_1} + R_2^2\left[\frac{1}{2}\left(\frac{W}{s_2}-1\right)^2 W_{220_2} + \frac{W}{R_2}\left(\frac{W}{s_2}-1\right)W_{131_2} + 2\frac{W^2}{R_2^2}W_{040_2}\right]$$
$$G^{COF}_{decenter} = -R_2^3\left[2\left(\frac{R_2}{s_2}\right)\left(\frac{W}{s_2}+1\right)W_{220_2} + \left(\frac{2W}{s_2}+1\right)W_{131_2} + 4\frac{W}{R_2}W_{040_2}\right]$$
$$G^{COF}_{tilt} = -R_2^2\left[2\left(\frac{W}{s_2}+1\right)W_{220_2} + \frac{W}{R_2}W_{131_2}\right]$$

which is the form for the COF wavefront delay that appears in §1.3.

1.13 Apendix D: Distortion

The distortion field patterns can additionally be derived from the wavefront delay caused by a single optic. Again expanding equation (1.17) in terms of pupil coordinates, but now retaining only those terms which vary as ρ on the pupil and vary

linearly with the misalignments or less yields the expression for the distortion contribution of a single mirror which is despaced by W, decentered by $\vec{\ell}$ and tilted by $\vec{\alpha}$:[15]

$$
\begin{aligned}
G_i^{distortion} = &-\left[2\frac{W}{R}\left(\frac{W}{s}-1\right)^2(W_{220}+W_{222})+3\frac{W^2}{R^2}\left(\frac{W}{s}-1\right)W_{131}+4\frac{W^3}{R^3}W_{040}\right](\frac{\vec{\rho}}{R}\cdot\vec{\sigma})(\vec{\sigma}\cdot\vec{\sigma}) \\
&-\left[4\left(\frac{W}{s}\right)\left(\frac{W}{s}-1\right)W_{220}+2\left(\frac{W}{s}-1\right)\left(\frac{2W}{s}-1\right)W_{222}\right. \\
&\qquad\left.+4\frac{W}{R}\left(\frac{3W}{2s}-1\right)W_{131}+8\frac{W^2}{R^2}W_{040}\right](\frac{\vec{\rho}}{R}\cdot\vec{\sigma})(\vec{\sigma}\cdot\frac{\vec{l}}{R}) \\
&-\left[2\frac{W}{R}\left(\frac{W}{s}-1\right)(2W_{220}+W_{222})+2\frac{W^2}{R^2}W_{131}\right](\frac{\vec{\rho}}{R}\cdot\vec{\sigma})(\vec{\sigma}\cdot\vec{\alpha}) \\
&-\left[2\left(\frac{W}{s}-1\right)^2W_{220}+2\left(\frac{W}{s}\right)\left(\frac{W}{s}-1\right)W_{222}\right. \\
&\qquad\left.+2\frac{W}{R}\left(\frac{3W}{2s}-1\right)W_{131}+4\frac{W^2}{R^2}W_{040}\right](\frac{\vec{\rho}}{R}\cdot\frac{\vec{l}}{R})(\vec{\sigma}\cdot\vec{\sigma}) \\
&-\left[2\frac{W}{R}\left(\frac{W}{s}-1\right)W_{222}+\frac{W^2}{R^2}W_{131}\right](\frac{\vec{\rho}}{R}\cdot\vec{\alpha})(\vec{\sigma}\cdot\vec{\sigma})
\end{aligned}
\tag{1.22}
$$

For a two mirror telescope, only the secondary contributes to the distortion wavefront delay, as the primary is by construct not despaced from its entrance pupil. Grouping the coefficients in the above equation into terms of field dependences yields the form for distortion in §1.3:

$$
\begin{aligned}
G^{distortion} &= G_{Seidel}^{distortion}\sigma^3\rho\cos(\phi-\theta) \\
&+ G_{decenter,\sigma}^{distortion}\sigma^2\ell\cos(\theta-\phi_\ell)\rho\cos(\phi-\theta)+G_{decenter,\rho}^{distortion}\sigma^2\ell\rho\cos(\phi-\phi_\ell) \\
&+ G_{tilt,\sigma}^{distortion}\sigma^2\alpha\cos(\theta-\phi_\alpha)\rho\cos(\phi-\theta)+G_{tilt,\rho}^{distortion}\sigma^2\alpha\rho\cos(\phi-\phi_\alpha)
\end{aligned}
\tag{1.23}
$$

The coefficients are given by:

[15] As noted in §1.3, we have omitted the W_{311} coefficient as it is equal to zero.

$$G_{Seidel}^{distortion} = \frac{1}{R}\left[2\frac{W}{R}\left(\frac{W}{s}-1\right)^2(W_{220}+W_{222}) + 3\frac{W^2}{R^2}\left(\frac{W}{s}-1\right)W_{131} + 4\frac{W^3}{R^3}W_{040}\right] \tag{1.24}$$

$$G_{decenter,\sigma}^{distortion} = -\frac{1}{R^2}\left[4\left(\frac{W}{s}\right)\left(\frac{W}{s}-1\right)W_{220} + 2\left(\frac{W}{s}-1\right)\left(\frac{2W}{s}-1\right)W_{222} + 4\frac{W}{R}\left(\frac{3W}{2s}-1\right)W_{131} + 8\frac{W^2}{R^2}W_{040}\right]$$

$$G_{decenter,\rho}^{distortion} = -\frac{1}{R^2}\left[2\left(\frac{W}{s}-1\right)^2 W_{220} + 2\left(\frac{W}{s}\right)\left(\frac{W}{s}-1\right)W_{222} + 2\frac{W}{R}\left(\frac{3W}{2s}-1\right)W_{131} + 4\frac{W^2}{R^2}W_{040}\right]$$

$$G_{tilt,\sigma}^{distortion} = -\frac{1}{R}\left[2\frac{W}{R}\left(\frac{W}{s}-1\right)(2W_{220}+W_{222}) + 2\frac{W^2}{R^2}W_{131}\right]$$

$$G_{tilt,\rho}^{distortion} = -\frac{1}{R}\left[2\frac{W}{R}\left(\frac{W}{s}-1\right)W_{222} + \frac{W^2}{R^2}W_{131}\right]$$

where all mirror properties and object distances refer to the secondary mirror, and the chief ray angle is the chief ray angle on the primary mirror.

Chapter 2

Analytic PSF Correction for Gravitational Flexion Studies

Published 12/2013 by Publications of the Astronomical Society of the Pacific
Volume 125, issue 934, pp.1474-1495
http://www.jstor.org.libproxy.mit.edu/stable/10.1086/674333?seq=0

2.1 Abstract

Given a galaxy image, one cannot simply measure its flexion. An image's spin one and three shape properties, typically associated with F- and G-flexion, are actually complicated functions of the galaxy's intrinsic shape and the telescope's PSF, in addition to the lensing properties. The same is true for shear. In this work we create a completely analytic mapping from apparent measured galaxy flexions to gravitational flexions by (1) creating simple models for a lensed galaxy and for a PSF whose distortions are dominated by atmospheric smearing and optical aberrations, (2) convolving the two models, and (3) comparing the pre- and post-convolved flexion-like shape variations of the final image. For completeness, we do the same for shear. As expected, telescope astigmatism, coma, and trefoil can corrupt measurements of shear, F-flexion, and G-flexion, especially for small galaxies. We additionally find that PSF size dilutes the flexion signal more rapidly than the shear signal. Moreover, mixing

between shears, flexions, and asymmetric aberrations can create additive offsets in lensing measurements that vary with both galaxy size and galaxy ellipticity and flexion values. But all is not lost; by measuring the patterns, we can correct for them.

2.2 Introduction

Weak gravitational lensing is one of the key tools with which we can probe the dark matter content of our universe and by extension explore its structure and formation history. Tyson et al. [30] were the first to measure the statistical apparent alignment of many galaxies caused by gravitational shear. Since their initial measurement, weak lensing has been used to measure mass structure and substructure in regimes outside of strong lensing's reach. Flexion, the next order gravitational effect that transforms weakly sheared galaxy images into arcs, has the potential to bridge the gap between shear and strong lensing by probing scales between the two and providing orthogonal constraints on the mass estimates of each. Goldberg & Bacon [6] made the first measurement of flexion, and Velander et al. [31] and Cain et al. [4] made notable progress in this area.

But lensing measurements must still be honed if they are to live up to their theoretical potential. Observationally, weak lensing is the science and art of measuring small shape distortions imparted to galaxy images by foreground masses– a measurement which faces many practical encumbrances. Weak lensing signals are by definition small; shear measurements are swamped by scatter in intrinsic galaxy ellipticities; flexion signals mix with galaxy ellipticity and gravitational shear and are then quickly degraded by low signal to noise [32, 31, 23].

To circumvent these issues, we might (and do) average shears and flexions over many objects. But averages aren't a foolproof way to boost the signal. Imperfect masking of stars and neighboring galaxies limit available lensing targets over which averages can be made [4, 23] and can impart net biases in the flexion measurements for those which we do consider [31]. For ground based images, the atmosphere di-

lutes the lensing signal, biasing measured lensing signals low. Telescope jitter can add asymmetries to the PSF and consequently impart directional bias to shear and flexion measurements. Optical aberrations and detector effects add field variable asymmetric distortions to the images, such that the PSF varies in both magnitude and direction with field location [29, 27]. Accordingly, directional offsets in shear and flexion measurements are variable in the field.

The 2008 and 2010 GRavitational lEnsing Accuracy Testing challenges, GREAT08 and GREAT10, [3, 12] were controlled lensing simulations specifically deployed to test "the accuracy of current shape measurement methods" used to detect the weak lensing shear signal. The GREAT10 challenge was an improvement over its predecessor in that it simulated the field variability of the shear-like signal often present in a point spread function (PSF). In evaluating the results of the GREAT10 challenge, Kitching et al. [12] note two biases relating to the PSF that we quote here:

- "Despite the PSF being known exactly we find contributions to biases from PSF size, but less so from PSF ellipticity. The methods with the largest biases have a strong PSF-size correlation."

- "For large galaxies well sampled by the PSF, with scale radii $\gtrsim 2$ times the mean PSF size we find that methods meet requirements on bias parameters for the most ambitious experiments. However if galaxies are [relatively] unresolved with radii $\lesssim 1$ time the PSF size, biases become significant."

Properly accounting for the PSF, whether symmetric or asymmetric, seems to demand future improvement for various lensing measurement techniques, especially when analyzing galaxies of small size relative to the PSF. If lensing surveys are to be conducted from the ground, as is proposed with with Large Synoptic Survey Telescope [19], accounting for large, atmospherically induced PSFs will be critical. The GREAT challenges do not address measurements of gravitational flexion and how they may be affected by symmetric and asymmetric PSFs.

There are two primary methods for determining weak lensing flexion (and by default some information about shear) in galaxy images: by measuring moments of

galaxy images and by fitting the images to models. Moment measuring techniques notably include Higher Order Lensing Image Characteristics (HOLICS) of Okura et al. [21], based on the work of Kaiser et al. [11] (KSB). For KSB, weighted second image moments are related to shear. HOLICs extends the principles of KSB, measuring moments through fourth to obtain the flexion signal as well. Image fitting methods include shapelets [24, 25] and the Analytic Image Method (AIM) [4]. For image fitting techniques, a model of an unlensed galaxy is artificially lensed by shear and flexion and then fit to the galaxy image. For the shapelets method, image data are decomposed into cartesian or polar shapelets, a basis of two-dimensional Gauss-Hermite polynomials (cartesian) or modified Laguerre polynomials (polar), and the coefficients of the decomposition are fit against an artificially sheared and flexed model galaxy represented in that same basis. For AIM, a flexed galaxy model, comprised of an unlensed galaxy model lensed by (variable) shear and flexion, is fit directly to the image data, with no prior decomposition step.

Different groups deal with the PSF in different ways. Kaiser et al. [11] proposed a semi-empirical method of PSF correction whereby biases in the shear are corrected ignoring the effects of seeing, and then the 'seeing induced suppression [of shear] as a function of image size' is calibrated out using artificially smeared and degraded HST data. The KSB method accounts for anisotropies in the PSF, but overall the form of the PSF required by this deconvolution method needs to be rather simple. Okura & Futamase [20] expanded on the traditional KSB approach using Elliptical-HOLICs, dividing the PSF into elliptical components orthogonal and parallel to the galaxy shear rather than into isotropic and anisotropic components.

Melchior et al. [18] introduced an alternate PSF deconvolution technique for moments methods that avoids some of the shortcomings of the traditional KSB approach. DEIMOS, short for 'deconvolution in moments space', is a method for separating the PSF's moments from a sheared galaxy's moments, without assuming an a priori form for the PSF, or splitting the PSF into isotropic and anisotropic (or orthogonal/parallel) components. While the weighting functions required to accurately measure moments in noisy fields necessarily make this method mathematically

approximate, the technique is still highly accurate, and only requires the same computational time as the traditional KSB approach. This same principle of deconvolving the PSF in moments space which is applied to shear measurements in Melchior et al. [18] could be extended to higher order for flexion studies.

Groups using the shapelets method account for the PSF before even fitting the galaxy data to a model. As detailed in Kuijken [13] and Velander et al. [31], a model for the PSF is created by decomposing stellar images into shaplets. Next, a model for each lensed galaxy is created by superposing circularly symmetric shapelets. The galaxy model is then translated, sheared and flexed, and finally convolved with the model PSF. This lensed, convolved galaxy model is represented in the polar shapelets basis. Finally, the image data is decomposed in the polar shapelets basis, and this decomposed galaxy data is fit to the aforementioned galaxy model. The resulting best fit lensing parameters are therefore pre-corrected for the PSF. This method of PSF 'deconvolution' allows for as complex a PSF as the image resolution and the CPU performing the convolution can handle.

While one can always treat each individual case numerically, analytic estimates permit the design of observing programs without resorting to massive simulation. We therefore seek an analytic conversion from measured image properties to true lensing parameters. In order to achieve this end we create simple, analytic models for the galaxy and the PSF. For the galaxy model, we draw heavily on the work of Cain et al. [4] and AIM. For the PSF model, we use the fact that, in the presence of atmospheric seeing, geometric optics suffice to describe the telescope aberrations, and the combination of seeing and the optically induced aberrations will dominate over other effects. We therefore draw from Jarvis et al. [9] to construct an analytic PSF model at individual field positions and refer the reader to Schechter & Levinson [27] for a model of PSF field variations. We convolve the models for the lensed galaxy and aberrated PSF, create a mapping from gravitational to measured lensing values, and invert to find the mapping from measured to gravitatoinal.

The outline of the paper is as follows. In §2, we demonstrate that weak lensing deflections and telescope aberrations are functionally equivalent, and thus will manifest

in images in very similar ways. In §3, we derive a simple model for a lensed galaxy by assuming that the unlensed galaxy can be approximated by a Gaussian radial profile. Next, we derive a simple model for an aberrated PSF by assuming that atmospheric smearing produces a stellar image with a Gaussian radial profile. For transparency, we choose to work directly with the Gaussian models of the galaxies, treating lensing and aberration effects as perturbations to Gaussians, and only switching to the shapelets basis of Refregier [24] and Refregier & Bacon [25] to perform convolutions between the PSF and galaxy, §4. In §4, we additionally present the form of the final convolved galaxy image, and infer the transformation from the measured to gravitational lensing terms. In §5 we conclude. A review of the complex vector notation that will be used throughout this work to express the aberration and lensing models and the effects of lensing shear and flexions on images can be found in appendix A.

2.3 Aberrations: glass or mass, it's all the same

Optical aberrations and gravitational lensing distortions are formally identical because they are computed nearly identically– from path length differences of rays, using the same small angle approximations and expansions in circular bases to extract leading order terms. We here outline the parallel procedures used to develop the two theories and so demonstrate their equivalence.

2.3.1 Telescope aberrations

Telescope aberrations are computed from the optical path length difference between the ray striking the center of the pupil (which defines the center of the unaberrated object in the image plane) and a ray from the same source object striking an arbitrary location on the pupil. These path length differences are non-linear functions of the mirror shape, but in practice they are linearized in order to quantify the most extreme distortions to the image. Because the pupil is usually circular, the natural basis in which to represent the aberrations as they vary on the pupil are Zernike polynomials [33], namely ($tilt_1$, $tilt_2$, $defocus$, $astigmatism_1$, $astigmatism_2$, $coma_1$,

$coma_2$, $trefoil_1$, $trefoil_2$, $spherical$, and higher-order aberrations). The higher-order aberrations will generally be negligibly small in magnitude [27].[1]

The mathematical forms for these aberrations as they vary with pupil coordinates ρ and ϕ are given in tables 2.1 and 2.2. The tables exclude terms that displace measured image locations rather than distort images. In practice, the orthonormality of the Zernikes is often dropped when discussing the aberrations, and we have done so here.[2] The derivation of the telescope aberrations through 3rd order can be found in chapter 5 in Schroeder [29]. For field variations and extension through 5th order,[3] see Schechter & Levinson [27].

2.3.2 Weak lensing aberrations

A gravitational lens is entirely analogous to a telescope, with the lens plane of a weak lensing system akin to the pupil plane of an aberrated lens system. Distortions are introduced to the weak lens system in the same way as they were in the telescope system, namely through the optical path length differences between the ray defining the center of an object in the lens/pupil plane (which defines the center of the undistorted object in the image plane) and a ray from the same source object striking an arbitrary location in the lens plane. These path length differences are non-linear functions of the lensing potential, but in practice they are linearized in order to quantify the most extreme distortions to the image. Due to convention and a desire to express lensing effects in terms of same-order derivatives of the lensing potential, the lensing community has adopted the following basis for representing aberrations as they vary with distance from the center of the source on the lensing plane ($convergence$, $shear_1$, $shear_2$, $F\text{-}flexion_1$, $F\text{-}flexion_2$, $G\text{-}flexion_1$, $G\text{-}flexion_2$).

[1] The low order aberrations may be small in magnitude by design, but misalignment of the telescope optics can quickly render them large again.

[2] It is safe to drop the orthonormality in this discussion as we're not trying to compute the magnitude of each aberration type from first principles, but rather trying to group the functional dependences, i.e even if some *5th order coma* sneaks into what we're calling *coma* it doesn't matter.

[3] Trefoil is in fact considered to be a 5th order aberration due to its 3rd order variation in field coordinate as well as pupil coordinate in an aligned system. It is thus smaller than the other listed aberrations. However, no other 3rd or 5th order aberrations vary with a similar spin symmetry. We include it because of its relevance to flexion measurements

Table 2.1. Optical and gravitational aberration patterns.

telescope aberration	pupil plane variation	gravitational aberration	lens plane variation
$defocus$	ρ^2	$convergence$	θ^2
$astigmatism_1$	$\rho^2 \cos 2\phi$	$shear_1$	$\theta^2 \cos 2\omega$
$astigmatism_2$	$\rho^2 \sin 2\phi$	$shear_2$	$\theta^2 \sin 2\omega$
$coma_1$	$\rho^3 \cos \phi$	$F\text{-}flexion_1$	$\theta^3 \cos \omega$
$coma_2$	$\rho^3 \sin \phi$	$F\text{-}flexion_2$	$\theta^3 \sin \omega$
$trefoil_1$	$\rho^3 \cos 3\phi$	$G\text{-}flexion_1$	$\theta^3 \cos 3\omega$
$trefoil_2$	$\rho^3 \sin 3\phi$	$G\text{-}flexion_2$	$\theta^3 \sin 3\omega$
$spherical$	ρ^4		

Telescope pupil radial and angular coordinates are ρ and ϕ. Source object radial and angular coordinates at the lens plane, centered on the object, are θ and ω. The aberrations are identical.

Table 2.2. Vector notation for optical and gravitational aberration patterns.

telescope aberration	pupil plane variation	gravitational aberration	lens plane variation
$defocus$	ρ^2	$convergence$	θ^2
$astigmatism$	$\vec{\rho}^2$	$shear$	$\vec{\theta}^2$
$coma$	$\rho^2\vec{\rho}$	$F\text{-}flexion$	$\theta^2\vec{\theta}$
$trefoil$	$\vec{\rho}^3$	$G\text{-}flexion$	$\vec{\theta}^3$
$spherical$	ρ^4		

Telescope pupil vector is $\vec{\rho}$. Source object vector at the lens plane is $\vec{\theta}$. The aberrations are identical.

The mathematical forms for these aberrations as they vary with lens plane coordinates centered on the object, θ and ω, are given in tables 2.1 and 2.2. *They are identical to the telescope aberrations but with pupil coordinates replaced by lensing plane coordinates.* Note that the net deflection imparted to the image by the lens would have the same form as $tilt_1$ and $tilt_2$, but this effect is not measurable in most weak lensing studies as the undeflected galaxy position is unknowable, so we have excluded those terms here.

Some may be unfamiliar with the lensing aberrations as computed from optical

path length differences as opposed to deflections, but one can compute distortions equally well from either. Deflections of light from a source are simply gradients in that light's wavefront. Consider that, in the thin lens approximation, the deflection of light from a source galaxy at the lens plane is given by the gradient of the lensing potential, Φ. It follows that Φ is analogous to the wavefront of the source at the lens plane.[4]

In the weak lensing approximation, one is assuming that the wavefront can be linearized locally. Using the notation discussed in the appendix, the optical path length difference between the ray from the center of the source and a ray emanating from elsewhere in the source, $\Phi(\theta) - \Phi(\theta_0)$, is given by

$$\begin{aligned}
\Phi(\theta) - \Phi(\theta_0) = & \left(\frac{\vec{\partial}}{\partial\theta} \Phi|_{\theta_0} \cdot \vec{\theta} \right) && \text{(deflection)} \\
& + \frac{1}{2} \left[\frac{1}{2} \left(\frac{\partial^2}{\partial\theta^2} \Phi|_{\theta_0} \theta^2 \right) + \frac{1}{2} \left(\frac{\vec{\partial}^2}{\partial\theta^2} \Phi|_{\theta_0} \cdot \vec{\theta}^2 \right) \right] && \text{(convergence \& shear)} \\
& + \frac{1}{4}\frac{1}{3} \left[\frac{3}{2} \left(\frac{\partial^2}{\partial\theta^2} \frac{\vec{\partial}}{\partial\theta} \Phi|_{\theta_0} \cdot \vec{\theta} \right) \theta^2 + \frac{1}{2} \left(\frac{\vec{\partial}^3}{\partial\theta^3} \Phi|_{\theta_0} \cdot \vec{\theta}^3 \right) \right]. && \text{(F- \& G-flexion)}
\end{aligned} \tag{2.1}$$

The net deflection of the object from the source to the lens plane is the vector first derivative of the lensing potential, $\frac{\vec{\partial}}{\partial\theta}\Phi|_{\theta_0}$. *Convergence* and *shear* are the spin zero and spin two second derivatives, $\frac{1}{2}\frac{\partial^2}{\partial\theta^2}\Phi|_{\theta_0}$ and $\frac{1}{2}\frac{\vec{\partial}^2}{\partial\theta^2}\Phi|_{\theta_0}$. *F-flexion* and *G-flexion* are the spin one and spin three derivatives, $\frac{1}{2}\frac{\partial^2}{\partial\theta^2}\frac{\vec{\partial}}{\partial\theta}\Phi|_{\theta_0}$ and $\frac{1}{2}\frac{\vec{\partial}^3}{\partial\theta^3}\Phi|_{\theta_0}$. Each term has the radial variation given in table 2.2.

To compute the resultant distortion imparted to the image one takes the gradient of this optical path length difference and recovers that the deflection term will be the

[4] A traditional, unaberrated wavefront at a telescope pupil consists of parallel rays emanating from a single point in space. The telescope's pupil is thus uniformly illuminated. For a gravitational lensing system, the image of the galaxy at the lens plane is composed of rays emanating from multiple locations on the galaxy, not from a single point. Therefore the lens plane 'pupil' does not contain a wavefront in the classical sense, but rather is filled with an unevenly illuminated image of the source galaxy. As is discussed in section §2.4, the differing illuminations of the telescope pupil and gravitational lens 'pupil' can change the *effects* of their (identical) wavefront aberrations.

same for all rays, simply displacing an image between source and image planes. Only second and third derivatives will vary with ray position and thus contribute to shape distortion. The above derivation could be inferred from many lensing works, though the fundamentals of lensing, flexion, and the imaginary number notation are set in Bartelmann & Schneider [2], Goldberg & Natarajan [7] and Goldberg & Bacon [6], and Bacon et al. [1] respectively.

2.4 Models for a lensed galaxy and an aberrated PSF

We aim here to capture the effects of shear, flexion, and corruptions to their measurable signals by an aberrated PSF. Desiring only leading order influences on the asymmetries of the true and convolved galaxy, we use the simplest physically plausible models for both the galaxy and the PSF:

- An elliptical Gaussian model for the unlensed galaxy.
- A circular Gaussian model for the effects of atmospheric seeing, in absence of telescope aberrations.

While adding more complexity to the radial profiles of the unlensed galaxy and atmospherically aberrated PSF models might yield results which can be better fine-tuned to a particular telescope's PSF (or a particular galaxy's morphology given adequate sampling to determine it), adding additional complexity to models can often obscure the physically motivated trends in the results. We therefore use simple Gaussians for the radial profiles of unlensed galaxies and symmetrically aberrated PSFs.

To create the galaxy model, we use shear and flexion to lens a model for an initially unlensed galaxy. The lensing wavefront variations are given by the rightmost components of table 2.2. In the weak lensing approximation, these delays are imparted onto the image of the galaxy at the plane of the lens. The final galaxy model only accounts for shape distortions imparted by the lensing terms onto the initially unlensed galaxy, and no further aberrations.

To create the PSF model, we assume the PSF obtains an initial broad shape from the atmosphere and is then further aberrated by defocus, astigmatism, coma, and trefoil arising in the telescope.[5] These leading order aberrations impart onto the image wavefront delays at the uniformly illuminated pupil of the telescope, see table 2.2. Analogous to the galaxy model, the final PSF model is the total image created by the symmetric atmospheric broadening and the possibly asymmetric effects of the telescope aberrations.

For the galaxy model, we consider all terms through second order in shear. These second order terms are cumbersome, but we keep them out of foresight, not malice. They will in some cases have a larger effect on the final PSF convolved image shape than terms varying linearly in telescope aberration asymmetries.

In order to provide physical intuition for the galaxy and PSF models, we will express them first using the complex number notation shorthand. Only when necessary will we switch to shapelets coefficients for convolution.

2.4.1 Generic model for a lensed galaxy, a review

A lensed galaxy in the image plane, $I(\vec{\theta})$, is exactly represented by

$$I(\vec{\theta}) = I\left(\vec{\beta}(\vec{\theta})\right). \tag{2.2}$$

for source plane coordinate $\vec{\beta}$ and image plane coordinate $\vec{\theta}$. However, as detailed in the previous section, the deflection from source to image plane is approximated by a truncated Taylor series of the lensing potential, and thus the mapping of coordinates from source to image plane $\vec{\beta}(\vec{\theta})$ is imperfect. Likewise, if we express $\vec{\beta} = \vec{\theta} + \delta\vec{\theta}$, $\delta\vec{\theta}$ is imperfect.

As most galaxy models have some form of exponential radial profile (e.g. Gaussian, Sersic), it is often best to move the approximation for $\delta\vec{\theta}$, the difference in angular distance between ray offset from galaxy center in the source and image planes, out of

[5]Spherical aberration is very small in telescopes by design and cannot be reintroduced by misalignment errors. While it can be reintroduced by despace errors between optical elements, these are usually well-controlled.

the exponent. Fortunately, $\delta\vec{\theta}$ is small, and this can be achieved via another Taylor expansion as is done in Goldberg & Bacon [6], and expanded here in vector notation as

$$I(\vec{\theta}) \approx I(\vec{\beta})|_{\vec{\beta}=\vec{\theta}} + \frac{\vec{\partial}}{\partial\beta} I(\vec{\beta})|_{\vec{\beta}=\vec{\theta}} \cdot \delta\vec{\theta} + \frac{1}{2}\left(\frac{1}{2}\frac{\vec{\partial}^2}{\partial\beta^2} I(\vec{\beta})|_{\vec{\beta}=\vec{\theta}} \cdot (\delta\vec{\theta})^2 + \frac{1}{2}\frac{\partial^2}{\partial\beta^2} I(\vec{\beta})|_{\vec{\beta}=\vec{\theta}} (\delta\theta)^2\right). \tag{2.3}$$

In practice, the second derivative in this second, galaxy Taylor expansion is often dropped, but we have included it here for completeness, as all terms through second order in shear (galaxy ellipticity) will be addressed fully as will terms that vary as the product of ellipticity and flexion. Those varying as the square of flexion will be dropped as they are yet smaller. For the remainder of this work, the first derivative in equation (2.3) will be referred to as the linear galaxy expansion term and the second as the quadratic galaxy expansion term. These expansions of the galaxy model are not to be confused with flexion and shear, which are expansions of the lensing potential.

Given that the deflection from source to image plane coordinates, $\vec{\alpha}(\vec{\theta})$ is the gradient of the linearized lensing potential from §2.3, equation (2.1), one can compute $\vec{\beta}(\vec{\theta})$ in vector form to be

$$\begin{aligned}
\vec{\beta}(\vec{\theta}) &= \vec{\theta} - \vec{\alpha}(\vec{\theta}) \\
&\approx \vec{\theta} - \vec{\alpha}_0 - \kappa\vec{\theta} - \vec{\gamma}\vec{\theta}^* - \frac{1}{4}\vec{\psi}_1'^*\vec{\theta}^2 - \frac{1}{2}\vec{\psi}_1'\theta^2 - \frac{1}{4}\vec{\psi}_3'(\vec{\theta}^*)^2 \\
\text{where } \vec{\alpha}_0 &= \frac{\vec{\partial}}{\partial\theta}\Phi|_{\theta_0} \\
\kappa &= \frac{1}{2}\frac{\partial^2}{\partial\theta^2}\Phi|_{\theta_0} \\
\vec{\gamma} &= \frac{1}{2}\frac{\vec{\partial}^2}{\partial\theta^2}\Phi|_{\theta_0} \\
\vec{\psi}_1' &= \frac{1}{2}\frac{\partial^2}{\partial\theta^2}\frac{\vec{\partial}}{\partial\theta}\Phi|_{\theta_0} \\
\vec{\psi}_3' &= \frac{1}{2}\frac{\vec{\partial}^3}{\partial\theta^3}\Phi|_{\theta_0}.
\end{aligned} \tag{2.4}$$

In the above equation, $\vec{\alpha}_0$ is the deflection from the center of the galaxy in the source plane to the center of the galaxy in the image plane, κ is the convergence, $\vec{\gamma}$ is the shear, and $\vec{\psi}_1'$ and $\vec{\psi}_3'$ are the unitful flexions. Since we are using $\vec{\theta}$ as the coordinate centered on the galaxy center in the image plane and $\vec{\beta}$ as the coordinate centered on the galaxy center in the source plane, we can drop the constant deflection, $\vec{\alpha}_0$ from the expression. Assuming that we will not have an independent measure of the gravitational magnification with which to break the mass sheet degeneracy, we also divide the equation through by $1-\kappa$, following Schneider & Er [28]. To simplify the notation, we introduce the reduced the shears and flexions ($\vec{g}$, $\vec{\psi}_1$, and $\vec{\psi}_3$) which are the unreduced shears and flexions each divided by $1-\kappa$. The source plane coordinate $\vec{\beta}$ is also divided by $1-\kappa$, however we absorb the coefficient into $\vec{\beta}$ and do not change the variable name. The resulting expression for $\vec{\beta}(\vec{\theta})$ is

$$\vec{\beta}(\vec{\theta}) = \vec{\theta} - \vec{g}\vec{\theta^*} - \frac{1}{4}\vec{\psi_1^*}\vec{\theta^2} - \frac{1}{2}\vec{\psi_1}\theta^2 - \frac{1}{4}\vec{\psi_3}(\vec{\theta^*})^2. \tag{2.5}$$

For the rest of this work, all shears and flexions will be reduced shears and flexions unless explicitly stated otherwise.

Unitless flexions are more appropriate for the following discussion as these quantities measure galaxy shape and thus are true properties of a measured image rather than properties of a deduced lensing potential. We therefore switch to unitless reduced flexions $\vec{F}$ and $\vec{G}$, where $\vec{\psi}_1$ and $\vec{\psi}_3$ are rendered unitless by multiplying by the galaxy half-light radius r_{hl}. The equation for the source plane coordinate $\vec{\beta}(\vec{\theta})$ becomes

$$\vec{\beta}(\vec{\theta}) = \vec{\theta} - \vec{g}\vec{\theta^*} - \frac{1}{4r_{hl}}\left(\vec{F^*}\vec{\theta^2} + 2\vec{F}\theta^2 + \vec{G}(\vec{\theta^*})^2\right). \tag{2.6}$$

Subtracting $\vec{\theta}$ from the above expression thus yields $\delta\vec{\theta}$ as

$$\delta\vec{\theta} = -\vec{g}\vec{\theta^*} - \frac{1}{4r_{hl}}\left(\vec{F^*}\vec{\theta^2} + 2\vec{F}\theta^2 + \vec{G}(\vec{\theta^*})^2\right), \tag{2.7}$$

a third order approximation of the deflection of rays about the center of the galaxy.

2.4.2 Test Case: Circular Gaussian model for the unlensed galaxy

First we will consider a circular model for the unlensed galaxy. While this model may seem overly simplistic, as a galaxy's intrinsic ellipticity is generally too large to be ignored, this test case provides insight into the final model for the image which uses an elliptical Gaussian as the prior for the unlensed galaxy.

To second order in shear, the model for a lensed (initially circular) galaxy with unlensed Gaussian width α is

$$
\begin{aligned}
I(\vec{\theta}) = \frac{I_0}{2\pi\alpha^2}\exp\left(-\frac{\theta^2}{2\alpha^2}\right) \times \Bigg[& 1 \\
& + \Bigg\{ \frac{1}{\alpha^2}\left(\vec{g}\cdot\vec{\theta^2}\right) + \frac{1}{4\sqrt{2\ln(2)}\alpha^3}\left[3\left(\vec{F}\cdot\vec{\theta}\right)\theta^2 + \left(\vec{G}\cdot\vec{\theta^3}\right)\right] \Bigg\} \\
& + \Bigg\{ -\frac{1}{4\alpha^2}g^2\theta^2 + \frac{1}{4\alpha^4}g^2\theta^4 + \frac{1}{4\alpha^4}\left(\vec{g}^2\cdot\vec{\theta^4}\right) \\
& \quad - \frac{1}{4\sqrt{2\ln(2)}\alpha^3}\left[3\left(\frac{1}{3}\left(2\vec{g}\vec{F^*} + \vec{g^*}\vec{G}\right)\cdot\vec{\theta}\right)\theta^2 + \left(\left(\vec{g}\vec{F}\right)\cdot\vec{\theta^3}\right)\right] \\
& \quad + \frac{1}{8\sqrt{2\ln(2)}\alpha^5}\left[\left(\left(3\vec{g}\vec{F^*} + \vec{g^*}\vec{G}\right)\cdot\vec{\theta}\right)\theta^4 + \left(\left(3\vec{g}\vec{F}\right)\cdot\vec{\theta^3}\right)\theta^2 + \left(\left(\vec{g}\vec{G}\right)\cdot\vec{\theta^5}\right)\right] \Bigg\} \Bigg].
\end{aligned}
\tag{2.8}
$$

In the above expression and all following discussion, we simplify all terms into 'polynomial' form, where products of aberrations multiply powers of $\vec{\theta}$.

The first row of the expression is the circular, unlensed galaxy simply moved to the image plane. The first braced term is the linear part of the galaxy expansion and varies linearly with shear and flexion. The second braced term containing the last three rows are the quadratic part of the galaxy expansion. These vary as the square of shear and the products of shear and flexion. For the moment, we shall retain all terms in equation (2.8) without further reduction. However, the observant reader will likely note that the flexion-like spin one and spin three terms with cubed radial dependence in row 4 can be incorporated into the linear expansion term through a

transformation of $\vec{F}$ and $\vec{G}$ to new variables $\vec{\tilde{F}}$ and $\vec{\tilde{G}}$ by shear.

2.4.3 Elliptical Gaussian model for the unlensed galaxy

Inserting a more physically realistic, intrinsically elliptical galaxy into equation (2.3), we find

$$
\begin{aligned}
I_e(\vec{\theta}) = \frac{I_0}{2\pi\alpha^2}\exp\left(-\frac{1}{2\alpha^2}\left((1+e^2)\theta^2 - 2\left(\vec{e}\cdot\vec{\theta^2}\right)\right)\right)\times\Bigg[1 \\
+\left\{\frac{1}{\alpha^2}\left(\vec{g}\cdot\vec{\theta^2}\right)+\frac{1}{4\sqrt{2\ln(2)}\alpha^3}\left[3\left(\vec{F}\cdot\vec{\theta}\right)\theta^2+\left(\vec{G}\cdot\vec{\theta^3}\right)\right]\right\} \\
+\Bigg\{-\frac{1}{4\alpha^2}g^2\theta^2+\frac{1}{4\alpha^4}g^2\theta^4+\frac{1}{4\alpha^4}\left(\vec{g}^2\cdot\vec{\theta^4}\right) \\
-\frac{1}{4\sqrt{2\ln(2)}\alpha^3}\left[3\left(\frac{1}{3}\left(2\vec{g}\vec{F}^*+\vec{g}^*\vec{G}\right)\cdot\vec{\theta}\right)\theta^2+\left(\left(\vec{g}\vec{F}\right)\cdot\vec{\theta^3}\right)\right] \\
+\frac{1}{8\sqrt{2\ln(2)}\alpha^5}\left[\left(\left(3\vec{g}\vec{F}^*+\vec{g}^*\vec{G}\right)\cdot\vec{\theta}\right)\theta^4+\left(\left(3\vec{g}\vec{F}\right)\cdot\vec{\theta^3}\right)\theta^2+\left(\left(\vec{g}\vec{G}\right)\cdot\vec{\theta^5}\right)\right]\Bigg\} \\
+\left\{-\left(2\vec{e}\vec{\theta^*}\right)\cdot\left(\frac{1}{\alpha^2}\left(\vec{g}\vec{\theta^*}\right)+\frac{1}{4\sqrt{2\ln(2)}\alpha^3}\left[\vec{F}^*\vec{\theta^2}+2\vec{F}\theta^2+\vec{G}(\vec{\theta^*})^2\right]\right)\right\}\Bigg]
\end{aligned}
\tag{2.9}
$$

where $\vec{e}$ is the intrinsic galaxy ellipticity, apart from induced shear $\vec{g}$. The Gaussian width is α in the limit of zero ellipticity.

The first row of the model is now the elliptical unlensed galaxy moved to the image plane. The next four rows are unchanged from the model created using a circular unlensed galaxy; the first braced term is the linear galaxy expansion and the second braced term is the quadratic lensing expansion. However, these terms now multiply an elliptical Gaussian 'base' galaxy rather than a circular Gaussian. In addition to modifying the exponential term, two new terms, both second order in asymmetries, are added to the expansion. These terms, contained in the last bracked row of the equation, are introduced by cross terms between the intrinsic galaxy ellipticity and the lensing terms which then carry down into the Taylor expansion.

It is useful to express the model for the galaxy image as a circular Gaussian plus

perturbations for two reasons: (1) to restrict the discussion to the most significant asymmetric terms only, i.e those varying to the lowest order in shear, intrinsic ellipticity, and flexion, and (2) to better facilitate convolutions in the shapelets basis. Therefore we will once again Taylor expand the expression, reducing the model to a circular Gaussian plus perturbations. We find

$$
\begin{aligned}
I(\vec{\theta}) = \frac{I_0}{2\pi\alpha^2}\exp\left(-\frac{\theta^2}{2\alpha^2}\right) \times \Bigg[& 1 && \text{(2.10a)}\\
& + \Bigg\{ \frac{1}{\alpha^2}\left(\vec{\tilde{g}}\cdot\vec{\theta^2}\right) + \frac{1}{4\sqrt{2\ln(2)}\alpha^3}\left[3\left(\vec{\tilde{F}}\cdot\vec{\theta}\right)\theta^2 + \left(\vec{\tilde{G}}\cdot\vec{\theta^3}\right)\right] \Bigg\} && \text{(2.10b)}\\
& + \Bigg\{ -\frac{1}{4\alpha^2}\left(\tilde{g}^2 + 2(\vec{g}\cdot\vec{e})\right)\theta^2 + \frac{1}{4\alpha^4}\tilde{g}^2\theta^4 + \frac{1}{4\alpha^4}\left(\vec{\tilde{g}}^2\cdot\vec{\theta^4}\right) && \text{(2.10c)}\\
& \quad + \frac{1}{8\sqrt{2\ln(2)}\alpha^5}\left[\left(\left(3\vec{\tilde{g}}\vec{F}^* + \vec{\tilde{g}}^*\vec{G}\right)\cdot\vec{\theta}\right)\theta^4 + \left(\left(3\vec{\tilde{g}}\vec{F}\right)\cdot\vec{\theta^3}\right)\theta^2 + \left(\left(\vec{\tilde{g}}\vec{G}\right)\cdot\vec{\theta^5}\right)\right] \Bigg\} \Bigg]. && \text{(2.10d)}
\end{aligned}
$$

The first row and braced term in the model, (2.10a) and (2.10b), are the same Gaussian model and linear expansion terms one would obtain by using a circular Gaussian as the unlensed galaxy model. However, shear and flexion in (2.10b) have been converted to new effective shears and flexions via the following transformations with galaxy ellipticity

$$
\begin{aligned}
&\vec{\tilde{g}} = \vec{g} + \vec{e} && \text{(2.11)}\\
&\vec{\tilde{F}} = \vec{F} - \frac{1}{3}(2\vec{\tilde{h}}\vec{F}^* + \vec{\tilde{h}}^*\vec{G})\\
&\vec{\tilde{G}} = \vec{G} - \vec{\tilde{h}}\vec{F}\\
&\text{where} \quad \vec{\tilde{h}} = \vec{g} + 2\vec{e}.
\end{aligned}
$$

We could have made a similar transformation of F and G to tilde space for the model created using a circular Gaussian for the unlensed galaxy, equation (2.8). In so doing,

we would have removed the redundant $\vec{\theta}\theta^2$ and $\vec{\theta}^3$ terms there as we have done here.

The above transformations quantify the extent to which the nature of the observed object changes depending on how much intrinsic galaxy ellipticity, lensing shear, and each of the two types of flexions is present. Lensing is measured as distortions to the galaxy image that are 'shear-like' and 'flexion-like' in the linear regime. For the Gaussian model, these variations are $\vec{\theta}^2$, $\vec{\theta}\theta^2$, and $\vec{\theta}^3$. As the ratios of intrinsic galaxy ellipticity, gravitational induced shear, and F- and G-flexions change, so do the amounts of each term that will contribute to any particular shape distortion in the non-linear regime. In the non-linear regime, shear and intrinsic galaxy ellipticity can combine with F-flexion (spin one, third derivative of the lensing potential) to contribute to the G-flexion-like galaxy distortion and vice versa. The resulting quadratic 'pseudoflexion' adds to the linear flexion to create the total effective flexion signal.

2.4.4 Consequences of pseudoflexions

The effective F-flexion, $\vec{\tilde{F}}$, can be modified by a mixing between the linear F-flexion and shear (or ellipticity) or between G-flexion and shear. G-flexion is simpler; the effective signal, $\vec{\tilde{G}}$ can only be altered by a combination of F-flexion and shear (or ellipticity). As an extreme example of lensing signals mixing to masquerade as each other, consider a galaxy whose intrinsic spin three shape accidentally cancels out its linear G-flexion lensing signal. In this case, shear (or ellipticity) and F-flexion could still produce a spin three pseudoflexion signal, which would impart a measurable $\tilde{G}$ lensing signal on the galaxy.

The above is an extreme example, but the quadratic pseudoflexions introduced by the non-linear expansion to the lensed galaxy model will generally contribute to the effective flexions by some amount. Lensing systems consistent with a Singular Isothermal Sphere (SIS) profile will have aligned shear and flexions in the ratio $-g : -2\frac{r_{hl}}{\theta_e}g^2 : 6\frac{r_{hl}}{\theta_e}g^2$, where r_{hl} and θ_e are the half light radii of the galaxy and the Einstein ring radius of the lens. Because shear and F-flexion have the same sign, unless the source galaxy has significant intrinsic ellipticity opposing the shear, the effective $\tilde{G}$-flexion will always be reduced by the combination of shear and F-flexion.

Likewise, the effective $\tilde{F}$-flexion, which is negative, will be rendered less negative by combinations of shear and itself and by shear and G-flexion. For a true SIS, the effective $\tilde{F}$-flexion will be reduced by the same fraction as $\tilde{G}$-flexion. Figure 2-1 shows the fractional reduction of apparent observable flexion, ($\tilde{F}$ or $\tilde{G}$ equivalently) for a SIS as a function of radial distance from the lens. For a SIS lens at the Einstein ring, flexion and shear will reduce the apparent flexions by a full sixth, assuming no intrinsic galaxy ellipticity.

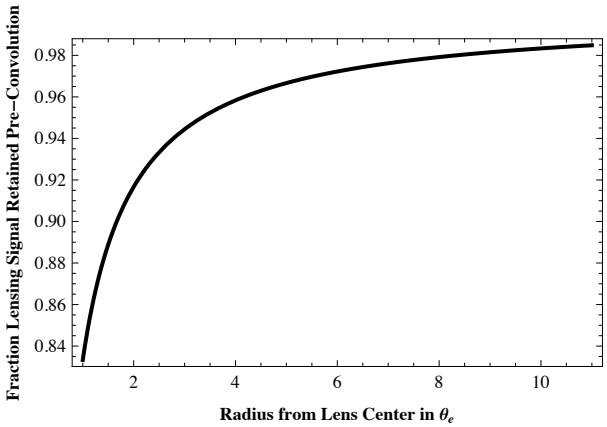

Figure 2-1 Fraction of flexion signal observed for a circular galaxy lensed by a SIS. Any ratio of $\frac{r_{hl}}{\theta_e}$ will produce these ratios of effective and true flexions. All apparent signal loss occurs prior to convolution with a PSF, and is caused by linear flexion signals mixing with shear terms to create a 'pseudoflexion' of opposite sign to the linear term.

If one were to consider only terms in the lensed galaxy model that vary like first order shears and flexions (i.e $\vec{\theta}^2$, $\vec{\theta}\theta^2$, and $\vec{\theta}^3$), one would not be able to distinguish between effective shears and flexions and the true lensing terms without some foreknowledge of either the shear or the intrinsic galaxy ellipticity. This degeneracy has nothing to do with convolution, but rather the ability to resolve second order lensing effects. Likewise, to first order in shear and flexion, one cannot distinguish between a model that uses a circular or an elliptical prior for the unlensed galaxy.

2.4.5 An Aside: Shear-flexion 'cross-talk' and pseudoflexion, similarities and differences

Using HOLICs, Viola et al. [32] were the first to quantify the corruption effects of shear-flexion mixing on flexion measurements. They named the effect 'cross-talk'.

The HOLICs method for computing flexion relies on measuring spin one and three distortion estimators. These distortion estimators are the spin symmetric third moments of the galaxy intensity, divided by the spin zero fourth moment, (see eqs. (18) and (19) in Viola et al. [32]). The estimators have units of inverse galaxy scale length.

Okura et al. [22] relate these estimators to flexions by making several simplifying assumptions, most notably that terms second order in shear and higher can be safely ignored. The result of these simplifying assumptions are linear mappings between flexions and the distortion estimators. Viola et al. [32] build on Okura et al. [22], retaining higher order terms, including products of shear and flexion. In so doing they find, as we do here, that the distortion estimators are in fact functions of both flexion *and* the products of shear and flexion. To test their results, Viola et al. [32] create synthetic flexed galaxies and measure their distortion estimators. They then compute the expected distortion estimators using the known gravitational values used to create the synthetic galaxies. They find that the expected distortion estimators computed using shear-flexion cross talk match the measured results to good agreement. In contrast the distortion estimators computed only using terms linear in shear and flexion are much smaller than the measured distortions.

The non-linear mapping between distortion estimators and flexions proposed by Viola et al. [32] is now an implicit part of the HOLICs code for converting image moments into flexions.

Based on Viola's results one can conclude that, using the linear relationship between the distortion estimators and flexion, the HOLICs method would predict flexions which are too large. Examining (2.11) of this work, one can see that a linear fitting model will predict flexions which are smaller than the gravitational flexion

values. While these two statements would seem opposed, both are true.

The spin one and three distortion estimators in the HOLICs methods measure *all* spin one and three distortions, irrespective of the order of radial variation on the galaxy.[6] Therefore the distortion estimators are sensitive to the quintic spin one and three terms created by shear flexion mixing. The spin three quintic cross term between shear and F-flexion drives the net spin three moment up, resulting in an overestimated flexion.

In contrast, modeling techniques, such as AIM, only see the corruption to the flexion-like, *cubic* spin one and three terms. The pseudoflexion in these cubic terms forces the linear estimate of flexion lower than the true gravitational flexion, as discussed in the previous subsection. Thus, the HOLICs and model fitting methods, while predicting opposite biases in the linear regime, are in complete agreement.

2.4.6 A minimal galaxy model for analyzing the effects of PSF convolution

Up to and including terms which vary as the product of galaxy ellipticity (shear induced and intrinsic) and flexion, the model created by assuming a circular unlensed galaxy is no worse an approximation for analyzing the effects of convolution on shear and flexion than the model created using an elliptical unlensed galaxy. In every place in the elliptical lensed galaxy model where shear and flexion appear, either the lensing terms can be mapped to effective shears and flexions in a way consistent with second order approximations, or the terms can be dropped from both the elliptical and circular lensed galaxy models without loss of accuracy to either. The result is that the elliptical lensed galaxy model can be rendered formally equivalent to the circular model, but with newly named, effective lensing variables.

To elaborate, in equation (2.10d) every flexion term appears in product with shear $\vec{\tilde{g}}$, and so to second order may be replaced by its respective $\tilde{F}$ or $\tilde{G}$ equivalent. In equation (2.10c), where shear cannot simply be mapped to tilde space, the offending

[6] Albeit not equally- the moments of a cubic and quintic function with the same spin will not necessarily be the same, even if they have identical coefficients.

θ^2 term can be modified or dropped as it is completely radially symmetric, and thus its inclusion in the model only modifies the steepness of the galaxy profile. We are approximating the symmetric shape of the unlensed galaxy by a Gaussian, in order to better understand the effects and interplays of asymmetries caused by gravitational lensing and an asymmetric PSF caused by telescope aberrations. Perturbations to the symmetric shape that affect the cuspiness of the final image are no more or less significant than the initial assumption that the unlensed galaxy model is Gaussian. Therefore both θ^2 terms and the θ^4 symmetric term in equation (2.10c) may be folded into the Gaussian radial approximation without any additional losses. With the conversion of shear and flexion to tilde space and the exclusion of symmetric terms, the model created using a circular Gaussian is identical to that created using an elliptical Gaussian unlensed galaxy.

We note here that Viola et al. [32] did explore the effects of higher order radial variations on shear and flexion measurements and found them to be non-negligible for flexion measurements obtained using moments. For this work where we seek general trends imparted to the flexion signal by the PSF and fast, analytic remediation for the same, we are ignoring these non-Gaussian radial variations of the galaxy. In the limit of low signal to noise or large PSF, variability in radial profiles galaxy to galaxy will wash out and this assumption should simply be crude, not devastating.

We also argue that, for the discussion of the deconvolution of the shear and flexion terms, we may additionally drop the terms from the model varying as $\vec{\tilde{g}}^2 \cdot \vec{\theta}^4$ and $\left(\vec{\tilde{g}}\vec{G}\right) \cdot \vec{\theta}^5$ in equation parts (2.10c) and (2.10d). While the elliptical and circular models are formally equivalent even without this step, dropping these superfluous terms makes the following discussion simpler. Each of these terms are second order in galaxy ellipticity and shear, and thus only their convolutions with symmetric parts of the PSF will be retained in the final expression for the convolved galaxy image- all convolutions of these second order terms with asymmetric PSF terms that vary as astigmatism, coma, or trefoil must necessarily be third order small. The former term has exclusive spin four symmetry and the latter has exclusive spin five symmetry. The convolution of a spin m symmetric function with a spin 0 (i.e. symmetric) one

will itself have spin m, and so these terms cannot affect measurements of shear and flexions which have spins one, two, and three. Thus, while $\vec{\tilde{g}}^2 \cdot \vec{\theta}^4$ and $\left(\vec{\tilde{g}}\vec{G}\right) \cdot \vec{\theta}^5$ in equation parts (2.10c) and (2.10d) will affect the appearance of the pre- and post-convolved galaxy, they will not affect measurements of shear or flexions in either and so can be dropped for this analysis.

The galaxy model we will be using for the remainder of this paper is thus

$$I(\vec{\theta}) = \frac{I_0}{2\pi\alpha^2}\exp\left(-\frac{\theta^2}{2\alpha^2}\right) \times \Bigg[1 + \left\{ \frac{1}{\alpha^2}\left(\vec{\tilde{g}} \cdot \vec{\theta}^2\right) + \frac{1}{4\sqrt{2\ln(2)}\alpha^3}\left[3\left(\vec{\tilde{F}} \cdot \vec{\theta}\right)\theta^2 + \left(\vec{\tilde{G}} \cdot \vec{\theta}^3\right)\right] \right\} \tag{2.12a}$$

$$+ \left\{ \frac{1}{4\sqrt{2\ln(2)}\alpha^5} \times \frac{1}{2}\left[\left(\left(3\vec{\tilde{g}}\vec{F}^* + \vec{\tilde{g}}^*\vec{G}\right) \cdot \vec{\theta}\right)\theta^4 + \left(\left(3\vec{\tilde{g}}\vec{F}\right) \cdot \vec{\theta}^3\right)\theta^2 \right] \right\}^{7} \Bigg] \tag{2.12b}$$

where the first order effects of the spin one, two, and three terms, $\vec{\tilde{F}}$, $\vec{\tilde{g}}$, and $\vec{\tilde{G}}$ are given in equation part (2.12a) and are shown separately and together for a circular galaxy lensed by a SIS in figure 2-2. The second order spin one and three effects are given in equation part (2.12b). The full model with these second order effects is also shown in figure 2-2. [8]

[7] The flexions $\vec{F}$ and $\vec{G}$ multiplying $\vec{\tilde{g}}$ in this non-linear term are intentionally left as true flexions and not effective flexions $\vec{\tilde{F}}$ and $\vec{\tilde{G}}$. While we earlier argued that, to second order, these terms *could* be replaced by their effective flexion counterparts, we do not *need* to replace them here. As the model is more accurate if we do not, we leave in the true flexions.

[8] The models in figure 2-2 have background artifacts, most notably a 'pinching' in the sheared model galaxy and an 'island' on the right of the fully lensed model galaxy. The 'pinching' in the sheared model is wholly accounted for by the approximation that we use for the purpose of convolving the galaxy model with seeing, but do not make in the AIM model for fitting data. This same approximation partially accounts for the 'island' in the fully lensed model. Even with this approximation, these artifacts are in fact benign, but are accentuated by the contour levels and zoom of the plots.

The first order Taylor expansion of an elliptical Gaussian with no flexion produces a nearly elliptical, positive intensity peak with broad, but shallow dimples along either side of the major axis. The peak intensity of these dimples is a few percent of the intensity of the central peak. The apparent 'pinching' in the shear model is actually the cross over from positive to negative intensity caused by these low intensity dimples– the outer edges of the dimples are out of the frame of the image. When *fitting data*, we use the AIM model, in which we do NOT Taylor expand the elliptical Gaussian unlensed galaxy into a circular Gaussian plus elliptical perturbations as we have done here. Rather,

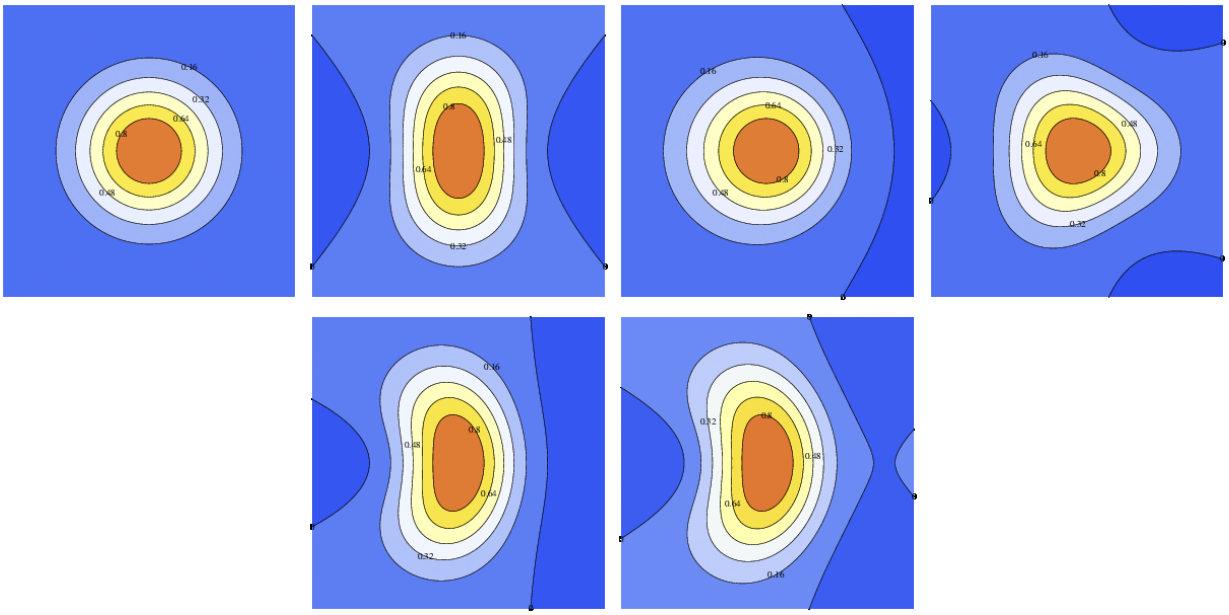

Figure 2-2 From left to right, top to bottom: a circular galaxy (a) unlensed, (b) lensed by shear $= -0.3$, (c) lensed by F-flexion $= -0.09$ only, (d) lensed by G-flexion $= 0.27$ only, (e) lensed by all three in an aligned orientation, using a model linear in lensing terms, and (f) with quadratic spin one and three perturbation terms included. Ratios of shears and flexions simulate a SIS lens with $\frac{r_{hl}}{\theta_e} = \frac{1}{2}$.

2.4.7 Shapelet basis decomposition of the model

The above model for the galaxy is physically intuitive, but for the convolution, it serves to move to the shapelets basis detailed in Refregier [24], Refregier & Bacon [25], Massey & Refregier [15], Massey et al. [16]. Polar shapelets are functions of the associated Laguerre Polynomials, and are convenient for representing and manipulating perturbations of Gaussian-like functions with various spin symmetries. As F-flexion, shear, and G-flexion have spins one, two, and three respectively, these lensing terms are contained in a small number of coefficients in this basis when using simple models for the unflexed galaxies.

---

we retain the ellipticity and its degenerate shear counterpart in the Gaussian's exponent and only expand the flexion terms. Therefore we do not get these negative intensity artifacts in an elliptical or sheared model galaxy.

A model galaxy which has been lensed by F-flexion or G-flexion alone has one or three low intensity dimples in addition to the central peak. The peak depth of these is only a few tenths of a percent of the central peak intensity. The 'island' in the plotted full model is actually where the sky level recovers to zero after having dropped to negative intensity.

Table 2.3. Conversion between lowest order shapelets and perturbations to a circular Gaussian.

Spin	Gaussian to Shapelets	Shapelets to Gaussian
	$\frac{1}{\sqrt{\pi}\alpha}\exp(-\frac{\theta^2}{2\alpha^2})[\quad] = [\quad]$	$[\quad] = \frac{1}{\sqrt{\pi}\alpha}\exp(-\frac{\theta^2}{2\alpha^2})[\quad]$
0	$1 = \chi_{00}$ $\theta^2 = \chi_{20} + \chi_{00}$ $\theta^4 = 2\chi_{40} + 4\chi_{20} + 2\chi_{00}$	$\chi_{00} = 1$ $\chi_{20} = \theta^2 - 1$ $\chi_{40} = \frac{1}{2}\theta^4 - 2\theta^2 + 1$
1	$(\vec{v}\cdot\vec{\theta}) = \frac{1}{2}\vec{v}\chi_{11} + \frac{1}{2}\vec{v}^*\chi_{1-1}$ $(\vec{v}\cdot\vec{\theta})\theta^2 = \vec{v}\left(\frac{1}{\sqrt{2}}\chi_{31} + \chi_{11}\right) + \text{c.c.}$ $(\vec{v}\cdot\vec{\theta})\theta^4 = \vec{v}\left(\sqrt{3}\chi_{51} + 3\sqrt{2}\chi_{31} + 3\chi_{22}\right) + \text{c.c.}$	$\vec{v}\chi_{11} + \vec{v}^*\chi_{1-1} = 2(\vec{v}\cdot\vec{\theta})$ $\vec{v}\chi_{31} + \vec{v}^*\chi_{3-1} = (\vec{v}\cdot\vec{\theta})\left(\sqrt{2}\theta^2 - 2\sqrt{2}\right)$ $\vec{v}\chi_{51} + \vec{v}^*\chi_{5-1} = (\vec{v}\cdot\vec{\theta})\left(\frac{1}{\sqrt{3}}\theta^4 - 2\sqrt{3}\theta^2 + 2\sqrt{3}\right)$
2	$(\vec{v}\cdot\vec{\theta}^2) = \frac{1}{\sqrt{2}}\vec{v}\chi_{22} + \text{c.c.}$ $(\vec{v}\cdot\vec{\theta}^2)\theta^2 = \vec{v}\left(\frac{\sqrt{3}}{\sqrt{2}}\chi_{42} + \frac{\sqrt{3}}{\sqrt{2}}\chi_{22}\right) + \text{c.c.}$	$\vec{v}\chi_{22} + \vec{v}^*\chi_{2-2} = \sqrt{2}(\vec{v}\cdot\vec{\theta}^2)$ $\vec{v}\chi_{42} + \vec{v}^*\chi_{4-2} = (\vec{v}\cdot\vec{\theta}^2)\left(\frac{\sqrt{2}}{\sqrt{3}}\theta^2 - \sqrt{6}\right)$
3	$(\vec{v}\cdot\vec{\theta}^3) = \frac{\sqrt{3}}{\sqrt{2}}\vec{v}\chi_{33} + \text{c.c.}$ $(\vec{v}\cdot\vec{\theta}^3)\theta^2 = \vec{v}\left(\sqrt{6}\chi_{53} + 2\sqrt{6}\chi_{33}\right) + \text{c.c.}$	$\vec{v}\chi_{33} + \vec{v}^*\chi_{3-3} = \frac{\sqrt{2}}{\sqrt{3}}(\vec{v}\cdot\vec{\theta}^3)$ $\vec{v}\chi_{53} + \vec{v}^*\chi_{5-3} = (\vec{v}\cdot\vec{\theta}^3)\left(\frac{1}{\sqrt{6}}\theta^2 - 2\frac{\sqrt{2}}{\sqrt{3}}\right)$
4	$(\vec{v}\cdot\vec{\theta}^4) = \sqrt{6}\vec{v}\chi_{44} + \text{c.c.}$	$\vec{v}\chi_{44} + \vec{v}^*\chi_{4-4} = \frac{1}{\sqrt{6}}(\vec{v}\cdot\vec{\theta}^4)$
5	$(\vec{v}\cdot\vec{\theta}^5) = \sqrt{30}\vec{v}\chi_{55} + \text{c.c.}$	$\vec{v}\chi_{55} + \vec{v}^*\chi_{5-5} = \frac{1}{\sqrt{30}}(\vec{v}\cdot\vec{\theta}^5)$

Conversion between lowest order shapelets and perturbations to a circular Gaussian with Gaussian width α and radial coordinate θ. Perturbations to the Gaussian have the form $\frac{1}{\sqrt{\pi}\alpha}\exp(-\frac{\theta^2}{2\alpha^2})\left[(\vec{v}\cdot\vec{\theta}^m)\theta^{n-m}\right]$, where the magnitude and direction of the perturbation are given by $\vec{v}$, and the radial and spin variance of the perturbation are n and m respectively.

Figure 2-3 Gaussian and spin zero through three perturbations with lowest radial dependences, in association with the left hand column of table 2.3. These perturbations are analogous to the shapelets basis functions, however they are not orthonormal. The left hand figures are for perturbations along the cartesian x axis (i.e $\vec{v}$ in table 2.3 is real). The right hand figures are for perturbations maximally orthogonal to the cartesian x axis ($\vec{v}$ in table 2.3 is strictly non-real). The Gaussian and spin zero perturbations have only a real component.

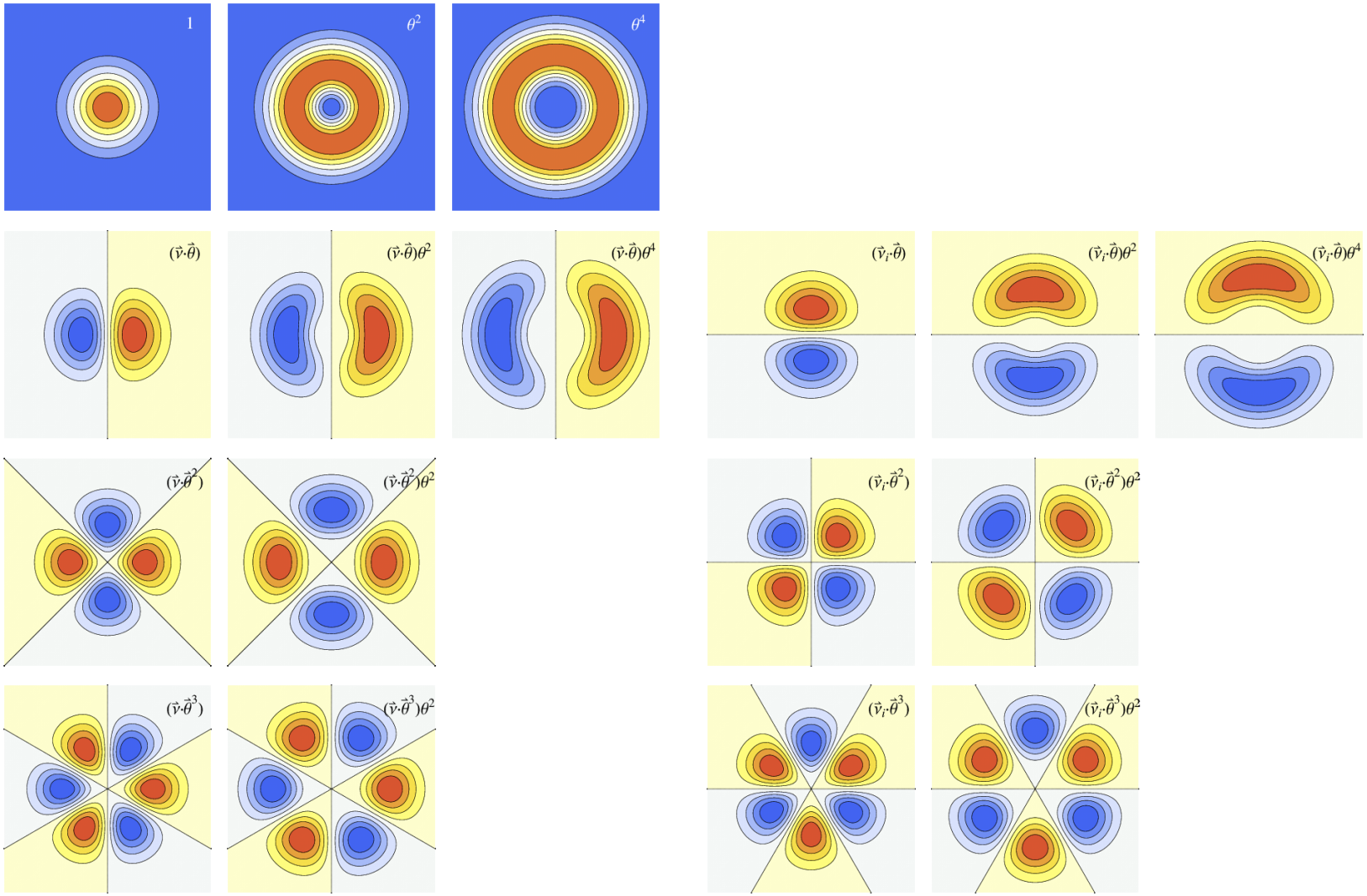

The relation between the lowest order shapelets and perturbations to the circular Gaussian function are given in table 2.3. For reference, the Gaussian perturbations used in the model and given in the table are plotted in figure 2-3. The polar shapelets, which are essentially the orthonormal versions of the shown functions, are depicted in Massey & Refregier [15], Massey et al. [16].

Following Massey & Refregier [15], but normalizing the flux to I_0, the function representing a galaxy of scale length α is

$$I(\vec{\theta}) = \frac{I_0}{2\sqrt{\pi}\alpha} \sum_{n=0}^{\infty} \sum_{m=-n}^{n} f_{nm} \chi_{nm}(\vec{\theta}; \alpha) \tag{2.13}$$

where χ_{nm} are the Polar shapelets and f_{nm} are unitless coefficients. The first subscript of the coefficient, n, denotes the radial dependence of the term, and the second, m, denotes the spin symmetry.

We note again here that the aberrations used in this work are all unitless quantities. This differs from shapelets convention, specifically that in Massey & Refregier [15] wherein flexions are unitful and always appear in multiple with the galaxy scale length when appearing in a shapelet coefficient.

The non-zero shapelets coefficients needed to represent the linear expansion of the lensed galaxy of equation (2.12a) are

$$
\begin{aligned}
f_{00} &= 1 \qquad (2.14a)\\
f_{22} &= \frac{1}{\sqrt{2}}\tilde{\vec{g}}\\
f_{31} &= \frac{1}{4\sqrt{2\ln(2)}}\frac{1}{\sqrt{2}}\left(3\tilde{\vec{F}}\right),\ f_{11} = \frac{1}{4\sqrt{2\ln(2)}}\left(3\tilde{\vec{F}}\right)\\
f_{33} &= \frac{1}{4\sqrt{2\ln(2)}}\sqrt{\frac{3}{2}}\tilde{\vec{G}}
\end{aligned}
$$

$$
\begin{aligned}
f_{51} &= \sqrt{3}\vec{p},\ f_{31} = 3\sqrt{2}\vec{p},\ f_{11} = 3\vec{p} \qquad (2.14b)\\
f_{53} &= \sqrt{6}\vec{q},\ f_{33} = 2\sqrt{6}\vec{p}\\
\text{where}\quad \vec{p} &= \frac{1}{4\sqrt{2\ln(2)}}\frac{1}{2}\left(3\tilde{\vec{g}}\vec{F}^{*} + \tilde{\vec{g}}^{*}\vec{G}\right)\\
\vec{q} &= \frac{1}{4\sqrt{2\ln(2)}}\frac{1}{2}\left(3\tilde{\vec{g}}\vec{F}\right).
\end{aligned}
$$

Only quantities with positive spin coefficients are listed, as negative spin coefficients are simply the complex conjugates of their positive counterparts. All other unlisted coefficients are zero, or will otherwise not affect the final measured spin one, two, or three image shape characteristics.

For clarity, we have broken up the shapelets coefficients into parts (2.14a) and (2.14b) which derive from the linear galaxy expansion terms in the model given by (2.12a), and the quadratic galaxy expansion terms in (2.12b), respectively. The total coefficients are sums of all components.

Terms varying linearly on the galaxy, χ_{11}, appear with non-zero coefficient, despite having no obvious counterpart in equation (2.12). These terms appear because the shapelets basis is orthonormal, and thus χ_{31} and χ_{51} have components which vary linearly with radius. As the lensing distortions are not orthonormal, the inclusion of the χ_{11} term is necessary in order to counter the part of the linearly varying χ_{31} and χ_{51} terms absent from the lensing model, see table 2.3. However, measurements of flexion are made by probing terms which vary as radius cubed on the galaxy, χ_{31} and

χ_{33} in this basis. Thus χ_{11} is merely a remainder of sorts.

2.4.8 Model of a PSF

As a Gaussian is a convenient model for an unlensed galaxy, it is also a convenient, simple approximation for a symmetric point spread function. Additionally, we argued in §2.3 that convergence and defocus are the same, shear and astigmatism are the same, F-flexion and coma are the same, and G-flexion and trefoil are the same. However, the lensing aberrations are applied to the galaxy image, which is non-uniformly illuminated, but the telescope aberrations are applied to a uniformly illuminated wavefront. We therefore cannot account for the telescope aberrations by applying deflections to the symmetric, atmospherically aberrated PSF image in the same way that we could treat the gravitational lens as applying deflections to the Gaussian, unlensed galaxy.

In order to account for the effects of the telescope aberrations on the PSF, we follow the work of Jarvis et al. [9], and compute the moments imparted onto images by wavefront gradients in the pupil plane. If we were to compute an infinite number of moments, we could reconstruct the exact form of the image. But, in the spirit of informed approximation, we shall compute exact moments through third, and then approximate the form of the PSF as Gaussian plus perturbations, similar to that of the Galaxy model. We choose to truncate our model at third moments, as the second and third image moments will affect shear and flexion measurements most significantly.

The PSF is the stellar image. Ignoring atmospheric effects, which add a series of random delays to the wavefront, the light reaching the pupil from a star is parallel. Summarizing from Jarvis et al. [9], in the limit of geometric optics wavefront aberrations will deflect light rays from a star hitting different areas on the pupil into beams with slightly different directions. If we assume no net tilt of the wavefront, an individual beam's deflection will be proportional to its final displacement from the star image's center in the image plane.[9] It thus follows that the moments of the stellar

[9] A net wavefront tilt will cause the entire star to be moved from its nominal position, shifting

images are proportional to the deflections of light at the pupil, i.e. the gradients of the wavefront.

A wavefront delay across the pupil, W' and its gradient, $\vec{\nabla}W'$, are given by the following functions of the normalized pupil coordinated $\vec{\rho}$ the radius of the pupil, R, and unitful aberrations defocus, d', astigmatism, $\vec{a}'$, coma, $\vec{c}'$, and trefoil, $\vec{t}'$,

$$\begin{aligned} W' &= d'\rho^2 + \vec{a}' \cdot \vec{\rho}^2 + \vec{c}' \cdot \rho^2\vec{\rho} + \vec{t}' \cdot \vec{\rho}^3 \\ \text{so } \vec{\nabla}W' &= \left(2\frac{d'}{R}\vec{\rho} + 2\frac{\vec{a}'}{R}\vec{\rho}^* + 2\frac{\vec{c}'}{R}\rho^2 + \frac{\vec{c}'^*}{R}\vec{\rho}^2 + 3\frac{\vec{t}'}{R}(\vec{\rho}^*)^2\right) \\ &= \zeta\left(2d\vec{\rho} + 2\vec{a}\vec{\rho}^* + 2\vec{c}\rho^2 + \vec{c}^*\vec{\rho}^2 + 3\vec{t}(\vec{\rho}^*)^2\right) \\ &= \zeta\vec{\nabla}W. \end{aligned} \tag{2.15}$$

We have introduced a unitless wavefront gradient $\vec{\nabla}W$ and unitless aberrations d, a, c, and t, which can be rendered unitful with the coefficient ζ. The scale ζ is arbitrary, but may be thought of as a 'typical' ray displacement or image size and thus has units of the same– angle of ray displacement, or equivalently angular image size. In radians, ζ is given by the ratio of a typical magnitude for a wavefront delay on the pupil (possibly one wave, though there are many conventions) and the pupil radius. The unprimed wavefront gradient $\vec{\nabla}W$, the defocus, d, astigmatism, $\vec{a}$, coma, $\vec{c}$, and trefoil, $\vec{t}$ are therefore unitless in all following discussion, however relating these unitless quantities to the physical delays in the wavefront at the telescope's pupil requires that one know the scale, ζ, and pupil radius, R.

Defining the zeroth moment to be one, and the first moments to be zero, i.e. normalized intensity and no tilt, there are four undetermined complex image moments up to and including third; a spin zero second moment, a spin two second moment, a spin one third moment, and a spin three third moment.

the central intensity; tilt imparts a net first moment.

$$
\begin{aligned}
Q_0 &= \zeta^2 \int\int \left|\vec{\nabla} W\right|^2 \rho d\rho d\phi \\
\vec{Q_2} &= \zeta^2 \int\int \left(\vec{\nabla} W\right)^2 \rho d\rho d\phi \\
\vec{Q_1} &= \zeta^3 \int\int \left|\vec{\nabla} W\right|^2 \vec{\nabla} W \rho d\rho d\phi \\
\vec{Q_3} &= \zeta^3 \int\int \left(\vec{\nabla} W\right)^3 \rho d\rho d\phi,
\end{aligned}
\tag{2.16}
$$

Using the relations for the wavefront gradients presented in equations (2.15), we find the resultant second and third moments for the aberrations are

$$
\begin{aligned}
Q_0 &= \zeta^2 \left(2d^2 + 2a^2 + \frac{2}{3}c^2 + 3t^2\right) \\
\vec{Q_2} &= \zeta^2 \left(4\vec{a}d + \frac{1}{3}\vec{c}^2 + 2\vec{c}^*\vec{t}\right) \\
\vec{Q_1} &= \zeta^3 \left(\frac{1}{3}\vec{c}\left(8d^2 + 4a^2 + c^2 + 9t^2\right) + 4\vec{c}^*\vec{a}d + 8\vec{t}\vec{a}^*d + 4\vec{a}^2\vec{t}^* + (\vec{c}^*)^2\vec{t}\right) \\
\vec{Q_3} &= \zeta^3 \left(3\vec{t}\left(4d^2 + c^2\right) + 4\vec{c}\vec{a}d + 4\vec{c}^*\vec{a}^2\right).
\end{aligned}
\tag{2.17}
$$

We will work under the assumption that the atmospheric effect will simply add to the spin zero second moment. Moreover, we shall assume that the atmosphere will only contribute to the spin zero moment. $\vec{Q_1}$, $\vec{Q_2}$, and $\vec{Q_3}$ remain the same, but Q_0 becomes

$$
Q_0 = \zeta^2 \left(2d^2 + 2a^2 + \frac{2}{3}c^2 + 3t^2 + 2S_{atm}^2\right), \tag{2.18}
$$

where S_{atm}^2 is the unitless second moment caused by atmospherically induced semi-random wavefront delays at the pupil. The factor of two is placed for convenience, so that the spin zero second moment of star aberrated by the atmosphere alone is $2\zeta^2 S_{atm}^2$. As the atmospheric effects become dominant over the telescope effects, $S_{atm}\zeta$

approaches the measured Gaussian width of the PSF.

We define the Gaussian width of the PSF as α so that a measured spin zero second moment is $2\alpha^2$, if the PSF is truly Gaussian. With this definition, the unitless Gaussian width is

$$\frac{\alpha}{\zeta} = \sqrt{\left(d^2 + a^2 + \frac{1}{3}c^2 + \frac{3}{2}t^2 + S_{atm}^2\right)}. \tag{2.19}$$

Like the second moment from which it is derived, the unitless Gaussian width is a measurable quantity.

In the absence of other asymmetric aberrations, each spin n wavefront delay produces a spin n moment whose magnitude is proportional to the product of itself and the defocus to some power. Therefore, analogous to the mappings from galaxy distortions $\vec{g}$, $\vec{F}$ and $\vec{G}$ to effective spin symmetric distortions $\tilde{\vec{g}}$, $\tilde{\vec{F}}$ and $\tilde{\vec{G}}$, we will define new, effective aberrations in tilde space which produce spin symmetric moments, namely

$$\begin{aligned}
\tilde{\vec{a}} &= \frac{1}{4\frac{\alpha^2}{\zeta^2}}\left(4\vec{a}d + \frac{1}{3}\vec{c}^2 + 2\vec{c}^*\vec{t}\right) \\
\tilde{\vec{c}} &= \frac{1}{24\frac{\alpha^3}{\zeta^3}}\frac{1}{3}\left(\frac{1}{3}\vec{c}\left(8d^2 + 4a^2 + c^2 + 9t^2\right) + 4\vec{c}^*\vec{a}d + 8\vec{t}\vec{a}^*d + 4\vec{a}^2\vec{t}^* + (\vec{c}^*)^2\vec{t}\right) \\
\tilde{\vec{t}} &= \frac{1}{24\frac{\alpha^3}{\zeta^3}}\left(3\vec{t}\left(4d^2 + c^2\right) + 4\vec{c}\vec{a}d + 4\vec{c}^*\vec{a}^2\right).
\end{aligned} \tag{2.20}$$

The magnitude of these effective aberrations for one wave (600nm) of astigmatic, comatic, or trefoil aberration mixed with one wave of defocus is shown in figure 2.4.8 for the Magellan 6.5m telescopes and the proposed LSST 8.4m telescope. For a constant wavefront delay due to telescope aberration, the magnitudes of the effective asymmetric aberrations decrease with increased atmospheric smearing.

Using the effective aberrations from equation (2.20), the spin zero, one, two and three moments simplify to,

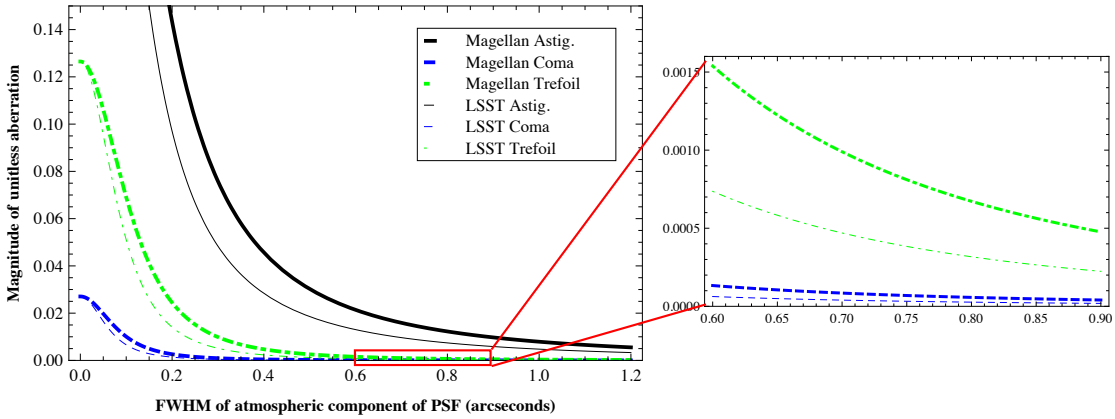

Figure 2-4 Magnitude of the effective, unitless astigmatism $\tilde{a}$ (black, solid), coma $\tilde{c}$ (blue, dashed), and trefoil $\tilde{t}$ (green, dot-dashed) aberrations for one wave (600nm delay at pupil edge) of the unitful aberration plus equal defocus. As a scale for the image size, ζ, we have used $0\farcs1$, which also corresponds to 100nm of wavefront delay for 1m of mirror radius. For a fixed wavefront delay, the magnitude of the *effective* aberration scales (inversely) with the width of the atmospheric smearing. We have zoomed in on the region between atmospherically induced PSF widths of FWHM = $0\farcs6$ and $0\farcs9$, to show detail in the effective coma and trefoil aberrations in the regime of traditional ground based observations.

$$
\begin{aligned}
Q_0 =& \zeta^2 \left(1 + \frac{d^2 + a^2 + \frac{1}{3}c^2 + \frac{3}{2}t^2}{S_{atm}^2}\right) = 2\alpha^2 \\
\vec{Q}_2 =& \zeta^2 4\frac{\alpha^2}{\zeta^2}\left(\vec{\tilde{a}}\right) = 4\alpha^2\left(\vec{\tilde{a}}\right) \\
\vec{Q}_1 =& \zeta^3 24\frac{\alpha^3}{\zeta^3}\left(3\vec{\tilde{c}}\right) = 24\alpha^3\left(3\vec{\tilde{c}}\right) \\
\vec{Q}_3 =& \zeta^3 24\frac{\alpha^3}{\zeta^3}\left(\vec{\tilde{t}}\right) = 24\alpha^3\left(\vec{\tilde{t}}\right)
\end{aligned}
\tag{2.21}
$$

There are many possible functions which will produce these first few moments. However, as stated in the beginning of this subsection, we seek only a first order approximation to the PSF, preferably one which can be easily represented as low order shapelets for convolution. As a Gaussian is a sufficient model for a symmetric PSF caused by atmospheric smearing, and spin one through three distortions will most severely affect the lensing measurement, we choose a functional form consisting

of a Gaussian plus spin one through three Gaussian perturbations which satisfies the above listed second and third moment constraints.

We argue that the spin asymmetric Gaussian perturbations with lowest order radial dependence are the most physically relevant and thus terms with redundant spin symmetries but higher order radial dependences should be dropped in the model. In the limit of geometric optics and in the absence of atmospheric effects, the telescope produces aberrations of finite extent. Defocus images stars into finite circular rings, perfect images of the pupil. Astigmatism does the same, unless in conjunction with defocus, which will convert the finite rings into finite ellipses. Coma, in its extreme, produces 'comet' images with a pointlike head and a dimmer, but still defined circular tail, an image of the outer ring of the pupil. Any infinite extent of the aberrations is caused by diffraction within the telescope and smearing due to atmospheric seeing. Therefore, the spin asymmetries introduced by telescope aberrations would logically affect terms with lower order radial dependence more strongly than terms with higher order radial dependence.

Therefore we will retain the astigmatic, spin two term varying as $\vec{\theta}^2$ and the trefoil, spin three term varying as $\vec{\theta}^3$, dropping all spin two and three terms with higher radial dependence. The comatic, spin one term has the same radial dependence on the pupil as trefoil (cubic, one order higher than shear's quadratic pupillary dependence), so it ought to have the same radial variation on the image. We therefore retain the $\vec{\theta}\theta^2$ spin one term, discarding the others. While this is an admittedly ad hoc approximation, it does allow us to create a completely constrained model using only second and third moments.

The complete model for the asymmetric point spread function as it will most significantly affect a lensed galaxy is therefore

$$I(\vec{\theta}) = \frac{I_0}{2\pi\alpha^2}\exp\left(-\frac{\theta^2}{2\alpha^2}\right) \times \Big[1 + \frac{1}{\alpha^2}\left(\vec{\tilde{a}}\cdot\vec{\theta}^2\right) + \frac{1}{4\sqrt{2\ln(2)}\alpha^3}\left(3\left(\vec{\tilde{c}}\cdot\vec{\theta}\right)\theta^2 + \left(\vec{\tilde{t}}\cdot(\vec{\theta})^3\right)\right)\Big], \tag{2.22}$$

exactly the same model as a the linear lensed galaxy, but with the telescope aberrations producing spin one, two, and three moments replacing lensing terms. The measurable Gaussian width of the PSF is α, which is equal to $S_{atm}\zeta$ in equations (2.17) in the limit of no telescope aberrations.

Though the aberrations $\vec{\tilde{a}}$, $\vec{\tilde{c}}$, and $\vec{\tilde{t}}$ are combinations of all the telescope aberrations, they are proportional to astigmatism, coma, and trefoil in the absence of other asymmetric aberrations, and produce spin two, one and three moments respectively. Therefore we shall loosely refer to them as astigmatism, coma, and trefoil respectively. In the limit that defocus is much larger than the asymmetric aberrations, this loose approximation improves. Optionally (and optimally), one could measure the second moment, measure the tilde space aberrations, and correct the telescope– this step would be straightforward and require no iterations.

Using the same vector conversions as for the galaxy model, one can infer that the shapelets coefficients needed to represent the PSF model are

$$\begin{aligned} f_{00} &= 1 \\ f_{22} &= \frac{1}{\sqrt{2}}\vec{\tilde{a}} \\ f_{31} &= \frac{1}{4\sqrt{2\ln(2)}}\frac{1}{\sqrt{2}}\left(3\vec{\tilde{c}}\right), \; f_{11} = \frac{1}{4\sqrt{2\ln(2)}}\left(3\vec{\tilde{c}}\right) \\ f_{33} &= \frac{1}{4\sqrt{2\ln(2)}}\sqrt{\frac{3}{2}}\vec{\tilde{t}}. \end{aligned} \tag{2.23}$$

2.5 Extracting gravitational lensing parameters from measured values

We convolve a lensed galaxy model of scale length η and shear and flexions $\vec{\tilde{g}}$, $\vec{\tilde{F}}$, and $\vec{\tilde{G}}$ with an aberrated PSF model of scale length σ and astigmatism, coma and trefoil, $\vec{\tilde{a}}$, $\vec{\tilde{c}}$, and $\vec{\tilde{t}}$ to determine the effects on the resultant image's apparent lensing characteristics, i.e what an observer measuring the image shape would naively take

the true shear and flexion values to be if he were not accounting for the PSF. Given these apparent flexion and shear values, we then provide a analytic formulae to extract the true lensing terms, given the PSF at the position of the galaxy.

We perform the convolution in two parts. First we convolve the lensed galaxy model with a symmetric PSF model, aberrated only by symmetric atmospheric smearing. Then we convolve the galaxy model with the asymmetric, telescope aberrated PSF model.

2.5.1 Convolution of the lensed galaxy model with the symmetric, atmospherically aberrated PSF model

The symmetric PSF is a simple Gaussian, or in the shapelets basis $f_{00} = 1$, and all other coefficients are zero.

Using the shapelets representation of the galaxy model given in equation (2.13) with coefficients in (2.14), it is straightforward to analytically compute the convolved galaxy form. One can perform this convolution either by computing a minimal number of relatively simple integrals, or by switching to cartesian shapelets and performing the matrix manipulations detailed in Refregier & Bacon [25]. As spin m shapelets will only map onto other spin m shapelets under convolution with a Gaussian, the mathematics are tractable using either method.

The scale length ξ of the convolved galaxy is predictably equal to the quadratic sum of the PSF and galaxy Gaussian widths, $\sqrt{\sigma^2 + \eta^2}$. This scale length dictates the scale length of the shapelets basis in which to optimally decompose the convolved image. Using this basis, we find the shapelets coefficients for the convolved galaxy are

$$
\begin{aligned}
f'_{00} &= 1 \\
f'_{22} &= \frac{1}{\sqrt{2}}\frac{1}{\xi^2}\left(\vec{\tilde{g}}\eta^2\right) \\
f'_{31} &= \frac{1}{4\sqrt{2\ln(2)}}\frac{1}{\sqrt{2}}\frac{1}{\xi^3}\left(3\vec{\tilde{F}}\eta^3\right),\ f'_{11} = \frac{1}{4\sqrt{2\ln(2)}}\frac{1}{\xi}\left(3\vec{\tilde{F}}\eta\right)\left(1+\frac{\sigma^2}{\xi^2}\right) \\
f'_{33} &= \frac{1}{4\sqrt{2\ln(2)}}\sqrt{\frac{3}{2}}\frac{1}{\xi^3}\left(\vec{\tilde{G}}\eta^3\right)
\end{aligned}
\tag{2.24}
$$

$$
\begin{aligned}
f'_{51} &= \sqrt{3}\frac{1}{\xi^5}\left(\vec{p}\eta^5\right),\ f'_{31} = 3\sqrt{2}\frac{1}{\xi^3}\left(\vec{p}\eta^3\right)\left(1+\frac{\sigma^2}{\xi^2}\right),\ f'_{11} = 3\frac{1}{\xi}\left(\vec{p}\eta\right)\left(1+\frac{\sigma^2}{\xi^2}\right)^2 \\
f'_{53} &= \sqrt{6}\frac{1}{\xi^5}\left(\vec{q}\eta^5\right),\ f'_{33} = 2\sqrt{6}\frac{1}{\xi^3}\left(\vec{q}\eta^3\right)\left(1+\frac{\sigma^2}{\xi^2}\right),
\end{aligned}
\tag{2.25}
$$

where $\vec{p}$ and $\vec{q}$ are the functions of $\vec{F}$ and $\vec{G}$ given in equation (2.14b).

We wish to extract terms which vary as $\vec{\theta}^2$, $\vec{\theta}\theta^2$, and $\vec{\theta}^3$ as these are the shear and flexion like terms in the model, $\vec{g}'$, $\vec{F}'$, and $\vec{G}'$. Naively, one obtains these terms by simply gathering the f'_{22}, f'_{31}, and f'_{33} coefficients. However, one must first remove the effects of the higher order variances which would be detected as a separate signal from the flexions, but 'trickle down' into these terms by virtue of the orthogonality of the shapelets basis.

We remove the $\vec{\theta}\theta^4$ and $\vec{\theta}^3\theta^2$ dependences, which would be detected as a separate signal with θ^5 radial dependence, and compare the remaining f'_{22}, f'_{31} and f'_{33} terms with the unconvolved galaxy model's coefficients. We find the following mapping from intrinsic ellipticity and gravitational shear and flexion to the apparent signal in a seeing degraded image to be[10]

[10]The flexions $\vec{F}$ and $\vec{G}$ multiplying $\vec{\tilde{g}}$ in the non linear terms of (2.26b) and (2.26c) are intentionally gravitational flexions and not effective flexions $\vec{\tilde{F}}$ and $\vec{\tilde{G}}$, consistent with equation (2.12).

$$\vec{g}'\xi^2 = \left(\vec{\tilde{g}}\eta^2\right) \tag{2.26a}$$

$$\vec{F}'\xi^3 = \left(\vec{\tilde{F}}\eta^3\right) + 2(\frac{\sigma}{\xi})^2\left(3\vec{\tilde{g}}\vec{F}^* + \vec{\tilde{g}}^*\vec{G}\right)\eta^3 \tag{2.26b}$$

$$\vec{G}'\xi^3 = \left(\vec{\tilde{G}}\eta^3\right) + 4(\frac{\sigma}{\xi})^2\left(3\vec{\tilde{g}}\vec{F}\right)\eta^3. \tag{2.26c}$$

To linear order in asymmetric terms, each apparent gravitational aberration is diluted by the ratio of the uncorrupted galaxy size to the measured galaxy size to a power equal to the radial dependence of the aberration on the galaxy.

The quadratic expansion to the galaxy model, which had formerly only contributed to the shear and flexion-like signals by altering the origin and magnitude of the pre-convolved flexion signals, $\vec{\tilde{F}}$ and $\vec{\tilde{G}}$, contribute to the apparent signals again after convolution. This new contribution is caused by a 'mixing down' of the quintic radial signal to a cubic radial signal on the galaxy via convolution with the PSF. These non-linear contributions to the apparent lensing signals are diluted by the PSF to the same power as the linear terms, but with an additional dilution factor of the ratio of the PSF size to the measured galaxy size, squared.

The ratio of the effective signal after convolution with a symmetric PSF (i.e. the measured signal) and the effective lensing signal before convolution is shown in figure 2-5. The horizontal axis contains the ratio of the PSF size to the unconvolved galaxy size. For both shear and flexion, the larger the PSF, the less lensing signal is retained post convolution, however the variation with PSF size differs for shear and the flexions. The fraction of $\tilde{F}$ and $\tilde{G}$-flexions retained post-convolution will generally depend on how much shear is present and the ratio of F- and G-flexions. As seen in equation (2.26b), for an SIS the 1:-3 ratio of F- to G-flexions will render the effect of convolution on $\tilde{F}$-flexion independent of shear. Therefore the accelerated dilution of $\tilde{F}$-flexion relative to the shear is caused by the PSF alone. The PSF causes the same dilution of $\tilde{G}$-flexion, however, the shear enhances the measured $\tilde{G}$-flexion in most lenses, counteracting the effect of the PSF, as can be seen in equation (2.26c). This is consistent with figure 2-5.

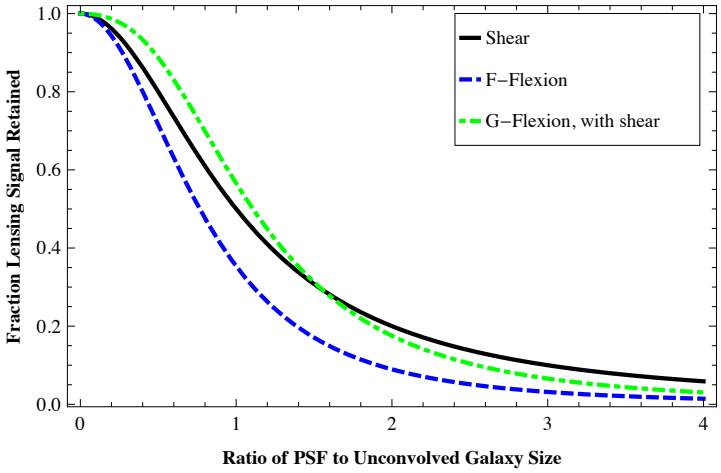

Figure 2-5 The fraction of the shear/ellipticity (black, solid) and F- and G-flexion (blue, dashed; green, dot-dashed) signals retained after convolution with a symmetric PSF of increasing size. The presence of intrinsic ellipticity or gravitational shear will generally alter the retained flexion signal, however for an SIS lens, the retained F-flexion is independent of shear. The retained G-flexion shown here is computed with shear and F-flexion present in the lensed galaxy, boosting the observed G' signal. The magnitude of the pre-degraded shear signal is -0.3, and it is aligned with $\tilde{F}$--flexion and anti-aligned with $\tilde{G}$-flexion. $\tilde{F}$- and $\tilde{G}$-flexions are in a ratio of 1:-3, approximately consistent with a SIS of any r_{hl}:θ_e ratio.

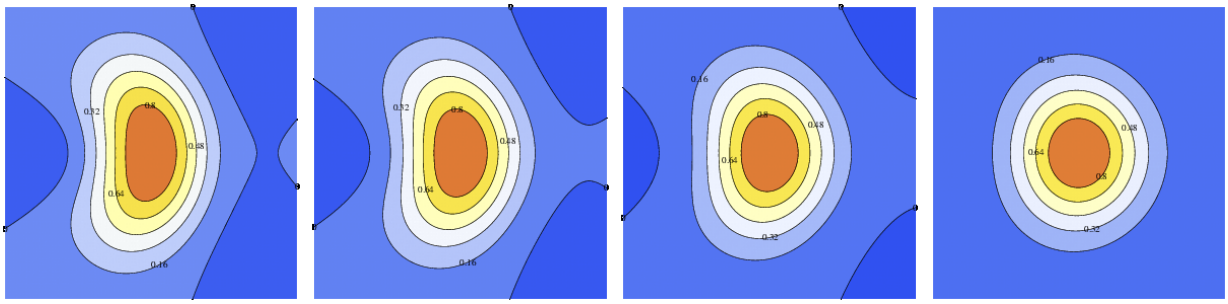

Figure 2-6 A circular galaxy lensed by aligned shear $= -0.3$, F-flexion $= -0.09$, and G-flexion $= 0.27$. (a) Unconvolved, and (b) convolved with PSFs with radii equal to half, (c) equal, and (d) twice the unlensed galaxy size. Ratios of shears and flexions simulate a SIS lens with $\frac{r_{hl}}{\theta_e} = \frac{1}{2}$. Images have been rescaled to highlight differences in asymmetries.

A contour plot of a lensed galaxy that is unconvolved, and convolved with PSFs of half, equal, and twice the unlensed galaxy size are shown in figure 2-6. When the radius of the PSF is only half of the size of the unconvolved galaxy, most of the overall image shape is retained, consistent with figure 2-5. Once the radius of the PSF is equal to the size of the unconvolved galaxy, the shear and flexion signals become more noticeably diminished. However, the spin three flexion signal is still apparent even when its spin one counterpart is nearly wiped out, because combinations of spin one flexion and shear can mix to create an additional apparent spin three flexion post-convolution. Convolutions with yet larger PSFs circularize the final galaxy image. These trends in signal dilution are in agreement with figure 2-5.

2.5.2 Convolution of the lensed galaxy with the asymmetrically aberrated PSF model

The asymmetrically aberrated PSF is formally the same as the linear order galaxy model. By exploiting symmetries in the two models, and only considering asymmetric perturbations to second order, we can analytically compute the convolution of the lensed galaxy with the asymmetrically aberrated PSF induced by telescope aberrations. As with the convolution of the galaxy and the symmetric PSF, this can be done either by computing a minimal number of relatively simple integrals, or by switching

to cartesian shapelets and performing the matrix manipulations detailed in Refregier & Bacon [25]. The shapelets coefficients for the convolved galaxy image are

$$
\begin{aligned}
f'_{00} &= 1 + \frac{\eta^2\sigma^2}{\xi^4}\left(\vec{\tilde{a}}\cdot\vec{\tilde{g}}\right) \qquad (2.27a)\\
f'_{22} &= \frac{1}{\sqrt{2}}\frac{1}{\xi^2}\Big[\left(\vec{\tilde{g}}\eta^2 + \vec{\tilde{a}}\sigma^2\right) + \frac{9}{8}\eta\sigma\left(\vec{\tilde{c}}\vec{\tilde{F}} + \frac{1}{\xi^4}\left(3\vec{\tilde{c}}\vec{\tilde{F}}\eta^2\sigma^2 - \vec{\tilde{c}}^*\vec{\tilde{G}} - \vec{\tilde{F}}^*\vec{\tilde{t}}\right)\right)\Big]\\
f'_{31} &= \frac{1}{4\sqrt{2\ln(2)}}\frac{1}{\sqrt{2}}\frac{1}{\xi^3}\Big[\left(3\vec{\tilde{F}}\eta^3 + \vec{\tilde{c}}\sigma^3\right)\\
&\qquad + \frac{\eta\sigma}{\xi^2}\frac{1}{2}\Big(\vec{\tilde{a}}\vec{\tilde{F}}^*\sigma(2\sigma^2-\eta^2) + \vec{\tilde{g}}\vec{\tilde{c}}^*\eta(2\eta^2-\sigma^2) - \vec{\tilde{a}}^*\vec{\tilde{G}}(\sigma\eta^2) - \vec{\tilde{g}}^*\vec{\tilde{t}}(\eta\sigma^2)\Big)\Big],\\
f'_{11} &= \frac{1}{4\sqrt{2\ln(2)}}\frac{1}{\xi}\Big[\left(3\vec{\tilde{F}}\eta\left(1+\frac{\sigma^2}{\xi^2}\right) + 3\vec{\tilde{c}}\sigma\left(1+\frac{\eta^2}{\xi^2}\right)\right)\\
&\qquad - \frac{\eta\sigma}{\xi^4}\frac{3}{2}\Big(\vec{\tilde{a}}\vec{\tilde{F}}^*\sigma(4\sigma^2+\eta^2) + \vec{\tilde{g}}\vec{\tilde{c}}^*\eta(4\eta^2+\sigma^2) - \vec{\tilde{a}}^*\vec{\tilde{G}}(\sigma\eta^2) - \vec{\tilde{g}}^*\vec{\tilde{t}}(\eta\sigma^2)\Big)\Big]\\
f'_{33} &= \frac{1}{4\sqrt{2\ln(2)}}\sqrt{\frac{3}{2}}\frac{1}{\xi^3}\Big[\left(\vec{\tilde{G}}\eta^3 + \vec{\tilde{t}}\sigma^3\right) + \frac{\eta\sigma}{\xi^2}6\Big(\vec{\tilde{a}}\vec{\tilde{F}}\sigma^3 + \vec{\tilde{g}}\vec{\tilde{c}}\eta^3\Big)\Big]
\end{aligned}
$$

$$
f'_{51} = \sqrt{3}\frac{1}{\xi^5}\left(\vec{p}\eta^5\right),\ f'_{31} = 3\sqrt{2}\frac{1}{\xi^3}\left(\vec{p}\eta^3\right)\left(1+\frac{\sigma^2}{\xi^2}\right),\ f'_{11} = 3\frac{1}{\xi}\left(\vec{p}\eta\right)\left(1+\frac{\sigma^2}{\xi^2}\right)^2 \qquad (2.27b)
$$

$$
f'_{53} = \sqrt{6}\frac{1}{\xi^5}\left(\vec{q}\eta^5\right),\ f'_{33} = 2\sqrt{6}\frac{1}{\xi^3}\left(\vec{q}\eta^3\right)\left(1+\frac{\sigma^2}{\xi^2}\right).
$$

Again, we wish to extract the manifestations of shear and flexion-like variations on the galaxy, the $\vec{\theta}^2$, $\vec{\theta}\theta^2$, and $\vec{\theta}^3$ terms. Following the steps in subsection §§2.5.1, we first account for the higher order shape variations that will be detected as separate signals, and then compare the coefficients f'_{22}, f'_{31}, and f'_{33} to their unconvolved counterparts to obtain the terms which vary as shear and F- and G-flexion respectively. We find

$$\vec{g}'\xi^2 = \left\{\vec{\tilde{g}}\eta^2 + \vec{\tilde{a}}\sigma^2\right\} + \left\{\frac{9}{8}\eta\sigma\left(\vec{\tilde{c}}\vec{F} + \frac{1}{\xi^4}\left(3\vec{\tilde{c}}\vec{\tilde{F}}\eta^2\sigma^2 - \vec{\tilde{c}}^*\vec{\tilde{G}}\eta^4 - \vec{\tilde{F}}^*\vec{\tilde{t}}\sigma^4\right)\right)\right\} \quad (2.28a)$$

$$\vec{F}'\xi^3 = \left\{\vec{\tilde{F}}\eta^3 + \vec{\tilde{c}}\sigma^3\right\} + \left\{2(\frac{\sigma}{\xi})^2\left(3\vec{\tilde{g}}\vec{F}^* + \vec{\tilde{g}}^*\vec{G}\right)\eta^3 \right. \quad (2.28b)$$
$$\left. + \frac{\eta\sigma}{\xi^2}\frac{1}{2}\left(\vec{\tilde{a}}\vec{\tilde{F}}^*\sigma(2\sigma^2 - \eta^2) + \vec{\tilde{g}}\vec{\tilde{c}}^*\eta(2\eta^2 - \sigma^2) - \vec{\tilde{a}}^*\vec{\tilde{G}}(\sigma\eta^2) - \vec{\tilde{g}}^*\vec{\tilde{t}}(\eta\sigma^2)\right)\right\}$$

$$\vec{G}'\xi^3 = \left\{\vec{\tilde{G}}\eta^3 + \vec{\tilde{t}}\sigma^3\right\} + \left\{4(\frac{\sigma}{\xi})^2\left(3\vec{\tilde{g}}\vec{F}\right)\eta^3 + \frac{\eta\sigma}{\xi^2}6\left(\vec{\tilde{a}}\vec{\tilde{F}}\sigma^3 + \vec{\tilde{g}}\vec{\tilde{c}}\eta^3\right)\right\}. \quad (2.28c)$$

The effects of telescope aberrations on the final convolved image can be broken down into terms which vary linearly with asymmetries due to lensing and telescope aberrations (first braced), and those which vary quadratically with lensing and telescope aberrations (second braced). For flexion, the terms quadratic in asymmetries have two distinct origins:

- The first group of non-linear terms vary as the product of shear and flexion (only with lensing aberrations, not with telescope aberrations). These are carry-overs from the convolution of the quadratic expansion of the galaxy model and the symmetric part of the PSF, and as such are also present in equation (2.26), the mapping for the lensing terms under convolution with a symmetric PSF.

- The second group of non-linear terms are cross terms between the telescope aberrations $\vec{\tilde{a}}$, $\vec{\tilde{c}}$, and $\vec{\tilde{t}}$ and gravitational lensing aberrations $\vec{\tilde{g}}$, $\vec{\tilde{F}}$, and $\vec{\tilde{G}}$. These terms are caused by mixing of spin signals under convolution to create signals with different spin symmetry. The apparent shear signal is also influenced by such cross terms.

The linear contributions of the telescope aberrations in the first braced terms of equations (2.28a), (2.28b), and (2.28c), highlight the similar forms of the PSF and lensing models- each lensing distortion adds to its telescope aberration counterpart (shear/astigmatism, F-flexion/coma, G-flexion/trefoil), but the lensing aberration is scaled by the size of the galaxy and the PSF aberration is scaled by the size of the PSF, each to the radial dependence of the aberration. The cross terms between the

telescope and lensing aberrations in the second braced part of the equations also show the intrinsic symmetries between the two types of aberrations. However, the parallelism between the lensing and telescope aberrations is broken by the fact that the galaxy model is expanded to quadratic order in lensing terms, while the PSF is truncated at linear order.

2.5.3 Interpretation of the apparent shear and flexions

Figure 2-7 shows the apparent shear and flexions on galaxies of varying intrinsic size for a PSF with fixed size and various asymmetries. In the limit of zero galaxy size, the apparent shear and F- and G-flexion signals are equal to the values of their corresponding telescope aberrations, astigmatism, coma, and trefoil. This result is somewhat intuitive, as a galaxy of zero width is a star, which produces the PSF when imaged by the telescope. In the other extreme, of very large galaxy size, the apparent lensing values approach the pre-convolved, effective lensing values and are virtually unaffected by the PSF and its aberrations. This is also expected.

To describe the behavior of the variations in the lensing terms between the zero and infinite galaxy size extremes for a fixed PSF size, we break down apparent shears and flexions into their contributions from linear and non-linear terms.

Referring back to figure 2-5, in absence of any telescope aberration, atmospheric smearing causes the lensing signal to be diluted by the ratio of the unconvolved to the convolved galaxy size, to the radial power of the lensing aberration. In absence of any asymmetric telescope aberration, this same relation holds here; shear approaches its true value as $\frac{\eta^2}{\xi^2}$ and flexion approaches its true value as $\frac{\eta^3}{\xi^3}$. However, note that figure 2-7 depicts a fixed PSF and increasing galaxy size on the horizontal axis whereas its predecessor had the inverse ratio on the horizontal axis.

Now including telescope aberrations, but only allowing terms linear in asymmetries (first braced terms of equation (2.28)), we find that the effect of asymmetric telescope aberrations is to add an offset to the post-convolved lensing terms which varies as the ratio of the PSF size to the convolved galaxy size, again, to the radial power of the aberration. For shear this is $\frac{\sigma^2}{\xi^2}$, and for flexion this is $\frac{\sigma^3}{\xi^3}$. In the limit

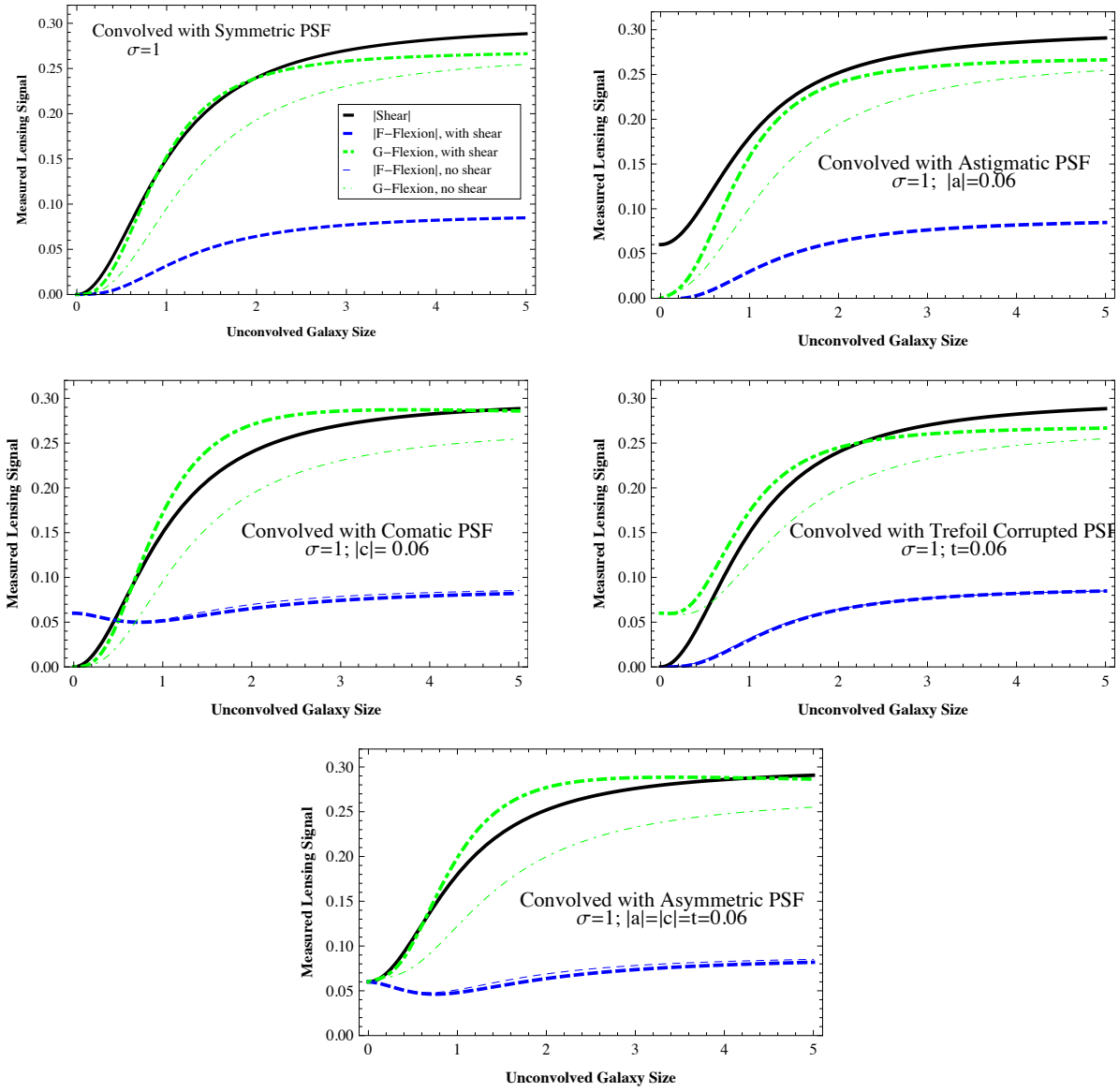

Figure 2-7 Shown within each plot are the apparent shear (black, solid) and F and G-flexion (blue, dashed; green, dot-dashed) signals for a circular galaxy model lensed by aligned shear $= -0.3$, $\tilde{F}$-flexion $= -0.09$, and $\tilde{G}$-flexion $= 0.27$. Also shown are the apparent F- and G-flexion signals for the same galaxy model if shear were not present (thin blue, dashed; thin green, dot-dashed), though these signals may be identical to their counterparts where shear is present. The unit of the galaxy radius on the horizontal axis is the PSF half light radius, σ. Top left to bottom right: the apparent signal after convolution with a PSF that is (a) symmetric, (b) astigmatic, ($\tilde{a} = -0.06$), (c) comatic, ($\tilde{c} = -0.06$), (d) corrupted by trefoil, ($\tilde{t} = 0.06$), and (e) corrupted by all of the listed aberrations. Pre convolved values for the lensing parameters approximately simulate a SIS lens with $\frac{r_{hl}}{\theta_e} = \frac{1}{2}$. Aberrations are large for the sake of illustration.

of a star, where $\xi = \sigma$, these constants are one, fully weighting the aberration; in the limit of a large galaxy, these constants approach zero, fully nulling the aberration.

For the sake of comparing the relative magnitudes of the terms linear and non-linear in asymmetries, it is mathematically advantageous to separate out the effect of atmospheric dilution from each term in equation (2.28). Once the effect of the atmosphere has been uncoupled, these terms can then be thought of as perturbations to the pre-convolved shear and flexions, which are then diluted by the atmosphere with them. This treatment of the effect of the atmosphere and telescope aberrations on the final apparent shears and flexions is perhaps less physically intuitive than the view where the effects of the telescope and atmosphere are coupled, but it does assist with the interpretation of the relative *sizes* of the biases introduced by different aberrations. Therefore, we decouple the effect of the atmosphere from the other terms here.

$$\vec{g}' = \frac{\eta^2}{\xi^2}\Big[\left\{\vec{\tilde{g}} + \vec{\tilde{a}}\frac{\sigma^2}{\eta^2}\right\} + \left\{\frac{9}{8}\left(\vec{\tilde{c}}\vec{\tilde{F}}\frac{\sigma}{\eta} + \frac{\eta^4}{\xi^4}\left(3\vec{\tilde{c}}\vec{\tilde{F}}\frac{\sigma^3}{\eta^3} - \vec{\tilde{c}}^*\vec{\tilde{G}}\frac{\sigma}{\eta} - \vec{\tilde{F}}^*\vec{\tilde{t}}\frac{\sigma^5}{\eta^5}\right)\right)\right\}\Big] \tag{2.29a}$$

$$\vec{F}' = \frac{\eta^3}{\xi^3}\Big[\left\{\vec{\tilde{F}} + \vec{\tilde{c}}\frac{\sigma^3}{\eta^3}\right\} + \frac{\eta^2}{\xi^2}\Bigg\{2\left(3\vec{\tilde{g}}\vec{\tilde{F}}^* + \vec{\tilde{g}}^*\vec{\tilde{G}}\right)\frac{\sigma^2}{\eta^2} \tag{2.29b}$$

$$+ \frac{1}{2}\Big(\vec{\tilde{a}}\vec{\tilde{F}}^*(2\frac{\sigma^4}{\eta^4} - \frac{\sigma^2}{\eta^2}) + \vec{\tilde{g}}\vec{\tilde{c}}^*(2\frac{\sigma}{\eta} - \frac{\sigma^3}{\eta^3}) - \vec{\tilde{a}}^*\vec{\tilde{G}}\frac{\sigma^2}{\eta^2} - \vec{\tilde{g}}^*\vec{\tilde{t}}\frac{\sigma^3}{\eta^3}\Big)\Bigg\}\Big]$$

$$\vec{G}' = \frac{\eta^3}{\xi^3}\Big[\left\{\vec{\tilde{G}} + \vec{\tilde{t}}\frac{\sigma^3}{\eta^3}\right\} + \frac{\eta^2}{\xi^2}\Bigg\{4\left(3\vec{\tilde{g}}\vec{\tilde{F}}\right)\frac{\sigma^2}{\eta^2} + 6\Big(\vec{\tilde{a}}\vec{\tilde{F}}\frac{\sigma^4}{\eta^4} + \vec{\tilde{g}}\vec{\tilde{c}}\frac{\sigma}{\eta}\Big)\Bigg\}.\Big] \tag{2.29c}$$

As the galaxy size becomes large with resect to the PSF, the ratio of the true to measured galaxy size, $\frac{\eta}{\xi}$, approaches one while the ratio of PSF to true galaxy size, $\frac{\sigma}{\eta}$ approaches zero. Assuming that most observers will either appropriately weight (or simply discard) galaxies for which PSF dilution will effectively wipe out any lensing signal, we take $\frac{\sigma}{\eta}$ to be small for most (priority) galaxies in a lensing survey.[11]

[11]For a given PSF, the smallest galaxies will have the noisiest measurements of PSF-corrected flexions, as the error in the measurement must propagate when removing the effects of PSF dilution. Thus the galaxies with the least noisy measurements will be the largest ones for which minimal dilution correction is required.

Accordingly we take $\frac{\eta}{\xi}$ to be non-negligible, order of one.

Examining equation (2.29), for shear, astigmatism perturbs the lensing distortion at a 'rate' of $\frac{\sigma^2}{\eta^2}$. Likewise, coma and trefoil each perturb their respective flexions at rates of $\frac{\sigma^3}{\eta^3}$. These effects of these perturbations drop off quickly for the large galaxies of primary interest. By contrast, the terms non-linear in asymmetries given in the second braced terms of equations (2.28) and (2.29) perturb their lensing distortions at rates up to $\frac{\sigma}{\eta}$. Thus, the effects of these cross terms can manifest in the measurements of shears and flexions in galaxies of much larger galaxy sizes than the linear terms can.

Anywhere in figure 2-7 where the apparent flexion signal is different when computed with and without the presence of shear in the galaxy is a demonstration of the effect of the non-linear asymmetric terms on the apparent signal. The apparent signal enhancement of G-flexion in figure 2-7c is an extreme effect; coma has been added to this PSF, not trefoil.

2.5.4 Extraction of the PSF from the lensing terms

If one can solve equations (2.28) for the pre-convolved lensing values, $\vec{\tilde{g}}$, $\vec{\tilde{F}}$, and $\vec{\tilde{G}}$, one can create a completely analytic method for deconvolving the effects of an asymmetric PSF from a measured galaxy image. We use the simplifying assumption that telescope coma, trefoil, and astigmatism are small enough that cross terms between them and flexion might be ignored. We do *not* make the same assumption for shear.

Using the variable μ for $\frac{\sigma}{\xi}$, and removing all references to η which is only measurable indirectly, we find the deconvolution of shear and flexion in terms of the properties of the PSF and the directly measurable properties of the galaxy,

$$\vec{\tilde{g}} = \left(\frac{1}{1-\mu^2}\right)\left(\vec{\tilde{g}}' - \vec{\tilde{a}}\mu^2\right) \tag{2.30a}$$

$$\vec{\tilde{F}} + 2\mu^2\left(3\vec{\tilde{g}}\vec{F}^* + \vec{\tilde{g}}^*\vec{G}\right) = \tag{2.30b}$$
$$\left(\frac{1}{1-\mu^2}\right)^{3/2}\left(\vec{F}' - \vec{\tilde{c}}\mu^3\right) - \mu\left(1-\mu^2\right)^{1/2}\left(\vec{\tilde{g}}\vec{\tilde{c}}^*\right) + \frac{1}{2}\mu^3\left(\frac{1}{1-\mu^2}\right)^{1/2}\left(\vec{\tilde{g}}\vec{\tilde{c}}^* + \vec{\tilde{g}}^*\vec{\tilde{t}}\right)$$

$$\vec{\tilde{G}} + 4\mu^2\left(3\vec{\tilde{g}}\vec{F}\right) = \tag{2.30c}$$
$$\left(\frac{1}{1-\mu^2}\right)^{3/2}\left(\vec{G}' - \vec{\tilde{t}}\mu^3\right) - \mu\left(1-\mu^2\right)^{1/2}\left(6\vec{\tilde{g}}\vec{\tilde{c}}\right).$$

This solution is, of course, recursive, but can be approximated to second order in aberrations, in uniformity with the rest of this work.

We hesitate in the case of either type of flexion to assign or plot a correction 'factor' as a function of PSF size. Ideally, such a correction factor could be used as a short-cut to convert from the apparent to the pre-convolved flexion values, or from the apparent to the 'true' flexion values specified by the derivatives of the lensing potential. Even for a completely symmetric PSF, such a factor must either ignore the mixing between shear and the two types of flexions that occurs both prior to convolution and during convolution, or assume some relation between the two types of flexion based on a particular lens model. Only the shear signal, when lensed by an atmospherically aberrated PSF in absence of asymmetric telescope aberrations can be corrected by a simple factor. Correction of either flexion signal requires knowledge of the shear and the other flexion.

2.6 Conclusion

Multiple influences bear upon the final measured values of the terms we think of as shear and F- and G-flexions in galaxy images. We summarize our findings here.

1. Mixing between shear and flexion alters the magnitude and origin of the F--flexion-like spin one signal and G-flexion-like spin three signal on the galaxy

even prior to convolution with a PSF. Intrinsic galaxy ellipticity also changes the magnitude of the pre-convolved flexion signals.

2. Under convolution with a symmetric PSF, the shear signal will drop off as the ratio of the unlensed to the lensed galaxy size, squared.

3. A symmetric PSF will have two effects on the measured flexion signals. (a) It will cause those spin one and three variations on the galaxy with cubed radial dependence to drop off as the ratio of the unlensed to the lensed galaxy size, cubed. This effect is analogous to the dilution in shear, but higher order. (b) It will cause those spin one and three variations on the galaxy with quartic radial dependence to mix down into the corresponding spin one and three flexion-like signals, possibly enhancing the flexion-like signal on the galaxy.

4. Shear and F- and G-flexion have telescope aberration counterparts, astigmatism, coma, and trefoil, with matching deflection properties. For asymmetric PSFs, each apparent lensing aberration will approach the value of its corresponding telescope aberration in the limit that the unconvolved galaxy size is small compared to the PSF size. When the seeing is equal to the width of the unsmeared galaxy, the contributions of the telescope aberrations and the contributions of the gravitational distortions to the final measured image are equally weighted.

5. Under convolution with an asymmetric PSF, the pre-convolved shear and flexions can mix with the PSF asymmetries to corrupt to final convolved signals of the other lensing terms. For example, the apparent spin three signal in a convolved galaxy image might have contributions from spin two shear mixed with spin one coma. This effect may be relatively large in certain PSF regimes.

One must account for all of the above when using measurements of 'shear' and 'flexion' to reconstruct the true lensing parameters. This work corroborates, and more importantly quantifies, the well-known signal dilution of shear caused by atmospheric

seeing, and bias to the same introduced by spin two fields in the PSF (i.e. astigmatism). Moreover, we have analyzed the effect of the PSF on F- and G-flexion, and have found that the atmospheric dilution is not the same for these lensing terms as it is for shear. Importantly, one must carefully account for cross terms between shear and flexions when reconstructing the flexion signals, a detail not required for accurately reconstructing the shear signal.

As always, a small PSF, either due to a steady, absent, or controlled atmosphere (e.g. with wide-field adaptive optics) is of primary importance to retaining the gravitational lensing signal. However, a well-maintained telescope focus will be especially critical to obtaining unbiased flexion measurements, as focus will dictate the severity of the effective astigmatic, comatic, and trefoil aberrations. These aberrations, which can create corruptive signals on their own or interplay with shear and flexion to create non-linear distortions, will be much harder to measure with certainty and recover from in post processing than simple signal dilution from the PSF or shear-flexion mixing. The telescope that can best control its aberrations will surely be most suited to measure flexion. For the rest, we must do the best we can to measure aberrations and account for them.

Acknowledgements: I would like to thank Paul L. Schechter for his guidance and many reviews of this paper. This work was supported by the National Science Foundation through a Graduate Research Fellowship to Rebecca Sobel Levinson and through AST-0607601.

Bibliography

[1] Bacon, D. J., Goldberg, D. M., Rowe, B. T. P., & Taylor, A. N. 2006, MNRAS, 365, 414

[2] Bartelmann, M., & Schneider, P. 2001, Phys. Rep., 340, 291

[3] Bridle, S., Balan, S. T., Bethge, M., et al. 2010, MNRAS, 405, 2044

[4] Cain, B., Schechter, P. L., & Bautz, M. W. 2011, ApJ, 736, 43

[5] Cropper, M., Hoekstra, H., Kitching, T., et al. 2012, arXiv:1210.7691

[6] Goldberg, D. M., & Bacon, D. J. 2005, ApJ, 619, 741

[7] Goldberg, D. M., & Natarajan, P. 2002, ApJ, 564, 65

[8] Heymans, C., Van Waerbeke, L., Bacon, D., et al. 2006, MNRAS, 368, 1323

[9] Jarvis, M., Schechter, P., & Jain, B. 2008, arXiv:0810.0027

[10] Kaiser, N. 1992, ApJ, 388, 272

[11] Kaiser, N., Squires, G., & Broadhurst, T. 1995, ApJ, 449, 460

[12] Kitching, T. D., Balan, S. T., Bridle, S., et al. 2012, MNRAS, 423, 3163

[13] Kuijken, K. 2006, A&A, 456, 827

[14] Laureijs, R., Amiaux, J., Arduini, S., et al. 2011, arXiv:1110.3193

[15] Massey, R., & Refregier, A. 2005, MNRAS, 363, 197

[16] Massey, R., Rowe, B., Refregier, A., Bacon, D. J., & Bergé, J. 2007, MNRAS, 380, 229

[17] Massey, R., Hoekstra, H., Kitching, T., et al. 2013, MNRAS, 429, 661

[18] Melchior, P., Viola, M., Schäfer, B. M., & Bartelmann, M. 2011, MNRAS, 412, 1552

[19] Committee for a Decadal Survey of Astronomy and Astrophysics; National Research Council. 2010, New Worlds, New Horizons in Astronomy and Astrophysics, (Washington, DC: The National Academies Press)

[20] Okura, Y., & Futamase, T. 2012, ApJ, 748, 112

[21] Okura, Y., Umetsu, K., & Futamase, T. 2007, ApJ, 660, 995

[22] Okura, Y., Umetsu, K., & Futamase, T. 2008, ApJ, 680, 1

[23] Rowe, B., Bacon, D., Massey, R., et al. 2012, arXiv:1211.0966

[24] Refregier, A. 2003, MNRAS, 338, 35

[25] Refregier, A., & Bacon, D. 2003, MNRAS, 338, 48

[26] Schechter, P. L., et al. 2003, Proc. SPIE, 4837, 619

[27] Schechter, P. L., & Levinson, R. S. 2011, PASP, 123, 812

[28] Schneider, P., & Er, X. 2008, A&A, 485, 363

[29] Schroeder, D. J. 1987, San Diego, CA, Academic Press, Inc, 363 p.

[30] Tyson, J. A., Wenk, R. A., & Valdes, F. 1990, ApJL, 349, L1

[31] Velander, M., Kuijken, K., & Schrabback, T. 2011, MNRAS, 412, 2665

[32] Viola, M., Melchior, P., & Bartelmann, M. 2012, MNRAS, 419, 2215

[33] Zernike, F. 1934, MNRAS, 94, 377

2.7 Appendix: Using vectors and complex numbers to represent lensing

In weak lensing, convergence, shear, and flexion are often expressed as components of matrices and tensors acting upon vector coordinates in the lens plane. A complex number formalism for flexions as vectors and 'pseudovectors' with various spin symmetries was introduced to weak lensing by Bacon et al. [1] in order to simplify the discussion of flexion.[12] However, this complex formalism for vectors is typically only used to describe the lensing terms themselves; matrices and tensors are still relied upon to describe the distortions to images imparted by shears and flexions. Cain et al. [4] is a notable exception.

Here we shall avoid matrices and tensors, as the physical origins and spin symmetries of the lensing terms can easily be obscured within them. We shall instead rely solely on vectors to capture the effects of the lensing terms on images. For ease of notation, we will use the complex number formalism to express these vectors and pseudovectors. For those unfamiliar with imaginary number notation as a tool to manipulate vectors, we review it here.

2.7.1 Spin n vectors

Lensing distortions have magnitude, direction, and spin symmetry. They are pseudovectors that may be expressed as

[12] As tensors, ellipticities have been treated near identically to pseudovectors since at least Kaiser [10], however the complex number formalism wasn't explicitly used there.

$$\vec{v} = v_1 + iv_2 = ve^{in\phi} \tag{2.31}$$
$$\text{where } v_1 = v\cos(n\phi)$$
$$\text{and } v_2 = v\sin(n\phi)$$

where v, ϕ, and n are the vector magnitude, direction, and spin. A pseudovector's spin reflects its rotational symmetry; a pseudovector with spin n requires a rotation of $\frac{2\pi}{n}$ to be mapped back onto itself. Therefore an ordinary vector is spin one, requiring a full circle rotation before pointing back onto it's initial direction. However the vector describing the magnitude and orientation of an equilateral triangle is spin three, as any rotation of $\frac{2\pi}{3}$ will map the object back onto itself. A spin zero object is a scalar.

The complex conjugate of a vector is simply another vector given by

$$\vec{v}^* = v_1 - iv_2 = ve^{-in\phi} \tag{2.32}$$

The vector multiplication of two vectors $\vec{u}$ and $\vec{v}$ is the multiplication of the complex numbers used to express them,

$$\vec{v}\vec{u} = (v_1u_1 - v_2u_2) + i(v_2u_1 + v_1u_2) = uve^{i(n_v\phi_v + n_u\phi_u)}. \tag{2.33}$$

The dot product of two vectors in this notation works exactly like the dot product of two ordinary vectors in any other notation. Namely

$$\vec{v} \cdot \vec{u} = (v_1u_1 + v_2u_2), \tag{2.34}$$

the result being a real number. Equivalently, a dot product can be expressed as

$$\vec{v} \cdot \vec{u} = \frac{1}{2}\left(\vec{v}\vec{u}^* + \vec{v}^*\vec{u}\right), \tag{2.35}$$

an expansion that will be used often in this paper to simplify expressions. Thus, any

vector taken in dot product with itself, or in multiple with its complex conjugate, will be expressed as its magnitude squared, in agreement with equations (2.34) and (2.35): $\vec{v} \cdot \vec{v} = \vec{v}\vec{v}^* = v^2$. However, a vector squared and its magnitude squared are very different, see equation (2.33), and so vector quantities in this paper will *always* be denoted as such, and all quantities not denoted as vectors may be assumed to be scalars.

2.7.2 Partial derivatives

Partial derivatives with respect to a vector are also vectors and will be denoted by a vector sign.

A vector first derivative is given by

$$\frac{\vec{\partial}}{\partial\theta} = \frac{\partial}{\partial\theta_x} + i\frac{\partial}{\partial\theta_y} \tag{2.36}$$

and operates on a scalar, converting it into a spin one vector. The vector first derivative is the gradient operator $\vec{\nabla}$ and may be written and referred to as such.

There are two second derivatives, one which is spin zero and will map a scalar onto another scalar, and one which is spin two and will map a scalar onto a vector. The spin zero second derivative is the product of the first derivative (spin one) and its complex conjugate (spin negative one). The spin two second derivative is the vector product of the first derivative and itself. They are respectively expressed as

$$\frac{\partial^2}{\partial\theta^2} = \left(\frac{\vec{\partial}}{\partial\theta}\right)^* \frac{\vec{\partial}}{\partial\theta} = \frac{\partial^2}{\partial\theta_x^2} + \frac{\partial^2}{\partial\theta_y^2} \tag{2.37}$$

$$\frac{\vec{\partial}^2}{\partial\theta^2} = \frac{\vec{\partial}}{\partial\theta}\frac{\vec{\partial}}{\partial\theta} = \left(\frac{\partial^2}{\partial\theta_x^2} - \frac{\partial^2}{\partial\theta_y^2}\right) + i\left(2\frac{\partial}{\partial\theta_x}\frac{\partial}{\partial\theta_y}\right). \tag{2.38}$$

Extensions of the same principles can be made for third, fourth, and higher order derivatives. The spin one and spin three vector third derivatives which are needed to derive the F- and G-flexions from the lensing potential are

$$\frac{\partial^2}{\partial\theta^2}\frac{\vec{\partial}}{\partial\theta} = \frac{\vec{\partial}}{\partial\theta}\left(\frac{\vec{\partial}}{\partial\theta}\right)^* \frac{\vec{\partial}}{\partial\theta} = \left(\frac{\partial^3}{\partial\theta_x^3} + \frac{\partial^3}{\partial\theta_x\partial\theta_y^2}\right) + i\left(\frac{\partial^3}{\partial\theta_x^2\partial\theta_y} + \frac{\partial^3}{\partial\theta_y^3}\right) \tag{2.39}$$

$$\frac{\vec{\partial}^3}{\partial\theta^3} = \frac{\vec{\partial}}{\partial\theta}\frac{\vec{\partial}}{\partial\theta}\frac{\vec{\partial}}{\partial\theta} = \left(\frac{\partial^3}{\partial\theta_x^3} - 3\frac{\partial^3}{\partial\theta_x\partial\theta_y^2}\right) + i\left(3\frac{\partial^3}{\partial\theta_x^2\partial\theta_y} - \frac{\partial^3}{\partial\theta_y^3}\right). \tag{2.40}$$

Chapter 3

A failure to measure galaxy-galaxy flexion in Abell 1689, and the role of shape noise at $z \sim 1$

3.1 Abstract

We set out to measure halo truncation in the cluster galaxies of Abell 1689 using galaxy-galaxy lensing flexion. While we were able to reproducibly measure spin-1 and 3 galaxy perturbations for objects down to 26th magnitude in our wide field images taken with Megacam on the Magellan Clay telescope, our measurement of a galaxy-galaxy lensing signal was thwarted by the intrinsic shape noise in our source galaxy population. We detail in this work how we detect and measure flexion for the galaxies in our images using DoPHOT, compensate for telescope aberrations which mimic gravitational flexion in our data, and ultimately find a null result for galaxy--galaxy flexion. We then analyze the inherent flexion-like shapes of galaxies in the local universe and in the population of source galaxies at $z \sim 1$. We find that the standard deviations in the intrinsic dimensionless flexion vector components of Abell 1689's source galaxy population are approximately 0.101 for F-flexion and 0.126 for G-flexion when measured in the r' filter. These deviations are much larger than those

found for the local population, 0.028 and 0.031 for F- and G-flexions respectively. Based on the lessons learned from the observational shortcomings which led to the null measurement, we recommend that future attempts to measure galaxy-galaxy flexion in clusters use yet deeper, redder, and possibly space based, imaging, and a wider variety of filters than we employ here.

3.2 Introduction

Measuring flexion is a tricky business. Flexion was first introduced to the lensing community as the lensing octupole moment by Goldberg & Natarajan [26]. Goldberg & Bacon [24] and Bacon et al. [2] gave flexion its current name, and expanded upon it as a complement to shear for cluster lensing, galaxy-galaxy lensing, and cosmological lensing measurements. Since these initial works, many authors have suggested how we might best measure lensing flexion, by using shapelets [45, 25], Higher Order Lensing Image Characterizations (henceforth HOLICs; Irwin & Shmakova 32, Okura et al. 52), or the Analytic Image Method (henceforth AIM; Cain et al. 15). Others have expanded on how we might best use flexion, either in tandem with shear to constrain mass profiles and substructure in clusters [53, 1], or for galaxy-galaxy lensing studies, especially to measure eccentricities in galaxy halo profiles [28, 20, 19, 21]. However, observations of flexion have not kept up with this plethora of theory. Goldberg & Bacon [24] measure flexion in the Deep Lens Survey and two HST clusters. Velander et al. [65] analyze flexion in the HST Cosmic Evolution Survey (COSMOS) fields. All other measurements of flexion in unsimulated data have been on the cluster Abell 1689 [25, 37, 52, 38, 15].

For a summary of the flexion formalism, we refer the reader to Goldberg & Bacon [24] or any of the authors cited in the previous paragraph. Qualitatively, weak lensing flexion results in the apparent spin-1 and spin-3 distortions (lopsidedness and triangularity) of galaxy images, just as shear manifests as the elongation (spin-2 distortion) of galaxy images. The final image shape of a lensed galaxy will therefore be at least as complex as the unlensed galaxy shape, and any perfect representation

of the imaged galaxy requires either: (a) perfect knowledge of the unlensed galaxy shape and the lensing potential, or (b) the ability to completely model any random galaxy shape. Fortunately, perfect representations of galaxies are not needed in order to capture the effects of weak lensing flexion, and learn from it.

Even though galaxy shapes are complex, flexion in galaxies can be well-captured by simple measurements or simple models. As demonstrated by Goldberg & Leonard [25], Okura et al. [51, 52], one can characterize flexion in galaxy images by measuring a handful of low order image moments. Alternately, one can capture the essence of galaxy shapes and their flexions by fitting models of relatively few, low-order shapelets [7, 54, 55]. Goldberg and & Bacon's initial flexion measurements were made using shapelets. Massey et al. [45] refined the method, and Leonard et al. [37] and Velander et al. [65] successfully used shapelets to measure cluster flexion in Abell 1689 and galaxy-galaxy lensing flexion in the COSMOS fields, respectively.

There is reason to believe that one can model galaxy shapes even more simply and still capture the effects of gravitational lensing. The 2008 and 2010 GRavitational lEnsing Accuracy Testing challenges, GREAT08 and GREAT10, [13, 35] demonstrate that simple model fitting methods can do quite well in capturing the shear lensing signal. Cain et al. [15] successfully measures lensing flexion in Abell 1689, using the AIM method of fitting a simple lensed elliptical Gaussian model directly to the imaged source galaxies.

Notwithstanding these successes, efforts to measure flexion have encountered various hurdles over the last decade. Viola et al. [66] first quantified shear-flexion mixing and the detrimental effect it can have on the HOLICs measurement technique. Levinson [40] independently found and quantified the effect of the shear flexion mixing on the AIM method, and also discovered additional corruptions of the spin-1 and spin-3 flexion measurements that arise in the presence of atmospheric smearing and telescope aberrations. Fortunately, these corruptions of the spin-1 and spin-3 flexion can be accounted for in either method.

On top of shear-flexion mixing, scatter in intrinsic galaxy shapes, measurement (photon) noise, and pixelization all affect flexion measurements. Goldberg & Bacon

[24], Goldberg & Leonard [25] put the scatter in the inherent magnitudes of the unitless flexion-like asymmetries of galaxies at ~ 0.03, where the flexions are rendered dimensionless by the galaxies' semi-major axes. While this flexion scatter is 1/10th of the shear scatter, it is still not insignificant when compared with the weaker gravitational flexion signal. Okura et al. [52] place the dispersion of the unitful F-flexion vector components in the background galaxies of Abell 1689 higher, $0.112/''$, corresponding to a standard deviation in the dimensionless flexion vector components of ~ 0.146. Rowe et al. [56] create a simulation of flexed HST data specifically to address the measurement challenges for flexion. Their results suggest that photon noise will be the limiting factor to flexion measurements, as the flexion signal degrades quickly with decreasing signal-to-noise as compared to shear. They additionally find that the recoverable flexion signal also drops off for objects of smaller angular size, i.e. with size and resolution.

In addition, the Rowe et al. [56] simulations address an often under-appreciated aspect of flexion measurement, crowded fields and overlapping objects. Rowe et al. [56] use SExtractor [8] to extract and deblend their simulated HST images, and note in particular that "significant numbers of objects are being affected by noise in the determination of their properties at the SExtractor detection and deblending stage." Cain et al. [15] note similar difficulties in their analysis of cluster lensing in Abell 1689. They use SExtractor in two passes, one to detect large obejcts and known cluster members, and a second pass, to detect potential background source galaxies, after removing all objects found in the first pass. Even so, they find that corruption of dim objects by nearby neighbors accounts for many of their rejected flexion measurements.

Despite these known obstacles to flexion measurements, we sought to measure galaxy-galaxy flexion for cluster galaxies, using ground-based observations,[1] in order to chart galaxy halo truncation as a function of position in the cluster. During cluster formation, mass is tidally stripped from the outer parts of the non-BCG cluster

[1]Ground based observations are less expensive than space based observations, but extracting the flexion signal from the ground is more difficult. Just how much more difficult is a lesson we learned from our efforts.

members. This tidal stripping results in galaxies whose mass profiles are truncated at small radii. Numerical simulations of cluster formation by Limousin et al. [43] predict that this stripping is most severe for the innermost cluster members and that the half mass radii of galaxies in clusters will trend upwards by roughly a factor of five between 0.3 and 3Mpc from the cluster center. The simulations predict that the dark matter is preferentially stripped before the luminous matter, so galaxies of comparable luminosity in different parts of the cluster can be compared more or less directly to infer halo stripping. As gravitational flexion is more sensitive to substructure and small scale variations in mass than shear, but can be used to probe a wider field than strong lensing, it is an ideal tool for halo truncation measurements in clusters.

Previous successes with strong and weak lensing suggested that we might also be successful. Natarajan et al. [50] combine strong and weak lensing measurements in five clusters to find evidence of truncation in subhalo substructure. Halkola et al. [27] use strong lensing measurements in Abell 1689, a cluster rich with multiply lensed systems [42], to measure the halo truncation of the innermost cluster members in that system. They find that "the cluster galaxy halos in Abell 1689 are strongly truncated" as compared to the halos of field galaxies. Limousin et al. [41] measure halo truncation in galaxies using gravitational shear. Notably, this measurement is made using ground based data. Encouraged by these measurements and by the cluster flexion measured on Abell 1689 by Goldberg & Leonard [25], Leonard et al. [37], Okura et al. [52], Cain et al. [15], Leonard & King [38], we set about measuring galaxy-galaxy flexion in this system.

Ultimately, we failed in our efforts to measure galaxy-galaxy flexion in Abell 1689. This failure was mostly due to our underestimation of shape noise in galaxies at $z \sim 1$. We were also hindered by a lack of understanding of the scale and true nature of the hurdles involved in a galaxy-galaxy flexion measurement. In §3.3 of this paper, we outline our data, methods, and noise laden result. We then analyze why we failed to measure galaxy-galaxy flexion. In §3.4 we first establish those areas in which we did not fail: (a) in robustly measuring image shape distortions and (b) in correctly compensating for image aberrations in our flexion predictions. We then analyze the

areas where we did not fully anticipate the challenges and therefore fell short: (§3.5) intrinsic galaxy shape noise, (§3.6) required signal-to-noise for flexion measurements, and (§3.6) required ranges of filters needed for photometric redshift determination. In the process of understanding these failures, we make measurements of the spread of intrinsic flexion in the source population behind Abell 1689, and map the increase in uncertainty of the flexion measurement with decreased signal-to-noise. In §3.7 we look more closely at the 20 systems for which we would expect to see the most galaxy-galaxy gravitational lensing flexion, and confirm our non-detection. In §3.8, we provide flexion measurements for a number of lensed galaxies in our field so that future works may compare their measurements to our own. We conclude in §3.9, with a breakdown of how one might, with the advantage of hindsight, succeed in measuring galaxy-galaxy lensing flexion in clusters.

3.3 How we set out measuring galaxy-galaxy flexion

3.3.1 Target selection

Abell 1689 is an ideal observational target for measuring halo truncation in galaxies using flexion. In brief, Abell 1689 is among the richest in Abell's catalog, with the largest Einstein ring (in arcseconds), and with many massive galaxies to act as lenses. The cluster is relatively low redshift ($z = 0.18$) and therefore has an abundance of $z \sim 1$, relatively bright background sources. It is relatively relaxed and has been shown to contain inner galaxies with more truncated halos than field galaxies [27]. The inner regions of the cluster have been imaged extensively, allowing for mass models of the cluster from both strong and weak lensing studies (Broadhurst et al. [14], Limousin et al. [42], Halkola et al. [27], and many, many others). SDSS overlap with the field provides easy photometric calibration, and publicly available spectroscopy from Frye et al. [22], Houghton et al. [30] allows for the calibration of a Faber-Jackson relation for the cluster. Last, Abell 1689 is literally the poster child

for flexion studies [25, 37, 52, 38, 15], so any flexion measurements from this study can be weighed against the existing literature.

3.3.2 Observations

Megacam [48] on the Magellan telescope Clay is almost certainly the best instrument on the ground with which to observe the variation of flexion effects across a cluster of galaxies. As noted in Levinson [40] and detailed further below, flexion measurements require small and stable PSFs. Moreover, measurements of the variation in halo truncation across a cluster require a field large enough to capture the entire cluster, so that comparisons can be made between a cluster's center and edge galaxies. Megacam has a $25' \times 25'$ field of view with $0''.08$ pixels, which we binned by 2x for our observations of Abell 1689. During our run in November 2010 with this instrument, we obtained images as good as $0''.38$ (FWHM). These varied by only $\pm 0''.03$ (full range) across its half degree field.[2] High et al. [29] are able to use the small, stable PSF provided by Megacam on Clay to measure weak lensing shear with rms ellipticity residuals of better than 0.005 for five galaxy clusters.

Since a small PSF is critical to the flexion measurement, one might question why we are observing from the ground rather than with HST. While HST does not suffer from atmospheric effects, and thus has a much smaller PSF than ground based imagers, Megacam has a substantially larger field of view.[3] Additionally, observing from the ground allows us to test the feasibility of ground-based flexion measurements in anticipation of the several new ground-based wide-field surveys that propose to make detailed lensing measurements – in particular the recently initiated Dark Energy Survey (DES) on the Blanco Telescope, the Kilo-Degree Survey (KiDS) with the VST, and ultimately the Large Synoptic Survey Telescope (LSST).

We chose to observe in three filters: i' and r' for measuring flexion in the galaxies, and g' for color discrimination of the cluster and source galaxies. We initially chose

[2]Unfortunately Abell 1689 was not observable during this November run. Our best images on Abell 1689 were $0''.48$ (FWHM) in r'.

[3]MIT also has guaranteed 10% time on Magellan, giving us a foot in the door for longer and repeated observations.

observations times to achieve similar depths in each filter (i' has less throughput and a higher expected background than r', but a superior PSF). However, the i' band images suffer from severe fringing. In order to be able to remove this fringing, we were required to dither our exposures, thus relinquishing control of the (field-dependent!) PSF. Additionally, due to the size of the brighter galaxies and saturation on the brighter stars, we were never able to perfectly flatten exposures in the i' band. Therefore, after our first observation run, we switched to observing primarily in r'.

While we sought to obtain as deep data as was possible, the times of year for which Megacam was available on Clay restricted how often and for how long we could observe a given field.[4] We were able to obtain 10.75 total hours on the cluster, (355 mins in r', 210 mins in i', and 80 mins in g'), 9 hours of which was with seeing better than our threshold of 0.″75. Our data are summarized in table 3.1.

Date	# exposures			notes
	g'	i'	r'	
2011 May	3	16	8	
2012 April	8	2	10	Used for g' only. $> 0.''7$ seeing.
2013 June	5	24	53	Best data. 0.″48 FWHM

Table 3.1 Observations of Abell 1689. All science exposures are 300s.

3.3.3 Reduction, data rejection, coaddition, and weighting

Data from 2013 June were reduced at the Harvard Center for Astrophysics (CfA)[48]. The CfA's Megacam reduction pipeline includes overscan correction, bias correction, flat fielding with twilight flat exposures, fringe correction for the i' filter, and an illumination correction when possible. The 2011 May and 2012 April data were reduced with IRAF [63], using the MSCRED [64] and MEGARED [48] packages. These images underwent the same overscan correction, bias correction, flat fielding, and i' filter fringe corrections as the 2013 June data.

[4]Megacam at Magellan requires an f/5 secondary mirror to be mounted on the Clay telescope, blocking the default f/11 secondary mirror. The overhead of installing and then removing such a large instrument and its requisite secondary mirror necessitates the allocation of pre-scheduled f/5 observing blocks agreed upon by and divided between the members of the LCO consortium. All of our observations with Megacam had to fit within the windows that the camera was on the telescope.

After basic reduction, we performed a simple analysis of the positions and zeroth through second moments of bright stars in each chip of each image, in order to determine the approximate transparency, seeing, and linear position offset of each image. We then used these parameters to estimate the quality of each image and fitness for inclusion in the final coadded images. We use the following metric to evaluate image quality:

$$\text{quality} = \left(\frac{0\farcs7}{\text{FWHM}}\right)^2 (\text{transparency loss}) \left(\frac{1}{1 + \text{uncertainty in shift (pixels)}}\right). \tag{3.1}$$

The first term degrades images taken in poor seeing conditions, as measurable shear dilutes as the second power of seeing [40]. The flexion signal will actually dilute as the third power of seeing, but here we are being generous to the lower quality images. We use $0\farcs70$ as a reference point for the PSF quality.

The second term will down-weight images taken in low transparency conditions. The scale factor is an approximation of the signal-to-noise degradation in dim galaxies due to any lack of transparency. Assuming that dim galaxies of interest for flexion studies will have peak central intensities of approximately 1/2 the sky intensity, we can estimate the signal-to-noise loss from transparency from the corrected stellar central intensities in each image, I, and the max stellar central intensity, I_{Max}, following:

$$I = I_{measured} \left(\frac{FWHM_{measured}}{0\farcs7}\right)^2 \tag{3.2}$$

$$\text{signal-to-noise} = \sqrt{gain}\frac{I}{\sqrt{I + \text{sky}}} \tag{3.3}$$

$$\left(\frac{\text{signal-to-noise}}{\text{signal-to-noise}_{Max}}\right)_{\text{fixed seeing}} = \frac{I}{I_{Max}} \frac{\sqrt{1 + \text{sky}/I_{Max}}}{\sqrt{I/I_{Max} + \text{sky}/I_{Max}}}$$

$$\text{transparency loss} = \left(\frac{\text{signal-to-noise}}{\text{signal-to-noise}_{Max}}\right)_{\text{dim galaxy, fixed seeing}} = \frac{I}{I_{Max}} \frac{\sqrt{3}}{\sqrt{I/I_{Max} + 2}} \tag{3.4}$$

Here, the subscript Max denotes the observation with the brightest scaled stellar

intensity. As the intensity of the stars will drop by the same ratio as the intensity of the galaxies, the ratio of the intensity of stars of the brightest exposure to the given exposure can be used with equation 3.4 to compute the signal-to-noise loss due to decreased transparency of the galaxies in the given exposure.

All of the images of Abell 1689 were taken under nearly photometric conditions,[5] so the transparency loss term varies very little from image to image.

The third component of the quality metric gauges how well the stars align between a given image and the reference image on which the stellar positions were initially measured. Images whose various stars predict differing linear field offsets from the reference image are more likely to be rotated with respect to the reference or have a significantly different distortion pattern. Coadding these rotated or differently distorted images with the reference frame would significantly degrade the quality of the final output due to the misalignment of edge objects. As any deviation between stars in their proposed linear image offsets will increase the uncertainty in the averaged, optimal image shift, we use the uncertainty in the offset as a metric of the image's fitness for coaddition with the reference.

The best images in each filter are grouped by their quality, and coadded using a weighted average of the data. We chose not to resample the images when coadding them, as resampling will corrupt the PSF and apparent shapes of the galaxies. Instead, images are shifted linearly by integer pixel amounts in order to optimally align stars across the field, and then coadded by pixel. Consequently, we only coadd images with similar field rotations, distortion patterns, and PSF sizes, i.e. those with large quality metric values. Images which are deemed poor by this metric, (< 0.40 for i' and r'), are discarded and not used to create the final coadded images.

Weight images are additionally generated. A friends of friends algorithm modified from 'image-object-extractor' [39] is used to identify all pixels associated with saturated objects and objects larger than the BCG, and these pixels are assigned zero weight in the weight images. By masking saturated and very large objects, we enable

[5]There were some clouds on the nights of the 2011 May observations, but none observable during the observations of Abell 1689. As a caution, we coadd and calibrate the images from this run separately from the images in the other runs.

faster and more robust image analysis using DoPHOT in the following step.

We can cleanly coadd 215 mins of exposures in the r' filter and 80 mins in the i' filter. The other data in i' and r' have more degraded PSFs. We choose to divide the r' and i' data into 105 min and 110 min, and 45 min and 35 min, coadded images in order to further isolate the best data and also to have a second set of images in each filter with which to verify that our measurements are reproducible. The PSFs for the two r' coadded images have radially averaged FWHMs of $0''.50$ and $0''.58$. These values are computed using the second moments of stars on the chip containing the cluster center. The corresponding FWHMs in the two i' filters are $0''.54$ and $0''.56$. In order to obtain photometric data on the brightest objects, we retain some of the lesser quality r' images, in which fewer objects are saturated. We coadd these degraded images separately from the higher quality ones. Table 3.2 contains a list of the final coadded images used for the rest of this analysis.

Image	total depth	FWHM ($''$)	avg. quality
g' 1	35 mins	$0''.86$	0.203
g' 2	30 mins	$1''.06$	0.168
i' 1	45 mins	$0''.54$	0.466
i' 2	35 mins	$0''.56$	0.466
r' 1	105 mins	$0''.50$	1.574
r' 2	110 mins	$0''.58$	1.174
r' 3	25 mins	$0''.68$	0.846
r' 4	30 mins	$0''.84$	0.455

Table 3.2 Coadded images of Abell 1689. While we perform the same analyses on all filters, the first two coadded r' images and the first two coadded i' images have the smallest PSFs and are therefore the best images for measuring flexion. The third and fourth r' images and the g' images are mostly useful for photometry, though they may occasionally yield flexion measurements as well. The PSF FWHMs shown here are computed for the chip containing the cluster center.

3.3.4 DoPHOT object extraction and shape fitting

In anticipation of the effects of object contamination in crowded fields, and embracing the notion that one might do well-with a simple model, we employ DoPHOT [58] to analyze the galaxies in Abell 1689. DoPHOT is a model fitting photometry package

initially designed to measure accurate stellar photometry in crowded star fields. After some modification, we have optimized it for galaxy fields. DoPHOT will detect objects above a specified noise threshold, classify those objects as stars, double stars, galaxies, or artifacts (e.g. cosmic rays), fit a simple model to the objects, and subtract that model from the images so that faint neighbors can be detected in the regions surrounding brighter objects. DoPHOT performs the aforementioned object detection autonomously and iteratively by brightness, refitting each object with every iteration so that object models can be improved as their neighbors are better subtracted from the image. DoPHOT additionally maintains a noise file for the image, keeping track of those objects which it subtracts, so that the noise estimate in model determination is tractable.

Following the work of Levinson [40], the galaxy model used by DoPHOT is that of an elliptical Gaussian galaxy lensed by both shear and gravitational flexion and convolved with an atmospherically smeared, asymmetrically aberrated PSF:

$$I_e(\vec{\theta}) = I_0 \exp\left(-\frac{1}{2\alpha^2}\left((1+g'^2)\theta^2 - 2\left(\vec{g'}\cdot\vec{\theta^2}\right)\right)\right)\times \left[1+\frac{1}{4\sqrt{2\ln(2)}\alpha^3}\left[3\left(\vec{F'}\cdot\vec{\theta}\right)\theta^2+\left(\vec{G'}\cdot\vec{\theta^3}\right)\right]\right]. \tag{3.5}$$

A detailed explanation of the vector notation used here can be found in the appendix of Levinson [40].

In the above 11 parameter model, $\vec{\theta}$ denotes the position of the galaxy, I_0 is the galaxy's central intensity, and α is the observed Gaussian width of the galaxy, including the broadening effects of atmospheric smearing. A constant sky level is also fitted with the galaxy parameters, though it is omitted in the equation above. Dimensionless spin-1, 2, and 3 galaxy asymmetries, denoted by $\vec{F'}$, $\vec{g'}$, and $\vec{G'}$, comprise the last six free parameters in the model. While these terms are traditionally associated with gravitational shear and gravitational F- and G-flexions, apparent galaxy asymmetries are generally caused by telescope aberrations and inherent galaxy shapes in addition

to gravitational lensing. In the special case where first order gravitational shear and flexions are they only origins of asymmetry in the galaxy, and there is no atmospheric smearing, the fitted dimensionless parameter $\vec{g'}$ is equal to the gravitational shear, and the fitted dimensionless parameters $\vec{F'}$ and $\vec{G'}$ can be related to the dimensioned shear derivatives $\vec{\partial}^*\vec{\gamma}$ and $\vec{\partial}\vec{\gamma}$ following

$$\begin{aligned} \vec{F'} &= \frac{\theta_{1/2}}{1-\kappa}\vec{\partial}^*\vec{\gamma} = \frac{\sqrt{2\ln(2)}\alpha}{1-\kappa}\vec{\partial}^*\vec{\gamma} \\ \vec{G'} &= \frac{\theta_{1/2}}{1-\kappa}\vec{\partial}\vec{\gamma} = \frac{\sqrt{2\ln(2)}\alpha}{1-\kappa}\vec{\partial}\vec{\gamma}, \end{aligned} \tag{3.6}$$

where $\theta_{1/2}$ is the observed half light radius of the galaxy, and κ is the gravitational convergence. Here, in absence of atmospheric smearing, the observed galaxy half light radius is the unsmeared, but still gravitationlly magnified half light radius of the galaxy. The factor of $\frac{1}{1-\kappa}$ converts the shear derivatives into reduced flexions [5].

Henceforward, when we refer to gravitational flexion in this work, we will be referring to the dimensionless quantity in equation 3.6, not the dimensioned shear derivative. Moreover, whenever we refer to a 'flexion' caused by any source, i.e. aberrations, mixing, inherent galaxy shape, or gravitational lensing, we will be referencing the dimensionless quantity.

In contrast to the model presented in Levinson [40], the shear and intrinsic ellipticity in the DoPHOT model given in equation 3.5 are retained in the exponential term, rather than expanded out. The retention of the shear term in the exponent yields a model with a truer shape to that of an intrinsically elliptical galaxy or gravitationally sheared object. However, the flexion terms have been Taylor expanded out of the exponential, for both consistency with Levinson [40] and to avoid erroneous peaks in the model that may occur in the limit of large flexion and large spatial separations from the galaxy center.

In order to more facilitate more robust convergence of the model on the data, the exponential in equation (3.5) is implemented as an 11th order pseudo-Gaussian.[6] In

[6]Not to be confused with the 11 parameter model. The expansion of the exponential function

the pseudo-Gaussian approximation, $\exp[-z]$ is expanded as $(1 + z/2! + z^2/3!... + z^{11}/11!)^{-1}$. A second order pseudo-Gaussian approximation is used in the initial versions of DoPHOT [46, 58].[7] Unlike a traditional Taylor expansion of a negative exponential, the pseudo-Gaussian approximation has the advantage of gradually approaching 0 when far from 0, rather than approaching $\pm\infty$. The 11th order approximation used here is very close to the unapproximated exponential.

This 11 parameter model will sometimes fail to converge on very dim objects for which the signal-to-noise is insufficient to support 11 free parameters. It will also sometimes fail on very well-resolved objects, where the object's substructure renders it sufficiently distinct from the model. In these cases, DoPHOT will attempt to fit the object with a less complex, seven parameter elliptical pseudo-Gaussian model. This model is identical to that presented in equation 3.5, however the flexion terms are fixed to zero. For the dimmest objects and objects otherwise unable to converge on the 11 or 7 parameter model, an even simpler, four parameter star model, varying only the position, sky and intensity levels of the elliptical pseudo-Gaussian, is used to fit the object. This failure mode still allows the object to be detected, flagged as unusual, and crudely subtracted from the image so as not to corrupt other image measurements. It also yields usable photometry for those cases where the object is star-like in shape.

For the $160''$x$360''$ chip adjacent the cluster center in the 105 minute coadded r' image of Abell 1689, DoPHOT finds 1205 objects when searching down to $5\sigma_{\rm sky}$ above the sky level. Of these found objects, DoPHOT is able to fit 834 to the full, 11 parameter, flexed galaxy model. Of the remaining objects, 269 are successfully fit to the 7 parameter model.

DoPHOT could detect more objects and produce a cleaner residual image if we

does not add any free parameters to the model.

[7]The second order pseudo-Gaussian approximation converges much more rapidly and robustly on data than an unapproximated Gaussian function. However, the second order expansion is insufficient to faithfully and unbiased-ly reflect the asymmetries imposed upon Gaussian galaxy images by flexion. An 11th order pseudo-Gaussian expansion (or greater) is required. We kept the 11th order pseudo-Gaussian approximation rather than reverting to an unapproximated Gaussian partially out of inertia, and also in recognition that the expanded function will generally fit the data more effectually than the exponential.

set the detection floor closer to the noise limit. However, we chose to set a very conservative detection floor as the conservative floor (1) lowers the number of objects which are found, but are of limited utility for flexion analysis as they are too faint for an 11 parameter model to be fitted to them, (2) lowers the chance of detecting false objects in the residuals of the brightest galaxies, thus corrupting these galaxies' photometry, and (3) allows DoPHOT to conduct a speedy analysis of each image, as it doesn't spend undue time on the aforementioned false or dim objects. In §3.6, we more closely examine the percentage of all objects for which we can retrieve meaningful flexion measurements and find that for the dimmest objects identified above this detection floor, we can only measure the flexion signal at any confidence for $< 15\%$ of the objects. Detecting dimmer objects therefore would not gain us very much.

Fig. 3-1 shows a representative region at the edge of the chip containing the cluster center before and after DoPHOT has subtracted out models for each of the objects. DoPHOT is able to successfully find, fit, and subtract out excellent models for most of the objects brighter than the imposed $5\sigma_{\rm sky}$ detection limit. The saturated stars are masked out before fitting (i.e. assigned zero weight in the noise file) and therefore not identified or modeled by DoPHOT. The brightest, most morphologically resolved galaxies have a characteristic 'bulls-eye' residual, indicating that the cuspiness of the object is not captured by the Gaussian model- a Sérsic would likely do better. However, the overall asymmetry (ellipticity or flexion-like shape) of the objects is still captured in an unbiased way [15] by the elliptical Gaussian plus flexion model.

3.3.5 Matching objects observed in multiple filters

Object detections in different coadded images are matched with the help of *SCAMP* [9] and *wcsutil* [59]. *SCAMP* and *BIG-Macs-calibrate* [34] analyses of the different coadded images provide relative photometric offsets between the coadded frames and absolute photometric zero-points for each filter. Aperture photometry provided by DoPHOT is averaged between redundant measurements within each filter, accounting for the relative photometric offsets. Measurements of galaxy half light radii, shear,

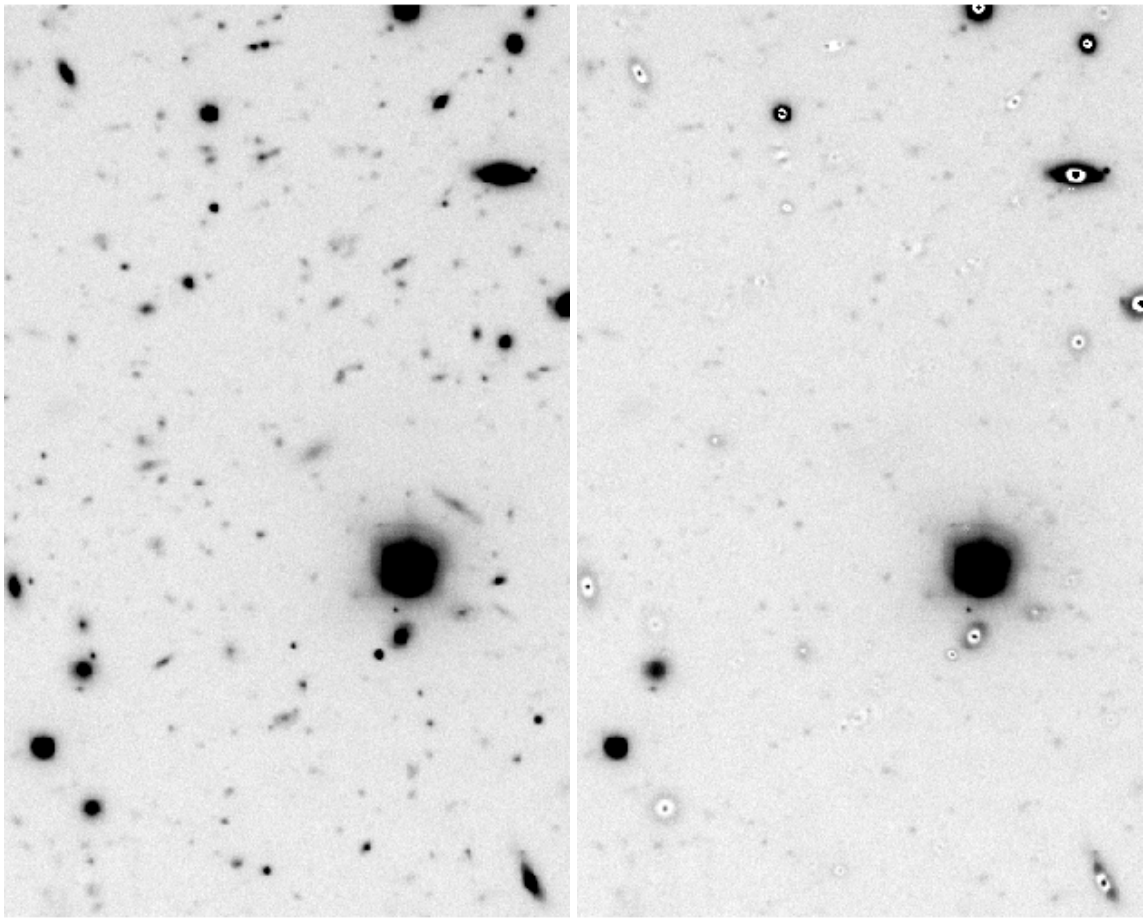

Figure 3-1 Before and after images of DoPHOT's analysis of a 57″x92″ region centered on ($13^h11^m20^s.0$, $-01°20''55\farcs8$), just below the cluster center. The image has a coadded depth of 105 minutes in r'. The right image is a copy of the left, minus DoPHOT's best fitted models for all found objects. The two saturated stars are masked out prior to DoPHOT's analysis and therefore are not modeled or subtracted from the image. The brightest, most morphologically resolved galaxies generally have a characteristic 'bulls-eye' residual, indicating that the cuspiness of the object is not captured by the Gaussian model. One such bright galaxy, to the right and above the lower left saturated star, appears to be un-modeled entirely. However this is a trick of the galaxy's morphology and the scaling used to display the image. The galaxy has a very sharp and bright core which DoPHOT models and subtracts from the image. However, the galaxy's outer parts are not captured by this model, resulting in a bright residual image. Had we set the noise floor for detecting objects lower, DoPHOT would likely have fit this residual image as a separate low surface brightness galaxy. However, this double detection of the galaxy would have negatively impacted our photometry.

and flexion in each image are NOT averaged, as they will in general differ with the image quality and aberrations, see 3.3.8. Instead, all of the shape measurements for each galaxy are retained along with the associated PSF of the image and chip from which the measurements were taken.

3.3.6 Pairing sources and lensing galaxies: color-magnitude selection

We use color-magnitude selection to separate the cluster members and potential background and foreground galaxies in the field. We then implement a magnitude cut on the non-cluster galaxies in order to isolate background galaxies from the foregrounds. Once the populations of cluster members and background source galaxies is determined, we search for background source galaxies in the region around each cluster member. Any background galaxies found within the influence of a lensing cluster member are 'paired' to that lens. Once a galaxy-galaxy lensing pair is established, all subsequent lensing predictions are made assuming that the background source galaxy is lensed by the cluster member galaxy to which it is paired.

For a clean galaxy-galaxy lensing measurement required to measure the radial profile of the lensing galaxy's halo, background source galaxies should ideally be influenced by one lensing galaxy only.[8] We assess the influence of potential lensing galaxies by the strength of their imposed F-flexion signal, which falls off as the square inverse of the radial separation of the lensing foreground galaxy and background source galaxy. If a background galaxy is found to be influenced by three or more possible lensing galaxies, it is discarded from further analysis. If the background galaxy is found to be influenced by two lensing galaxies, we evaluate the gravitational pull of each lensing galaxy at the position of the source. If both lensing galaxies have nearly equal gravitational influence on the background source galaxy, the source is discarded. However, if one lensing galaxy has significantly more influence on the source than the other, (i.e the SIS predicted flexion caused by lens A is at least

[8] A lensing galaxy, of course, may lens many sources

12x greater than the SIS predicted flexion caused by lens B), then the background source galaxy is paired to whichever lensing galaxy has greater gravitational influence. Background galaxies influenced by one lensing galaxy only, are naturally paired to that lensing galaxy.

Because we are interested in galaxy-galaxy lensing flexion, and must pair all identified potential background source galaxies with cluster member lensing galaxies, we walk a fine line when identifying cluster member galaxies and background galaxies. It is imperative to identify the cluster members (potential lensing galaxies) correctly, neither erroneously excluding too many cluster members from the list, nor overpopulating the cluster member list with foreground objects and background galaxies. The first danger of being too stingy in our cluster member selection is straightforward: if we fail to identify potential lensing galaxies, our statistics suffer and we have fewer lensing systems with which to beat down the intrinsic shape noise. More detrimentally, if we fail to identify a lensing cluster member galaxy, but do manage to identify a background galaxy that it lenses, that background source may be erroneously paired to another, weaker lensing galaxy that just happens to be nearby. This mistakenly matched source/lens pair throws an essentially random data point into our galaxy-galaxy flexion analyses.

The danger of being too generous in our selection of cluster members is similar: if there are too many erroneous objects in our list of cluster members, the odds that a background source galaxy will be paired with a random, unassociated foreground or background object jumps.

Being too generous or stingy in the selection of potential background galaxies carries the same detriments: too few galaxies and we will not have enough objects for any statistics, too many false background galaxies and we will have too many blatantly incorrect measurement predictions.

Therefore, when selecting cluster members and background source galaxies in color-magnitude space, we must be cautious. The 'red-and-dead' elliptical galaxies in a cluster will tend to lie along a straight line in color-magnitude space [10, 11]. However, foreground or background galaxies may lie near or on the cluster line, and

less evolved cluster member galaxies may lie slightly off of that cluster line. Gladders et al. [23] use galaxy morphology and restrict their sample to those galaxies with high central concentration in order to emphasize the cluster line in their higher redshift Abell clusters. However, visual assessment of each potential cluster member is not feasible for this work. Instead, in order to minimize the contamination of background and foreground galaxies in the lens population and cluster members in the background source galaxy population, we use a narrow swath around the cluster line to select cluster members, and designate regions close to this line in color magnitude space as ambiguous, i.e. objects which fall into those regions of color-magnitude space are neither selected as cluster members nor as background source galaxies. In order to improve the chances of cluster members to fall within the narrow cluster line, we insist that all objects be detected in all three filters,[9] and use two colors (g'-r') and (g'-i') for object selection. Colors are determined using aperture magnitudes rather than fit magnitudes as the lensing galaxies often have visible substructure that is not entirely captured by the model.[10] If an object falls onto the cluster line in either color-magnitude plot, it is categorized as a cluster member and potential lensing galaxy. If an object falls far enough from the cluster line, in either color-magnitude plot, so as to provide some certainty that it is not a cluster member, it is designated as a possible background source galaxy.[11] Finally, if the object is designated as ambiguous in both colors, it is neither designated as a lensing galaxy nor a potential background source galaxy. This last criterion is wasteful of potential lensing and source galaxies, but necessary to avoid contamination. The color-magnitude plots are shown in figure 3-2.

As a diagnostic for the color-magnitude selection of cluster members and sources, we examine the spatial distributions of the found cluster members and potential background galaxies. We expect that the regions closest to the cluster center will contain a higher density of cluster members than at the field edges. In contrast, the

[9]The object does not need to be detected in all of the coadded images, but it must be detected in at least one of the images in each filter.

[10]Even allowing for galaxy substructure, the fitted magnitudes provide excellent relative photometry within each image. However, variations in the PSF from image to image render the fitted magnitudes variable between images. Therefore we use aperture photometry to compute colors from our g' data taken in poor seeing conditions and our better r' and i' data.

[11]Although it might possibly be a foreground galaxy.

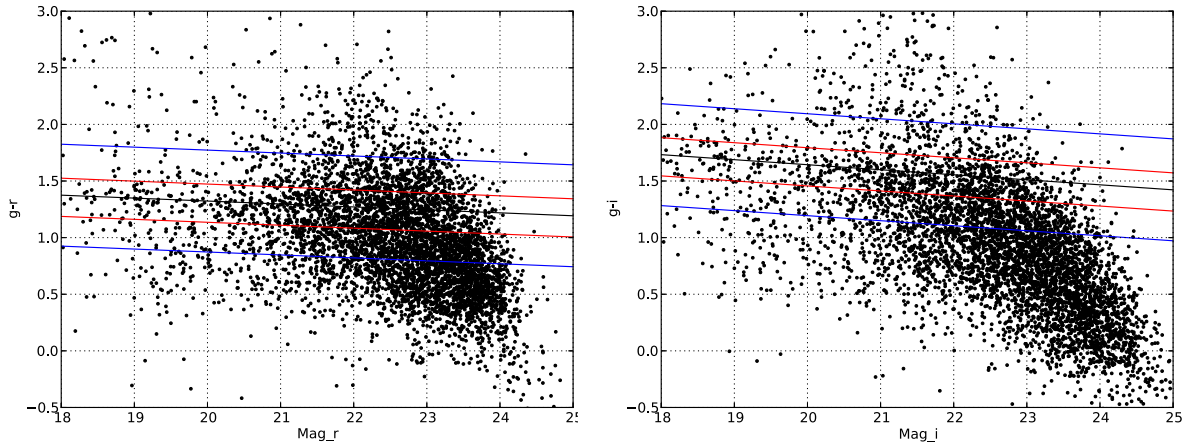

Figure 3-2 Color-magnitude diagrams used for selection of cluster members and background source galaxy candidates. Colors are computed using aperture magnitudes which are computed from the images after models for all neighboring objects have been subtracted off. The plot contains galaxies only; objects small enough to be designated as a star in any filter are discarded prior to plotting. In each image, the black line traces the best found cluster line. Red lines enclose the region containing cluster members. This region is intentionally asymmetric, including more objects bluer than the "red and dead" objects on the cluster line, and fewer redder objects. Objects outside the blue lines are considered as potential background source galaxies. Objects between the red and blue lines are neither cluster members nor potential background sources unless selected in the other color-magnitude space.

sources should be approximately evenly distributed throughout the field. As can be seen in figure 3-3, the density of cluster members is peaked at the cluster center, and the distribution of sources is approximately flat, indicating that our selection criteria for both groups is adequate.

The objects selected in color-magnitude space as cluster members and potential background sources undergo additional filtering before being considered in further analysis.

1. Any object classified by DoPHOT as a star in any filter is discarded from both the cluster member and the background source galaxy lists.

2. We discard dim cluster members, i.e. any with a predicted SIS Einstein ring of less than $0\farcs1$. These objects gravitationally influence too small of a region to be of concern and/or use in our analysis.

3. We remove any background source galaxies for which DoPHOT is not able to fit a full 11 parameter model. These objects are often still found and fit to

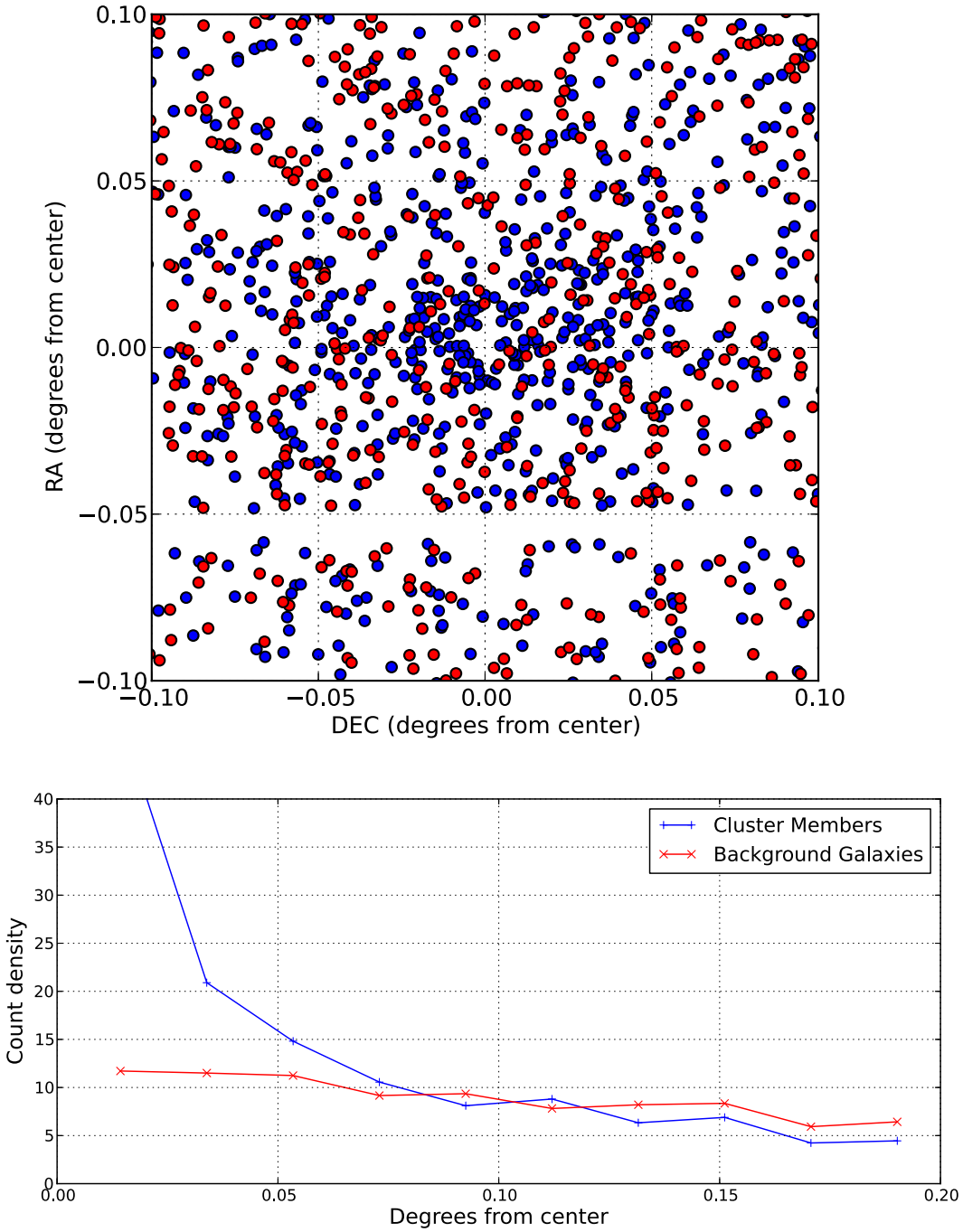

Figure 3-3 Distributions of color-magnitude selected cluster members (blue) and potential background source galaxies (red). The top image shows the spatial distribution of the objects over the interior $10'$ (radius) of the field. The axes show the distance from the approximate cluster center. The absence of sources at RA $\sim 0.06°$ is caused by Megacam's large chip gap. The bottom image shows the density of cluster members and background galaxies out to $20'$. Units for the density are normalized counts per square degree of sky: counts per $0.02°$ bin, normalized over the $20'$ sampling region, and divided by 2π times the radial distance of the bin from the cluster center in degrees. As one would expect, the density of cluster members is peaked at the cluster center and drops off towards the edge of the field. The density of background source galaxies is approximately constant throughout the field, however a small drop-off towards the edge of the field is noticeable. This drop-off can be partially attributed to the degraded PSF at field edge, which makes objects at any redshift harder to detect, though some contamination from cluster members is possible.

simpler, seven parameter flexion-less models, and therefore contribute useful photometric and positional information. However, if an object has no flexion measurement in any filter, it is not of use as a source.[12]

4. We discard any background source galaxies for which the measured half light radius is less than 1.5x the PSF half light radius. Any gravitational flexion signal in these objects will be too degraded by the PSF for analysis to be significant. This selection removes most of the flexion measurements in the g' filter from consideration.

5. We further refine the background source galaxy candidates by an empirically determined magnitude cut of 22.75 in g', and 22.00 in r' and i'. We find that objects brighter than this threshold are more often than not cluster members with visible substructure.

Color-magnitude selection isolates 1600 potential cluster members and 3369 potential non-cluster member galaxies in our field. Of the cluster members, 592 have a sufficiently large Einstein ring to render them efficient lensing galaxies. Of the non--cluster members 1345 are dim, large, and have measured flexions, rendering them useable background galaxies for lensing studies. However, only 92 (7%) of these potential source galaxies are located within 20 Einstein rings of a lens. Of these lensed sources, 42 (46%) are influenced by multiple lensing galaxies, leaving only 50 source galaxies which are galaxy-galaxy lensed by a single galaxy.

3.3.7 Setting velocity dispersion of lenses with a Faber-Jackson relation

In order to identify the sphere of influence of a cluster member galaxy and to estimate its lensing effect on a given background source galaxy, we estimate the cluster member galaxy's velocity dispersion by using the Faber-Jackson relation between galaxy

[12]Such objects are still perfectly fine lensing galaxies, as all useful information for a lens comes from its location and photometry. In fact, many promising lensing galaxies will not converge on the 11 parameter model, as they have too much detectable substructure not captured by the model. Simple 7 parameter elliptical Gaussian models often do converge in these cases.

magnitude and velocity dispersion. Houghton et al. [30] analyze the Faber-Jackson relation in the inner regions of Abell 1689, and make their photometry and spectroscopy publicly available [31]. We use their derived Faber-Jackson relation for Abell 1689, adjust the relation for the relative slope between their modeled object magnitudes and our aperture magnitudes,[13], and calibrate a zeropoint for the relation using our magnitudes and the provided spectroscopy. Figure 3-4 shows the relation between the velocity dispersion and the magnitudes for galaxies in Abell 1689 that fall on the cluster line.

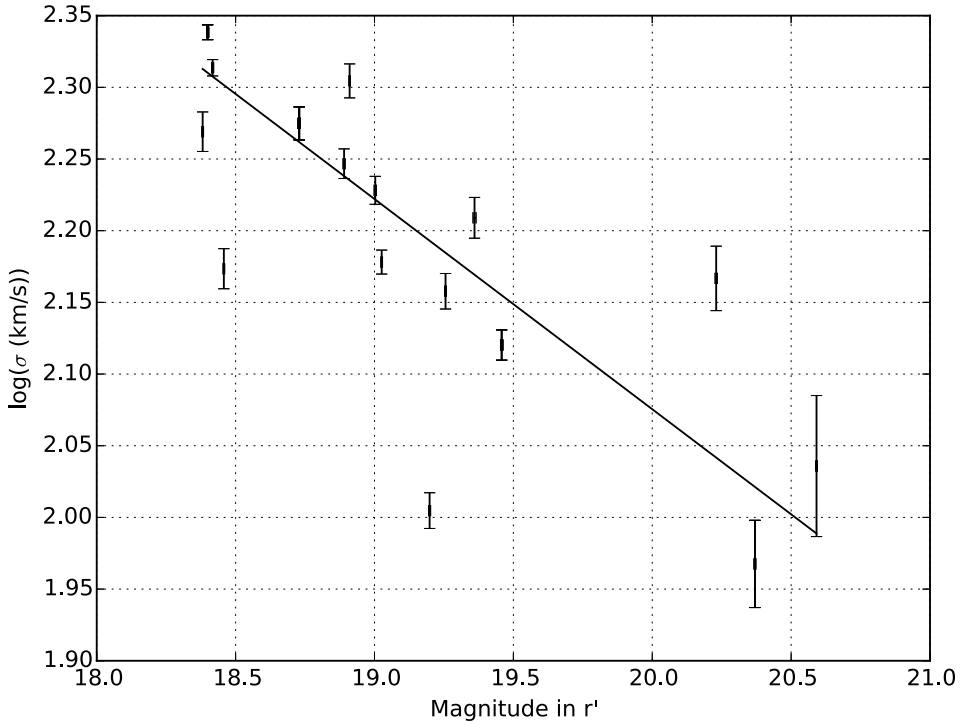

Figure 3-4 Faber-Jackson relation for central chips in Abell 1689. Velocity dispersions provided by Houghton et al. [31]. Magnitudes are computed using DoPHOT's measured aperture fluxes for the galaxies after subtracting out models for neighboring objects. The slope of the magnitude luminosity relationship is derived from Houghton et al. [30] and corresponds to $\sigma \sim L^{0.368}$.

[13]Houghton et al. [30] use De Vaucouleurs and Sérsic profiles to compute their photometry.

3.3.8 Predicting the flexion measurements

We predict the gravitational flexion at the location of each background source galaxy by assuming that the source galaxy is influenced by the cluster potential plus the cluster member galaxy to which it is paired. We assume a singular isothermal sphere (SIS) profile for both the cluster and the cluster member galaxy, as an SIS is a simple and very good approximation to cluster and galaxy mass profiles, even if an NFW profile is technically more accurate. To compute the Einstein ring radius of the lensing galaxy, we use the luminosity of the galaxy to estimate its velocity dispersion, using the Faber-Jackson relation discussed in the previous subsection. We assume that the lensing galaxies lie at $z = 0.18$ and that the background source galaxy population lies at $z \sim 1$ [42]. Assuming that the source galaxies are all located at the average redshift of the source galaxy population is a benign approximation, as the dependence of the Einstein ring radius with the redshift of the source galaxy population is slow around $z = 1$; the Einstein ring radius varies less than 15% from its value at $z = 1$ for galaxies as near as $z = 0.6$ or as far as $z = 3$. We take the Einstein ring radius of the cluster to be 50" [49, 16, 14].

The radial components of the shear and dimensionless flexions, (γ_r, F_r, and G_r), for an SIS lensing potential are given by

$$\begin{aligned} \kappa &= \frac{1}{2}\frac{\theta_E}{\theta} \\ \gamma_r &= \frac{-1}{1-\kappa_{total}}\frac{1}{2}\frac{\theta_E}{\theta} \\ F_r &= \frac{1}{1-\kappa_{total}}\frac{1}{2}\left(\frac{\theta_{1/2}}{\theta_E}\right)\left(\frac{\theta_E}{\theta}\right)^2 \\ G_r &= \frac{-1}{1-\kappa_{total}}\frac{3}{2}\left(\frac{\theta_{1/2}}{\theta_E}\right)\left(\frac{\theta_E}{\theta}\right)^2 \end{aligned} \tag{3.7}$$

where κ is the convergence of the SIS, κ_{total} is the total convergence of all lenses acting on the source galaxy, θ is the radial separation between the source galaxy and the

center of mass of the lens, θ_E is the Einstein ring radius of the lensing galaxy, and $\theta_{1/2}$ is the (unaberrated but still gravitationally magnified) half light radius of the source galaxy. The half light radius of the source galaxy is required in order to render the shear derivative unitless, so that flexion, like shear, is a scale independent property of the gravitationally distorted galaxy. The $\frac{1}{1-\kappa}$ multiplier for the shears and flexions indicates that we are dealing with reduced values [5]. The tangential components of the shears and flexions for an SIS are zero.

As each source galaxy is influenced by the cluster potential as well as the lensing galaxy to which it is paired, the total gravitational shear and dimensionless flexion are given by

$$\begin{aligned}
\kappa_{total} &= \frac{1}{2}\left[\left(\frac{\theta_{E,galaxy}}{\theta_{galaxy}}\right) + \left(\frac{\theta_{E,cluster}}{\theta_{cluster}}\right)\right] \qquad (3.8)\\
\vec{\gamma}_{total} &= \frac{-1}{1-\kappa_{total}}\frac{1}{2}\left[\left(\frac{\theta_{E,galaxy}}{\theta_{galaxy}}\right)\hat{\theta}_{galaxy} + \left(\frac{\theta_{E,cluster}}{\theta_{cluster}}\right)\hat{\theta}_{cluster}\right]\\
\vec{F}_{total} &= \frac{1}{1-\kappa_{total}}\frac{1}{2}\left[\left(\frac{\theta_{1/2}}{\theta_{E,galaxy}}\right)\left(\frac{\theta_{E,galaxy}}{\theta_{galaxy}}\right)^2\hat{\theta}_{galaxy} + \left(\frac{\theta_{1/2}}{\theta_{E,cluster}}\right)\left(\frac{\theta_{E,cluster}}{\theta_{cluster}}\right)^2\hat{\theta}_{cluster}\right]\\
\vec{G}_{total} &= \frac{-1}{1-\kappa_{total}}\frac{3}{2}\left[\left(\frac{\theta_{1/2}}{\theta_{E,galaxy}}\right)\left(\frac{\theta_{E,galaxy}}{\theta_{galaxy}}\right)^2\hat{\theta}_{galaxy} + \left(\frac{\theta_{1/2}}{\theta_{E,cluster}}\right)\left(\frac{\theta_{E,cluster}}{\theta_{cluster}}\right)^2\hat{\theta}_{cluster}\right].
\end{aligned}$$

Gravitational effects are not the only actors on the final spin-1, 2, and 3 signals measurable in a lensed galaxy. In addition to a galaxy's intrinsic ellipticities and flexion-like shapes, mixing between the shear/ellipticity and the flexions causes additional pseudo-flexions which are detectable in the image [40]. Additionally, atmospheric smearing and telescope aberrations will affect flexion measurements in a strongly non-linear fashion [66, 40].

However, the mixing effect can be analytically modeled, and aberrations can be measured, modeled, and subsequently accounted for in order to predict the flexion-like signal in the final image.[14]

[14]We loosely refer to the spin-1 and spin-3 signals in an image as flexions, even though they can

We use the following relations simplified from equations 28a-c of Levinson [40], in order to make predictions of DoPHOT's dimensionless flexion measurements:[15]

$$\vec{\tilde{g}} = \left(\frac{1}{1-\mu^2}\right)\left(\vec{g}' - \vec{\tilde{a}}\mu^2\right) \tag{3.9a}$$

$$\vec{F}' = \left(1-\mu^2\right)^{3/2}\left(\vec{\tilde{F}} + 2\mu^2\left(3\vec{\tilde{g}}\vec{F}^* + \vec{\tilde{g}}^*\vec{G}\right)\right) \tag{3.9b}$$
$$+ \mu\left(1-\mu^2\right)^2\left(\vec{\tilde{g}}\vec{\tilde{c}}^*\right) - \frac{1}{2}\mu^3\left(\frac{1}{1-\mu^2}\right)\left(\vec{\tilde{g}}\vec{\tilde{c}}^* + \vec{\tilde{g}}^*\vec{\tilde{t}}\right) + \mu^3\vec{\tilde{c}}$$

$$\vec{G}' = \left(1-\mu^2\right)^{3/2}\left(\vec{\tilde{G}} + 4\mu^2\left(3\vec{\tilde{g}}\vec{F}\right)\right) \tag{3.9c}$$
$$+ 6\mu\left(1-\mu^2\right)^2\left(\vec{\tilde{g}}\vec{\tilde{c}}\right) + \mu^3\vec{\tilde{t}}$$

$$\text{and} \quad \mu = \frac{\theta_{1/2,PSF}}{\theta_{1/2,galaxy}},$$

where $\vec{F}'$ and $\vec{G}'$ are the measured dimensionless flexions for each source galaxy, and $\vec{g}'$ is the measured total ellipticity in the galaxy image. The ratio of the PSF and measured galaxy sizes is given by μ. The unitless spin-1, 2, and 3 PSF distortions at the location of the galaxy are given by $\vec{\tilde{c}}$, $\vec{\tilde{a}}$, and $\vec{\tilde{t}}$. These asymmetries of the PSF are most often associated with coma, astigmatism, and trefoil wavefront delays, though each spin-n asymmetry is generally comprised of a combination of telescope aberrations [40]. However, just as we refer to the dimensionless spin-1, 2, and 3 galaxy asymmetries in an image as flexions, even though their origin may not be strictly gravitational, we refer to the dimensionless spin-1, 2, and 3 PSF asymmetries as coma, astigmatism, and trefoil. We reproduce the relations between the unitless coma, astigmatism, and trefoil values and their associated wavefront delays in the appendix for completeness.

The gravitational component of the flexion signal and shear signals will degrade as the ratio of the PSF to the observed galaxy size, μ, increases. Astigmatism, coma, and

be caused by mixing, intrinsic galaxy shapes, and aberrations as well as gravitational flexion. When we are referring to the gravitational component specifically, we will be sure to identify it as such.

[15] "Predictions of the measurement" may seem overly verbose, however, it is important to clarify and emphasize that the predictions are for the expected dimensionless flexion-like signal in the aberrated images, not just the gravitation signal that contributes to it. When we "predict the measurement", we are using the model for a smeared, aberrated, and flexed galaxy to predict the flexion-like signal that DoPHOT should measure for a given object in the image.

trefoil aberrations will add offsets to the measured flexions when the source galaxy is of comparable size to the PSF.

The effective shears and dimensionless flexions denoted by a tilde in the above equations, ($\vec{\tilde{g}}$, and $\vec{\tilde{F}}$, $\vec{\tilde{G}}$), can be computed from the reduced gravitational shear, the inherent galaxy ellipticity, and dimensionless reduced flexions, ($\vec{\gamma}$, $\vec{e}$, and $\vec{F}$, $\vec{G}$) following

$$\begin{aligned} \vec{\tilde{g}} &= \vec{\gamma} + \vec{e} \\ \vec{\tilde{F}} &= \vec{F} - \frac{1}{3}(2\vec{\tilde{h}}\vec{F}^{*} + \vec{\tilde{h}}^{*}\vec{G}) \\ \vec{\tilde{G}} &= \vec{G} - \vec{\tilde{h}}\vec{F} \\ \text{where} \quad \vec{\tilde{h}} &= \vec{\gamma} + 2\vec{e}.^{16} \end{aligned} \tag{3.10}$$

In order to resolve the degeneracy between shear and intrinsic galaxy ellipticity, we treat the gravitationally predicted shear as correct, and assume all other ellipticity is inherent to the galaxy. DoPHOT's measurements of F' and G' are therefore fully predictable, assuming that there is no intrinsic flexion-like signal in the unlensed source galaxy, and the measurements of the telescope aberrations at the position of the background source galaxies are accurate.

[16]The factor of 2 in front of the inherent ellipticity in this term is not a typo. The mixing between the shear, $\vec{g}$, and the flexion comes from the transformation from the source plane to the image plane of the symmetric component of the unlensed galaxy, (see equations 10 and 11 of Levinson [40]). In contrast, the mixing between the inherent galaxy ellipticity, $\vec{e}$, and the flexion comes from the transformation of the asymmetric component of the unlensed galaxy from the source plane coordinate to the image plane coordinate. While the first order effects of shear and galaxy ellipticity are the same, this is merely a consequence of the form we chose for inherent galaxy ellipticity. We could just as well have dropped the ellipticity contribution from the symmetric term of the unaberrated galaxy model and dropped the factor of 2 from the asymmetric term. Then $\vec{g}$ and $\vec{e}$ would appear to be very unalike, despite both resulting in an effective elongation of the galaxy. Moreover, even with this specially chosen form for the un-lensed galaxy model, the second order factors of shear and inherent galaxy ellipticity betray that these distortion vectors do not simply behave as one summed vector describing galaxy elongation, even in absence of lensing flexion. So it should not be entirely jarring that the mixing between shear and flexion is NOT the same as the mixing between galaxy ellipticity and flexion.

3.3.9 The null result

Using the models for flexion discussed in the previous subsection, we predict DoPHOT's measured flexions for each of the found galaxy-galaxy lensed sources. We present the result in figure 3-5.

While there is plausible correlation between the flexion measurements and the predictions, especially visible in the binned images, that correlation is primarily caused by the mixing of the galaxy ellipticity (and shear) with the telescope aberrations, and our successful prediction of the effect of that mixing on the measurable flexion. Because the measured spin-1 and 3 image moments are not primarily attributable to gravitational lensing, the magnitudes of the radial and tangential components are, on average, nearly equal in scale.

In order to uncover any underlying trend caused by gravitational lensing, we remove the predicted effects of the asymmetric aberrations from the flexion measurements and compare the result to the flexion prediction in absence of those aberrations. The resulting measurements and predictions of the de-aberrated flexion are shown in figure 3-6. These de-aberrated flexions show what we would have measured if the telescope were aberration-free.[17]

Figure 3-6 shows that we do predict a non-negligible gravitational flexion signal for some of the galaxies especially in the radial components, even considering atmospheric dilution. However the measured signal does not generally match the prediction, especially in the regimes where the predicted magnitudes of the de-aberrated flexions are large. The trend towards overly large, positive F-flexions could possibly be a consequence of imperfect subtraction of the lensing galaxy; a residual brightness at the location of the lensing galaxy after it is removed from the image would create a gradient in the background luminosity that would appear as F-flexion in the direction of the lens. The larger the predicted gravitational flexion, the closer the lens and source galaxies, and thus the more likely the overestimation of the radial F-flexion measure-

[17]The theoretical measurement in absence of asymmetric telescope aberrations is only as accurate as our prediction of the aberration contributions. In 3.4, we discuss in more detail the accuracy of our predictions, finding them to suffice for the large galaxies considered here.

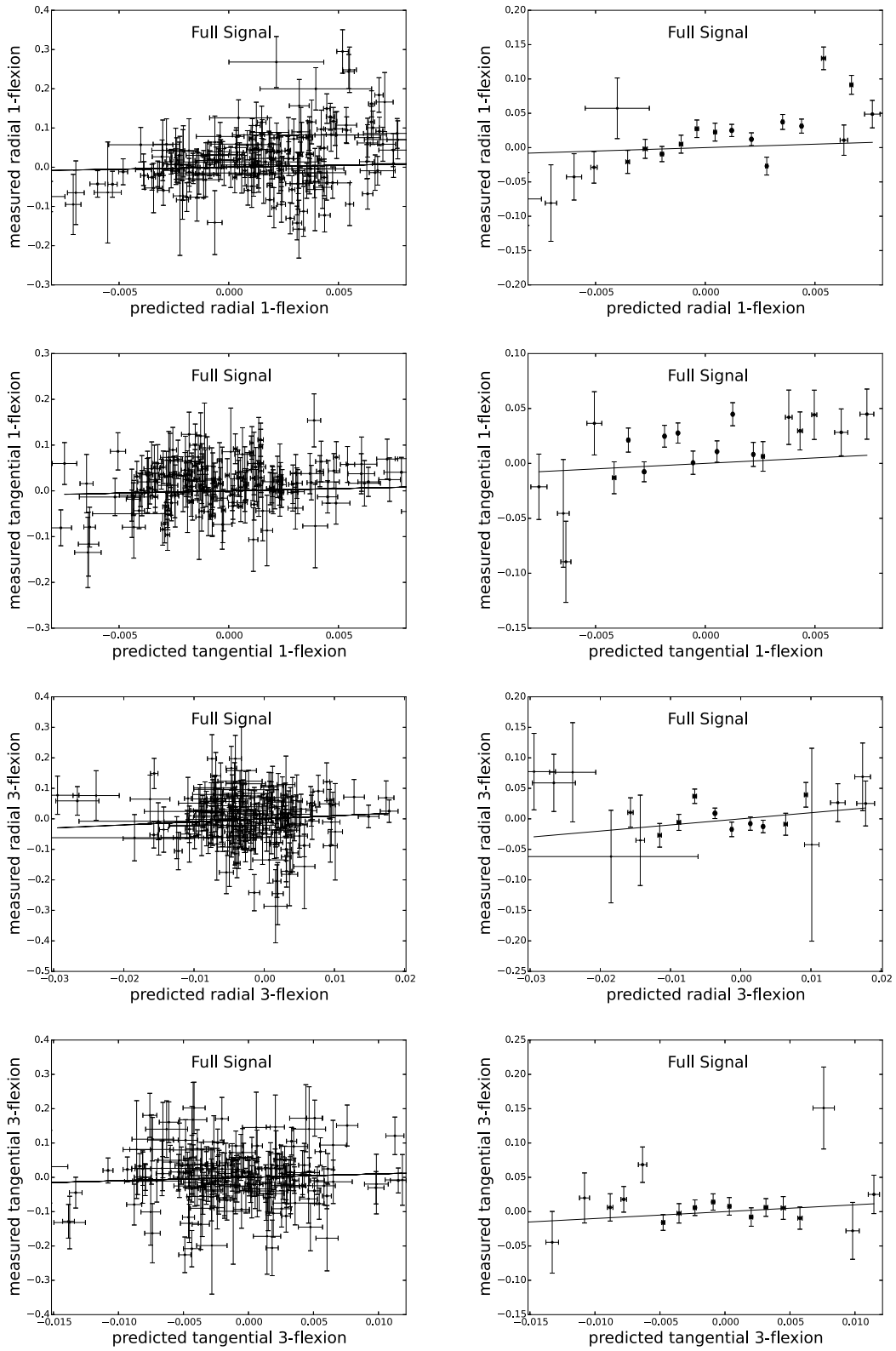

Figure 3-5 Relationship between measured and predicted flexions for the 50 found background source galaxies in the vicinity of a cluster member lensing galaxy. There are 177 total flexion measurements of these objects from data in the multiple i', r', and g' filter images. Left: All measurements plotted with errors. Right: Objects have been binned by their predicted flexions and the measured flexions have been averaged within each bin. The size of each point is proportional the inverse error of the weighted average. For both binned and unbinned plots, the line shows the ideal 1-1 relation, and not a best fit.

ment for the source due to an imperfectly subtracted model for the lens. However, the scatter in the measurements, even when binned, makes these hypotheses difficult to confirm.

Even though there are some possible trends present in the de-aberrated flexions, the measured signals are highly scattered. This scatter is likely caused by a combination of:

1. intrinsic galaxy shape noise,

2. imperfect gravitational lensing predictions due to ambiguous redshifts of the sources and corresponding ambiguity of in the lensing strengths of cluster and individual lensing galaxies at the position of the source,

3. or erroneous flexion predictions caused by improperly identified cluster members or sources.

We further explore these failures in §3.5 and §3.6.

3.4 Where we succeeded

While we failed to measure galaxy-galaxy lensing flexion, we did succeed on two important points– in extracting galaxies and their shape properties when these galaxies are in close vicinity to brighter objects, and in measuring and compensating for atmospheric and telescope aberrations. This section contains a more thorough analysis of our success in these two areas.

3.4.1 Measurement and prediction of spin-1 and spin-3 galaxy shapes

In order to verify the accuracy of the lensed galaxy model from §3.3.8, and DoPHOT's ability to extract spin 1-3 galaxy shapes in fields of potentially overlapping galaxies, test DoPHOT on synthetic data sets.

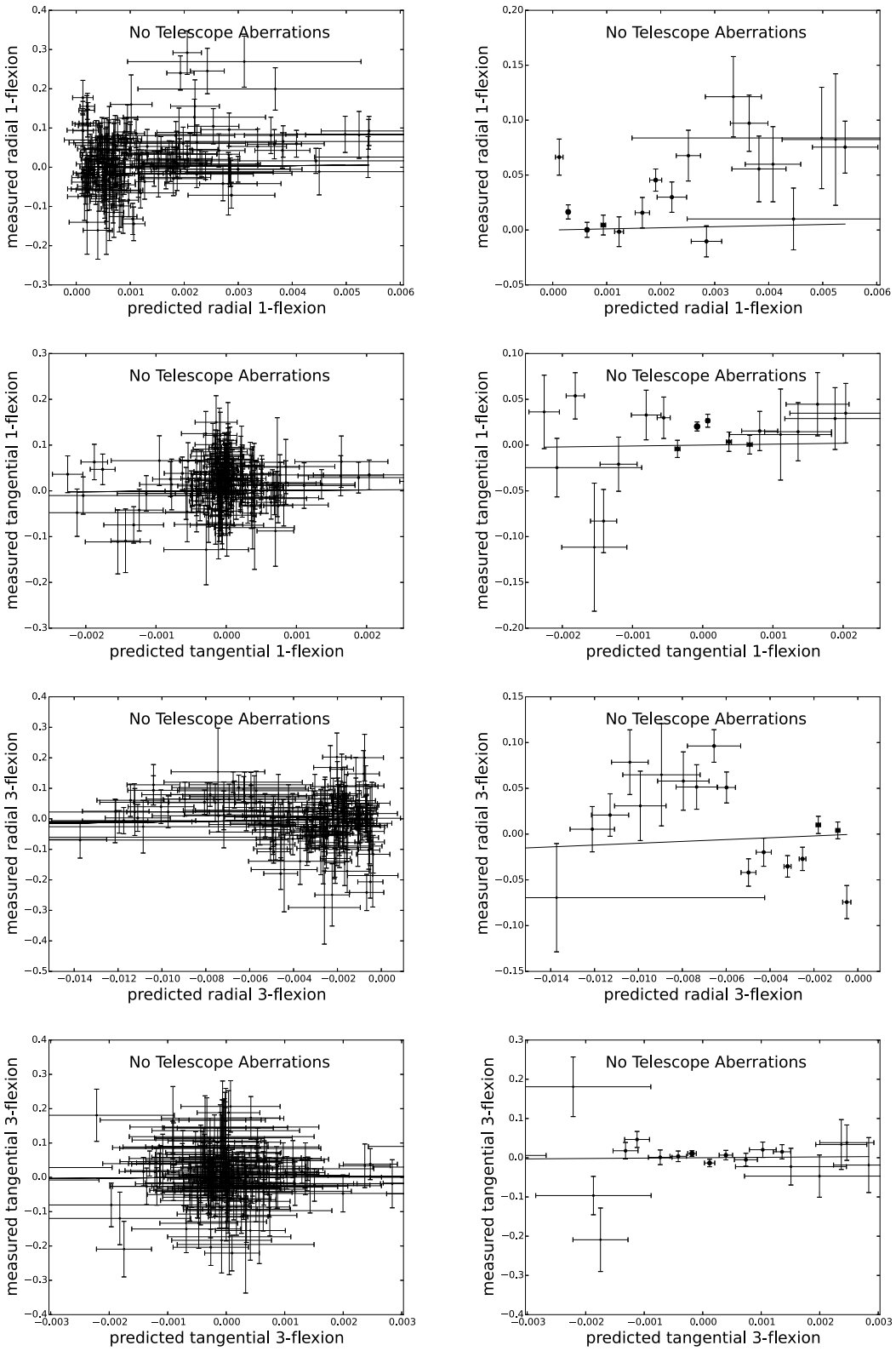

Figure 3-6 Measured v. predicted de-aberrated flexions for the 50 found sources in the vicinity of a lensing galaxy in the cluster. The de-aberrated flexion measurements reported here are the differences between the total measured flexion in the image and the predicted aberrational component, i.e the plots show the measured and predicted flexions in the hypothetical case where the telescope introduces no asymmetric aberrations onto the images. However, atmospheric dilution and shear-flexion mixing still contribute to both the measurements and predictions. Left: All measurements plotted with errors. Right: Objects have been binned by their predicted flexions and the measured flexions have been averaged within each bin. The size of each point is proportional the inverse error of the weighted average. For both binned and unbinned plots, the line shows the ideal 1-1 relation, and not a best fit.

Each data set consists of 60 objects: 20 simulated stars, 20 elliptical Gaussian lensing galaxies, and 20 source galaxies. The stars and lensing galaxies are placed randomly in a 1024x2048 image, and each source galaxy is placed randomly around its lensing galaxy at a separation of 3-6 Einstein rings. We separately test sets of source galaxies whose unlensed shapes are intrinsically elliptical and circular. In both cases the radial profile of the unlensed galaxy is Gaussian. Each circular or elliptical source galaxy is lensed by its associated lensing galaxy, assuming an SIS profile for the galaxy mass. As the form of the lensing potential is completely known for this simulation, the lensing transformation is performed without invoking the weak lensing approximation.

Finally the image is numerically convolved with a symmetric or asymmetric (comatic, astigmatic, and trefoiled) PSF of our construction. Beyond the pixelization, no noise is intentionally added to the synthetic image. This final convolved image is analyzed by DoPHOT for the shape parameters of each object, and these fitted parameters are compared to the predictions of the weak lensing model from §3.3.8. Table 3.3 details the parameter ranges for each object in the simulation.[18]

The results of DoPHOT's analyses of the synthetic data sets are shown in figures 3-7 and 3-8. While large ellipticities in the source galaxies introduce some scatter between the modeled and predicted measurements, DoPHOT's measurements still quite faithfully reflect the predictions.

We do note that decreasing the size of the galaxies with respect to the size of the PSF increases the scatter. This scatter is largely caused by the imperfection of the model in predicting the effect of cross talk between the galaxy ellipticity and the asymmetric aberrations. The range of galaxy sizes tested here produce measured galaxy sizes which are $1.5-2.5\times$ the size of the PSF. Recall from the previous section that we reject all source galaxies whose measured half light radii are smaller than 1.5x the PSF.[19] The largest source galaxies in our data are closer to 2.0x the PSF size than

[18]This analysis is designed to test DoPHOT's ability to extract flexion from inherently noiseless data with potentially overlapping objects, and to demonstrate that the model is effective at predicting DoPHOT's measured flexions. This is NOT a test of DoPHOT's robustness to noise (Poisson or otherwise) in the galaxy or the sky.

[19]This rejection of small galaxies would be prudent even with a completely accurate cross talk

Synthetic Data Sets	
Sky intensity	500 DN
Central intensity of stars	1600 DN
Central intensity of lensing galaxies	800 DN
Central intensity of source galaxies	100 DN
Lensing galaxy unaberrated half light radius	$(1.68 - 3.44)$pixels $= (0\farcs27 - 0\farcs55)$
Source galaxy unlensed, unaberrated half light radius	$(1.68 - 3.44)$pixels $= (0\farcs27 - 0\farcs55)$
Separation of source from lens	$(3.0 - 6.0)$ Einstein rings
Einstein ring radius	8.4pixels $= 1\farcs35$
Intrinsic ellipticity	normal about 0, $\sigma = 0.20$
PSF half light radius	1.5pixels $= 0\farcs24$
Effective astigmatism	0.020
Effective coma	0.020
Effective trefoil	0.020

Table 3.3 Parameters used to generate the stars, galaxies, and PSFs in the synthetic data sets. All central intensities are the pre-convolved intensities; simulated atmospheric smearing will dilute the final measurable intensity. The astigmatism, coma, and trefoil are only non-zero when testing the effects of an asymmetric PSF. Similarly, we perform separate analyses of cases where the unlensed source galaxies are inherently circular and where they are inherently elliptical. For the simulations of inherently elliptical galaxies, both components of the ellipticity are drawn from the above stated normal distribution.

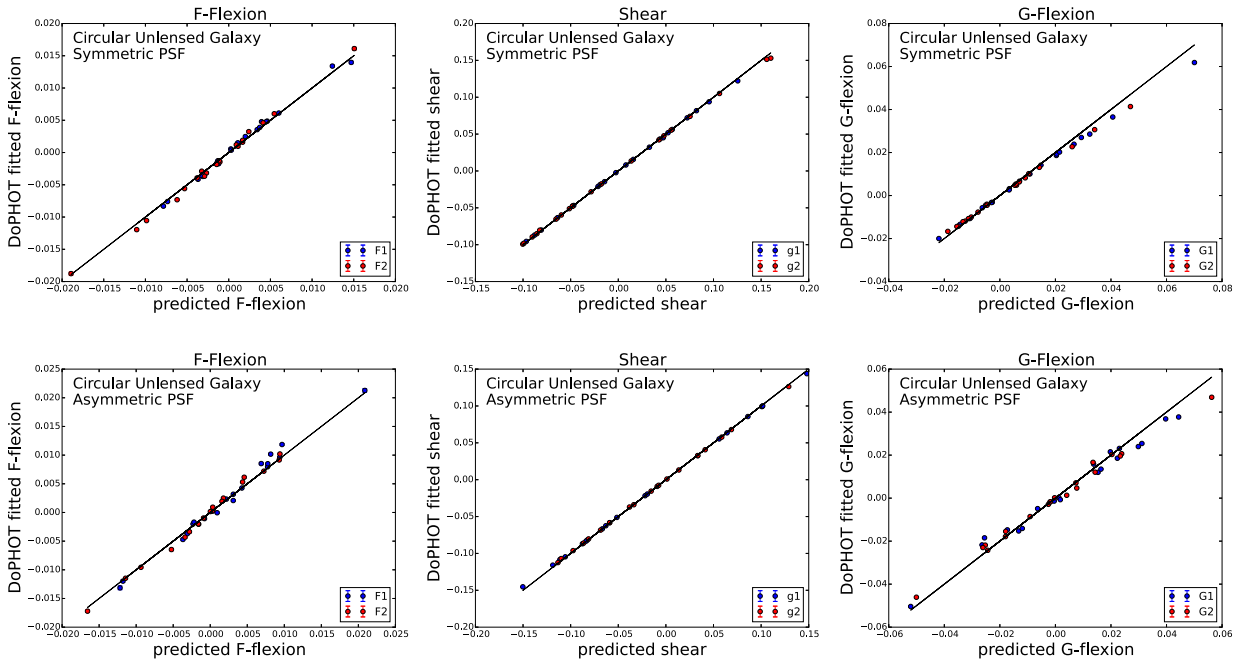

Figure 3-7 Measured v. Predicted F-Flexion (left), Shear (middle), and G-flexion (right), for synthetic data. The unlensed galaxies are circular Gaussians. They are then lensed by randomly oriented SIS potentials, and numerically convolved with a PSF. The top figures compare DoPHOT's measurements of the galaxy parameters and the model's predictions for those same paramters when the convolution PSF is symmetric. The bottom shows the measurements and predictions for an image where the PSF is corrupted by astigmatism, coma, and trefoil aberrations.

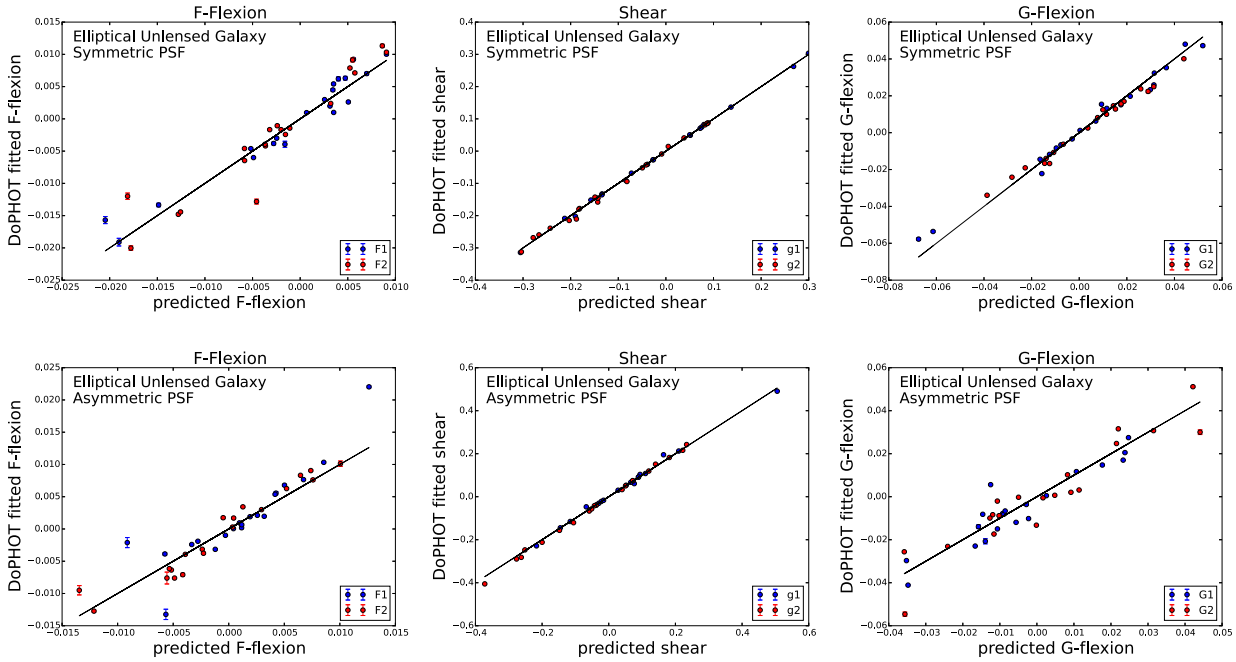

Figure 3-8 Same as figure 3-7, but for intrinsically elliptical source galaxies. Again, the top figures compare measurements and predictions for images convolved with a symmetric PSF. The bottom figures compare measurements and predictions for images convolved with an asymmetric PSF.

2.5.

In §3.5, we perform a full analysis of the reproducibility of measurements. Here it suffices to say that the measurements are indeed reproducible to within reported errors, even in the presence of realistic noise. In §3.6, we provide a detailed analysis of how our ability to measure flexion in galaxies degrades for objects with lower signal to noise.

3.4.2 Measurement and compensation for aberrations

One can see in equations 3.9b and 3.9c that atmospheric smearing and telescope aberrations contribute significantly to all flexion predictions. The amount of the contribution will depend on the ratio of the PSF half light radius and the observed galaxy half light radius, and also on the elongation of the galaxy. Table 3.4 shows the contribution of aberrations to the final G flexion signal for demonstrative PSF to observed galaxy

prediction, as the measured flexion is diluted by $(1-\mu^2)^{3/2}$, where μ is the ratio of the PSF size to the measured galaxy size.

size ratios, $\mu = PSF/\theta_{1/2}$, of 1/2 and 2/3. For $\mu = 1/2$, dimensionless coma = 0.02, and galaxy elongation = 0.3, the contribution of coma to the final G-flexion signal can be greater than the atmospherically diluted gravitational G-flexion signal caused by an SIS lensing galaxy at a separation of 8.6 Einstein rings. Therefore, in order to correctly predict the flexion signal in the images, we must accurately characterize the aberrations in each image.

	Aberration contribution ($\times 10^3$)		Diluted gravitational G-flexion ($\times 10^3$)		
μ	coma	trefoil	$\theta = 5\theta_E$	$\theta = 10\theta_E$	$\theta = 15\theta_E$
1/2	10.1	2.50	21.7	5.12	2.24
2/3	7.41	5.93	13.8	3.27	1.43

Table 3.4 Contributions of coma (magnitude 0.020) and trefoil (magnitude 0.020) to the predicted G-flexion of a galaxy with ellipticity 0.3. Predictions assume that the coma and galaxy elongation are oriented to create a maximal effect on the final G-flexion signal. Contributions of aberrations to the flexion signal will generally depend on the ratio of the PSF to the measured galaxy size, μ. For reference, the atmospherically diluted G-flexion imparted by an SIS lensing galaxy at 5, 10, and 15 Einstein rings of separation from the galaxy are also shown. The ratio of the measured galaxy half light radius to the Einstein ring radius is taken to be 0.5. Effects of mixing between galaxy elongation and gravitational flexion are ignored because this mixing can either dilute or enhance the flexion signal depending on the relative orientations of the elongation and flexions.

While it is possible to model the variation of image aberrations across a field [57], we choose to treat the aberrations across each chip as constant. We use this simplification for the following reasons:

1. The relative heights and tilts of each chip will require each chip to have its own defocus and tilt model [33, 61]. For Megacam, which has 36 chips, this chip variation alone contributes 108 parameters to a model that otherwise has relatively few parameters.

2. The aberrations in Megacam are fairly constant across the field, and even less variable across each chip [48].

In order to determine the effective aberrations in each chip, we average the astigmatism, coma, and trefoil, (i.e the measured shear, F-flexion, G-flexion, see Levinson [40]) measured in each of the stars found in that chip. The found half light radii,

astigmatism, and coma for the brightest stars on each chip in the deepest i' and r' coadded images are depicted in figure 3-9. The average aberrations by chip for the same images are given in table 3.12. In appendix 3.11 we perform the same aberration analysis on the best individual exposures in r' and i', demonstrating that the aberrations present in the coadded image are very similar to the aberrations in the individual images and are thus unlikely to have been introduced by the coaddition.

Following Levinson [40], the aberrations which we here refer to as astigmatism, coma, and trefoil are actually the spin-2, 1, and 3 components of the model used to fit the stars. This is the same model used to fit the galaxies, given in eq. 3.5, but with astigmatism replacing shear/ellipticity, coma replacing F-flexion, and trefoil replacing G-flexion. The wavefront aberrations on the pupil can in principle be derived from these unitless aberrations by following eqs (18) and (19) in Levinson [40]. However, the relation between the measured unitless spin properties of the PSF and the physical aberrations that cause them is decidedly non-linear, and in order to use them, one must additionally know the atmospheric seeing, in absence of telescope aberrations, at the time of the observation.[20] We perform this exercise of converting the PSF spin-1, 2, and 3 moments to wavefront delays in appendix 3.10

As mentioned in the previous subsection, the predicted flexions are in excellent agreement with DoPHOT's measurements, even in the presence of the asymmetric telescope aberrations discussed here. Table 3.3 contains the simulation details, and figures 3-7 and 3-8 show the resulting relations between the predicted flexions and DoPHOT's best fit parameters for images convolved with both symmetric and asymmetric PSFs.

[20]The DIMM seeing can provide a reasonable estimate of atmospheric smearing. For Clay, one can additionally estimate this value by using Baade's reported seeing, as Baade has real-time wavefront correction for the mirror during normal operations. Clay has the same correction capability, but it cannot be used with the f/5 secondary needed for Megacam.

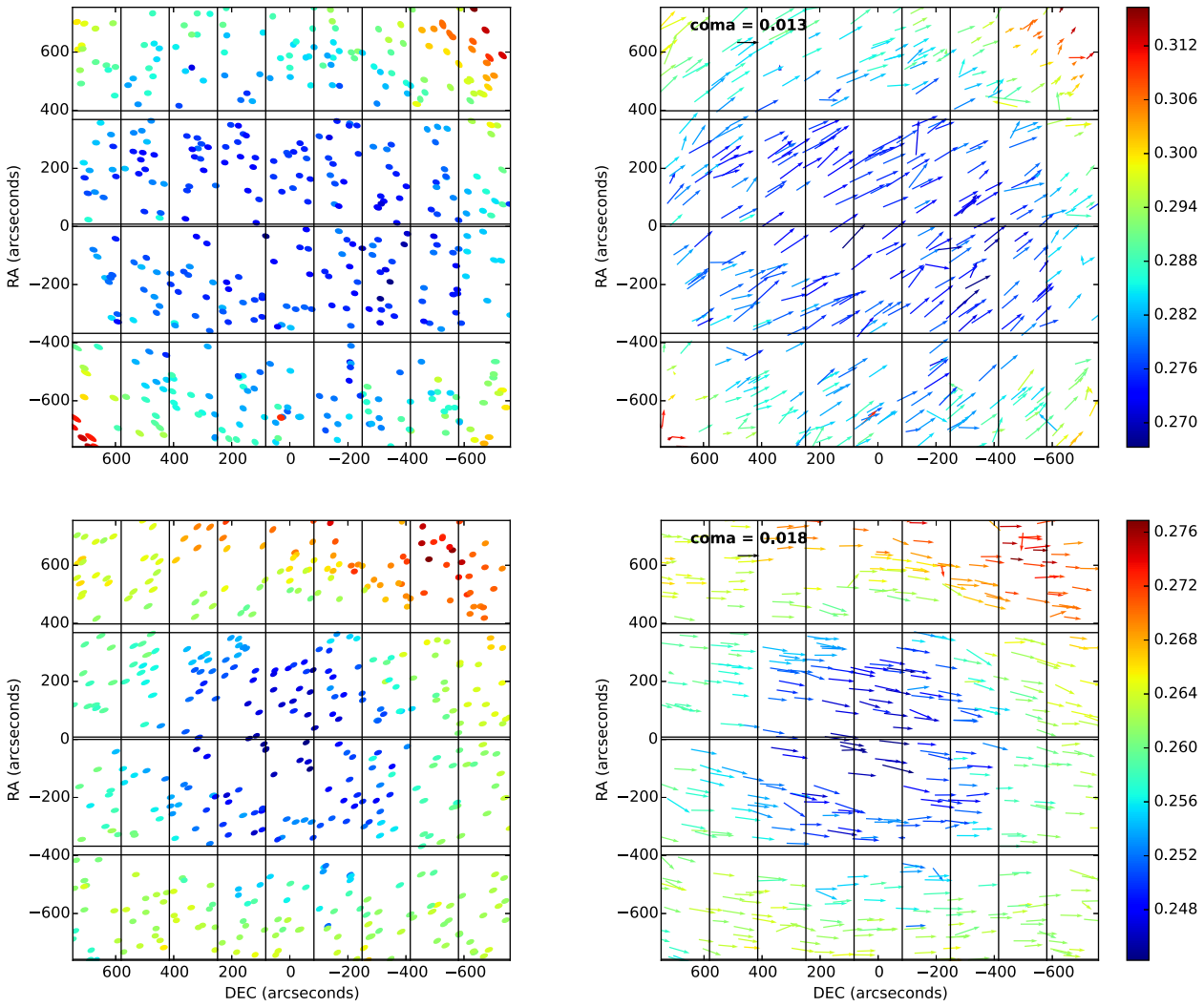

Figure 3-9 Unitless astigmatism (left) and coma (right) in the deepest coadded images in the i' filter (top) and r' filter (bottom). Each ellipse (astigmatism plots) or vector (coma plots) represents the measurement from one star. Chip boundaries are shown as black lines. For the astigmatism images, the size, eccentricity, an orientation of each ellipse shows the object's measured half light radius, astigmatism magnitude (exaggerated x5), and orientation. For the coma images, the direction and size of the vector correspond to the direction and size of the measured coma. The color of each ellipse or vector indicates the half light radius (″) of the object, as indicated by the color scale to the right of the images. Objects which are 2σ outliers in PSF size are excluded from the plot, as these are likely mis-characterized small galaxies, not stars. Coma and astigmatism are both largely field constant. The field variable astigmatism underlying the field constant pattern does not follow the predicted patterns for field symmetric or misalignment astigmatism, leading us to believe that the pattern is ground into one of the optical elements. The average aberrations by chip are given in table 3.12.

3.5 Where we failed: intrinsic shape noise at $z \sim 1$

In the limit of perfectly fitted data with no image noise- Poisson noise, readnoise, pixelization or otherwise- one would still only be able to detect the gravitational lensing signal if there were enough measurements to beat down the shape noise of the lensed galaxies. Galaxies have physical ellipticities, lopsidednesses (i.e. inherent F-flexion), and triangularities (i.e inherent G-flexion). These shape properties are not imposed on a galaxy's image due to a lensing effect or telescope aberrations, but rather are present in the galaxies themselves due to their unique formation or merger history. The spread in these inherent ellipticities, F-flexions, and G-flexions are termed 'shape noise', as the random spread of shapes among a galaxy population will add an effective noise to any measurement of gravitational flexion in the population.

Goldberg & Bacon [24] measure the inherent dimensionless F-flexion in the Deep Lens Survey, (DLS) and in two HST galaxy clusters. For the galaxies in these fields, they find that the scatter in the magnitude of the inherent F-flexion is 0.040 (DLS) and 0.029 (HST). Goldberg & Leonard [25] analyze non-cluster member galaxies in HST images of Abell 1689 and find scatters in the magnitudes of the inherent flexions of 0.03 for F-flexion and 0.04 for G-flexion, after accounting for the additional scatter added by measurement noise. Okura et al. [52] independently analyze the inherent dimensional F-flexion in the population of galaxies behind Abell 1689, finding somewhat conflicting spreads in the vector components of the flexion. They find that the standard deviation of the distribution of the dimensionful flexion vector components are $0.112/''$, corresponding to a standard deviation in the dimensionless flexion vector components of $\sim 0.067-\sim 0.224$. Given the large flexions in our data when compared to the gravitational and aberrational flexion predictions, we here consider the inherent flexions in our galaxies more carefully.[21]

[21] As the distribution of the vector components of the flexion should be approximately normal about zero, we will use the standard deviations of these one-dimensional flexion distributions to describe the width of the spread. In contrast, flexion magnitudes are strictly positive quantities that are not distributed normally. We will therefore quantify to the spreads of flexion magnitudes as 'scatter', where the scatter is the rms of the flexion magnitudes, NOT the standard deviation about zero. As always, all flexions are unitless unless explicitly stated otherwise.

3.5.1 Estimates of shape noise in the nearby EFIGI sample

In order to put new constraints on the inherent dimensionless flexions (triangularities and lopsidednesses) of galaxies, we analyze the galaxies in the EFIGI (Extraction de Formes Idealisées de Galaxies en Imagerie) [4, 3] data set. The EFIGI project was designed to address the challenges in classifying galaxy morphology, and its data are a collection of multi-wavelength observations, including imaging in Sloan g, r, and i, filters, of 4458 nearby, well-resolved galaxies of all Hubble types. Because the sample of galaxies is in the local universe and the galaxies are sufficiently larger than the PSF, any flexion measurable in these objects is not caused by gravitational lensing, or telescope aberrations, but rather reflects the innate asymmetries in the galaxy itself, inherent flexion.

To render the data usable for our purposes, we clean the g, r, and i filter galaxy images of stellar contaminants using a friends of friends algorithm. We then visually select the 925 galaxies which are adequately isolated in all three filters using this method, bin those images down by 7 pixels to 1 so that the flexion model can converge quickly on the data,[22] and analyze the data for flexion with DoPHOT. Of the 925 galaxies DoPHOT analyzed, 286 g filter, 214 r, and 180 i images are successfully fit to the flexed galaxy model. Those galaxies which fail to converge on a single flexed galaxy model are the largest and most well-resolved, even after binning.

The distribution of the fitted one-dimensional (i.e. vector component) F- and G-flexions in the r filter of the EFIGI data set are shown in figure 3-10. The distributions in the other filters are presented in table 3.5. We choose to report the standard deviations of the distributions of the F- and G-flexion vector components, rather than the distributions of the magnitudes of the flexions, as these one-dimensional flexions should be symmetrically distributed about zero, and have the same widths for both of

[22]DoPHOT is optimized to analyze many, poorly resolved objects quickly. If an object is too well-resolved, DoPHOT may attempt to fit the object as multiple objects, e.g. the core and disk will be fit separately, as two different objects. Alternately, the object will not be modeled as two, but rather the flexion parameters in the single galaxy model will not converge, as the object is too radially disparate from a Gaussian. The binning used here leaves the galaxies well above Nyquist sampled, with the average fitted half light radii equal to 2.15 pixels in g, 1.98 pixels in r, and 1.90 pixels in i. Moreover, we find the same flexion results if we bin the objects by 5x or 9x instead of 7x.

the vector components. Therefore, the symmetry of the inherent flexion distributions about zero, and the similarity of the distributions for the two vector components of each of the flexions provides a check for the soundness of the distributions. As can be seen in figure 3-10, the distributions of the one-dimensional flexions are approximately normal about zero, and the widths of the distributions are similar for both components of the F-flexion and for both components of the G-flexion.

The spread in the measured flexions can be attributed to the variation in inherent flexions between the galaxies, and also any measurement error. We estimate the measurement error by comparing flexion measurements for the same object observed in r and i filters. The distribution of the differences in the flexion measurements between filters can be used as a proxy for the contribution of measurement error to our distribution. After subtracting off this measurement noise in quadrature, we find that the distributions of the inherent dimensionless F-flexion vector components in the r' filter have standard deviations of approximately 0.028. The corresponding standard deviations in the vector components of the inherent G-flexion are approximately 0.031. The standard deviations for each vector component of the flexions are presented in table 3.5, along with the uncorrected and corrected deviations in inherent flexion for the other two filters, and the deviations in differences between the filters which we use to correct for the measurement noise.

The spread of inherent flexions observed in the g filter is wider than that observed for the r and i filters. This effect is likely caused by morphology- the bluer components of galaxies generally have more complex shapes, whereas the redder components of galaxies might be attributed to more uniform cores. Goldberg & Bacon [24] note the related phenomenon that the scatter in flexion is smaller for the (redder) early type galaxies than for the (bluer) late type galaxies.

Figure 3-11 shows that our flexion measurements are on the whole quite consistent between filters, and also confirms that there is more deviation between g and r, and g and i, than between r and i. If the disparity between flexions measured in r and i is an estimate for measurement noise, then at least some of the dissimilarity between flexions measured in g and r and g and i must be attributed to actual deviations in

the physical galaxy shapes in different colors.

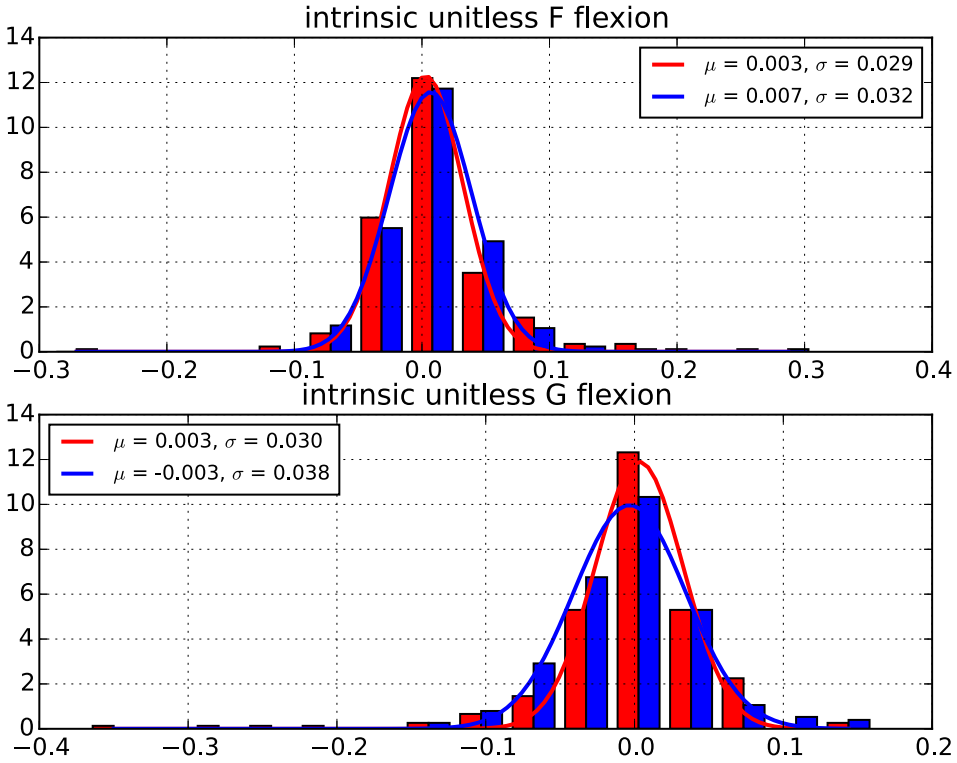

Figure 3-10 Distribution of the vector components of the unitless flexions in the r filter of the EFIGI data set. These galaxies are in the local universe ($z = 0$) and well-resolved, and therefore should not be subject to gravitational lensing effects or significant atmospheric dilution. Therefore, the spread in flexions reflects measurement error and the real spread in the galaxies' inherent flexions. Distributions in g' and i' are similar, and their standard deviations are given in table 3.5.

3.5.2 Flexion v. shear signal-to-noise

As a point of comparison to the scale of the inherent galaxy flexions, we plot the expected gravitational flexion signals induced by a SIS lens in figure 3-12. As mentioned in §3.3.8, derivatives of shear are dimension-ful. Therefore, in order to discuss the gravitational effect on apparent galaxy shape caused by this term, we must render the components of the flexions dimensionless by multiplying them with the lensed galaxy's half light radius, $\theta_{1/2}$. The larger the half light radius of the source galaxy, the larger the apparent shape distortion that is imposed on it by the same lens (see equation 3.9). For figure 3-12 and the following discussion of the magnitude of the

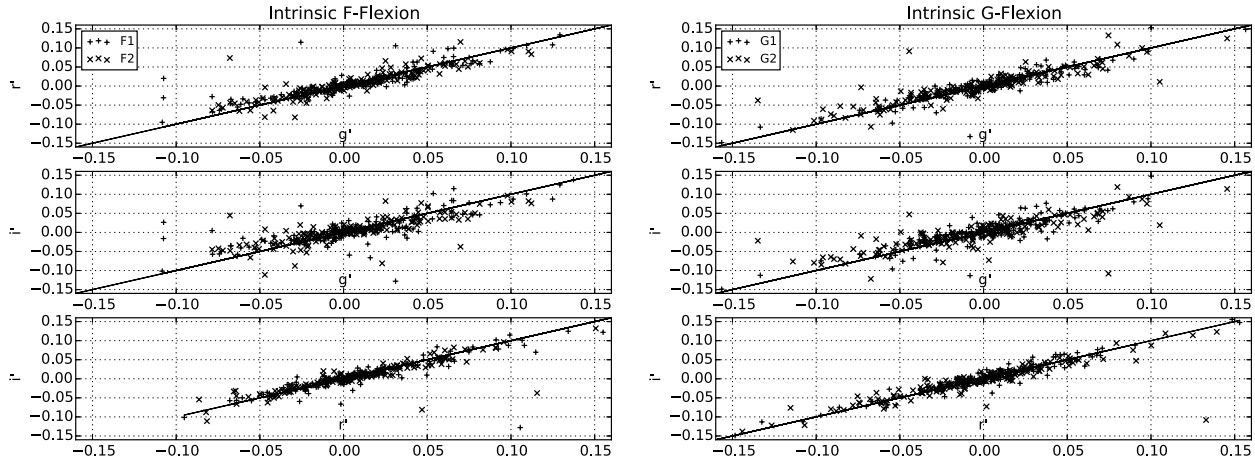

Figure 3-11 Comparisons between measured one-dimensional F-flexions (left) and G-flexions (right) in different filters of the EFIGI data set. Both vector components of each type of flexion are shown. The standard deviations in each vector component of either flexion should be the same. The variations between measurements in different filters are quantified in table 3.5.

	Measured standard deviations				Implied intrinsic standard deviations			
filter	F1	F2	G1	G2	F1	F2	G1	G2
g'	0.038	0.039	0.040	0.045	0.036	0.037	0.037	0.042
r'	0.029	0.032	0.030	0.038	0.026	0.030	0.026	0.035
i'	0.024	0.028	0.029	0.033	0.021	0.025	0.025	0.029
g'-i'	0.019	0.020	0.017	0.019				
g'-r'	0.016	0.016	0.019	0.018				
r'-i'	0.012	0.012	0.016	0.015				

Table 3.5 Standard deviations in inherent one-dimensional flexions in the g, r, and i filters of the EFIGI data set. These galaxies are in the local universe ($z = 0$) and well-resolved, and therefore should not be subject to gravitational flexion, aberrational flexion, or significant atmospheric dilution. Therefore, the distributions of measured flexions in this data set are caused by the spread in the galaxies' inherent flexions and measurement error. The measurement error can be estimated as the distribution of the differences in the measurements between filters, provided at the bottom of the table. The implied standard deviation in the inherent one-dimensional galaxy flexion for each filter, after removing this estimated measurement error, is given in the right hand columns of the table. Bluer filters tend to have a broader spreads in inherent flexion.

flexion lensing effect, we use an optimistically large, but still plausible, intrinsic half light radius of $0\farcs48$. We take the Einstein ring radius, θ_E to be $1\farcs35$, consistent with a L* lensing galaxy at $z = 0.18$ acting on a source at $z \sim 1$. As shown in the figure, the magnitude of the measurable flexion signal in the direction of the lens will vary with the amount and orientation of any inherent ellipticity in the source galaxy. The figure does not include the effects of the PSF, which will generally degrade the signal.

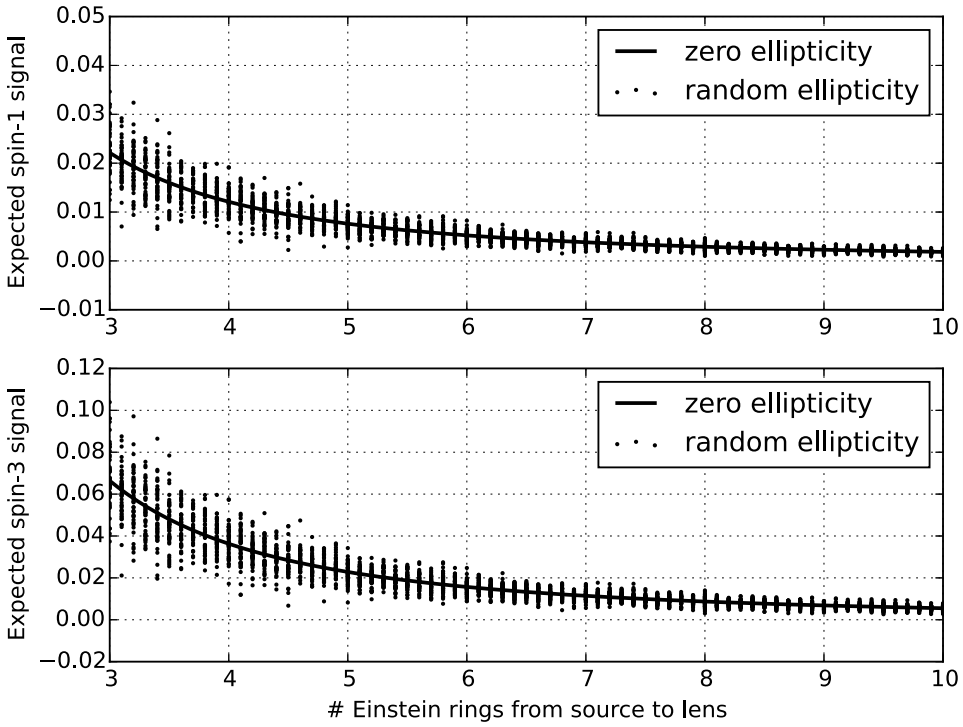

Figure 3-12 Predicted radial flexion signal strength for a Gaussian model galaxy with $\theta_{1/2} = 0\farcs48$ lensed by a SIS with $\theta_E = 1\farcs35$. The predicted flexion signal will vary with the magnitude and orientation of the source galaxy's intrinsic ellipticity with respect to the lens. The points show the range of possible magnitudes of the radial flexion predictions for source galaxies with random ellipticities about zero with standard deviation 0.3. The line is the magnitude of the radial component of the predicted flexion measurement when the source has zero intrinsic ellipticity. These predictions ignore effects of atmospheric smearing, which will reduce the signal substantially.

For a set of low redshift galaxies where the distribution of one-dimensional inherent flexions has a standard deviation of 0.03, one would need to average at least nine flexion measurements at each radial separation from the lensing galaxy in order to have an error in the mean measurement be less than 0.01- the gravitational F-flexion value for a $0\farcs48$ source galaxy at 4.5 Einstein rings, and the gravitational G-flexion

value at 7.6 Einstein rings. One needs to average 36 measurements in order to have an error in the mean be less than 0.005- the F-flexion value at 6.2 Einstein rings and the G-flexion value at 10.6 for this optimistic case. If one wants to measure F-flexion at 10 Einstein rings with any confidence, one needs over 160 measurements of galaxies lensed at that radial separation from the lensing galaxy.

But in theory, even allowing for a distribution of inherent one-dimensional flexions with a standard deviation of 0.03, flexion can still be a better tool than shear for probing the shapes of gravitational potentials (Leonard et al. [36], Bacon et al. [1], Hawken & Bridle [28]). If shear and flexion measurements are limited by inherent shape noise, flexion's smaller inherent variation of 0.03 makes the flexion signal-to--noise greater than the shear signal-to-noise, at least close in to the lens. However, if the spread in intrinsic flexion is twice that previously estimated, 0.06, shear has superior signal-to-noise than flexion. Figure 3-13 shows the flexion signal-to-noise for both low and high spread in intrinsic flexion.

3.5.3 Intrinsic flexions in the source population behind Abell 1689

The $z = 0$ population is far less morphologically complex than populations at higher redshift. Galaxies most likely underwent mergers and periods of increased star formation in order to reach their current state. We therefore would expect galaxies at higher redshifts to have larger inherent flexions than their $z = 0$ counterparts.

In order to better understand the scatter in inherent flexions in the population of galaxies behind Abell 1689, we follow in the footsteps of Goldberg & Leonard [25], Okura et al. [52] and directly compute the distribution of the inherent flexions of the 1345 background source galaxies in our data that (a) have a half light radius greater than 1.5× the PSF half light radius, (b) most likely are not cluster member galaxies, as determined by color-magnitude selection and the other selection criteria discussed in §3.3.6,[23] and (c) have derived intrinsic flexions and ellipticities with

[23]Some of these galaxies may still lie in front of the cluster. However, the magnitude cut does help to eliminate these forgerounds.

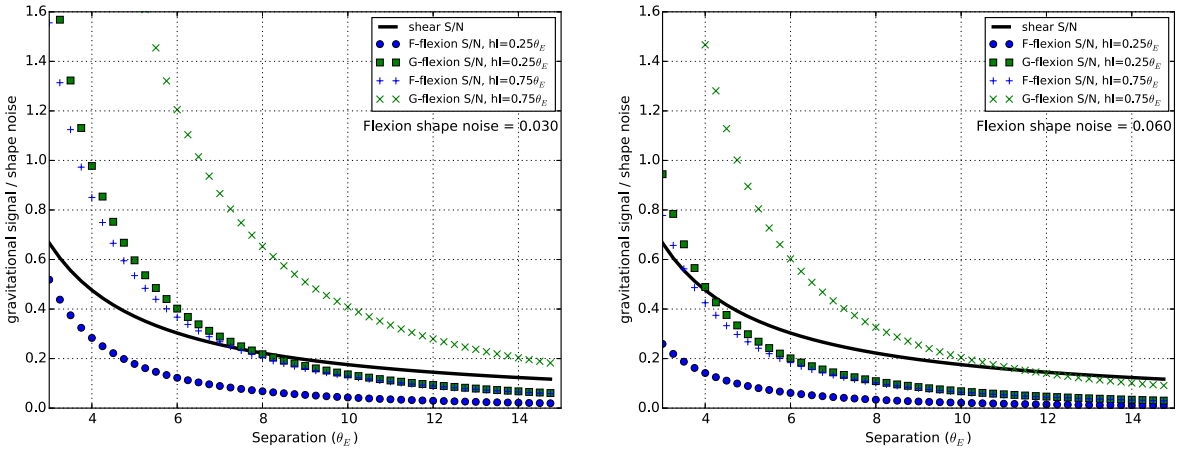

Figure 3-13 Predicted signal-to-noise (S/N) in gravitational flexion and shear for systems where the spread in inherent galaxy ellipticities and flexions dominate over all other forms of noise. The left plot shows the predicted signal-to-noise if the inherent one-dimensional flexion standard deviation is 0.030, as it is in the local universe. The right plot shows the predicted signal-to-noise in the hypothetical case where inherent shape noise in the one-dimensional flexion is 0.060, 2× larger than measured in the EFIGI data set and by Goldberg & Bacon [24], Goldberg & Leonard [25]. The black curves are the predicted shear signal-to-noise, which is the same in both plots. The blue curves depict possible F-flexion signal-to-noises, and the green curves depict possible G-flexion signal-to-noises. For each of the F- and G flexions we show the expected signal-to-noises for systems with intrinsic half light radii equal to $0.25\theta_E$, and for systems with (optimistic) half light radii equal to $0.75\theta_E$. For Abell 1689, most of the lensed sources we consider for have intrinsic half light radii closer to $0.25\theta_E$.

magnitude less than 0.8.[24]

We compute the inherent flexion values for each object by taking the measured flexions and correcting them for shear-flexion mixing, telescope aberrations, any gravitational shear and flexion caused by the cluster and the BCG (assuming as always an SIS mass profile for each), and atmospheric dilution. In order to facilitate the correction for gravitational lensing by the cluster and also to assess any possible errors induced by the SIS lens approximation, we decompose the shear and flexion into components that are radially and tangentially oriented to the cluster center. We analyze the inherent shears and flexions in these components individually. We do not correct for galaxy-galaxy lensing effects from cluster galaxies other than the BCG, as the majority of the objects that we detect behind the cluster do not have an identified lensing galaxy in their vicinity.

When considering all of the galaxies in our $z \sim 1$ source population, we find that the standard deviations of the inherent flexion vector components are 0.101 for F, and 0.126 for G in the r' filter. We show a histogram of the computed one-dimensional inherent flexions in the r' filter in figure 3-14.

Both the spread in inherent flexions as well as measurement error contribute to the width of the plotted distribution. Following our analysis of the EFIGI data set, we estimate the the measurement error by comparing flexion measurements for the same objects observed in two images. The distribution of the differences in the flexion measurements between two images in the same filter can be used as a proxy for the contribution of measurement error to the distribution. We subtract off this measurement noise in quadrature. Values for the uncorrected and corrected distributions of one-dimensionalinherent flexions are presented in table 3.6 for both the i' and r' filters. The table also shows the distribution of the differences between the measured deviations in the r' and i' filters that we use to make the noise corrections. The corrected standard deviations in the i' filter are smaller than those in r', as we would

[24]The 0.8 cut for inherent flexions and ellipticities removes 0.6% of the galaxies from the sample, and does not alter the shape of the distribution in any meaningful way. Galaxies with such extreme shapes are very likely to be two galaxies fit as one object, or to be very small and dim, possibly rendering the correction for the atmospheric dilution inaccurate.

expect for the redder components of galaxies, however the i' data are much noisier than the r' data, resulting in noisier measurements of the inherent flexions and a greater measured spread before correcting for the measurement noise.

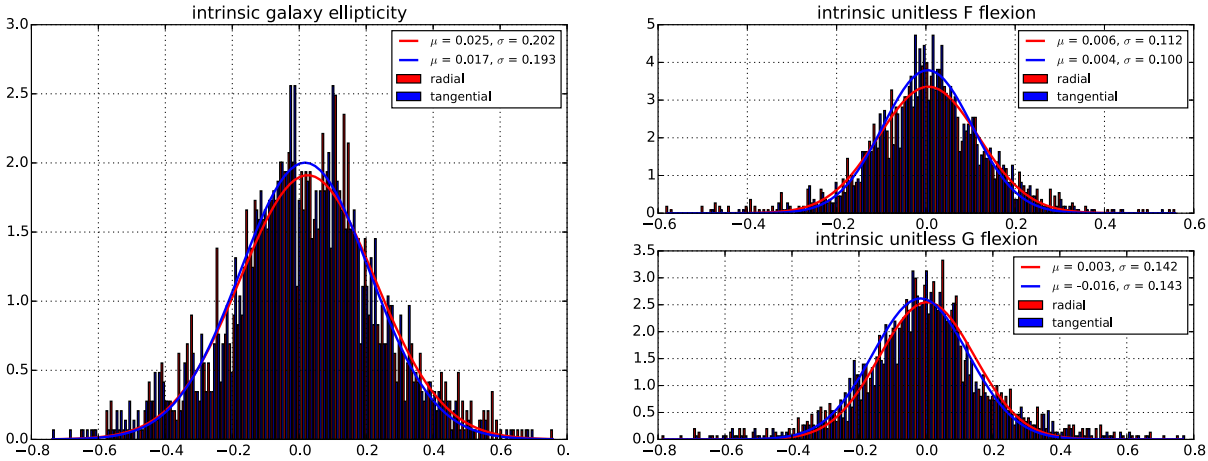

Figure 3-14 Distribution of one-dimensional ellipticities (E) and flexions (F & G) in the r' filter for the 1115 large galaxies in the background galaxy population of Abell 1689 that are detected in this filter. These data have not been corrected for measurement noise. Flexions and shears have been decomposed into directions oriented radially and tangentially with respect to the cluster center.

Two sample K-S tests show that components of the one-dimensional inherent galaxy ellipticities oriented radially towards and tangential to the cluster center were drawn from the same sample with high likelihood, see table 3.7. This sameness between the radial and tangential ellipticity distribution shows that the simple SIS approximation is a very good, if imperfect, model for the cluster shear effect, and that we are not introducing substantial bias into our models by using this approximation for the lensing potential.

The distribution of one-dimensional intrinsic flexions is also approximately normal and equally distributed in both components. Flexion drops off quickly with radius, as compared to shear, and therefore this evenness of distribution indicates that there

	Standard deviations in inherent shapes for all background galaxies											
	not corrected for measurement error						corrected for measurement error					
image	E_r	E_t	F_r	F_t	G_r	G_t	E_r	E_t	F_r	F_t	G_r	G_t
r'_1	0.202	0.193	0.112	0.100	0.142	0.143	0.201	0.192	0.106	0.095	0.127	0.124
i'_1	0.199	0.185	0.109	0.100	0.154	0.160	0.195	0.182	0.086	0.083	0.087	0.102
$r'_1 - r'_2$	0.020	0.019	0.035	0.031	0.063	0.071						
$i'_1 - i'_2$	0.038	0.033	0.067	0.056	0.127	0.123						

Table 3.6 Standard deviations in inherent ellipticities and flexions in the r and i filters of the 1345 large galaxies in the background galaxy population of Abell 1689. Both shape noise and measurement error contribute to the derived scatter in the inherent shapes. We estimate the measurement error as the distribution of the differences in the measurements between two images in the same filter. These are provided at the bottom of the table. The corrected standard deviations in the vector components of the intrinsic shapes, after removing this estimated measurement error, are given in the right hand columns of the table.

is no overall bias in the flexion measurements. As with shear, two sample KS tests show that the components of inherent flexion oriented radially and tangentially with respect to the cluster center were likely drawn from the same distribution.

K-S Test Results: Radial v. Tangential Components		
	K-S Statistic	p-value
Ellipticity	0.046	0.167
Intrinsic F-Flexion	0.046	0.189
Intrinsic G-Flexion	0.056	0.061

Table 3.7 Results from 2 sample K-S test performed to compare the radial and tangential components of the source galaxies' intrinsic ellipticities and flexions. The results confirm the null hypothesis that the radial and tangential shape properties of the galaxies are drawn from the same sample. Consequently, it is very unlikely that the measurement technique or lensing model is adding bias to either component of the flexions or shears.

3.5.4 Discrepancies in the inherent flexions in the galaxy population behind Abell 1689

The large standard deviation in one-dimensional inherent flexions found here is in apparent disagreement with the 0.03 scatter in F-flexion magnitude found by Goldberg & Bacon [24], and the 0.03 and 0.04 scatters in inherent F- and G-flexion magnitudes found by Goldberg & Leonard [25]. The discrepancy with Goldberg & Leonard [25] deserves particular attention, as they, like us, make their measurements on the background galaxy population of Abell 1689.

We note two conventional differences between Goldberg & Bacon [24], Goldberg & Leonard [25] and our own work.

- Goldberg & Bacon [24], Goldberg & Leonard [25] render their flexions dimensionless by multiplying the unitful (shear derivative) flexion with the galaxy semi-major axis as defined in Bertin & Arnouts [8]. In contrast, we render the unitful shear derivative dimensionless using the galaxy half light radius. For a Gaussian, the semi-major axis is 1.7× the half light radius, rendering Goldberg & Bacon's, and Goldberg & Leonard's measurement of the scatter in intrinsic flexion magnitudes seemingly even more discrepant with ours.

- Goldberg & Bacon [24], Goldberg & Leonard [25] report the scatters of the flexion magnitudes, whereas we report the standard deviations of the one--dimensional flexion components. We interpret Goldberg & Bacon's and Goldberg & Leonard's scatters to be the averages of the square magnitudes of the flexions, $< F^2 >$.[25] For normally distributed and uncorrelated flexion vector components with standard deviation σ, the scatter in the magnitude of the vector is $\sqrt{2}\sigma$.[26]

Converting Goldberg & Bacon's and Goldberd & Leonard's found scatters in the flexion magnitudes into standard deviations of the flexion components comparable with our own yields 0.012 in the one-dimensional F-flexion and 0.017 in the one-dimensional G-flexion. These numbers are $\sim 1/2$ the spreads in inherent flexion that

[25]Goldberg & Bacon [24] plot distributions of inherent galaxy shear and unitless flexion in figure 1 of their work. The shears and flexions in these plots are strictly positive, indicating that they are analyzing the vector magnitudes of the shears and flexions. When referring to the spread of those distributions, Goldberg & Bacon [24] use both the terms 'scatter' and 'standard deviation'. Goldberg & Leonard [25] also plot the distribution of the magnitude of the inherent flexions, but only refer to the spread of that distribution as 'scatter'. Our understanding is that 'scatter' is rms flexion magnitude, while 'standard deviation' is the rms flexion about the average. For flexion magnitude, whose average is strictly positive, 'scatter' and 'standard deviation' are distinct quantities. As (1) Goldberg & Leonard [25] only use the term scatter, (2) there is no reason for the convention to vary between the Goldberg & Bacon [24] and Goldberg & Leonard [25], and (3) the rms flexion magnitude is a more reasonable measure of the inherent flexion spread than standard deviation about the mean, we assume that both works are reporting the rms flexion magnitudes, not the standard deviations.

[26]If we have misinterpreted their findings and they are reporting the standard deviations about the mean, then the ratio between their reported spread in the flexion magnitudes and the standard deviation in the components is 0.655, rendering their findings in closer agreement with our own.

we find for the nearby EFIGI galaxies and $\sim 1/8\times$ the spreads we report here for Abell 1689.

Okura et al. [52] also measure the spread in the F-flexion in the background population of Abell 1689, observing in the i' filter with Subaru. Their reported value for the standard deviation in the dimension-ful flexion vector components are $0.112/''$, from which we can infer a standard deviation in the dimensionless inherent flexion vector components of $0.067 - 0.224$ given the range in galaxy sizes of $0\farcs6 - 2\farcs0$ that they consider in that work.[27] Okura et al. [52] very likely find more galaxies with $0\farcs6$ half light radii than with $2\farcs0$ radii, indicating that their measured flexion spread is likely closer to the smaller value of 0.067 than 0.244.

What is the cause of this apparent discrepancy between Goldberg & Bacon [24], Goldberg & Leonard [25], Okura et al. [52], and this work? The devil is, as always, in the details. In the following subsections, we address each prior measurement individually.

Goldberg & Bacon (2005)

Goldberg & Bacon [24] use two data sets to make their measurements of the scatter in inherent galaxy F-flexion magnitude: a set of two clusters imaged with HST, and the fields from the Deep Lens Survey (DLS). They do not correct flexion measurements in either data set for the effect of the PSF, but rather limit their flexion measurements to the largest and brightest galaxies, whose flexions are less likely to be significantly diluted by the PSF. For the HST fields, Goldberg & Bacon [24] use only objects which are sufficiently large and bright to be well-classified morphologically by eye. They do not directly specify the galaxy size cutoff for measurements of flexion scatter in the DLS fields, however for their analysis of gravitational flexion in the DLS fields, they limit their flexion measurements to those galaxies with semi-major axes greater than $0\farcs9$. Even with this galaxy size cut, Goldberg & Bacon [24] only use the relative

[27] While Okura et al. [52] do not specifically state that they are reporting the scatter in the one-dimensional F-flexion, they report an average value for the flexion distribution of $0.000223/''$. Since the distribution is so well centered on 0, whereas the distribution of a magnitude must have a substantial positive average, we assume here that Okura et al. [52] are reporting standard deviations and averages for the one-dimensional F-flexion.

orientation between flexion and shear, not the flexion magnitude, to draw conclusions about the lensing field.

The brightest, most well-resolved galaxies in a field are more likely to be at lower redshift than the dimmer, less well-resolved galaxies. This preferential selection of low-redshift galaxies will bias measurements of the flexion scatter low in two ways.

- Galaxies at high redshift are more morphologically complex than galaxies at low redshift. This morphological complexity is a result of the increased rate of star formation and increased rate of galaxy mergers at $z \sim 1$ compared to the present day. Therefore by limiting flexion measurements to the brightest, most well-resolved galaxies, which are more likely to be at lower redshift than high, one will measure a smaller scatter in inherent flexions than if one had included the dimmer, higher redshift population. One can alternately, but equivalently make this same argument based on color. There are more red-ellipticals in the present universe than at $z \sim 1$. As found in Goldberg & Bacon's own work, redder galaxies have a lower scatter in inherent flexion than the bluer galaxies; they find that the scatter in inherent flexion for spirals is 0.041 while the scatter in inherent flexion for ellipticals is a much more modest 0.012. By limiting measurements to the brightest and lowest-redshift galaxies, the galaxy sample is preferentially red, and the measured scatter in inherent flexion is pushed low.

- From the analysis of the EFIGI galaxies, we know that galaxies' bluer features are more lopsided and triangular than galaxies' redder features. By the time the light reaches Earth, the blue features in high redshift galaxies will have shifted to be observable in redder filters. Consequently, observations of galaxies at high redshift should yield wider spreads in inherent flexion than observations in the same filter of galaxies at low redshift, even if those galaxies are otherwise physically identical. Because brighter, well-resolved galaxies are more likely to be at lower redshifts than dimmer ones, limiting flexion measurements to only these galaxies biases the scatter low.

Of course, if the selected galaxies are not sufficiently well-resolved, the measured

flexions will be diluted by the PSF. If the PSF isn't then fully compensated for, the measured spread in inherent flexions will be low.[28] Therefore, using only the brightest, most well-resolved galaxies for an analysis of the inherent flexion distribution rather than correcting for the PSF creates a Catch-22: both more restrictive galaxy selection and less restrictive galaxy selection will lead to an underestimation of the flexion spread.

To test this predicted effect of using only the brightest galaxies in a field to measure inherent flexion, we perform another analysis of the spread in inherent flexions in the background galaxy population of Abell 1689, but now using only the brightest 1/8th of these galaxies.[29] These 172 bright galaxy objects yield a much tighter distribution than the full sample. After removing the measurement noise from the flexion distribution as we did with the measurements of flexion spread in the full population of background galaxies, we find a standard deviation in the one-dimensional inherent F-flexion of 0.056 and a standard deviation in the one-dimensional inherent G-flexion of 0.085 for the r' filter. The distribution histograms and computed standard deviations in the r' filter are provided in figure 3-15 and table 3.8.

The standard deviation in one-dimensional inherent flexions that we find in this population of brightest background galaxies is still in disagreement with Goldberg & Bacon's (2005) measurement. However, if we assume that Goldberg & Bacon's (2005) measured flexions are diluted somewhat by the PSF, we can close some of the gap between our measured flexion distributions and theirs. While Goldberg & Bacon [24] do not explicitly report their PSF sizes and mean galaxy sizes, we can make educated inferences. For the DLS fields, a PSF FWHM of $0\farcs85$ is reasonably optimistic. If we assume that most of the galaxies used for their flexion study have semi-major axes

[28] Correcting for the PSF is of course a double edged sword. While undercompensating for the PSF biases the measurement of inherent flexion low, overcompensating will bias the measurement high.

[29] If the background source galaxy population includes some erroneous foreground galaxies, then the mean redshift of the brightest galaxies will be driven yet lower. However, the magnitude cut, excluding all galaxies brighter than 22.00 magnitude in r' from the source galaxy population, helps to mitigate this foreground contamination.

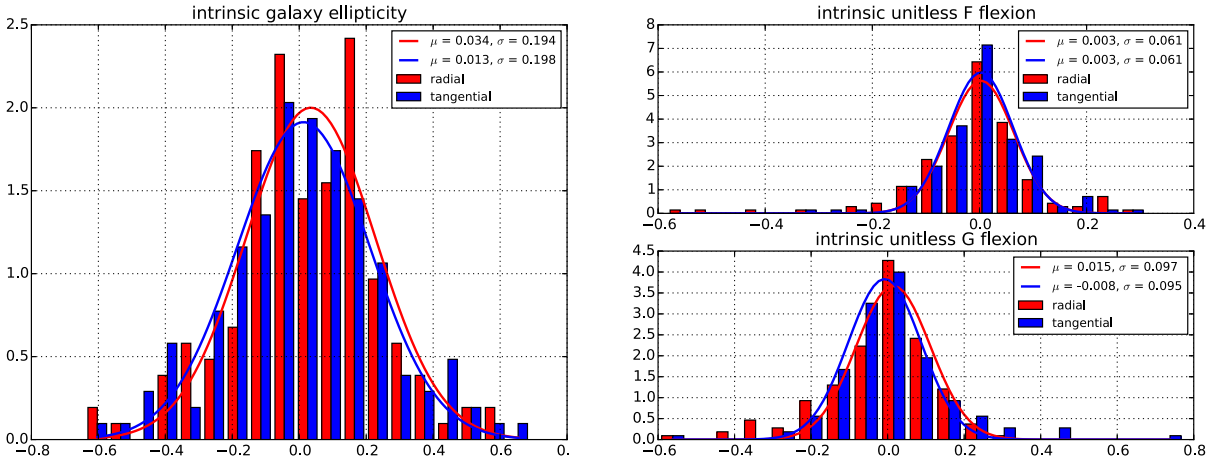

Figure 3-15 Distribution of one-dimensional inherent ellipticities and flexions in the r' filter for the 172 brightest galaxies in the background galaxy population of Abell 1689 that are detected in this filter. These data have not been corrected for measurement noise.

	Standard deviation in inherent shapes for brightest background galaxies											
	not corrected for measurement error						corrected for measurement error					
image	E_r	E_t	F_r	F_t	G_r	G_t	E_r	E_t	F_r	F_t	G_r	G_t
r'_1	0.194	0.198	0.061	0.061	0.097	0.095	0.194	0.198	0.055	0.058	0.085	0.085
i'_1	0.182	0.193	0.066	0.062	0.103	0.110	0.181	0.191	0.051	0.047	0.066	0.080
$r'_1 - r'_2$	0.013	0.013	0.026	0.018	0.047	0.042						
$i'_1 - i'_2$	0.021	0.026	0.042	0.040	0.079	0.075						

Table 3.8 Standard deviation in one-dimensional inherent ellipticities and flexions in the r and i filters of the 172 brightest galaxies in the background galaxy population of Abell 1689. Both shape noise and measurement error contribute to the derived standard deviations in the inherent shapes. We estimate the measurement error as the distribution of the differences in the measurements between two images in the same filter. These are provided at the bottom of the table. The corrected standard deviations in the intrinsic shapes, after removing this estimated measurement error, are given in the right hand columns of the table.

of $\sim 1\farcs0$ (recall that Goldberg & Bacon [24] use galaxies with semi-major axes of $0\farcs90$ and above for their gravitational flexion analyses), then their measurements of flexion are diluted to 1/3 of their inherent values. Correcting for the effect of this dilution on their reported scatter yields an amended standard deviation in inherent one-dimensional flexion for the DLS fields of 0.050, in closer agreement with the distribution measured in this work. [30]

Goldberg & Bacon's (2005) measurements of flexion in HST data (using WFPC-2), would naturally not have required a PSF correction as large as that required for their ground based measurements. However, even HST's PSF can impart a non-trivial dilution to the flexions of the smaller galaxies. While we can only guess at the sizes of the galaxies used by Goldberg & Bacon [24], we can reasonably assume a PSF FWHM of $\sim 0\farcs10$. This PSF would dilute the observed flexions in galaxies with half light radii of $0\farcs1$, (semi-major axis of $\sim 0\farcs17$), to $\sim 65\%$ of their inherent values. While these galaxies are quite small compared to those used for the ground based measurements, they are large compared to the $0\farcs046$ pixels on the Planetary Camera, and thus might plausibly have been used for this scatter analysis.

Goldberg & Leonard (2007)

Goldberg & Leonard [25] measure the scatter in inherent flexion in the background galaxy population of Abell 1689 using HOLICs.[31] While they provide a procedure by which they could correct for their PSF, they do not correct for the PSF but rather restrict their galaxy selection to the largest galaxies only. However, they use HST data only, implying that any PSF correction required for their measurements is small compared to the correction needed for ground based measurements. Still, their

[30] For the DLS fields Goldberg & Bacon [24] report a somewhat higher scatter in the F-flexion, 0.040, than they report for their HST fields. To compute the amended DLS flexion scatter, we use this 0.040 starting point, convert the flexions from units of semi-major axis to units of half light radius, and divide by $\sqrt{2}$ to infer the standard deviation in the one-dimensional flexion rather than the scatter in the magnitude of the flexion. We then correct for the effects of dilution. We note again that the conversion from units of semi-major axis to half light radii and from scatter in flexion magnitude to standard deviation in the flexion vector components will make the numerical descriptor of the flexion spread smaller.

[31] They make measurements of the gravitational flexion using both HOLICs and shapelets. However the reported scatter is attributed to the measurements made using HOLICs.

measured scatter in inherent F- and G-flexions of 0.03 and 0.04 are still in seeming conflict with our own.

Before addressing possible points of disagreement between Goldberg & Leonard [25] and this work, we note first that Goldberg & Leonard's proposed correction for effects of a symmetric PSF agrees with our correction of $(1-\mu^2)^{-3/2}$. Here μ is the ratio of the PSF size to the measured galaxy size, as in eq. 3.9. Goldberg & Leonard's correction factor for dimension-ful G-flexion is the linear ratio of the symmetric fourth moments of the un-aberrated and smeared galaxies. So long as the PSF and the galaxy have the same radial profile, this is equivalent to a correction factor of $(1-\mu^2)^{-2}$. However, in the HOLICs method, the measurement of the unitful G-flexion, prior to adding atmospheric correction, is the ratio of the measured spin-3 third moment, and the measured symmetric fourth moment. This ratio of moments is equivalent to a dimensionless spin-3 shape divided by a proxy for the measured galaxy size, both of which are uncorrected for the effects of the PSF. After correcting this measured dimension-ful flexion for the effects of the PSF, the flexion must be rendered dimensionless so that it reflects the scale-independent inherent shape of the galaxy. The flexion is rendered dimensionless by multiplying the dimension-ful value by the true (i.e PSF corrected) galaxy size. The resulting extra ratio of the smeared and unsmeared galaxy sizes that arises when the flexion measurement is rendered unitless provides the additional factor of $(1-\mu^2)^{1/2}$ that makes Goldberg & Leonard's correction the same as our own.[32]

Because Goldberg & Leonard [25] measure flexion using only very large galaxies in their sample, and the HST PSF dilutes the flexion signal from these largest objects very little, PSF dilution likely did not affect their measured flexion scatters. Rather, we believe that the source of the discrepancy between the scatter in inherent flexion magnitudes measured by Goldberg & Leonard [25] and the standard deviation of the one- dimensional inherent flexions found in this work can be attributed to the

[32]The form of the PSF correction for the F-flexion in the HOLICs method is slightly more complicated than the correction for the G-Flexion. The added complexity is caused by centroid shift [24]. However, the correction for the F-flexion term is still fundamentally the same as the correction for the G-flexion term.

same cause as the discrepancy between those reported by Goldberg & Bacon [24] and ourselves. Namely, by using only the brightest and largest galaxies they preferentially select low-redshift galaxies with relaxed morphology.

Additionally, Goldberg & Leonard [25] report the median flexion scatter for their g, r, i, and z filter images. It is possible that the inclusion of the lower scatter i and z measurements lowered their final reported scatter measurement. However, this effect would be somewhat offset by the inclusion of the g filter measurements.

Okura, Umetsu, & Futamase (2008)

Okura et al. [52] also use the HOLICs method to analyze the spread in inherent flexions in the background galaxy population of Abell 1689. They use Subaru to make their observations, observing exclusively in the i' filter, and obtaining images with PSF FWHM of $0\farcs88$. For their flexion analyses, Okura et al. [52] reject all objects from their sample of background galaxies that have measured FWHM less than $0\farcs6$ or greater than $2\farcs0$. This exclusion of small galaxies is similar to our own insistence that galaxies have half light radii of at least $1.5x$ the PSF's. After removing the small galaxies from their sample, Okura et al. [52] measure flexions for each of the objects, accounting for both the isotropic and anisotropic effects of the PSF on their flexion measurements. Their findings, like their selection methods, are not dissimilar to our own.

Okura et al. [52] find a standard deviation of $0.11245/''$ for the distribution of the unitful F-flexion vector components. They do not use or report on the noisier G-flexion measurements. Assuming that Okura et al. [52] find many more smaller galaxies than larger ones, as did we, we find that the equivalent standard deviation in the distribution of the dimensionless flexion vector components is $\sim 0.067 - 0.146$.[33]

[33]We use the assumption that the standard deviation in the distribution of the dimensionless flexion is approximately equal to the product of the standard deviation of the distribution of the dimension-ful flexion and the mean of the half light radii. This assumption likely isn't entirely correct as larger galaxies will tend to be more symmetric and smaller galaxies will tend to be more triangular and lopsided, but it is sufficient to provide a rough sense of the true value. Because there are likely more small galaxies than large galaxies in their sample of $0\farcs6 - 2\farcs0$ FWHM objects, the mean of the half light radius will between $0\farcs6$ and $1\farcs3$, yielding the above stated range for the standard deviation of the distribution of the dimensionless flexion vector components.

We note that Okura et al. [52] do not account for the contribution of measurement error to the spread of flexion values, and therefore the standard deviation in the spread of the inhernet flexions may be smaller than they report.[34] However, if we assume that their measurement error is similar to our own, their findings are still in relative good agreement with ours.

3.5.5 Can we beat down the shape noise at all?

Prior to this work, we had not predicted this substantial spread in the inherent flexion in the source galaxy population behind Abell 1689, and it is one of the primary reasons why we failed in our endeavor to measure galaxy-galaxy gravitational flexion in that cluster. We did not obtain flexion measurements for a large enough sample of galaxy--galaxy lensed sources in order to beat down the intrinsic shape noise. As indicated by figure 3-13, for all but the very largest galaxies, we might as well have been using shear.

However, if we remove the restriction that the background galaxies have a nearby lensing galaxy, we have many more objects (1345) with which to explore the cluster potential. Can we use these galaxies to measure the cluster centered symmetric lensing potential? Certainly the answer must be no. Flexion drops off as the square of the separation from the lensing mass center, and is thus much more sensitive to substructure than the underlying symmetric mass profile of the cluster.[35] Moreover, any trend in the flexion with radius from the cluster center would be a trend in the shear derivative, i.e. untiful flexion. For the range of sizes of galaxies in our data set, the approximate standard deviation in dimension-ful F- and G-flexions are $0.28/''$ and $0.35/''$. For comparison, the cluster centered lensing flexion at 2 Einstein rings from the cluster center, ($\theta_E \sim 50''$), is $1/3001/''$ for F-flexion and $1/1001/''$ for G-flexion.

[34] At least they do not account for it explicitly, as do Goldberg & Bacon [24], Goldberg & Leonard [25].

[35] The magnification will help, which is why we can see arcs behind galaxy clusters. However, only those source galaxies very close to the cluster center will benefit enough from this magnification to make the imposed flexion very large. And for those galaxies, the magnitude of the induced shear is also substantial, rendering the galaxy very un-galaxy-like, and thus our tools for galaxy detection and flexion extraction unsuitable.

However, having nothing to lose, we look for a flexion trend anyway.

For each of the background source galaxies, regardless of its association with a cluster member lensing galaxy, we predict the gravitational flexion imparted by the cluster itself, using the zero-order approximation that the mass distribution of the cluster is a SIS. We do not consider substructure. We then use the predicted gravitational flexion to predict the measurable flexion in the image, considering shear-flexion mixing, atmospheric dilution, and the effects of asymmetric telescope aberrations.[36]

In figure 3-16 we show the flexion measurements for each of the background source galaxies lensed by the cluster and their associated predictions. As flexion drops off as the squared inverse of the radial separation of the lensed background galaxy and the cluster center, most of the flexion associated with gravitational lensing from the cluster is effectively zero. We plot the de-aberrated flexions in figure 3-17 in order to demonstrate this point. While it is promising that we can correctly predict the effects of asymmetric aberrations on sheared and flexed galaxies, that plot is not proof of a measurement of gravitational flexion by the cluster.

3.6 Secondary points of failure

Scatter in inherent flexion is not the lone culprit in our failure to observe galaxy-galaxy lensing flexion in Abell 1689. As inherent galaxy flexion is unbiased in orientation, we might have overcome it if we had enough galaxy-galaxy lensing systems for which (a) we were confident in the classification of the background source galaxies and cluster member lensing galaxies, (b) the source galaxies were sufficiently well sampled for accurate flexion measurements, and (c) we had an accurate redshift for the source galaxy. Put more simply, if shape noise were the only noise in our data, theoretically, we could have beaten it.

[36] We also model the effect of the BCG, though it only alters the flexion predictions for the innermost galaxies. Inclusion of the BCG in the cluster lensing analysis is a matter of convenience, as the analysis pipeline for galaxy-galaxy flexion is designed to compute lensing effects for the cluster plus one other (nearby) lensing galaxy.

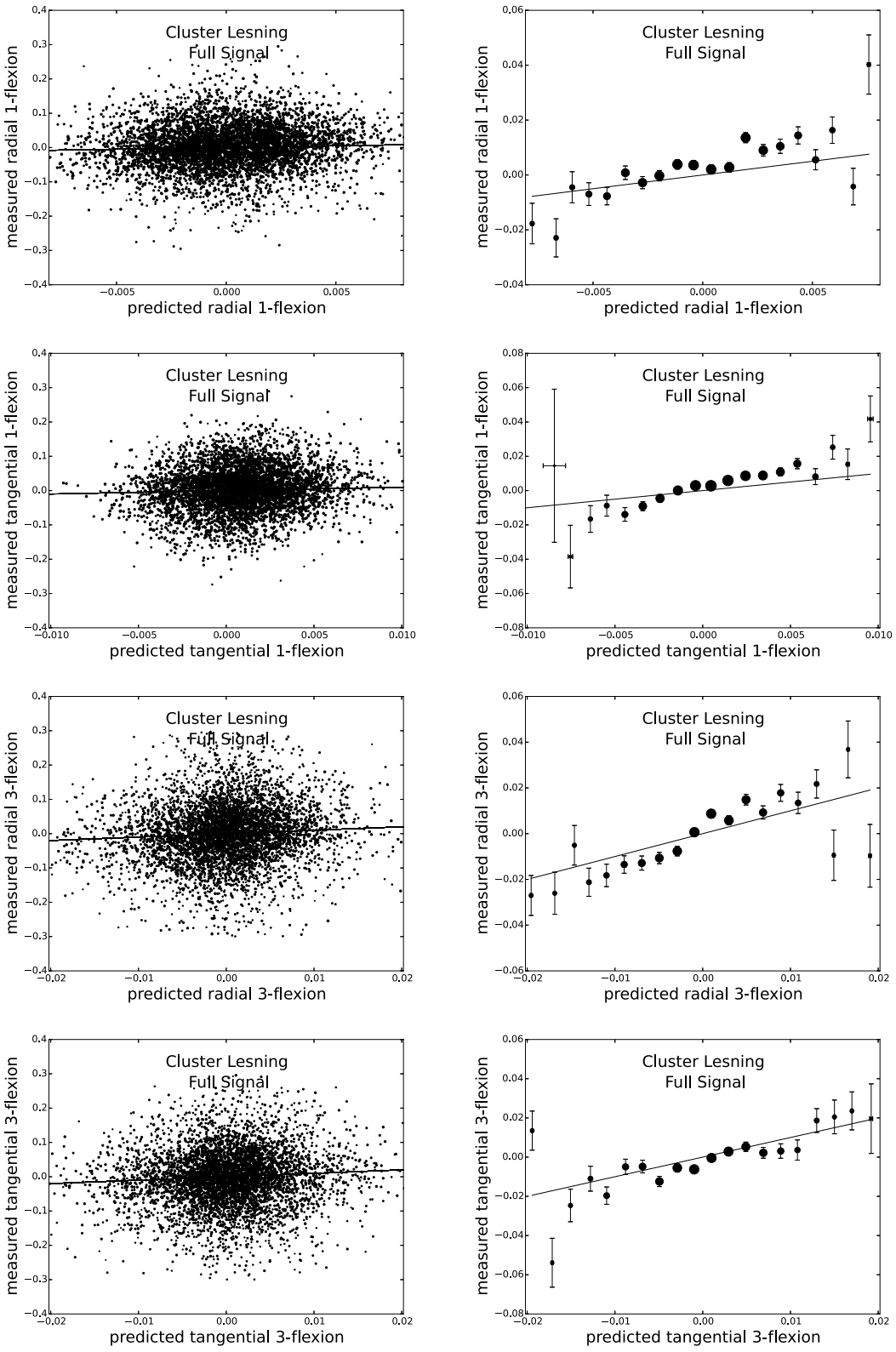

Figure 3-16 Relationship between measured and predicted flexions for background source galaxies, regardless if a suitable lensing cluster member galaxy is found its vicinity. Predicted flexions include the effects of gravitational lensing by the cluster, shear-flexion mixing, atmospheric dilution, and telescope aberrations. There are 5002 total cluster flexion measurements for these 1345 source objects, however most objects are sufficiently far from the cluster center that the predicted gravitational lensing is effectively zero. Left: All measurements plotted. Error bars are excluded so as to better show the scatter between points. Right: Objects have been binned by their predicted flexions and the measurements have been averaged within each bin. The size of each point is proportional the inverse error of the weighted average. For both binned and unbinned plots, the line shows the ideal 1-1 relation, and not a best fit.

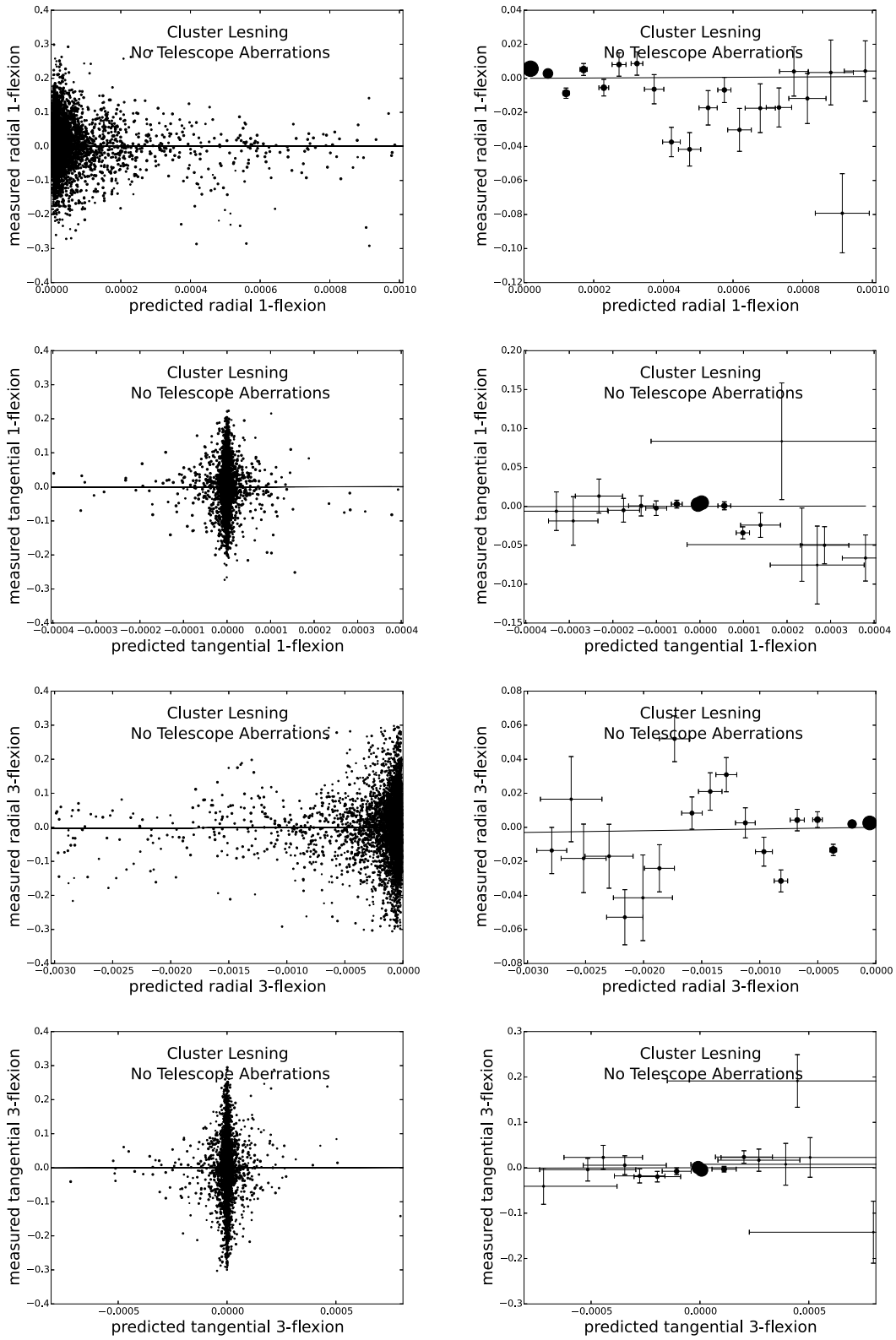

Figure 3-17 Relationship between the measured and de-aberrated flexion for all background source galaxies, regardless if a suitable lensing galaxy is found in its vicinity. The de-aberrated flexion is the difference between the total measured flexion and the predicted aberrational component. Left: All measurements plotted. Error bars are excluded so as to better show the scatter between points. Right: Objects have been binned by their predicted de-aberrated flexions and the measurements have been averaged within each bin. The size of each point is proportional the inverse error of the weighted average. The line shows the ideal 1-1 relation, and not a best fit.

Velander et al. [65] do beat the shape noise in their study of galaxy-galaxy flexion in the COSMOS fields. With 216,873 background source galaxies with signal-to-noise greater than 10 and known photomometric redshifts, Velander et al. [65] are able to use their measured F-flexions to constrain galaxy density profiles, finding that, on average, the density profiles are consistent with an isothermal sphere. The G-flexions were sufficiently noisy to be consistent with 0 as well as gravitational lensing from by an isothermal sphere. However, even with their large sample of background source galaxies, they call for yet more data so that they can reduce the noise enough to explore trends with lensing galaxy redshift or mass.

This section details the lessons we learned with hindsight, so that others trying to measure lensing flexion might start with greater foreknowledge of the avoidable observational hurdles. We detail the two areas where we underestimated the extent of assailable obstacles, and which we caution others to consider more carefully in future studies: the first is requisite image depth, and the second is cluster member selection and photometric redshift determination.

3.6.1 Failure: insufficient signal to photon noise for flexion measurements

The gravitational flexion signal is approximately 1/10 as strong as the shear signal. Using the flexions and shears from an SIS lensing potential, given in equation 3.7, we find that $|F/\gamma| = \theta_{1/2}/\theta = (\theta_{1/2}/\theta_E) \times (\theta_E/\theta)$. As $\theta_{1/2}/\theta_E$ is approximately 1/2, at least for the galaxy-galaxy lensing systems in Abell 1689, we can expect that Flexion will be $1/10 - 1/30$ the magnitude of shear for systems $5 - 15$ Einstein rings from their sources. We'll use the optimistic value of 1/10.

Using the similarly simplified approximation that the signal-to-noise needed for a measurement scales as $\sqrt{N_{\rm photons}}$, in order to measure a gravitational flexion signal with similar confidence as our current measurement of the shear signal, we must image systems 100x more deeply. Alternately, we can accept that for an image in which we can measure shear in objects down to magnitude M_γ, we will only be able to measure

flexion in objects down to magnitude $M_\gamma - 5$.

We show in figures 3-18 and 3-19 our experimental results for how the flexion measurement degrades with magnitude in our 1.75 hour coadded r' image. Figure 3-18 shows the fraction of objects for which DoPHOT was able to fit a flexed elliptical-Gaussian model as compared to the number of objects for which it was able to fit at least an elliptical-Gaussian model. The drop off at bright magnitudes is caused by the increased resolution and apparent substructure in relatively nearby objects. In order to measure flexion in these objects, we would have to bin the data, switch to a flexed Sérsic model for the galaxy, or perhaps use low order shapelets to make the measurement. However these brightest objects are more often than not too nearby to be gravitationally lensed, and therefore their flexion is not interesting for lensing studies. Contrastingly, the dimmer objects ARE of interest for lensing studies. Unfortunately, the insufficient signal-to-noise in the data causes the drop off in flexion measurements at the dim magnitude end.

Figure 3-19 shows how the signal to reported error drops for flexion with fainter magnitudes. The signal-to-noise of the F-flexion measurement tends to be better than the signal-to-noise of the G-flexion measurement, despite trending with image magnitude in nearly the same way. This result is in agreement with Rowe et al. [56], who find that the dispersion estimators for the F- and G-flexions derived from shapelets analysis have similar power law slopes but different amplitudes when plotted against the log scale signal-to-noise of the objects in their simulation, (see figure 10 of that work).

The signal-to-noise flattens at both the bright and dim ends of the magnitude spectrum. The flattening at the bright end of the spectrum is caused by the high resolution of the galaxies and the galaxies' non-conformance to a Gaussian shape. The flexion errors will increase as the well-resolved galaxy becomes more and more disparate from the model. The raised tail in the flexion signal-to-noises at the dim end of the spectrum is an artifact of the exclusion of objects for which no flexion measurement is obtainable. Were we to include those galaxies for which there is no convergence for the flexion parameters, and set the errors for those flexion measure-

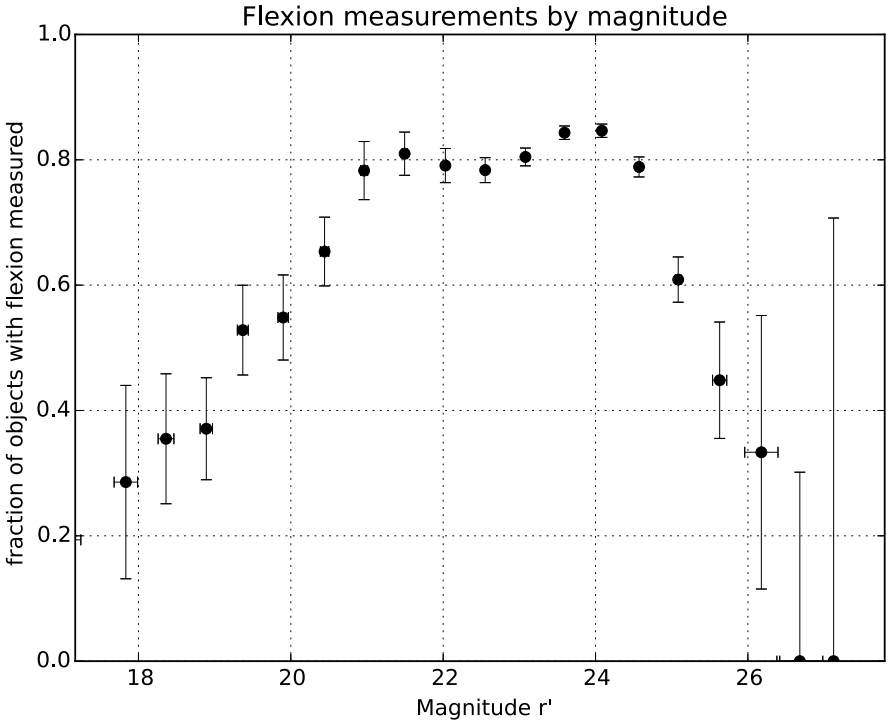

Figure 3-18 Fraction of objects, by magnitude, for which DoPHOT can fit flexion parameters in the deepest r' image. This fraction is obtained by dividing the number of objects for which a sheared and flexed galaxy model it fitted, by the total number of objects for which a sheared galaxy model could be fitted, regardless of flexion. The drop-off at bright magnitude is caused by increased object resolution, while the drop off at faint magnitude is caused by insufficient signal-to-noise with which to fit an eleven parameter flexed galaxy model. Shown errors reflect the number of objects in each magnitude bin, with fewer objects producing poorer statistics.

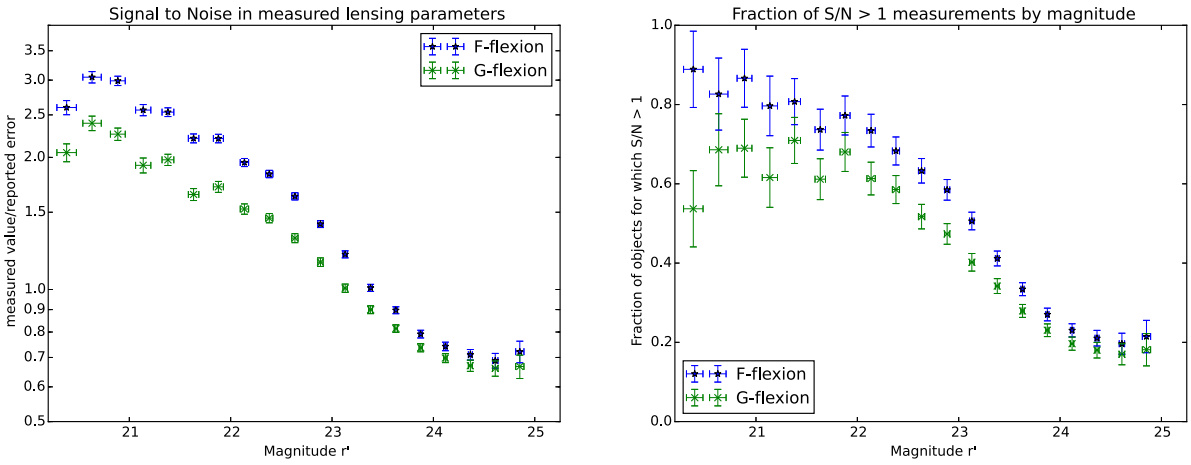

Figure 3-19 Left: Fraction of the fitted dimensionless flexoin signal to the reported error in that signal as a function of object magnitude. Values have been binned by magnitude and averaged. Right: Fraction of objects fitted with signal-to-noise greater than 1.

ments very large, the signal-to-noise in the measurement would continue to drop as one would expect.

It is clear from these figures that increased depth on our fields would yield many more high signal-to-noise flexion measurements with which to perform our analysis. In the 1.75 hour coadded r' image, DoPHOT can fit 80% of galaxy objects between magnitudes of 21 and 24 to the eleven parameter flexion model. At the bright end of this range, we can obtain F- and G-flexion measurements with signal-to-noise of at least 1 for 80% (F-flexion) and 60% (G-flexion) of the objects. At the faint end of this spectrum, the percentage of objects for which we can obtain significant flexions is closer to 25% and 20%. To extend the range of well-fitted objects at the faint magnitude end, (which is more interesting for gravitational lensing studies than the bright magnitude end), we must push deeper. In order to obtain the same percentage of high signal-to-noise flexion measurements in the set of 25th magnitude objects as we currently do for the 24th magnitude objects, we would need to increase our exposure times to 8.5 hours per image. For 26th magnitude, 46.6 hour images are required.

While we did image Abell 1689 as deeply as our allotted telescope time and weather allowed, our images were nowhere near deep enough to get adequate signal on enough source galaxies in order to make a galaxy-galaxy flexion measurement. After removing all small galaxies for which the gravitational flexion effect is minimal and the atmospheric smearing washes out any signal that is present, and all galaxies whose color and magnitude indicate a potential association with the cluster, we were left with only 1345 source galaxies. Of these, only 50 were found to be in the vicinity of one, and only one, lensing galaxy. This is not enough data points with which to beat down the shape noise discussed in the previous subsection.

Considering this signal-to-noise analysis, one might be inclined to believe that we should not have excluded the lowest quality images from coaddition, but rather pushed for as much depth as possible. However, increasing the effective size of the point spread function by including low quality images in the coaddition will dilute the measurable flexion signal, leaving our ultimate signal smaller. Our only option is

to go deeper using images of comparable quality.

3.6.2 Failure: imprecise color selection of cluster members and photometric redshifting

In §3.3.6 we detailed our color-magnitude selection criteria for Abell 1689. In order to obtain relatively clean samples of cluster members and background source galaxies, we establish a large exclusion region around the cluster line in color-magnitude space. While the spatial distributions of the selected cluster members and background source galaxies suggest that this selection method can produce relatively uncorrupted catalogs of both cluster members and background galaxies, it does so at the expense of discarding many potentially useful objects.

Differentiating cluster members and source galaxies is not a new problem. Color-magnitude selection of cluster members is not foolproof; in their study of the cluster elliptical red sequence, Gladders et al. [23] refine their red sequence galaxy selection based on visually inspected morphology. Houghton et al. [30] analyze the color--magnitude relation for Abell 1689, and, even only using objects with magnitudes measured better than 0.1, find many cluster members that deviate into the blue. In their weak lensing analysis of halo truncation in cluster galaxies using the Canada France Hawaii Telescope's 12K camera, Limousin et al. [41] are able to determine redshifts for source galaxies using photometry in the the B, V and I filters. They use HYPERZ with an additional prior based on the luminosity function to constrain the degeneracies in the redshift probability distribution. However, they find that their determined redshifts are only reliable for objects above redshift 0.5. In particular they note that the ellipticals in their $z \sim 0.2$ clusters "are assigned a Bayesian redshift between 0.35 and 0.45, systematically overestimating their redshift." They therefore use color-magnitude selection to determine which objects are cluster members. Limousin et al. [42], analyzing Abell 1689, use the same Bayesian redshift method to determine the redshift of their $z > 0.5$ objects. However, in order to select cluster members, they require additional data. They compute for each galaxy the fraction of the prob-

ability distribution which is beyond some redshift z, and then use spectroscopy from 239 galaxies [17] in Abell 1689 to find the redshift and corresponding probability that successfully distinguishes the cluster members from the background source galaxies.

Originally, we had hoped to use photometric redshifts to further refine our cluster member and background source galaxy selections beyond simple color-magnitude selection. We initially attempted to determine redshift for our objects using the Bayesian Photometric Redshift Code BPZ [6]. In so doing, we rediscovered the systematic overestimation of the redshift of $z \sim 0.2$ objects noted in Limousin et al. [41]. We later switched to the redshift software, EAZY [12].[37] While we were not expecting great precision in redshift determination from three filters, we did not properly anticipate the degeneracy in redshifts that we encountered. Ultimately we ignored the redshift information returned by either software package and chose to rely on color-magnitude selection alone, but not before conducting a thorough analysis as to why the redshift solutions fail so completely on our data.

In order to rule out user error, and any problems that might be introduced by inaccuracies or inconsistencies in DoPHOT's photometry or our calibrations, we conducted tests on the COSMOS photometry provided in Skelton et al. [60]. In that work, the authors compile multi-wavelength observations for five fields, spanning 147 distinct imaging sets, and determine photometric redshifts for the objects therein. They generously make both the photometry, spectroscopy, and their derived photometric redshifts available to the public through the VizieR catalog access tool.

Figure 3-20 compares the reported photometric redshifts from Skelton et al. [60], (determined from 44 filters using EAZY), to those derived using the same software, but using only the three Solan filters corresponding to our Abell 1689 observations, (g', r', and i'). While the photometric redshifts derived from 3 filters follows the 44 filter photometric redshift on average, the determinations for individual galaxies are quite scattered, especially for galaxies near redshift of 1.5.

[37] We switched because we were convinced that we must be using the software incorrectly to get such inaccurate results for our cluster galaxies. Had we carefully read Limousin et al.'s 2007 work before attempting redshift measurements, we might have known that this redshift overestimation was expected.

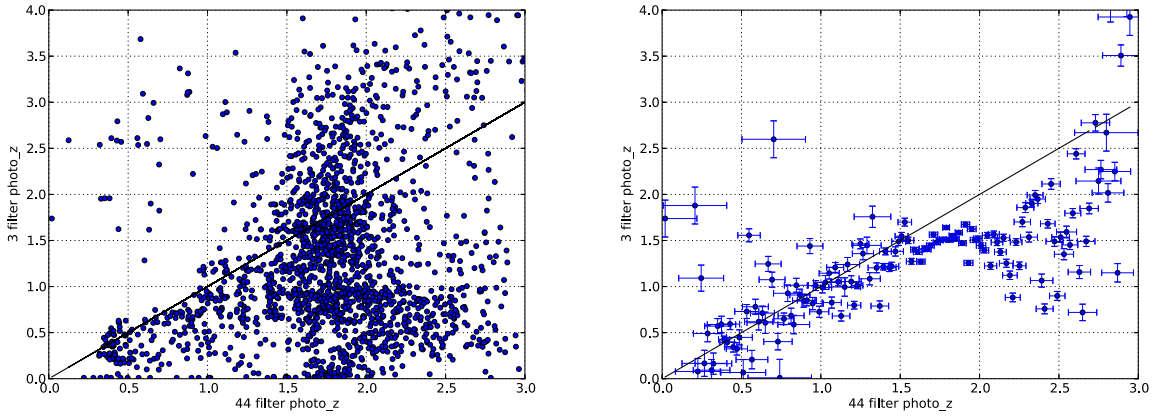

Figure 3-20 Comparison of photometric redshifts for the COSMOS field derived by Skelton et al. [60] using 44 filters, with those derived using only three Sloan filters. The left figure displays a random subset of 1014 of the 33881 objects with provided photometry. The right figure displays binned averages of the redshifts determined with three filters, in increments of 0.02 of the photometric redshift determined with 44 filters.

Therefore, even though there is information in the photometric redshift solutions obtained using the Sloan g', r', and i' filters, it is not reliable on a galaxy-by-galaxy basis, which is needed for the galaxy-galaxy lensing study we attempted here. As the transmission functions of the Megacam g', i', r' filters are very similar to the Sloan filters', we determined that photometric redshifts would not be useful for our analyses, either as a primary means of discriminating between cluster members and background source galaxies, or as a refinement of color-magnitude selection. Others attempting this measurement in the future would do well to obtain wide field spectroscopy and follow the methods of Limousin et al. [42], or obtain photometry in the infrared to complement the g', i', r' photometry.

3.7 The best cases

In an attempt to learn something about galaxy-galaxy flexion in clusters from our data, even if we lack the numbers to make a statistical argument, we isolate 20 sources from which we would expect to see the strongest evidence for galaxy-galaxy flexion and examine them more closely.

3.7.1 The selection metric

To select the best candidates for observing galaxy-galaxy lensing flexion, we establish the following dimensionless metric:

$$(\theta_{1/2}\theta_E)/\theta^2, \tag{3.11}$$

where $\theta_{1/2}$ is the unaberrated half light radius of the galaxy, θ_E is the lensing galaxy's Einstein ring radius, and θ is the separation of the lens from the source. Objects with large metric values are the largest sources galaxies, at the smallest separation from their lensing galaxies as measured in Einstein rings. They therefore should be the systems that are the most obviously flexed towards their lens galaxies.

We visually inspect those systems which are chosen as 'best' by this metric, and discard all objects for which

1. the background source galaxy is, in fact, most likely a cluster member or foreground galaxy,[38]

2. the background galaxy is a duplicate of a prior object, but due to its extendedness the object is fitted to have sufficiently different center coordinates in different frames and is thus treated as two objects,[39]

3. the background source galaxy is actually comprised of two objects, and was improperly modeled by DoPHOT as one object,[40] or

4. multiple lensing galaxies influence the background source galaxy, and therefore any galaxy-galaxy flexion prediction assuming one lensing galaxy only is likely inaccurate.[41]

Ideally, the selection criteria for background source galaxies should reject all cluster members and foreground galaxies, however, as discussed in the previous section, object selection is imperfect. Similarly, background source galaxies with multiple lenses

[38]Objects 11 & 22.
[39]Object 12 is a duplicate of object 8.
[40]Object 14.
[41]Objects 15, 17, 23, 24, & 28

should have been discarded from further analysis by our pairing algorithm. However, in the cases where the second cluster member galaxy is not identified by color-magnitude selection, the multiply-lensed background source galaxy slips through our filter.

Images for the top 20 selected lensing systems appear in figures 3-22 and 3-23. For each system, the top image shows the cluster member lensing galaxy and the lensed background source galaxy. We have drawn a $3\theta_E$ radius circle around each lensing galaxy as a reference for scale. The bottom three images for each object depict the identified background source galaxy (left), DoPHOT's best fitted model for the same (center), and the residual image after the model has been subtracted (right). The measured shears, g, and flexions, F & G, for these objects in the best two r' and i' coadded images are presented in table 3.14. These shears and flexions are decomposed into components which are radially and tangentially oriented with respect to the lensing galaxy. The table also contains the predicted flexions for each of the observations as well as the breakdown of the contribution of aberrational and the de-aberrated flexions for each prediction. Flexion models do not converge for every object in every filter, therefore flexion measurements are missing for some of the objects.

These top 20 galaxies, though selected because they are likely to have the largest apparent gravitational flexions, do not visually appear to be arced around their lensing galaxy. Furthermore, the measured radial components of the F- and G-flexions are, to within the error, as likely as not to point in the direction prefered by gravitational lensing.

3.7.2 Measurements for the top 20 objects are reliable

In order to establish that we are making valid measurements of the flexions in these top 20 objects, we analyze the measurements' reproducibility. The two deepest r' images have similar aberrations, as do the two deepest i' images. All of the r' exposures used to create the final coadded r' images were drawn from data collected on a single 3 night observing run. As these images were selected using the quality factor from equation

3.1 in §3.3.3, and not chosen based on aberration asymmetries, it follows that the two coadded r' images should have similar aberrations. It is perhaps more surprising that the two coadded i' images should have similar aberrations, as the individual exposures for each of these images were taken more than 2 years apart. However, the aberrations are very similar in both of the i' coadded images, and therefore objects detected in both coadded images in r' or both coadded images in i' should have similar flexion measurements in each.

To assess the reproducibility of the measurements, we take the differences between flexion measurements for objects observed in both coadded images of either the r' or i' filters, divide those differences by their expected errors, as computed from the reported flexion errors in the individual measurements, and compute the standard deviation in the resulting deviations. We report our findings in table 3.9. As the spread in the variances is less than one for both components of the F and G-flexions, the flexion measurements are reproducible to within the reported errors. Moreover, the reported errors are likely too pessimistic, and should be smaller.

3.7.3 Just not caused by gravitational lensing

Having established that (a) each of the top 20 objects are likely behind the cluster, as determined from the initial color selection and subsequent visual analysis of morphology, (b) each of these objects *should* be significantly lensed by a nearby cluster member galaxy, and (c) that the flexion measurements for these objects are real and reproducible, we plot in figure 3-21 the de-aberrated flexions against the predicted de-aberrated flexions for the top 20 objects only. As with the full set of galaxy-galaxy lensed objects, once we remove the effect of aberrations all that remains in the data are noise. Any gravitational flexion is buried beneath that shape noise, even for the strongest lensed objects.

We note again, as for figure 3-6, the trend towards overly large positive radial F-flexions. While we speculate that this may be a result of imperfectly removed lensing galaxies, the noise makes this hypothesis difficult to confirm.

To check if the shape noise in our top 20 source galaxies is anomalous, we use a K-S

object	filter	ΔF_r	ΔF_t	ΔG_r	ΔG_t
4	i	0.94	0.46	−0.42	0.79
7	i	−0.80	0.82	0.11	0.60
10	i	0.82	1.11	0.81	−0.15
17	i	0.15	−0.16	0.83	−1.10
21	i	0.25	1.08	−0.96	2.26
22	i	−0.03	−0.72	−0.90	1.69
26	i	−0.11	−0.57	0.40	0.66
27	i	−1.02	−0.14	−0.98	0.50
6	r	0.55	0.51	−0.66	0.17
7	r	−0.06	−0.10	−0.57	−0.62
8	r	1.36	0.35	1.25	−0.64
10	r	0.21	−0.25	0.65	1.16
13	r	0.34	−0.34	0.33	−0.81
17	r	−0.92	−0.51	−0.41	−0.66
20	r	1.03	0.25	1.28	−0.45
21	r	−1.03	0.04	−1.26	0.26
22	r	−1.50	0.79	0.11	−0.81
25	r	0.64	0.49	−0.10	−0.25
27	r	−0.14	0.14	0.47	1.57
avg.		0.04	0.17	0.00	0.22
dev.		0.79	0.55	0.78	0.96

Table 3.9 Deviations between measured flexion between two images in the same filter; $(\text{flexion}_1 - \text{flexion}_2)/\sqrt{\sigma_1^2 + \sigma_2^2}$, for measurement error σ_i in image_i. The two coadded images in i' and the best two coadded images in r' each have similar aberrations. Therefore, the difference between the measured flexions of a given object in either two images should be zero to within the error. The distribution of the deviations indicates that DoPHOT's reported errors are, if anything, too pessimistic, and should be smaller.

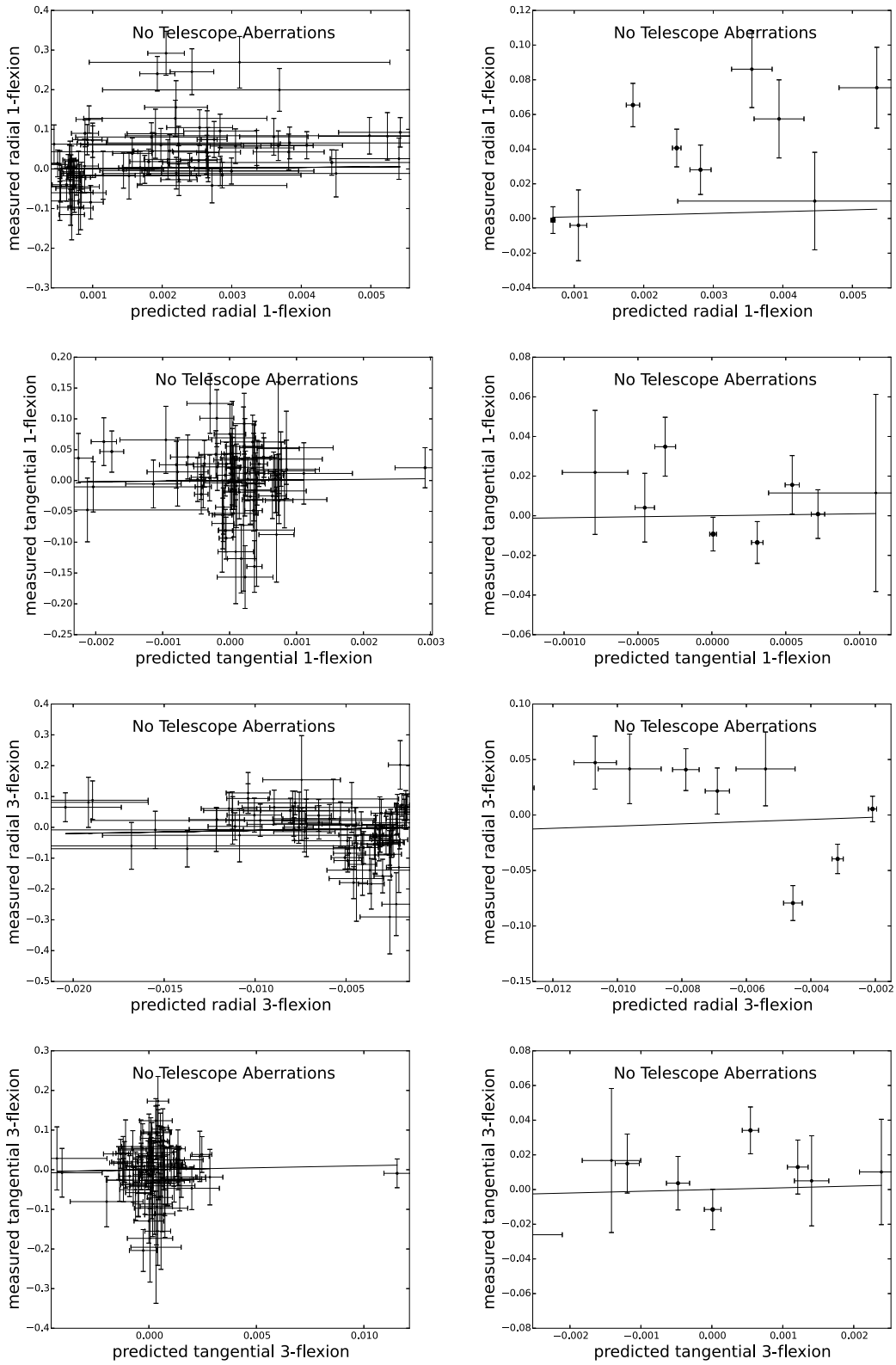

Figure 3-21 Relationship between the de-aberrated measured and predicted flexions for the top 20 source objects as determined by predicted amount of galaxy-galaxy flexion. The de-aberrated flexion is the difference between the total measured flexion and the predicted aberrational component, and represents what we would observe had the telescope imparted no asymmetric aberrations onto the image. Left: All measurements plotted. Right: Objects have been binned by their predicted de-aberrated flexions and the measured de-aberrated flexions have been averaged within each bin. The size of each point is proportional the inverse error of the weighted average. The line shows the ideal 1-1 relation, and not a best fit.

test to compare the inherent flexions in these 20 objects to the distribution of inherent flexions in the complete set of 1345 background source galaxies. We naturally remove any gravitational, aberrational, smearing or shear-flexion mixing effects from both sets of data so that we are comparing the inherent flexion values in each set. There is very little evidence that the flexoins measured in the selected top 20 background source galaxies and those measured in the full subset of background source galaxies are drawn from different distributions. The only potential evidence against the null hypothesis is a K-S statistic of 0.272 and corresponding p-value of 0.104 for the radial component of F-flexion. The full results of the K-S tests appear in table 3.10.

K-S Test Results: Top 20 Galaxy-Galaxy Lensed Sources v. All Lensed Sources			
		K-S Statistic	p-value
Ellipticity	radial	0.144	0.828
	tangential	0.144	0.824
Intrinsic F-Flexion	radial	0.272	0.104
	tangential	0.099	0.990
Intrinsic G-Flexion	radial	0.168	0.626
	tangential	0.242	0.192

Table 3.10 Results from 2 sample K-S test performed to compare the intrinsic ellipticities and flexions of the 20 most gravitationally flexed objects to that of the larger population of sources. The results confirm the null hypothesis that the intrinsic shapes of the sample of 20 most gravitationally lensed objects comes from the same distribution as the total source population.

3.7.4 Top 10 from color-magnitude ambiguous region

For the sake of ensuring that we did not throw away the best lensing candidates with our stringent selection criteria for the background source galaxies, we additionally review the top 10 galaxy-galaxy lensed objects from the set of galaxies previously excluded from lensing analysis. These are the galaxies which were not detected in all three filters and/or fell into the ambiguous region of color-magnitude space. As we did with the population of the more rigorously selected background source galaxies, we pair these objects to cluster member lensing galaxies, compute the predicted flexion and order the galaxies by expected galaxy-galaxy flexion as determined by

the dimensionless metric from §3.7.1. We then exclude those systems for which the predicted or measured gravitational flexion is unphysical, the flexion prediction or measurement is corrupted, or the lensed galaxy shows obvious morphology indicating that it is in fact a cluster member or foreground galaxy. The top 10 objects that survive these cuts are shown in figure 3-24.

For each system in figure 3-24, the top image shows the lensing galaxy and the background lensed source galaxy. We have drawn a $3\theta_E$ radius circle around each lensing galaxy as a reference for scale. The bottom three images for each object depict the identified background source galaxy (left), DoPHOT's best fitted model for the same (center), and the residual image after the model has been subtracted (right). The measured shears, g, and flexions, F & G, for these objects in the best two r' and i' coadded images are presented in table 3.15, along with the flexion predictions.

It is clear from both the images in figure 3-24 and the comparison the the predicted and measured flexions in table 3.15, that even though these galaxies are the ones for which we would expect to see the most galaxy-galaxy lensing flexion, gravitational flexion is not found to be present.

3.8 Individual flexion measurements in Abell 1689

Goldberg & Leonard [25], Okura et al. [52], Cain et al. [15], Leonard & King [38] all use flexion measurements in Abell 1689 to map substructure on top of a cluster potential preconstrained by strong lensing, weak lensing shear, or both. Here we sought to use flexion measurements alone to find an underlying trend in halo profiles. While we would have liked to make a statistical measurement showing galaxy-galaxy lensing flexion (or cluster lensing flexion) following a predicted trend, we were thwarted from doing so by inherent galaxy shape noise and the small signal from cluster flexion. However, just because we could not establish an underlying trend in the potentials does not mean we cannot measure flexion in individual galaxies at least as well as previous measurements.

In order to facilitate the comparison of the flexions found here with those in other

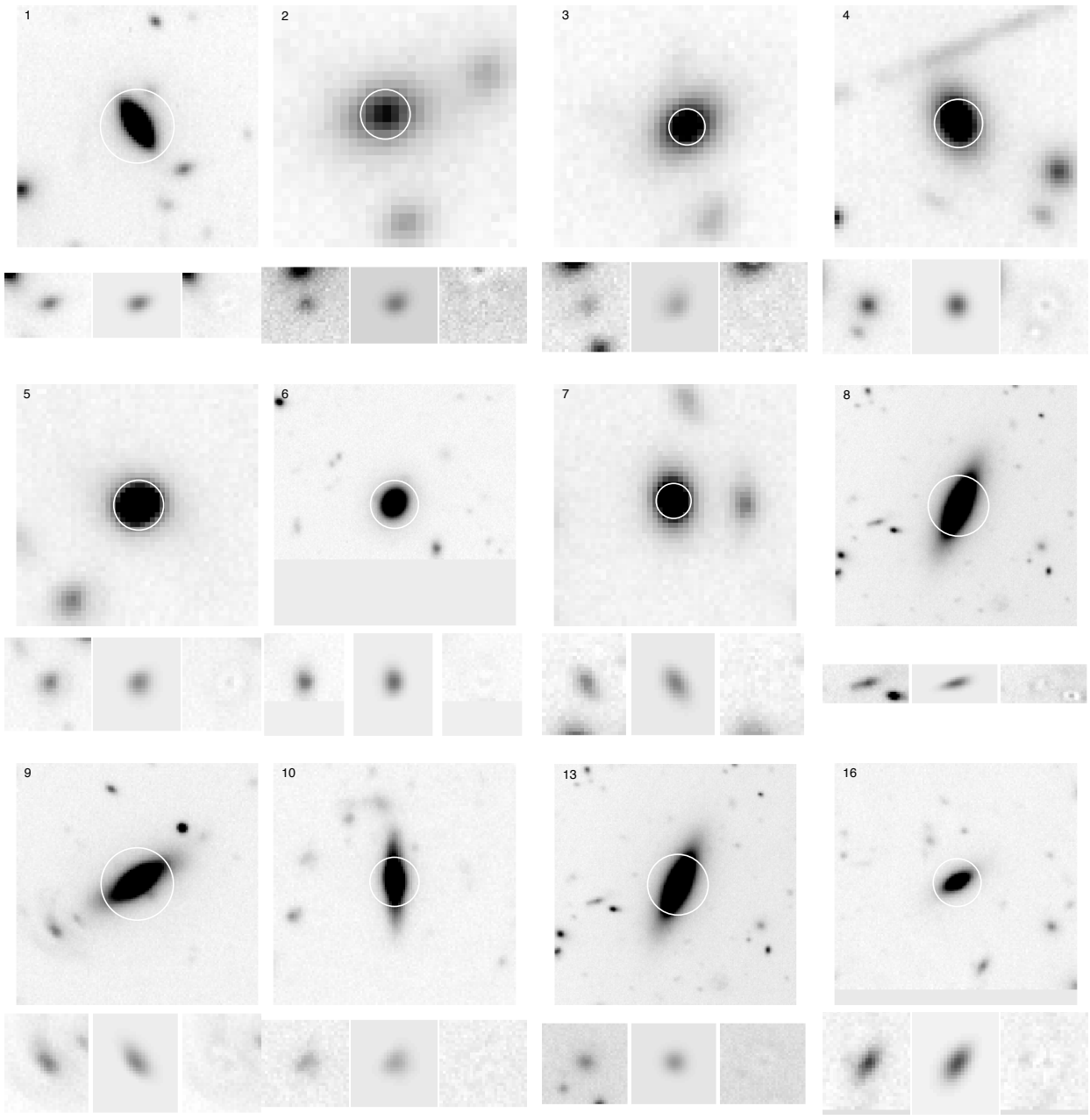

Figure 3-22 Image 1 of 2 of the pairs of background source galaxies and cluster member galaxy lenses for the systems for which we expect to see the greatest unitless gravitational flexion. White rings around lensing galaxies have a radius of $3\theta_E$. Subimages show the background source galaxy, DoPHOT's best fitted model, and the residual. Objects are ordered from most expected galaxy-galaxy lensing flexion (top left) to least (bottom right), with numbers corresponding to those in table 3.14.

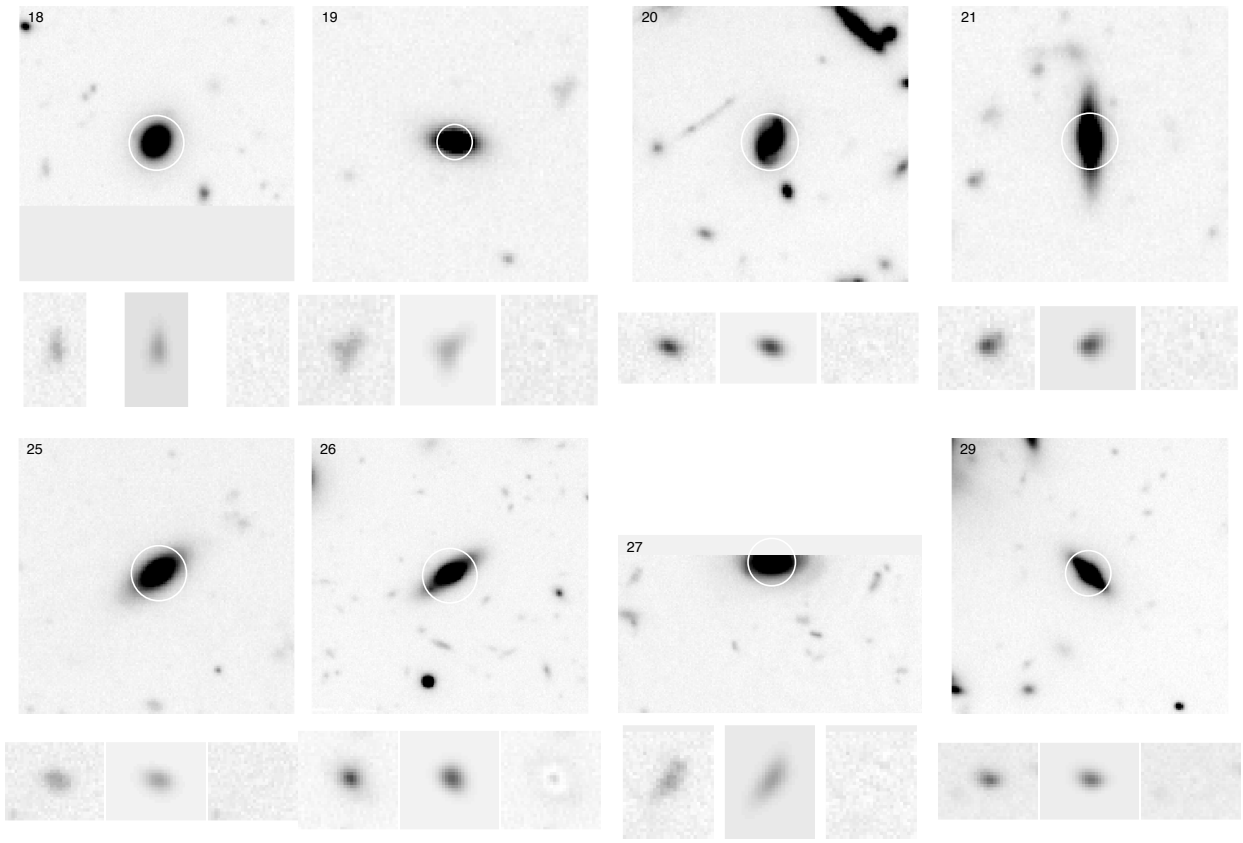

Figure 3-23 Image 2 of 2 of the pairs of background source galaxies and cluster member galaxy lenses for the systems for which we expect to see the greatest unitless gravitational flexion. White rings around lensing galaxies have a radius of $3\theta_E$. Subimages show the background source galaxy, DoPHOT's best fitted model, and the residual. Objects are ordered from most expected galaxy-galaxy lensing flexion (top left) to least (bottom right), continuing from image 3-22, with numbers corresponding to those in table 3.14.

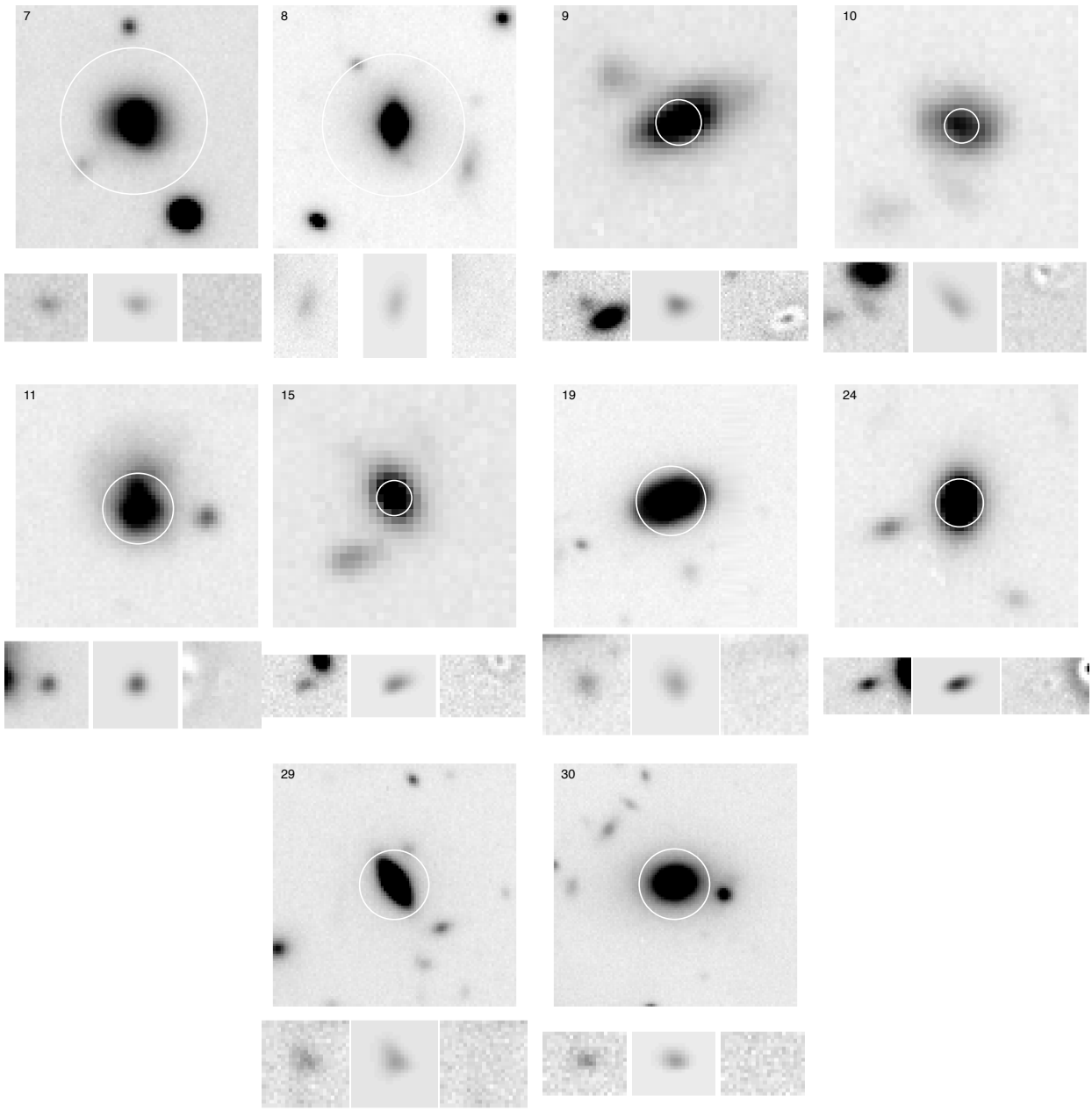

Figure 3-24 Top 10 pairs of background source galaxies and cluster member galaxy lenses for the systems previously rejected by color-magnitude selection. Background source galaxies in this set need not have been detected in all three filters, and may have been drawn from the 'ambiguous' region of color-magnitude space, where color alone is insufficient to determine the object's status as a cluster member or background galaxy. White rings around lensing galaxies have a radius of $3\theta_E$. Subimages show the background source galaxy, DoPHOT's best fitted model, and the residual. Objects are ordered from most expected galaxy-galaxy lensing flexion (top left) to least (bottom right), with numbers corresponding to those in table 3.15.

works, we report our measured and PSF corrected flexions for a selection of background source galaxies in tables 3.16, 3.17, and 3.18. The PSF corrected flexion measurements are the flexion values we would expect to measure were we observing from a completely unaberrated space-based telescope, and thus can be easily compared to measurements made using other telescopes and instruments.

Tables 3.16 and 3.17 contain flexion (and shear) values for those background source galaxies with the smallest reported noise in the flexion measurement.[42] Table 3.16 contains flexion measurements for background galaxies drawn from throughout the field, while table 3.17 contains measurements for galaxies which lie in the $480'' \times 360''$ region containing the cluster center. This inner three chip region is not much larger than the HST field, and therefore galaxies selected from this inner region are more likely to have prior or future flexion measurements. The region is depicted in figure 3-25, with circles around those galaxies with flexion measurements reported in the tables.

We supplement our quantitatively motivated object selections with qualitatively selected likely-lensed galaxies from the inner cluster region. Unlike the lowest noise objects, which are selected based on strict numerical criteria, these galaxies are hand-picked on a completely subjective basis; these are the galaxies that look like they are gravitationally flexed, with classic arc-like shapes. Measured flexion values for these hand-picked gravitationally flexed galaxies are reported in table 3.18. The positions of these galaxies are also shown in figure 3-25. Some, though by no means all, of these galaxies' shapes appear to encircle the cluster center. So that the measurement is less corrupted by the PSF, we filter our selection of hand-picked objects to contain only those galaxies with half light radii greater than $1.5\times$ the PSF half light radius. We additionally only consider those galaxies with r' magnitude's dimmer than 22, as brighter objects are more likely to be cluster members, and therefore inherently

[42]For consideration in this low noise sample, galaxies must have measured F- and G-flexions which are larger than the reported errors in those measurements. This criterion constrains the selection of galaxies to those with non-negligible flexion. We considered sorting the objects by highest signal to noise ratios instead of lowest overall noise in the measurement, but that standard preferentially selected objects with very large flexions that are more likely attributable to complex inherent galaxy structure than gravitational lensing.

flexed rather than gravitationally flexed.

Zoomed in images from selections of the lowest noise objects in tables 3.16 and 3.17, and the hand-picked gravitationally flexed objects in table 3.18 are shown in figures 3-26, 3-27, and 3-28. The best fit DoPHOT models and the residuals images (image minus model) are also shown in these figures. In order to show detail in the galaxy and model shapes, we colorize these images, with lower intensities shown as shades of blue, and higher intensities shown as green and then red. These flexed galaxy images are well-imitated by their respective models.

Last, in addition to presenting flexion measurements for our own lowest noise objects, in table 3.19 we report our flexion measurements for the objects analyzed in Cain et al. [15]. So that we can detect more objects overlapping with the HST measurements in that work, we analyze the inner region of our field more deeply than we do for our primary analysis of galaxy-galaxy flexion, allowing DoPHOT to detect and fit models to objects down closer to the nosie floor in the deepest r' image.[43] We only report on those objects in table 3 of Cain et al. [15] that are bright and well-resolved enough to be detected in our ground based images, and are additionally larger than 1.5× the PSF in the ground based images. Both the measured flexions and the PSF corrected flexions are provided. Unfortunately, even for these object which can be resolved from the ground, our inferred de-aberrated and atmospherically corrected flexions are still too noisy to draw a definitive relation with the flexion values reported in Cain et al. [15]. We therefore do not include a plot comparing our PSF corrected flexion values to those reported in Cain et al. [15].[44]

[43]Recall, we choose not to detect objects down to the noise floor in the main analysis of galaxy-galaxy lensing flexion as (1) the number of spurious or high noise objects entering our sample would be high, (2) we would not be able to get multi-filter photometry for the deepest detected objects in the best r' image, and (3) false objects found in the residuals of the brightest stars and galaxies can corrupt the photometry of those objects. Since we are using this deeper analysis to measure the flexion in objects selected by Cain et al. [15] or those selected visually, false detections do not pose a problem. Moreover, we are not using the photometry for the bright objects in this analysis, so corruption to photometric measurements on the brightest objects is not a concern.

[44]The PSF corrected shear values do vary linearly with slope 1 with those reported in Cain et al. [15]. However, shear is not the focus of this work.

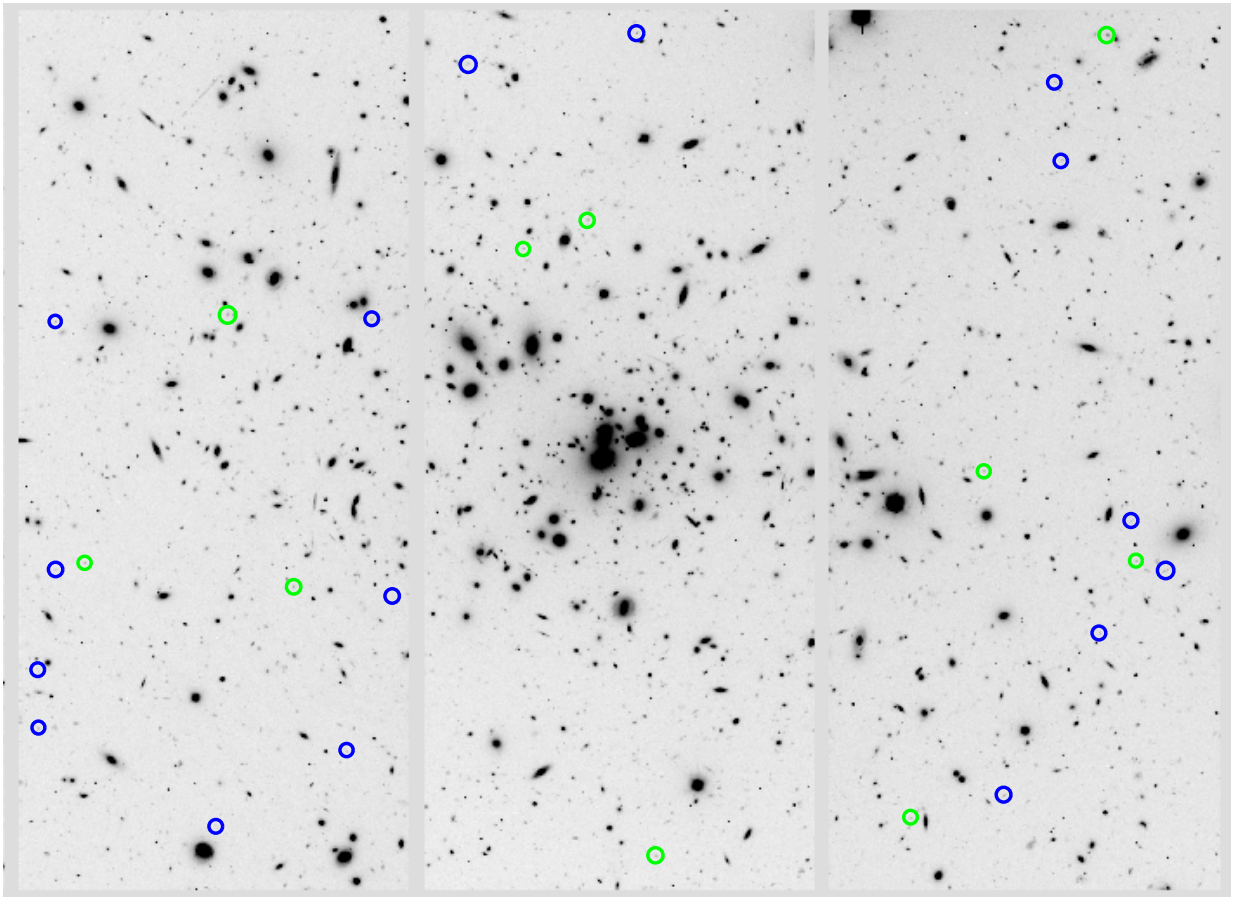

Figure 3-25 Abell 1689: 480″ × 380″ image in r' of the three chips containing the cluster center. The image is oriented with RA up and DEC increasing to the left, in agreement with Megacam's default orientation. The flexed background source galaxies with the lowest noise in measured flexion are circled in green. These objects correspond to those examined figure 3-27 and table 3.17. The sample of visually selected lensed background galaxies detailed in figure 3-28 and table 3.18 are circled in blue.

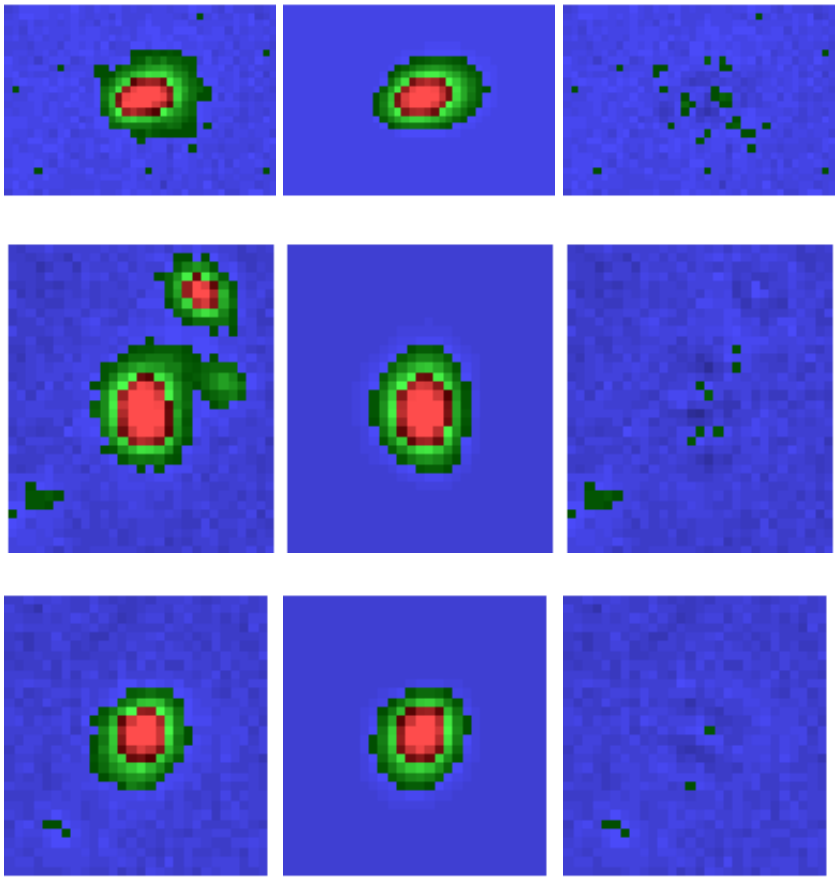

Figure 3-26 Background source galaxies with low noise in measured flexion. For each galaxy, the image (left), the best fit model (center), and the residual of the model subtracted from the image (right) are shown. The images are cropped to 11× the galaxy FWHM along each axis. Numerical values for the flexion measurements are given in table 3.16. The galaxies shown here correspond to numbers 5, 10, and 12 in the table. Colors vary with image intensity from blue to green to red, and color scales are consistent across each each galaxy triplet.

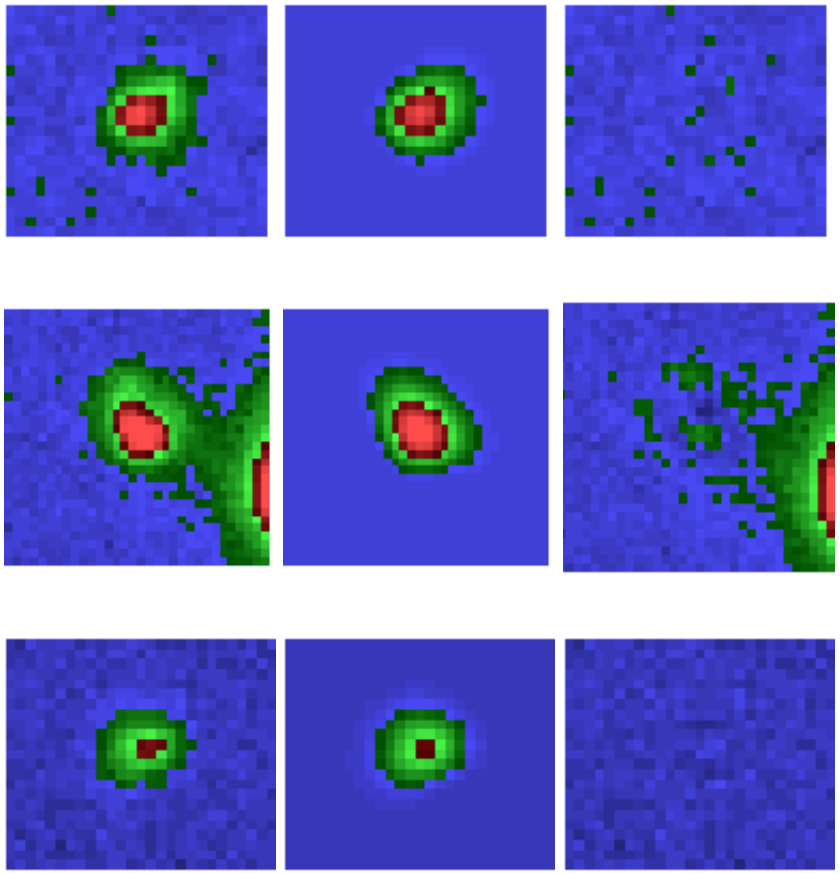

Figure 3-27 Background galaxies with lowest noise in measured flexion. Objects here are drawn from the three chips containing the cluster center, shown in figure 3-25. For each galaxy, the image (left), the best fit model (center), and the residual of the model subtracted from the image (right) are shown. he images are cropped to 11× the galaxy FWHM along each axis. Numerical values for the flexion measurements are given in table 3.17. Colors vary with image intensity from blue to green to red, and color scales are consistent across each each galaxy triplet.

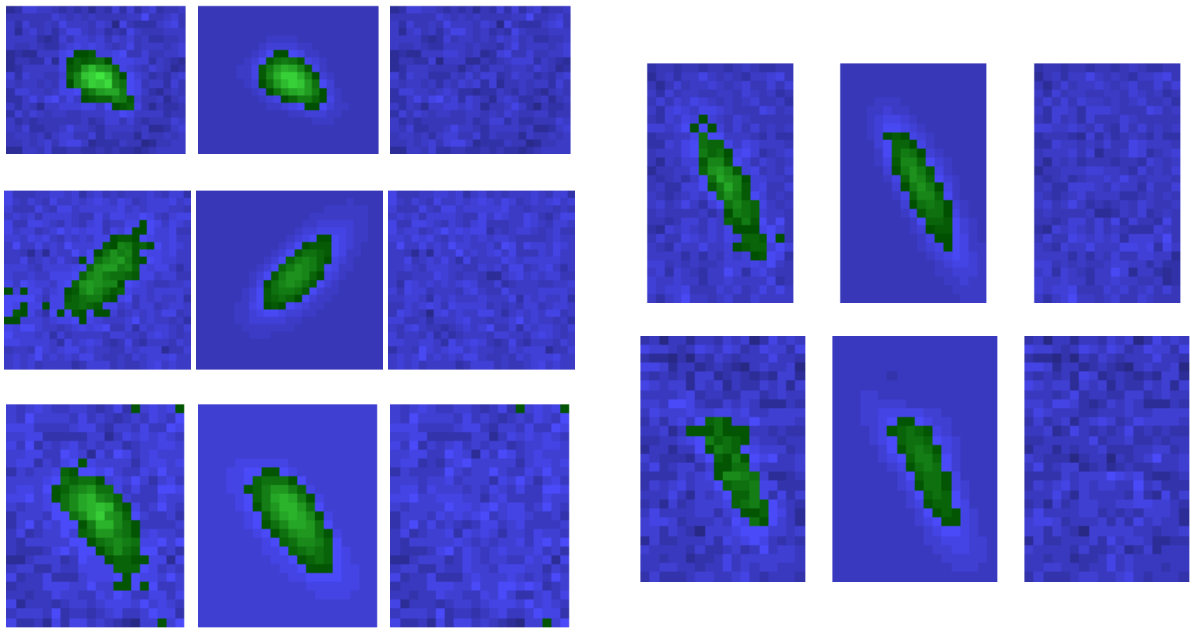

Figure 3-28 Hand-picked galaxies that appear to be gravitationally flexed. Objects here are drawn from the three chips containing the cluster center, shown in figure 3-25. There is no numerical justification for choosing to display flexions and models for these objects over any others; these are simply the objects which stand out visually as (1) lying behind the cluster (2) uncorrupted by light from neighboring objects and (3) very likely to be gravitationally flexed, with a classic arc-like shape. Visually selected objects are filtered by their half light radii, which must be greater greater than 1.5× the PSF half light radius. For each galaxy, the image (left), the best fit model (center), and the residual of the model subtracted from the image (right) are shown. The images are cropped to 11× the galaxy FWHM along each axis. Numerical values for the flexion measurements are given in table 3.18. Colors vary with image intensity from blue to green to red, and color scales are consistent across each each galaxy triplet.

3.9 Conclusion

We did not measure galaxy-galaxy lensing flexion in Abell 1689. Ultimately, our measurement was thwarted by the unforseen magnitude of inherent flexion shape noise at $z \sim 1$. We conclude with a recipe, constructed from hindsight, of how one might make this measurement in the future.

1. Start with deep measurements in good seeing conditions. Flexion measurements require 5 magnitudes more depth than shear measurements in order to overcome photon noise. 1.75 hours in r' with a coadded PSF of $0\farcs52$ (FWHM), is only sufficient to measure flexions with F-flexion signal to noise greater than 1 for $\sim 60\%$ of detected objects at magnitude 22, and $\sim 20\%$ of objects at magnitude 24. Only $\sim 50\%$ and $\sim 15\%$ of objects at magnitudes 22 and 24 have G-flexion measurements with signal to noise greater than 1. This is not enough data to beat down the intrinsic shape noise of 0.101 for F-flexion and 0.126 for G-flexion at $z \sim 1$.

2. Use IR imaging, such as is proposed for the Wide-Field InfraRed Survey Telescope [62]. The inherent shape noise of galaxies is smaller at redder wavelengths.

3. Use only objects with the largest half light radii. The shape distortions imposed on galaxy images by gravitational flexion scale linearly with the size of the source galaxy. Moreover, the seeing will degrade the measurable galaxy shapes as the cube of the ratio of the PSF and galaxy size. So a selection of comparatively large source galaxies is key to a low noise flexion measurement.

4. Use only the images with the best seeing, or alternately go to space where the PSF is smaller. While space based measurements will still require some PSF correction, this correction will be smaller for the largest galaxies, and will ultimately expand the range of galaxies usable for flexion analysis.

5. Either obtain spectroscopy for many objects in the field and use that spectroscopy to calibrate a photometric redshift solution, or supplement visual pho-

tometry with equally deep infrared in order to break the degeneracy in photometric redshift solutions determined by g', r', i' filters alone. When measuring the effect on individual background source galaxies by individual cluster member galaxies, accurately selecting the populations for each is critical. Color-magnitude selection, even using two colors, is sufficient for differentiating between source and cluster objects, but ultimately wasteful.

6. Use simple models to measure the flexion in images. Our eleven parameter model of an elliptical unlensed source galaxy plus lensing aberrations reproducibly measures flexion in low signal to noise galaxies in the crowded Abell 1689 field. While this simple model sometimes fails on more well-resolved galaxies, these objects are of minimal interest to lensing measurements anyway.

7. Measure image aberrations carefully and account for them in the image model. Most of the measurable 'flexion' in our images was in fact coma and trefoil, and a mixing of these telescope aberrations with galaxy ellipticity. Failure to properly compensate for these aberrations can easily lead to a perceived gravitational flexion measurement where there really is none.

Acknowledgements: This work was supported by the National Science Foundation through a Graduate Research Fellowship to Rebecca Sobel Levinson and through AST-0607601. This research has made use of the VizieR catalogue access tool, CDS, Strasbourg, France, and data products produced by the OIR Telescope Data Center, supported by the Smithsonian Astrophysical Observatory.

Bibliography

[1] Bacon, D. J., Amara, A., & Read, J. I. 2010, MNRAS, 409, 389

[2] Bacon, D. J., Goldberg, D. M., Rowe, B. T. P., & Taylor, A. N. 2006, MNRAS, 365, 414

[3] Baillard, A., Bertin, E., de Lapparent, V., et al. 2011, A&A, 532, A74

[4] Baillard, A., Bertin, E., Mellier, Y., et al. 2006, Astronomical Data Analysis Software and Systems XV, 351, 236

[5] Bartelmann, M., & Schneider, P. 2001, Phys. Rep., 340, 291

[6] Benítez, N. 2011, Astrophysics Source Code Library, 8011

[7] Bernstein, G. M., & Jarvis, M. 2002, AJ, 123, 583

[8] Bertin, E., & Arnouts, S. 1996, A&AS, 117, 393

[9] Bertin, E. 2006, Astronomical Data Analysis Software and Systems XV, 351, 112

[10] Bower, R. G., Lucey, J. R., & Ellis, R. S. 1992, MNRAS, 254, 589

[11] Bower, R. G., Lucey, J. R., & Ellis, R. S. 1992, MNRAS, 254, 601

[12] Brammer, G. B., van Dokkum, P. G., & Coppi, P. 2008, ApJ, 686, 1503

[13] Bridle, S., Balan, S. T., Bethge, M., et al. 2010, MNRAS, 405, 2044

[14] Broadhurst, T., Benítez, N., Coe, D., et al. 2005, ApJ, 621, 53

[15] Cain, B., Schechter, P. L., & Bautz, M. W. 2011, ApJ, 736, 43

[16] Clowe, D., & Schneider, P. 2001, A&A, 379, 384

[17] Czoske, O. 2004, Baryons in Dark Matter Halos

[18] Er, X., & Bartelmann, M. 2013, MNRAS, 428, 103

[19] Er, X., Mao, S., Xu, D., & Cao, Y. 2011, MNRAS, 417, 2197

[20] Er, X., & Schneider, P. 2011, A&A, 528, A52

[21] Er, X., Tereno, I., & Mao, S. 2012, MNRAS, 421, 1443

[22] Frye, B. L., Coe, D., Bowen, D. V., et al. 2007, ApJ, 665, 921

[23] Gladders, M. D., López-Cruz, O., Yee, H. K. C., & Kodama, T. 1998, ApJ, 501, 571

[24] Goldberg, D. M., & Bacon, D. J. 2005, ApJ, 619, 741

[25] Goldberg, D. M., & Leonard, A. 2007, ApJ, 660, 1003

[26] Goldberg, D. M., & Natarajan, P. 2002, ApJ, 564, 65

[27] Halkola, A., Seitz, S., & Pannella, M. 2007, ApJ, 656, 739

[28] Hawken, A. J., & Bridle, S. L. 2009, MNRAS, 400, 1132

[29] High, F. W., Hoekstra, H., Leethochawalit, N., et al. 2012, ApJ, 758, 68

[30] Houghton, R. C. W., Davies, R. L., Dalla Bontà, E., & Masters, R. 2012, MNRAS, 423, 256

[31] Houghton, R. C. W., Davies, R. L., Dalla Bonta, E., & Masters, R. 2013, VizieR Online Data Catalog, 742, 30256

[32] Irwin, J., & Shmakova, M. 2006, ApJ, 645, 17

[33] Jarvis, M., Schechter, P., & Jain, B. 2008, arXiv:0810.0027

[34] Kelly, P. L., von der Linden, A., Applegate, D. E., et al. 2014, MNRAS, 439, 28

[35] Kitching, T. D., Balan, S. T., Bridle, S., et al. 2012, MNRAS, 423, 3163

[36] Leonard, A., Deb, S., & Goldberg, D. M. 2006, American Astronomical Society Meeting Abstracts #207, 207, #206.09

[37] Leonard, A., Goldberg, D. M., Haaga, J. L., & Massey, R. 2007, ApJ, 666, 51

[38] Leonard, A., & King, L. J. 2010, MNRAS, 405, 1854

[39] Levinson, J. 2013, `https://github.com/pianojosh/image-object-extrator`

[40] Levinson, R. 2013, PASP, 125, 1474

[41] Limousin, M., Kneib, J. P., Bardeau, S., et al. 2007, A&A, 461, 881

[42] Limousin, M., Richard, J., Jullo, E., et al. 2007, ApJ, 668, 643

[43] Limousin, M., Sommer-Larsen, J., Natarajan, P., & Milvang-Jensen, B. 2009, ApJ, 696, 1771

[44] Massey, R., & Refregier, A. 2005, MNRAS, 363, 197

[45] Massey, R., Rowe, B., Refregier, A., Bacon, D. J., & Bergé, J. 2007, MNRAS, 380, 229

[46] Mateo, M., & Schechter, P. L. 1989, ESO/ST-ECF Data Analysis Workshop, 31, 69

[47] McLeod, B. A. 1996, PASP, 108, 217

[48] McLeod, B., Geary, J., Ordway, M., et al. 2006, Scientific Detectors for Astronomy 2005, 337

[49] Miralda-Escude, J., & Babul, A. 1995, ApJ, 449, 18

[50] Natarajan, P., Kneib, J.-P., Smail, I., & Ellis, R. 2004, arXiv:astro-ph/0411426

[51] Okura, Y., Umetsu, K., & Futamase, T. 2007, ApJ, 660, 995

[52] Okura, Y., Umetsu, K., & Futamase, T. 2008, ApJ, 680, 1

[53] Pires, S., & Amara, A. 2010, ApJ, 723, 1507

[54] Refregier, A. 2003, MNRAS, 338, 35

[55] Refregier, A., & Bacon, D. 2003, MNRAS, 338, 48

[56] Rowe, B., Bacon, D., Massey, R., et al. 2013, MNRAS, 435, 822

[57] Schechter, P. L., & Levinson, R. S. 2011, PASP, 123, 812

[58] Schechter, P. L., Mateo, M., & Saha, A. 1993, PASP, 105, 1342

[59] Sheldon, E. 2010, `https://code.google.com/p/esutil/source/browse/trunk/esutil/wcsutil.py`

[60] Skelton, R. E., Whitaker, K. E., Momcheva, I. G., et al. 2014, arXiv:1403.3689

[61] Sobel, R. & Schechter, P. L. 2010, Internal communication, "Measurement and compensation of aberration patterns in the IMACS f/2 camera"

[62] Spergel, D., Gehrels, N., Breckinridge, J., et al. 2013, arXiv:1305.5422

[63] Tody, D. 1986, Proc. SPIE, 627, 733

[64] Valdes, F. G., & Tody, D. 1998, Proc. SPIE, 3355, 497

[65] Velander, M., Kuijken, K., & Schrabback, T. 2011, MNRAS, 412, 2665

[66] Viola, M., Melchior, P., & Bartelmann, M. 2012, MNRAS, 419, 2215

[67] Wittman, D. M., Tyson, J. A., Dell'Antonio, I. P., et al. 2002, Proc. SPIE, 4836, 73

3.10 Wavefront delays to unitless coma, astigmatism, and trefoil aberrations

A wavefront delay at the edge of the pupil, W' and its gradient, $\vec{\nabla}W'$, are given by the following functions of the normalized pupil coordinate, $\vec{\rho}$, the radius of the pupil, R, and the magnitudes (in μm) of the defocus, astigmatism, coma, and trefoil, (d', $\vec{a}'$, $\vec{c}'$, and $\vec{t}'$, at the edge of the pupil:

$$W' = d'\rho^2 + \vec{a}' \cdot \vec{\rho}^2 + \vec{c}' \cdot \rho^2 \vec{\rho} + \vec{t}' \cdot \vec{\rho}^3 \tag{3.12}$$

$$\text{so } \vec{\nabla} W' = \left(2\frac{d'}{R}\vec{\rho} + 2\frac{\vec{a}'}{R}\vec{\rho}^* + 2\frac{\vec{c}'}{R}\rho^2 + \frac{\vec{c}'^*}{R}\vec{\rho}^2 + 3\frac{\vec{t}'}{R}(\vec{\rho}^*)^2 \right)$$

$$= \zeta \left(2d\vec{\rho} + 2\vec{a}\vec{\rho}^* + 2\vec{c}\rho^2 + \vec{c}^*\vec{\rho}^2 + 3\vec{t}(\vec{\rho}^*)^2 \right).$$

For ease of notation, we have introduced unitless wavefront aberrations d, a, c, and t, which can be converted into microns of aberration at the pupil edge by multiplying with the coefficient ζ. The scale of ζ is arbitrary, but may be thought of as a 'typical' ray displacement or image size and thus has units of the same– angle of ray displacement, or equivalently angular image size.

We define the Gaussian width of the PSF as α so that a measured spin-0 second moment of the spot created by the above wavefront delays and atmospheric smearing is $2\alpha^2$, if the PSF is truly Gaussian. With this definition, the Gaussian width is given by

$$\alpha = \zeta \sqrt{\left(d^2 + a^2 + \frac{1}{3}c^2 + \frac{3}{2}t^2 + S_{atm}^2 \right)}, \tag{3.13}$$

where we have assumed that any width added by the atmospheric smearing, S_{atm} adds in quadrature to the spot size caused by the wavefront delays.

Similarly, we define the dimensionless astigmatism, coma, and trefoil ($\vec{\tilde{a}}$, $\vec{\tilde{c}}$, $\vec{\tilde{t}}$) so that the spin-2 second moment and spin-1 and 3 third moments of the PSF are $4\alpha^2 \left(\vec{\tilde{a}}\right)$, $24\alpha^3 \left(3\vec{\tilde{c}}\right)$, and $24\alpha^3 \left(\vec{\tilde{t}}\right)$.[45] The resulting relation between the unitless astigmatism, coma, and trefoil and the telescope wavefront delays are:

[45] These relations ensure that the expressions for astigmatism, coma, and trefoil in the Gaussian model are identical to shear, F-flexion, and G-flexion. See Levinson [40] for details.

$$\vec{\tilde{a}} = \frac{1}{4\frac{\alpha^2}{\zeta^2}} \left(4\vec{a}d + \frac{1}{3}\vec{c}^2 + 2\vec{c}^*\vec{t} \right) \tag{3.14}$$

$$\vec{\tilde{c}} = \frac{1}{24\frac{\alpha^3}{\zeta^3}} \frac{1}{3} \left(\frac{1}{3}\vec{c}\left(8d^2 + 4a^2 + c^2 + 9t^2\right) + 4\vec{c}^*\vec{a}d + 8\vec{t}\vec{a}^*d + 4\vec{a}^2\vec{t}^* + (\vec{c}^*)^2\vec{t} \right)$$

$$\vec{\tilde{t}} = \frac{1}{24\frac{\alpha^3}{\zeta^3}} \left(3\vec{t}\left(4d^2 + c^2\right) + 4\vec{c}\vec{a}d + 4\vec{c}^*\vec{a}^2 \right).$$

These relations, combined with those in equation 3.12, map the unitless spin-1, 2, and 3 aberrations back to the microns of wavefront delay at the edge of the pupil that generates them.

However, the above relations between spin-n moments in the PSF and the wavefront delays only hold if the measured aberrations are caused by telescope aberrations. In the case where guiding error contributes to the measured spin-1 and spin-2 image aberrations, the guiding error contributions to these terms must be subtracted from the measured PSF moments before the wavefront delays can be derived.

We believe that guiding error is the primary contributor to the field constant coma and astigmatism measured in our images. The spin-1 aberration in the best individual r' image is too large to be associated with a coma wavefront delay; if the measured coma were caused by telescope aberrations, either the defocus would be so severe that the 'donut' pattern caused by the obstruction of light from the secondary mirror would be apparent in the images, or the coma would be sufficiently large that the classic comet pattern should start to be visible in the stellar images. We see neither of these in the images.

Additionally, we measure a large, constant spin-2 (astigmatism) aberration in the PSFs that is in the approximate direction of the coma. Piston of the mirrors causes a field quadratic astigmatism pattern, and mirror misalignments cause a large linear astigmatism pattern plus a very small constant term. Therefore, in absence of a large associated linear astigmatism pattern, the field constant term must be caused by either misshapen mirrors or a guiding error. During observations we ran wavefront sensing to reshape the primary mirror every 30 minutes to 1 hour. During those

corrections, we did not see an astigmatic error on the primary large enough to create PSFs with as much elongation as we measure in the images. It is therefore most likely that guiding error is the cause of the field constant coma and astigmatism aberrations.

Accounting for this probable guiding error by fixing the coma wavefront delay to zero and subtracting out the field constant contribution to the measured spin-2 ($\vec{a}$) aberration, we compute the wavefront delays at the edge of the pupil for images at the edge of the field (chip 36). In order to make this computation, we must also estimate the contribution of the seeing to the spin symmetric second moment of the PSF. Based on the reported seeing at the Baade telescope at the time of the observation, 0.″46 (FWHM), and the fact that the reported seeing at the Baade telescope was 0.″51 (FWHM), 10% larger than we measure in the images, we assume that the atmospheric seeing alone contributes 0.″178 to the measured Gaussian width of the PSF, 0.″195. From the seeing contribution to the PSF, we infer the contribution of the telescope aberrations to the Gaussian width of the PSF, 0.″080. We verify the relative contributions of the atmosphere and the aberrations to the PSF by examining the recorded wavefront delays from 2010 November.[46] The average drifts in Zernike defocus, astigmatism, coma, and trefoil between primary mirror corrections are $0.56\mu m$, $0.29\mu m$, $0.12\mu m$, and $0.10\mu m$ respectively. Converting these Zernike wavefront delays to arcseconds of wavefront delay at the edge of the pupil for the Magellan telescope, and inserting the values into equation 3.13, we find that a typical contribution of aberrations to the PSF Gaussian width is 0.″08, in complete agreement with the estimate inferred from Baade's seeing. The resulting wavefront delays are presented in table 3.11.

[46] Unlike most instruments on the Magellan telescopes, Megacam is too wide to allow for continuous Shack-Hartmann wavefront sensing (WFS) and continuous correction of the primary mirror during science exposures. Instead, two out-of-focus guide chips at the edges of the science camera are used to maintain guiding and focus during exposures, and the shape of the primary is maintained by intermittently halting science exposures, moving the Shack-Hartmann camera into the field, and performing a WFS. The aberrations measured by the Shack-Hartmann camera before the primary mirror corrections are implemented are used to estimate the drift in the telescope aberrations over the course of the science exposures. We use November 2010 data as this is the only observing run for which we recorded WFS data. The seeing on this run was excellent, making the aberrations very easy to measure.

Zernike wavefront delays	
defocus	$0.365\mu m$
astigmatism_1	$-0.025\mu m$
astigmatism_2	$-0.105\mu m$
trefoil_1	$-0.210\mu m$
trefoil_2	$-0.526\mu m$

Table 3.11 Zernike wavefront delays on the pupil for a chip at the edge of the field in the best r' image. These wavefront delays would produce the observed spin-3 PSF distortion and the field variable contribution to the spin-2 PSF distortion on chip 36 of Megacam. Coma and field constant astigmatism are assumed to be caused by guiding error, not wavefront delays.

3.11 Aberrations in individual exposures

To test that image coaddition did not unduly corrupt our images, we analyze the aberations in the best individual exposures in the i' and r' bands and compare those aberrations to those in the coadded r' and i' images. While the PSF half light radii in the coadded images are $\sim 10\%$ larger than those in these individual exposures, as is expeted from coadding these images with ones of lower quality, the aberrations are very similar in each. Compare figure 3-29 and table 3.13 to their counterparts in §3.4.

In the r' filter, the coma in the individual image is nearly identical to the coma in the coadded image, suggesting that coaddition did not impart any effective coma to the image. This seems only natural as we did not dither in r', and therefore the pointing offset between most exposures is zero to within the pointing error.

The astigmatism in the individual and coadded r' images corroborates this hypothesis that misalignments between the individual exposures are small enough so as to not corrupt the coadded image. The astigmatism is smaller, by 0.012, in the coadded image than the individual image, suggesting that the astigmatism varies slightly between the individual exposures, but the images are ultimately aligned, forcing the astigmatism to average out in the coaddition. This averaging would cause a slight broadening of the PSF, which we see in the coadded image.

In the i' filter, the magnitude of the coma in the individual image is the same as the magnitude of the coma in the final image, but the direction changes by $\sim 13^\circ$. This slight change in direction likely indicates that (a) the coma in the other exposures

is in a slightly different direction than the coma in this exposure, and/or (b) at least some of the coma in the coadded image is caused by the image addition. The latter is possible, as we did dither in the i' filter in response to the fringing, leaving ourselves vulnerable to non-integer pixel shifts between exposures. And since we coadd images by pixel, any dithers by offsets that are not evenly divisible by the pixel size necessitates adding together slightly offset images. However, it is unlikely that the coma in the final image is caused entirely by the coaddition, as image offsets alone would force the coma in the coadded image to have a larger magnitude than the coma in the individual images, and we do not see an increase in the magnitude of coma in the coadded image. More likely the direction shift in coma is cause by a combination of the differing coma in the individual image and slight offsets between the images.

The astigmatism in the coadded i' image is minimally smaller, by 0.003, than the astigmatism in the individual image, and has a directional offset of $\sim -10^{\circ}$ on average. This small decrease in the magnitude of the astigmatism indicates that the astigmatism was not as well averaged out in the i' coaddition as compared to the r' coaddition. This persistence of the astigmatism could be caused by (a) relative consistency in the astigmatism between exposures, (b) generally larger astigmatism magnitude in the other exposures (though possibly differing in direction between frames), and/or (c) slight spatial offsets between the individual exposures which are unresolved by the coaddition scheme. While it may contribute somewhat, it is unlikely that spatial offsets are the primary contributers to the final image astigmatism as the directions of the astigmatism in the individual and ocadded image are so similar.

We therefore conclude that the measured aberrations in the coadded r' images reflect aberrations present in the individual images, and we are not artificially introducing aberrations to the images with the r' coaddition. The coaddition may have added some minimal effective aberrations to the final coadded i' images, but the coma and astigmatism in these final images are no larger than the coma and astigmatism in the best individual i' exposure.

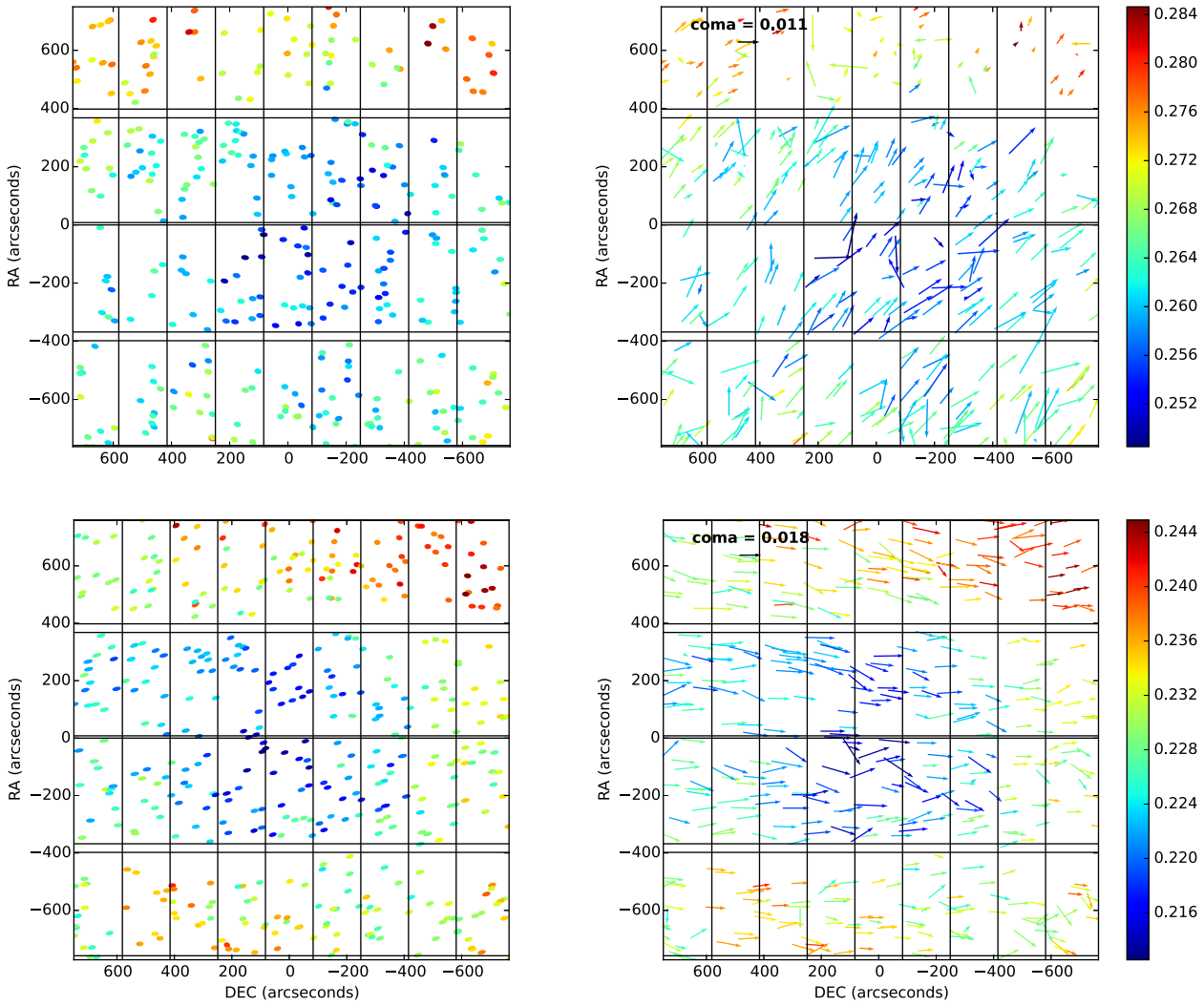

Figure 3-29 Unitless astigmatism (left) and coma (right) in the best single exposures in the i' filter (top) and r' filter (bottom). Compare to figure 3-9, which present the aberrations in the coadded images. Black lines denote the chip boundaries. Each ellipse (astigmatism plots) or vector (coma plots) represents the measurement from one star. For the astigmatism images, the size, eccentricity, an orientation of each ellipse shows the object's measured half light radius, astigmatism magnitude (exaggerated x5), and orientation. For the coma images, the direction and size of the vector correspond to the direction and size of the found coma. The color of each ellipse or vector indicates the half light radius (") of the object, as indicated by the color chart to the right of the images. Objects which are 2σ outliers in PSF size are excluded from the plot. Coma is largely field constant, while the astigmatism is a combination of field constant and field quadratic patterns. The average aberrations by chip are given in table 3.12.

aberrations in the coadded i' image							
chip	radius (“)	$shear_1$	$shear_2$	$coma_1$	$coma_2$	$trefoil_1$	$trefoil_2$
1	0.29	0.053	0.008	0.007	0.008	0.003	0.012
2	0.29	0.033	0.009	0.009	0.008	0.002	0.007
3	0.29	0.027	0.013	0.010	0.009	0.005	0.006
4	0.28	0.025	0.018	0.011	0.007	0.005	0.006
5	0.28	0.025	0.020	0.010	0.007	0.006	0.005
6	0.28	0.023	0.025	0.010	0.006	0.006	0.004
7	0.29	0.030	0.037	0.010	0.006	0.006	0.003
8	0.29	0.033	0.044	0.009	0.003	0.007	0.003
9	0.30	0.045	0.073	0.004	0.002	0.008	0.001
10	0.28	0.038	0.021	0.007	0.006	0.000	0.000
11	0.28	0.040	0.016	0.009	0.008	0.005	0.003
12	0.27	0.037	0.019	0.012	0.009	0.003	0.003
13	0.27	0.036	0.017	0.012	0.007	0.005	0.003
14	0.27	0.039	0.018	0.011	0.007	0.005	0.004
15	0.28	0.034	0.018	0.013	0.007	0.007	0.004
16	0.28	0.034	0.023	0.012	0.005	0.004	0.004
17	0.28	0.026	0.027	0.012	0.003	0.000	0.000
18	0.28	0.042	0.032	0.010	0.006	0.004	0.002
19	0.29	0.032	0.034	0.007	0.004	0.001	0.000
20	0.28	0.031	0.025	0.009	0.006	0.004	0.004
21	0.27	0.033	0.019	0.011	0.006	0.004	0.004
22	0.28	0.032	0.018	0.011	0.007	0.003	0.003
23	0.28	0.034	0.015	0.014	0.007	0.003	0.002
24	0.28	0.035	0.016	0.013	0.007	0.004	0.002
25	0.28	0.039	0.018	0.012	0.007	0.004	0.003
26	0.28	0.040	0.017	0.011	0.007	0.005	0.006
27	0.28	0.045	0.014	0.010	0.007	0.005	0.005
28	0.30	0.014	0.052	0.004	0.004	0.008	0.003
29	0.30	-0.002	0.029	0.005	0.003	0.008	0.002
30	0.29	0.008	0.023	0.009	0.004	0.009	0.005
31	0.29	0.018	0.014	0.009	0.005	0.006	0.008
32	0.28	0.018	0.009	0.010	0.004	0.005	0.007
33	0.28	0.019	0.003	0.007	0.004	0.002	0.004
34	0.28	0.022	0.003	0.011	0.006	0.004	0.007
35	0.28	0.028	-0.000	0.010	0.008	0.005	0.009
36	0.30	0.035	-0.002	0.011	0.009	0.007	0.010

aberrations in the coadded r' image							
chip	radius (“)	$shear_1$	$shear_2$	$coma_1$	$coma_2$	$trefoil_1$	$trefoil_2$
1	0.26	0.043	-0.046	0.017	-0.001	-0.018	0.000
2	0.26	0.042	-0.058	0.017	0.001	-0.023	-0.001
3	0.26	0.039	-0.059	0.017	0.001	-0.018	-0.002
4	0.26	0.028	-0.052	0.018	0.001	-0.019	-0.004
5	0.26	0.034	-0.042	0.016	0.001	-0.014	-0.003
6	0.26	0.028	-0.026	0.018	0.000	-0.018	-0.004
7	0.26	0.037	-0.020	0.018	-0.001	-0.018	-0.006
8	0.26	0.040	-0.020	0.017	-0.001	-0.019	-0.006
9	0.26	0.044	-0.029	0.015	-0.004	-0.014	-0.001
10	0.26	0.050	-0.040	0.014	-0.000	-0.016	-0.004
11	0.26	0.053	-0.053	0.017	-0.001	-0.020	-0.005
12	0.25	0.043	-0.049	0.019	0.000	-0.017	-0.002
13	0.25	0.037	-0.047	0.020	-0.001	-0.016	-0.001
14	0.25	0.034	-0.045	0.018	-0.002	-0.011	0.000
15	0.25	0.039	-0.042	0.021	-0.002	-0.014	-0.002
16	0.25	0.045	-0.039	0.019	-0.003	-0.017	-0.003
17	0.26	0.050	-0.031	0.018	-0.002	-0.015	-0.003
18	0.26	0.060	-0.037	0.019	-0.004	-0.023	-0.003
19	0.26	0.042	-0.027	0.016	-0.003	-0.013	-0.009
20	0.26	0.040	-0.023	0.018	-0.004	-0.016	-0.008
21	0.26	0.043	-0.035	0.018	-0.003	-0.012	-0.006
22	0.25	0.034	-0.039	0.019	-0.003	-0.012	-0.005
23	0.25	0.034	-0.047	0.020	-0.003	-0.012	-0.004
24	0.25	0.035	-0.056	0.020	-0.002	-0.014	-0.001
25	0.25	0.045	-0.059	0.019	-0.002	-0.015	-0.002
26	0.26	0.053	-0.067	0.018	-0.002	-0.016	-0.002
27	0.26	0.055	-0.061	0.016	-0.002	-0.020	-0.002
28	0.27	0.033	-0.016	0.016	-0.001	-0.006	-0.012
29	0.27	0.019	-0.014	0.016	-0.001	-0.009	-0.013
30	0.27	0.011	-0.013	0.018	-0.002	-0.011	-0.014
31	0.27	0.013	-0.027	0.017	-0.002	-0.008	-0.012
32	0.26	0.015	-0.045	0.017	-0.001	-0.012	-0.010
33	0.26	0.008	-0.058	0.014	-0.001	-0.011	-0.005
34	0.26	0.020	-0.068	0.014	0.000	-0.012	-0.003
35	0.26	0.030	-0.074	0.015	-0.000	-0.013	-0.002
36	0.26	0.035	-0.064	0.014	-0.001	-0.017	-0.005

Table 3.12 Unitless aberrations by chip in the deepest coadded i' and r' images. These measured aberrations are a combination of the telescope and atmospheric aberrations, plus any broadening and asymmetry introduced to the image during coaddition of individual images. While we use the terms astigmatism, coma, and trefoil to name the spin-2, 1, and 3 aberrations, each is in fact a non-linear combination of the associated wavefront delays.

aberrations in single i' image							
chip	radius (“)	shear_1	shear_2	coma_1	coma_2	trefoil_1	trefoil_2
1	0.27	0.046	0.002	0.010	0.011	0.001	0.007
2	0.26	0.041	-0.005	0.009	0.013	-0.001	0.006
3	0.26	0.035	-0.003	0.013	0.010	0.010	0.002
4	0.26	0.034	0.003	0.011	0.012	0.005	0.005
5	0.27	0.026	0.011	0.008	0.007	0.002	0.008
6	0.26	0.030	0.016	0.012	0.012	0.002	0.008
7	0.27	0.036	0.026	0.009	0.007	-0.000	0.010
8	0.26	0.034	0.030	0.006	0.009	0.007	0.006
9	0.27	0.038	0.021	0.009	0.010	0.004	0.010
10	0.26	0.053	0.004	0.010	0.008	0.001	0.001
11	0.26	0.048	-0.003	0.010	0.009	0.004	0.002
12	0.26	0.045	0.004	0.010	0.008	-0.003	0.002
13	0.25	0.043	0.003	0.009	0.007	0.003	0.004
14	0.25	0.045	0.011	0.007	0.010	0.005	0.007
15	0.26	0.050	0.015	0.010	0.010	0.004	0.004
16	0.26	0.048	0.015	0.005	0.011	0.008	0.004
17	0.26	0.053	0.015	0.009	0.010	0.008	0.010
18	0.26	0.052	0.015	0.009	0.007	0.004	0.009
19	0.26	0.049	0.008	0.011	0.000	0.001	0.002
20	0.26	0.044	0.009	0.006	0.005	0.001	0.001
21	0.26	0.042	0.005	0.006	0.005	-0.001	0.006
22	0.26	0.045	0.007	0.006	0.006	-0.001	0.004
23	0.26	0.045	0.004	0.006	0.011	-0.001	0.007
24	0.26	0.043	-0.001	0.005	0.008	0.002	0.009
25	0.26	0.045	-0.002	0.004	0.008	0.002	0.008
26	0.26	0.046	-0.003	0.006	0.007	0.005	0.007
27	0.26	0.049	-0.003	0.007	0.008	0.007	0.012
28	0.28	0.034	0.016	0.004	0.004	0.006	0.005
29	0.28	0.033	0.010	0.002	0.005	0.006	0.015
30	0.27	0.027	0.014	0.002	0.003	0.005	0.009
31	0.27	0.026	0.001	0.003	0.003	0.005	0.012
32	0.27	0.027	-0.007	0.002	0.003	0.003	0.014
33	0.27	0.032	-0.012	0.002	0.001	0.004	0.010
34	0.27	0.032	-0.017	0.007	0.002	-0.002	0.007
35	0.27	0.037	-0.021	0.006	0.003	0.002	0.010
36	0.27	0.038	-0.021	0.006	0.004	0.007	0.016

aberrations in single r' image							
chip	radius (“)	shear_1	shear_2	coma_1	coma_2	trefoil_1	trefoil_2
1	0.23	0.064	-0.040	0.012	-0.001	-0.016	-0.005
2	0.23	0.065	-0.048	0.014	0.000	-0.012	-0.007
3	0.23	0.060	-0.047	0.014	0.001	-0.011	-0.003
4	0.23	0.056	-0.042	0.015	0.001	-0.009	-0.008
5	0.23	0.050	-0.028	0.014	-0.000	-0.012	-0.006
6	0.23	0.055	-0.019	0.017	0.000	-0.009	-0.012
7	0.24	0.056	-0.009	0.016	0.001	-0.009	-0.013
8	0.23	0.062	-0.007	0.016	-0.001	-0.009	-0.011
9	0.23	0.067	-0.024	0.017	-0.003	-0.004	-0.001
10	0.23	0.074	-0.029	0.013	-0.001	-0.010	-0.008
11	0.23	0.077	-0.037	0.013	0.001	-0.010	-0.008
12	0.22	0.075	-0.037	0.014	0.002	-0.009	-0.007
13	0.22	0.068	-0.038	0.016	0.003	-0.004	-0.009
14	0.22	0.068	-0.035	0.015	0.002	-0.002	-0.005
15	0.22	0.069	-0.033	0.019	-0.001	-0.001	-0.008
16	0.22	0.073	-0.028	0.020	0.000	-0.004	-0.009
17	0.22	0.078	-0.024	0.020	-0.001	-0.010	-0.008
18	0.23	0.089	-0.019	0.020	-0.002	-0.011	-0.008
19	0.23	0.070	-0.016	0.014	0.002	-0.007	-0.011
20	0.23	0.068	-0.012	0.013	0.001	-0.003	-0.014
21	0.23	0.066	-0.021	0.017	-0.000	-0.002	-0.009
22	0.22	0.066	-0.028	0.017	-0.002	0.000	-0.006
23	0.22	0.063	-0.035	0.017	-0.001	0.005	-0.007
24	0.22	0.067	-0.038	0.022	-0.002	-0.001	-0.005
25	0.22	0.067	-0.041	0.019	-0.002	-0.004	-0.005
26	0.22	0.075	-0.043	0.021	-0.001	-0.006	-0.005
27	0.22	0.082	-0.040	0.020	-0.001	-0.001	-0.009
28	0.24	0.052	0.002	0.014	0.002	-0.005	-0.013
29	0.24	0.040	0.009	0.016	0.002	-0.002	-0.012
30	0.24	0.034	0.007	0.018	-0.001	-0.004	-0.014
31	0.24	0.031	-0.004	0.017	-0.004	0.003	-0.010
32	0.23	0.034	-0.024	0.019	-0.004	-0.002	-0.012
33	0.23	0.041	-0.035	0.019	-0.005	-0.002	-0.009
34	0.23	0.043	-0.047	0.019	-0.002	-0.004	-0.010
35	0.23	0.050	-0.053	0.019	-0.001	-0.005	-0.005
36	0.23	0.057	-0.045	0.019	-0.002	-0.004	-0.010

Table 3.13 Unitless aberrations by chip in the best single exposure in the i' and r' filters. Compare to table 3.12, which present the aberrations in the coadded images. These measured aberrations are a combination of the telescope and atmospheric aberrations, with no contribution from image coaddition. While we use the terms astigmatism, coma and trefoil to name the spin-2, 1, and 3 aberrations, each is in fact a non-linear combination of the various similarly named wavefront delays.

Table 3.14: Flexion measurements & predictions for the best 20 galaxy lensed background sources

obj # (ra, dec) M_r, $(\theta_{1/2}\theta_E)/\theta^2$	img	μ	data type	g_r	g_t	F_r	F_t	G_r	G_t	eF_r	eF_t	eG_r	eG_t
# 1 (13 : 11 : 30.0, −1 : 22 : 33.2) 24.59, 0.0237	i2	$\frac{0.''280}{0.''455}$	meas	-0.120	0.132	0.0820	0.0120	0.0763	0.0052	0.0518	0.0466	0.0756	0.0756
			pred			0.0049	-0.0028	-0.0239	-0.0032	0.0010	0.0005	0.0033	0.0012
			de-ab			0.0052	-0.0008	-0.0192	0.0004				
			aber			-0.0003	-0.0020	-0.0048	-0.0037				
	r1	$\frac{0.''250}{0.''423}$	meas	-0.098	0.149	0.0225	-0.0066	0.0773	0.0137	0.0427	0.0246	0.0550	0.0550
			pred			0.0020	-0.0021	-0.0294	0.0042	0.0010	0.0004	0.0031	0.0013
			de-ab			0.0054	-0.0011	-0.0189	0.0002				
			aber			-0.0035	-0.0009	-0.0105	0.0040				
# 2 (13 : 11 : 23.9, −1 : 21 : 45.9) 23.23, 0.0201	r3	$\frac{0.''341}{0.''588}$	meas	-0.073	-0.043	0.0825	-0.0134	-0.0079	-0.0107	0.0351	0.0276	0.0525	0.0525
			pred			0.0037	-0.0052	-0.0151	-0.0070	0.0035	0.0016	0.0113	0.0019
			de-ab			0.0050	-0.0020	-0.0155	-0.0040				
			aber			-0.0013	-0.0031	0.0004	-0.0030				
# 3 (13 : 11 : 46.0, −1 : 09 : 53.6) 22.75, 0.0180	i1	$\frac{0.''279}{0.''540}$	meas	-0.019	-0.080	0.1998	0.0997	0.0243	-0.0483	0.0449	0.0353	0.0709	0.0709
			pred			0.0040	-0.0015	-0.0093	0.0014	0.0025	0.0003	0.0078	0.0007
			de-ab			0.0037	-0.0002	-0.0112	-0.0006				
			aber			0.0003	-0.0013	0.0019	0.0020				
	i2	$\frac{0.''278}{0.''521}$	meas	-0.098	-0.139	0.2682	0.1235	-0.0209	0.0366	0.0577	0.0381	0.0808	0.0808
			pred			0.0022	-0.0018	-0.0059	-0.0044	0.0022	0.0003	0.0075	0.0010
			de-ab			0.0031	-0.0003	-0.0109	-0.0011				
			aber			-0.0009	-0.0015	0.0049	-0.0033				
# 4 (13 : 11 : 32.6, −1 : 21 : 02.0) 22.07, 0.0173	r1	$\frac{0.''249}{0.''502}$	meas	-0.018	-0.031	0.0135	0.0198	0.0016	-0.0091	0.0110	0.0125	0.0203	0.0203
			pred			0.0017	0.0020	-0.0041	0.0115	0.0024	0.0004	0.0005	0.0006
			de-ab			0.0044	0.0029	-0.0034	0.0115				
			aber			-0.0028	-0.0009	-0.0007	-0.0000				
# 5 (13 : 10 : 59.4, −1 : 16 : 28.9) 22.56, 0.0125	i1	$\frac{0.''281}{0.''511}$	meas	0.049	-0.048	-0.0400	-0.0562	0.0514	0.0546	0.0319	0.0315	0.0535	0.0535
			pred			0.0045	-0.0008	-0.0092	0.0003	0.0011	0.0001	0.0031	0.0005
			de-ab			0.0027	-0.0001	-0.0076	-0.0003				
			aber			0.0017	-0.0007	-0.0016	0.0006				
	r1	$\frac{0.''259}{0.''492}$	meas	0.055	0.003	-0.0141	-0.0961	0.0798	-0.0080	0.0124	0.0158	0.0237	0.0237
			pred			0.0042	-0.0028	-0.0071	0.0035	0.0011	0.0001	0.0031	0.0004
			de-ab			0.0029	-0.0001	-0.0078	-0.0000				
			aber			0.0013	-0.0027	0.0007	0.0036				
	r2	$\frac{0.''305}{0.''554}$	meas	0.058	-0.012	-0.0041	-0.0842	0.0567	-0.0020	0.0133	0.0170	0.0259	0.0259
			pred			0.0041	-0.0030	-0.0059	0.0018	0.0012	0.0001	0.0032	0.0003
			de-ab			0.0030	-0.0001	-0.0081	-0.0001				
			aber			0.0011	-0.0029	0.0021	0.0019				

Table 3.14: Flexion measurements & predictions for the best 20 galaxy lensed background sources

obj # (ra, dec) M_r, $(\theta_{1/2}\theta_E)/\theta^2$	img	μ	data type	g_r	g_t	F_r	F_t	G_r	G_t	eF_r	eF_t	eG_r	eG_t
# 6 (13 : 11 : 17.6, −1 : 22 : 52.7) 22.50, 0.0120	i1	$\frac{0.''276}{0.''535}$	meas	-0.035	-0.102	0.0803	-0.0207	0.0585	-0.0592	0.0354	0.0312	0.0528	0.0528
			pred			0.0027	-0.0016	-0.0070	-0.0018	0.0005	0.0002	0.0016	0.0006
			de-ab			0.0036	0.0001	-0.0113	-0.0005				
			aber			-0.0009	-0.0018	0.0042	-0.0014				
	i2	$\frac{0.''280}{0.''546}$	meas	-0.002	-0.181	0.0414	0.0098	0.0661	-0.0184	0.0335	0.0199	0.0435	0.0435
			pred			0.0023	-0.0017	-0.0061	-0.0031	0.0005	0.0002	0.0015	0.0005
			de-ab			0.0038	0.0002	-0.0114	-0.0009				
			aber			-0.0016	-0.0020	0.0053	-0.0022				
	r1	$\frac{0.''250}{0.''526}$	meas	0.018	-0.135	0.0576	0.0350	0.0280	-0.0157	0.0164	0.0112	0.0230	0.0230
			pred			0.0018	-0.0018	-0.0090	-0.0036	0.0005	0.0001	0.0015	0.0004
			de-ab			0.0041	0.0005	-0.0121	-0.0003				
			aber			-0.0022	-0.0023	0.0032	-0.0032				
	r2	$\frac{0.''295}{0.''556}$	meas	0.002	-0.120	0.0559	0.0331	0.0055	-0.0400	0.0222	0.0165	0.0321	0.0321
			pred			0.0008	-0.0027	-0.0086	-0.0027	0.0005	0.0002	0.0015	0.0006
			de-ab			0.0037	0.0000	-0.0111	-0.0007				
			aber			-0.0028	-0.0028	0.0025	-0.0020				
# 7 (13 : 11 : 43.9, −1 : 25 : 02.9) 23.48, 0.0116	i2	$\frac{0.''279}{0.''430}$	meas	0.051	0.154	-0.0203	-0.0268	-0.1346	0.0252	0.0503	0.0347	0.0697	0.0697
			pred			-0.0014	0.0049	0.0007	0.0017	0.0010	0.0006	0.0024	0.0012
			de-ab			0.0015	0.0008	-0.0037	0.0014				
			aber			-0.0030	0.0041	0.0044	0.0003				
	r1	$\frac{0.''254}{0.''434}$	meas	0.055	0.222	0.0588	-0.0131	-0.0367	-0.0252	0.0289	0.0185	0.0361	0.0361
			pred			0.0003	0.0045	0.0017	-0.0009	0.0012	0.0005	0.0029	0.0009
			de-ab			0.0020	0.0007	-0.0049	0.0015				
			aber			-0.0016	0.0038	0.0066	-0.0024				
	r2	$\frac{0.''300}{0.''477}$	meas	0.049	0.234	0.0783	0.0166	0.0149	-0.0474	0.0198	0.0397	0.0488	0.0488
			pred			-0.0004	0.0062	0.0039	0.0015	0.0011	0.0007	0.0027	0.0013
			de-ab			0.0018	0.0011	-0.0045	0.0020				
			aber			-0.0022	0.0051	0.0084	-0.0005				
# 8 (13 : 12 : 02.2, −1 : 08 : 32.7) 22.38, 0.0102	i1	$\frac{0.''279}{0.''479}$	meas	0.459	0.077	0.0120	-0.0709	-0.0587	0.0658	0.0343	0.1025	0.1039	0.1039
			pred			0.0014	0.0018	-0.0111	-0.0062	0.0001	0.0001	0.0007	0.0004
			de-ab			0.0022	0.0002	-0.0025	0.0004				
			aber			-0.0008	0.0016	-0.0085	-0.0066				
	r1	$\frac{0.''258}{0.''489}$	meas	0.457	0.051	0.0410	-0.1200	-0.1398	0.1028	0.0558	0.0787	0.0958	0.0958
			pred			0.0027	-0.0044	-0.0236	0.0098	0.0002	0.0003	0.0008	0.0007
			de-ab			0.0027	0.0001	-0.0041	0.0003				
			aber			0.0000	-0.0045	-0.0195	0.0095				
	r2	$\frac{0.''304}{0.''541}$	meas	0.433	0.050	0.0744	-0.1300	-0.2051	0.1007	0.0662	0.0469	0.0762	0.0762
			pred			0.0029	-0.0031	-0.0253	0.0056	0.0001	0.0002	0.0007	0.0006
			de-ab			0.0026	0.0002	-0.0036	0.0004				
			aber			0.0003	-0.0033	-0.0217	0.0052				

Table 3.14: Flexion measurements & predictions for the best 20 galaxy lensed background sources

obj # (ra, dec) M_r, $(\theta_{1/2}\theta_E)/\theta^2$	img	μ	data type	g_r	g_t	F_r	F_t	G_r	G_t	eF_r	eF_t	eG_r	eG_t
# 9 (13 : 11 : 35.1, −1 : 21 : 26.0) 22.10, 0.0099	i2	$\frac{0.''279}{0.''540}$	meas	-0.213	-0.061	0.2951	0.0633	0.1177	0.0356	0.0466	0.0245	0.0591	0.0591
			pred			0.0052	-0.0015	-0.0042	0.0043	0.0003	0.0002	0.0012	0.0004
			de-ab			0.0021	-0.0019	-0.0104	0.0024				
			aber			0.0031	0.0003	0.0061	0.0019				
	r1	$\frac{0.''249}{0.''508}$	meas	-0.276	-0.058	0.2437	0.0475	0.1046	0.0337	0.0317	0.0147	0.0372	0.0372
			pred			0.0055	-0.0012	0.0007	-0.0023	0.0003	0.0002	0.0012	0.0005
			de-ab			0.0019	-0.0018	-0.0104	0.0025				
			aber			0.0035	0.0005	0.0111	-0.0047				
# 10 (13 : 11 : 19.5, −1 : 22 : 36.6) 22.44, 0.0098	i1	$\frac{0.''276}{0.''504}$	meas	-0.073	0.086	0.0902	-0.0867	0.0168	-0.1718	0.0542	0.0710	0.1039	0.1039
			pred			0.0033	0.0017	-0.0034	0.0014	0.0004	0.0003	0.0018	0.0011
			de-ab			0.0019	0.0007	-0.0072	0.0001				
			aber			0.0014	0.0010	0.0038	0.0014				
	i2	$\frac{0.''280}{0.''524}$	meas	-0.013	0.151	0.1566	0.0524	0.1582	-0.1988	0.0601	0.1038	0.1402	0.1402
			pred			0.0032	0.0014	-0.0032	-0.0028	0.0005	0.0003	0.0021	0.0012
			de-ab			0.0022	0.0007	-0.0074	0.0003				
			aber			0.0010	0.0006	0.0042	-0.0031				
	r1	$\frac{0.''250}{0.''555}$	meas	-0.027	0.074	0.0979	-0.0255	0.0237	-0.2079	0.0299	0.0211	0.0430	0.0430
			pred			0.0049	0.0002	-0.0088	-0.0044	0.0005	0.0002	0.0019	0.0006
			de-ab			0.0028	0.0006	-0.0097	-0.0003				
			aber			0.0020	-0.0005	0.0009	-0.0041				
	r2	$\frac{0.''295}{0.''580}$	meas	-0.037	0.091	0.1072	-0.0332	0.0653	-0.1340	0.0335	0.0221	0.0471	0.0471
			pred			0.0054	0.0002	-0.0084	-0.0045	0.0005	0.0002	0.0018	0.0007
			de-ab			0.0025	0.0007	-0.0090	-0.0000				
			aber			0.0028	-0.0005	0.0005	-0.0045				
# 13 (13 : 12 : 01.9, −1 : 08 : 55.0) 22.61, 0.0084	i1	$\frac{0.''279}{0.''592}$	meas	0.020	-0.013	-0.0112	-0.0037	0.0177	0.0183	0.0263	0.0257	0.0450	0.0450
			pred			0.0016	-0.0012	-0.0050	-0.0006	0.0002	0.0001	0.0007	0.0005
			de-ab			0.0022	0.0001	-0.0065	-0.0000				
			aber			-0.0006	-0.0013	0.0015	-0.0006				
	i2	$\frac{0.''278}{0.''650}$	meas	0.009	0.007	0.0225	-0.0024	0.0197	0.0913	0.0223	0.0228	0.0389	0.0389
			pred			0.0019	-0.0006	-0.0084	0.0000	0.0002	0.0000	0.0006	0.0004
			de-ab			0.0026	0.0000	-0.0079	0.0000				
			aber			-0.0007	-0.0006	-0.0005	0.0000				
	r2	$\frac{0.''304}{0.''678}$	meas	0.030	0.007	-0.0013	-0.0148	-0.0046	0.0378	0.0119	0.0133	0.0214	0.0214
			pred			0.0012	-0.0007	-0.0066	0.0025	0.0002	0.0001	0.0006	0.0003
			de-ab			0.0027	0.0000	-0.0079	0.0000				
			aber			-0.0014	-0.0007	0.0013	0.0025				

Table 3.14: Flexion measurements & predictions for the best 20 galaxy lensed background sources

obj # (ra, dec) M_r, $(\theta_{1/2}\theta_E)/\theta^2$	img	μ	data type	g_r	g_t	F_r	F_t	G_r	G_t	eF_r	eF_t	eG_r	eG_t
# 16 (13 : 11 : 17.7, −1 : 18 : 15.0) 22.78, 0.0070	i1	$\frac{0.''273}{0.''492}$	meas	-0.069	-0.183	0.0381	0.0665	-0.0563	0.0581	0.0245	0.0511	0.0627	0.0627
			pred			0.0004	-0.0027	0.0050	-0.0006	0.0003	0.0004	0.0012	0.0009
			de-ab			0.0016	0.0000	-0.0046	-0.0004				
			aber			-0.0012	-0.0027	0.0096	-0.0002				
	i2	$\frac{0.''281}{0.''533}$	meas	-0.064	-0.254	0.0445	0.0543	0.0193	-0.0422	0.0355	0.0564	0.0657	0.0657
			pred			0.0011	-0.0010	0.0035	0.0003	0.0003	0.0003	0.0010	0.0006
			de-ab			0.0019	0.0002	-0.0053	-0.0005				
			aber			-0.0008	-0.0012	0.0088	0.0007				
	r1	$\frac{0.''247}{0.''487}$	meas	-0.054	-0.267	0.0141	0.0515	-0.0874	0.0200	0.0098	0.0190	0.0216	0.0216
			pred			-0.0026	-0.0030	0.0057	-0.0108	0.0003	0.0001	0.0008	0.0004
			de-ab			0.0018	0.0004	-0.0051	-0.0004				
			aber			-0.0044	-0.0034	0.0107	-0.0104				
	r2	$\frac{0.''292}{0.''531}$	meas	-0.045	-0.229	-0.0052	0.0402	-0.0999	-0.0003	0.0185	0.0113	0.0219	0.0219
			pred			-0.0023	-0.0037	0.0031	-0.0079	0.0003	0.0001	0.0008	0.0004
			de-ab			0.0017	0.0000	-0.0049	-0.0006				
			aber			-0.0040	-0.0037	0.0081	-0.0073				
# 18 (13 : 11 : 17.8, −1 : 22 : 37.4) 22.65, 0.0048	i1	$\frac{0.''276}{0.''516}$	meas	-0.242	0.158	-0.0569	-0.0160	-0.1561	-0.0988	0.1005	0.1074	0.1352	0.1352
			pred			0.0039	-0.0003	0.0057	-0.0012	0.0004	0.0002	0.0015	0.0012
			de-ab			0.0008	0.0004	-0.0044	0.0006				
			aber			0.0031	-0.0007	0.0101	-0.0017				
	r1	$\frac{0.''250}{0.''503}$	meas	-0.270	0.148	-0.0941	0.0007	-0.1717	-0.0793	0.0456	0.0183	0.0424	0.0424
			pred			0.0055	-0.0010	0.0032	-0.0088	0.0002	0.0001	0.0008	0.0006
			de-ab			0.0008	0.0003	-0.0046	0.0005				
			aber			0.0047	-0.0013	0.0078	-0.0093				
# 19 (13 : 11 : 36.9, −1 : 11 : 15.8) 23.63, 0.0047	i2	$\frac{0.''279}{0.''507}$	meas	0.029	0.290	-0.0181	0.0236	-0.0505	-0.0196	0.0527	0.0731	0.0944	0.0944
			pred			-0.0011	0.0023	-0.0002	0.0098	0.0005	0.0003	0.0013	0.0009
			de-ab			0.0012	0.0002	-0.0034	0.0007				
			aber			-0.0023	0.0021	0.0032	0.0091				
	r1	$\frac{0.''256}{0.''524}$	meas	0.063	0.156	0.0434	-0.0251	-0.4061	-0.2640	0.0435	0.0242	0.0545	0.0545
			pred			-0.0007	0.0030	0.0034	0.0024	0.0005	0.0002	0.0014	0.0008
			de-ab			0.0015	-0.0000	-0.0041	0.0002				
			aber			-0.0021	0.0030	0.0075	0.0022				
	r2	$\frac{0.''301}{0.''534}$	meas	0.105	0.146	0.1206	-0.0041	-0.2523	-0.3178	0.0606	0.0822	0.1072	0.1072
			pred			-0.0016	0.0044	0.0051	0.0000	0.0007	0.0006	0.0021	0.0019
			de-ab			0.0012	0.0002	-0.0031	0.0005				
			aber			-0.0028	0.0042	0.0082	-0.0005				

Table 3.14: Flexion measurements & predictions for the best 20 galaxy lensed background sources

obj # (ra, dec) M_r, $(\theta_{1/2}\theta_E)/\theta^2$	img	μ	data type	g_r	g_t	F_r	F_t	G_r	G_t	eF_r	eF_t	eG_r	eG_t
# 20 (13 : 11 : 26.6, −1 : 20 : 52.9) 22.75, 0.0046	i1	$\frac{0.''273}{0.''501}$	meas	-0.157	-0.089	0.0340	-0.0058	0.0547	-0.0156	0.0272	0.0217	0.0375	0.0375
			pred			0.0073	0.0041	0.0196	0.0025	0.0015	0.0002	0.0018	0.0005
			de-ab			0.0037	0.0038	0.0140	0.0015				
			aber			0.0036	0.0003	0.0056	0.0011				
	i2	$\frac{0.''279}{0.''476}$	meas	-0.149	-0.102	0.0428	0.0338	0.0020	0.1083	0.0221	0.0297	0.0401	0.0401
			pred			0.0057	0.0033	0.0160	0.0017	0.0012	0.0002	0.0015	0.0005
			de-ab			0.0025	0.0032	0.0118	0.0003				
			aber			0.0033	0.0001	0.0043	0.0014				
	r1	$\frac{0.''249}{0.''470}$	meas	-0.168	-0.108	0.0303	-0.0036	0.0449	-0.0093	0.0142	0.0101	0.0183	0.0183
			pred			0.0052	0.0025	0.0240	-0.0021	0.0015	0.0002	0.0017	0.0004
			de-ab			0.0039	0.0036	0.0142	0.0016				
			aber			0.0013	-0.0011	0.0098	-0.0038				
	r2	$\frac{0.''294}{0.''499}$	meas	-0.151	-0.090	0.0107	-0.0030	0.0110	-0.0022	0.0126	0.0129	0.0196	0.0196
			pred			0.0047	0.0012	0.0218	-0.0037	0.0012	0.0002	0.0014	0.0004
			de-ab			0.0026	0.0033	0.0122	0.0005				
			aber			0.0021	-0.0021	0.0097	-0.0042				
# 21 (13 : 11 : 19.3, −1 : 22 : 35.6) 23.25, 0.0045	i1	$\frac{0.''276}{0.''424}$	meas	0.160	0.072	0.0763	0.0135	0.0408	0.0387	0.0236	0.0430	0.0566	0.0566
			pred			0.0033	0.0013	-0.0041	-0.0036	0.0002	0.0001	0.0007	0.0005
			de-ab			0.0009	0.0004	-0.0022	0.0007				
			aber			0.0024	0.0009	-0.0020	-0.0043				
	i2	$\frac{0.''280}{0.''446}$	meas	0.098	0.018	0.0750	-0.0254	-0.0291	0.1706	0.0312	0.0332	0.0538	0.0538
			pred			0.0036	0.0007	-0.0059	-0.0020	0.0002	0.0001	0.0007	0.0005
			de-ab			0.0010	0.0003	-0.0028	0.0004				
			aber			0.0026	0.0004	-0.0031	-0.0025				
	r1	$\frac{0.''250}{0.''403}$	meas	0.097	0.038	0.1287	-0.0519	-0.0579	0.1052	0.0163	0.0146	0.0264	0.0264
			pred			0.0046	-0.0028	-0.0099	0.0033	0.0002	0.0001	0.0006	0.0004
			de-ab			0.0009	0.0004	-0.0026	0.0005				
			aber			0.0037	-0.0031	-0.0073	0.0028				
	r2	$\frac{0.''295}{0.''449}$	meas	0.090	0.026	0.0944	-0.0351	-0.0537	0.0750	0.0160	0.0154	0.0266	0.0266
			pred			0.0054	-0.0029	-0.0076	0.0055	0.0002	0.0001	0.0006	0.0004
			de-ab			0.0009	0.0004	-0.0024	0.0005				
			aber			0.0045	-0.0032	-0.0052	0.0050				

Table 3.14: Flexion measurements & predictions for the best 20 galaxy lensed background sources

obj # (ra, dec) M_r, $(\theta_{1/2}\theta_E)/\theta^2$	img	μ	data type	g_r	g_t	F_r	F_t	G_r	G_t	eF_r	eF_t	eG_r	eG_t
# 25 (13 : 11 : 01.8, −1 : 20 : 20.6) 23.39, 0.0035	i1	$\frac{0.''281}{0.''528}$	meas	-0.117	0.063	0.0089	0.0738	0.0081	-0.0367	0.0614	0.0375	0.0841	0.0841
			pred			0.0024	-0.0014	-0.0045	-0.0028	0.0002	0.0002	0.0010	0.0009
			de-ab			0.0009	0.0000	-0.0031	0.0001				
			aber			0.0015	-0.0014	-0.0014	-0.0030				
	r1	$\frac{0.''260}{0.''527}$	meas	-0.137	0.091	-0.0831	0.0254	-0.0574	0.0249	0.0299	0.0182	0.0393	0.0393
			pred			0.0019	-0.0015	-0.0067	-0.0081	0.0002	0.0001	0.0007	0.0006
			de-ab			0.0010	-0.0000	-0.0034	0.0001				
			aber			0.0009	-0.0014	-0.0032	-0.0082				
	r2	$\frac{0.''307}{0.''554}$	meas	-0.144	0.091	-0.0588	0.0417	-0.0632	0.0107	0.0230	0.0280	0.0404	0.0404
			pred			0.0009	-0.0017	-0.0080	-0.0066	0.0002	0.0001	0.0006	0.0005
			de-ab			0.0008	0.0000	-0.0032	0.0002				
			aber			0.0000	-0.0017	-0.0048	-0.0068				
# 26 (13 : 11 : 20.6, −1 : 20 : 15.5) 22.48, 0.0033	i1	$\frac{0.''273}{0.''441}$	meas	0.008	-0.098	-0.0102	0.0017	0.0513	0.0128	0.0154	0.0199	0.0295	0.0295
			pred			-0.0024	-0.0040	0.0005	-0.0049	0.0002	0.0001	0.0004	0.0004
			de-ab			0.0007	-0.0004	-0.0018	-0.0012				
			aber			-0.0031	-0.0036	0.0022	-0.0036				
	i2	$\frac{0.''279}{0.''445}$	meas	0.035	-0.087	-0.0128	-0.0130	0.0680	0.0401	0.0187	0.0165	0.0292	0.0292
			pred			-0.0018	-0.0034	-0.0001	-0.0028	0.0001	0.0001	0.0004	0.0003
			de-ab			0.0007	-0.0004	-0.0016	-0.0012				
			aber			-0.0025	-0.0030	0.0016	-0.0016				
	r2	$\frac{0.''294}{0.''482}$	meas	0.028	-0.092	-0.0256	-0.0235	0.0774	0.0368	0.0134	0.0113	0.0208	0.0208
			pred			-0.0035	-0.0017	0.0028	-0.0047	0.0002	0.0001	0.0004	0.0004
			de-ab			0.0008	-0.0004	-0.0019	-0.0013				
			aber			-0.0043	-0.0013	0.0047	-0.0034				
# 27 (13 : 11 : 41.9, −1 : 12 : 43.7) 24.45, 0.0030	i1	$\frac{0.''280}{0.''569}$	meas	-0.041	0.335	-0.0104	-0.0443	-0.1248	-0.1628	0.0757	0.0319	0.0758	0.0758
			pred			0.0016	-0.0012	0.0031	-0.0074	0.0001	0.0001	0.0007	0.0006
			de-ab			0.0007	-0.0001	-0.0021	0.0004				
			aber			0.0009	-0.0011	0.0052	-0.0078				
	i2	$\frac{0.''279}{0.''581}$	meas	-0.094	0.278	-0.0949	-0.0571	-0.2452	-0.1009	0.0342	0.0878	0.0974	0.0974
			pred			0.0024	-0.0014	0.0019	-0.0075	0.0002	0.0001	0.0008	0.0008
			de-ab			0.0007	-0.0001	-0.0022	0.0003				
			aber			0.0017	-0.0012	0.0042	-0.0079				
	r1	$\frac{0.''256}{0.''585}$	meas	-0.078	0.324	-0.0190	0.0012	-0.0006	-0.1281	0.0324	0.0220	0.0347	0.0347
			pred			0.0036	-0.0033	-0.0047	-0.0138	0.0001	0.0001	0.0005	0.0005
			de-ab			0.0008	-0.0003	-0.0024	0.0003				
			aber			0.0028	-0.0031	-0.0022	-0.0141				
	r2	$\frac{0.''301}{0.''604}$	meas	-0.078	0.307	-0.0260	0.0051	0.0244	-0.0446	0.0358	0.0155	0.0403	0.0403
			pred			0.0044	-0.0036	-0.0044	-0.0133	0.0001	0.0001	0.0006	0.0005
			de-ab			0.0007	-0.0001	-0.0022	0.0004				
			aber			0.0037	-0.0035	-0.0021	-0.0137				

Table 3.14: Flexion measurements & predictions for the best 20 galaxy lensed background sources													
obj # (ra, dec) M_r, $(\theta_{1/2}\theta_E)/\theta^2$	img	μ	data type	g_r	g_t	F_r	F_t	G_r	G_t	eF_r	eF_t	eG_r	eG_t
# 29 (13 : 11 : 26.7, −1 : 22 : 41.6) 22.17, 0.0028	i1	$\frac{0.''276}{0.''560}$	meas	-0.029	-0.099	0.0212	0.0078	-0.0346	0.0071	0.0238	0.0159	0.0335	0.0335
			pred			0.0020	0.0006	-0.0019	0.0031	0.0001	0.0001	0.0006	0.0004
			de-ab			0.0007	0.0007	-0.0031	0.0014				
			aber			0.0013	-0.0002	0.0012	0.0017				
	i2	$\frac{0.''280}{0.''559}$	meas	-0.039	-0.080	0.0241	0.0021	0.0476	0.0155	0.0219	0.0171	0.0328	0.0328
			pred			0.0019	0.0002	-0.0014	0.0032	0.0001	0.0001	0.0006	0.0003
			de-ab			0.0007	0.0007	-0.0031	0.0013				
			aber			0.0013	-0.0004	0.0017	0.0019				
	r1	$\frac{0.''250}{0.''530}$	meas	-0.062	-0.090	0.0050	0.0095	-0.0233	0.0245	0.0075	0.0114	0.0161	0.0161
			pred			0.0010	-0.0006	0.0031	0.0008	0.0001	0.0001	0.0005	0.0003
			de-ab			0.0007	0.0007	-0.0031	0.0014				
			aber			0.0003	-0.0013	0.0062	-0.0006				
	r2	$\frac{0.''295}{0.''573}$	meas	-0.052	-0.088	0.0059	0.0120	-0.0184	0.0158	0.0080	0.0118	0.0170	0.0170
			pred			0.0012	-0.0013	0.0035	-0.0000	0.0001	0.0001	0.0005	0.0003
			de-ab			0.0006	0.0007	-0.0030	0.0013				
			aber			0.0006	-0.0020	0.0065	-0.0013				

Table 3.14: Flexion measurements and predictions for the 20 objects for which we expect to see the greatest galaxy-galaxy lensing flexion as defined by the unitless metric $(\theta_{1/2}\theta_E)/\theta^2$. Objects are ordered by this expected galaxy-galaxy flexion, from most to least. However objects whose flexion measurements or predictions are found by inspection to be corrupted are excluded from the list. Both the (de-ab)errated prediction and (aber)rational component of the flexion are provided with the full (pred)iction of the flexion.

Table 3.15: Flexion measurements & predictions for the best 10 galaxy lensed background sources drawn from the color-magnitude ambiguous region

obj # (ra, dec) M_r, $(\theta_{1/2}\theta_E)/\theta^2$	img	μ	data type	g_r	g_t	F_r	F_t	G_r	G_t	eF_r	eF_t	eG_r	eG_t
# 7	r1	$\frac{0.''259}{0.''457}$	meas	0.002	0.084	-0.0356	-0.0052	-0.0931	-0.0575	0.1144	0.0906	0.1666	0.1666
(13 : 11 : 13.4,			pred			0.0183	-0.0033	-0.0465	0.0037	0.0031	0.0008	0.0113	0.0033
−1 : 22 : 20.9)			de-ab			0.0153	-0.0003	-0.0444	0.0032				
23.50, 0.0459			aber			0.0030	-0.0030	-0.0021	0.0006				
# 8	g1	$\frac{0.''438}{0.''817}$	meas	-0.228	-0.162	0.0651	-0.0288	0.0800	0.0193	0.0341	0.0586	0.0705	0.0705
(13 : 11 : 29.9,			pred			0.0225	-0.0166	-0.0636	-0.0373	0.0024	0.0013	0.0085	0.0025
−1 : 21 : 47.6)			de-ab			0.0219	-0.0158	-0.0803	-0.0304				
22.96, 0.0444			aber			0.0007	-0.0008	0.0167	-0.0069				
# 9	r3	$\frac{0.''353}{0.''681}$	meas	0.081	0.083	0.0525	-0.0657	-0.1135	0.1583	0.0370	0.0512	0.0737	0.0737
(13 : 10 : 55.7,			pred			0.0152	0.0015	-0.0388	-0.0022	0.0074	0.0009	0.0202	0.0013
−1 : 23 : 32.7)			de-ab			0.0139	0.0009	-0.0375	0.0022				
23.74, 0.0426			aber			0.0013	0.0006	-0.0013	-0.0043				
# 10	r1	$\frac{0.''263}{0.''549}$	meas	-0.022	0.274	0.2057	-0.1083	-0.1313	-0.0878	0.0650	0.0259	0.0796	0.0796
(13 : 12 : 18.7,			pred			0.0131	-0.0045	-0.0417	-0.0008	0.0074	0.0019	0.0227	0.0021
−1 : 11 : 52.0)			de-ab			0.0108	-0.0026	-0.0328	0.0024				
22.58, 0.0333			aber			0.0023	-0.0019	-0.0089	-0.0032				
# 11	i1	$\frac{0.''284}{0.''451}$	meas	-0.033	0.036	0.0549	-0.0201	-0.0435	0.0131	0.0215	0.0177	0.0340	0.0340
(13 : 12 : 31.3,			pred			0.0040	-0.0006	-0.0217	-0.0013	0.0014	0.0003	0.0047	0.0007
−1 : 18 : 01.7)			de-ab			0.0061	0.0007	-0.0205	0.0010				
22.78, 0.0305			aber			-0.0021	-0.0013	-0.0013	-0.0023				
	i2	$\frac{0.''280}{0.''436}$	meas	-0.016	0.012	0.0157	-0.0304	-0.0374	0.0266	0.0196	0.0225	0.0357	0.0357
			pred			0.0029	-0.0015	-0.0205	0.0008	0.0014	0.0003	0.0042	0.0008
			de-ab			0.0057	0.0004	-0.0182	0.0004				
			aber			-0.0028	-0.0018	-0.0023	0.0004				
	r1	$\frac{0.''264}{0.''405}$	meas	-0.023	0.012	0.0064	0.0049	-0.0311	0.0784	0.0117	0.0180	0.0251	0.0251
			pred			-0.0003	0.0009	-0.0148	0.0061	0.0012	0.0004	0.0039	0.0009
			de-ab			0.0050	0.0007	-0.0166	0.0011				
			aber			-0.0053	0.0002	0.0019	0.0050				
# 15	i1	$\frac{0.''286}{0.''469}$	meas	0.080	-0.220	0.1600	0.0702	-0.2129	0.0634	0.0522	0.0238	0.0668	0.0668
(13 : 11 : 09.1,			pred			0.0069	-0.0019	-0.0158	-0.0005	0.0046	0.0013	0.0118	0.0031
−1 : 12 : 12.9)			de-ab			0.0059	-0.0016	-0.0150	-0.0040				
22.73, 0.0248			aber			0.0011	-0.0002	-0.0008	0.0035				
	i2	$\frac{0.''292}{0.''451}$	meas	0.001	-0.291	0.1052	0.0585	-0.0902	0.0409	0.0614	0.0281	0.0729	0.0729
			pred			0.0072	-0.0032	-0.0096	0.0029	0.0035	0.0025	0.0108	0.0046
			de-ab			0.0045	-0.0032	-0.0137	-0.0061				
			aber			0.0027	0.0001	0.0041	0.0090				

Table 3.15: Flexion measurements & predictions for the best 10 galaxy lensed background sources drawn from the color-magnitude ambiguous region

obj # (ra, dec) M_r, $(\theta_{1/2}\theta_E)/\theta^2$	img	μ	data type	g_r	g_t	F_r	F_t	G_r	G_t	eF_r	eF_t	eG_r	eG_t
# 19			meas	0.098	0.031	0.1032	0.0188	-0.0867	0.0235	0.0277	0.0381	0.0565	0.0565
(13 : 11 : 22.8,	r1	$\frac{0.''252}{0.''522}$	pred			0.0081	-0.0040	-0.0223	0.0026	0.0013	0.0003	0.0036	0.0009
−1 : 25 : 16.6)			de-ab			0.0082	-0.0011	-0.0213	-0.0006				
23.64, 0.0208			aber			-0.0001	-0.0030	-0.0010	0.0031				
			meas	0.296	-0.015	0.0460	-0.0681	-0.0486	0.0703	0.0330	0.0169	0.0387	0.0387
	r1	$\frac{0.''249}{0.''394}$	pred			0.0136	-0.0007	-0.0294	0.0172	0.0044	0.0014	0.0075	0.0015
# 24			de-ab			0.0114	0.0038	-0.0147	0.0076				
(13 : 11 : 29.4,			aber			0.0022	-0.0046	-0.0147	0.0096				
−1 : 19 : 27.8)			meas	0.266	0.003	0.0645	-0.0195	-0.0636	0.0404	0.0191	0.0252	0.0340	0.0340
22.69, 0.0178	r2	$\frac{0.''294}{0.''447}$	pred			0.0142	0.0000	-0.0254	0.0173	0.0044	0.0016	0.0074	0.0017
			de-ab			0.0115	0.0044	-0.0142	0.0083				
			aber			0.0027	-0.0044	-0.0112	0.0090				
# 29			meas	0.070	0.082	0.0913	0.1066	0.3633	-0.0011	0.0897	0.0688	0.1409	0.1409
(13 : 11 : 29.8,	i1	$\frac{0.''276}{0.''455}$	pred			0.0046	-0.0036	-0.0097	0.0045	0.0007	0.0005	0.0022	0.0015
−1 : 22 : 32.0)			de-ab			0.0035	-0.0000	-0.0072	0.0014				
24.25, 0.0138			aber			0.0011	-0.0036	-0.0025	0.0031				
			meas	-0.248	0.006	0.0176	-0.0362	0.0234	-0.1470	0.0298	0.0372	0.0505	0.0505
	i1	$\frac{0.''273}{0.''568}$	pred			0.0039	-0.0058	-0.0242	0.0035	0.0002	0.0006	0.0029	0.0008
# 30			de-ab			0.0035	-0.0060	-0.0248	-0.0059				
(13 : 11 : 32.4,			aber			0.0005	0.0002	0.0006	0.0093				
−1 : 21 : 33.4)			meas	-0.253	-0.033	-0.0493	-0.0063	-0.0701	-0.0590	0.0323	0.0131	0.0321	0.0321
23.61, 0.0136	r2	$\frac{0.''294}{0.''583}$	pred			0.0074	-0.0056	-0.0161	-0.0003	0.0002	0.0005	0.0028	0.0006
			de-ab			0.0033	-0.0058	-0.0248	-0.0057				
			aber			0.0041	0.0001	0.0088	0.0054				

Table 3.15: Flexion measurements and predictions for the 10 objects for which we expect to see the greatest galaxy-galaxy lensing flexion as defined by the unitless metric $(\theta_{1/2}\theta_E)/\theta^2$. Objects here need not have been detected in all three filters, and may have been drawn from the'ambiguous' region of color-magnitude space, where color alone is insufficient to determine the object's status as a cluster member or background galaxy. Objects are ordered from most expected galaxy-galaxy flexion to least. However objects whose flexion measurements or predictions are found by inspection to be corrupted are excluded from the list. Both the (de-ab)errated prediction and (aber)rational component of the flexion are provided with the full (pred)iction of the flexion.

Table 3.16: Lowest noise flexion measurements

(ra, dec), M_r		$\theta_{1/2}$	g_r	g_t	F_r	F_t	G_r	G_t
(13 : 11 : 45.0, −1 : 27 : 23.3) 22.16	meas	0.439	0.140	0.055	0.0076	0.0255	0.0387	-0.0083
	err	0.002	0.004	0.004	0.0070	0.0072	0.0113	0.0113
	corr	0.358	0.215	0.110	0.0078	0.0231	0.0331	-0.0146
	err	0.002	0.006	0.006	0.0143	0.0145	0.0202	0.0202
(13 : 10 : 54.2, −1 : 26 : 12.4) 22.31	meas	0.394	0.186	0.112	0.0060	-0.0766	-0.0318	0.0658
	err	0.002	0.004	0.004	0.0045	0.0099	0.0111	0.0111
	corr	0.295	0.301	0.155	0.0255	-0.1395	-0.1204	0.1759
	err	0.002	0.007	0.007	0.0131	0.0216	0.0232	0.0232
(13 : 10 : 58.4, −1 : 12 : 43.4) 22.23	meas	0.438	0.082	-0.109	0.0156	-0.0522	0.0360	0.0184
	err	0.002	0.004	0.004	0.0080	0.0066	0.0119	0.0119
	corr	0.350	0.141	-0.147	0.0076	-0.0528	0.0491	0.0272
	err	0.002	0.007	0.007	0.0165	0.0145	0.0220	0.0220
(13 : 11 : 59.0, −1 : 30 : 00.7) 22.10	meas	0.398	-0.075	0.112	-0.0044	0.0144	-0.0052	-0.0227
	err	0.002	0.004	0.004	0.0064	0.0085	0.0121	0.0121
	corr	0.298	-0.123	0.232	-0.0025	0.0083	-0.0033	-0.0175
	err	0.002	0.008	0.008	0.0171	0.0203	0.0258	0.0258
(13 : 11 : 51.1, −1 : 29 : 42.7) 22.34	meas	0.457	0.182	-0.106	-0.0820	-0.0042	0.0967	-0.0280
	err	0.002	0.004	0.004	0.0056	0.0095	0.0116	0.0116
	corr	0.374	0.273	-0.136	-0.0699	-0.0168	0.1320	-0.0270
	err	0.002	0.006	0.006	0.0121	0.0174	0.0203	0.0203
(13 : 12 : 02.6, −1 : 29 : 28.0) 22.19	meas	0.452	0.100	-0.051	-0.0228	0.0011	-0.0448	0.0191
	err	0.002	0.005	0.004	0.0059	0.0089	0.0124	0.0124
	corr	0.367	0.162	-0.057	-0.0204	-0.0039	-0.0385	0.0261
	err	0.003	0.007	0.007	0.0134	0.0175	0.0224	0.0224
(13 : 11 : 49.6, −1 : 16 : 13.5) 22.27	meas	0.406	0.098	0.015	-0.0354	-0.0668	0.0237	-0.0312
	err	0.002	0.004	0.004	0.0081	0.0068	0.0126	0.0126
	corr	0.319	0.128	-0.010	-0.0358	-0.0771	0.0348	-0.0080
	err	0.002	0.007	0.007	0.0177	0.0159	0.0242	0.0242
(13 : 12 : 24.1, −1 : 21 : 31.4) 22.21	meas	0.475	-0.159	0.027	-0.0041	-0.0167	0.0025	0.0292
	err	0.002	0.004	0.004	0.0093	0.0062	0.0128	0.0128
	corr	0.395	-0.220	0.020	-0.0039	-0.0161	0.0023	0.0155
	err	0.003	0.007	0.006	0.0172	0.0131	0.0217	0.0217
(13 : 12 : 11.5, −1 : 12 : 40.0) 22.11	meas	0.475	0.055	-0.126	-0.0402	-0.0162	0.1010	-0.0402
	err	0.002	0.004	0.004	0.0097	0.0059	0.0124	0.0124
	corr	0.395	0.051	-0.204	-0.0427	-0.0233	0.1135	-0.0552
	err	0.003	0.006	0.007	0.0178	0.0128	0.0214	0.0214

Table 3.16: Lowest noise flexion measurements								
(ra, dec), M_r		$\theta_{1/2}$	g_r	g_t	F_r	F_t	G_r	G_t
(13 : 12 : 21.3, −1 : 09 : 18.3) 22.35	meas	0.421	-0.065	-0.054	0.0397	-0.0614	0.0206	-0.0565
	err	0.002	0.005	0.005	0.0076	0.0078	0.0131	0.0131
	corr	0.328	-0.145	-0.118	0.0358	-0.0530	0.0482	-0.0697
	err	0.003	0.008	0.008	0.0178	0.0180	0.0258	0.0258

Table 3.16: Lowest noise flexion measurements on background source galaxies. Objects are ordered by total F- plus G-flexion noise, from least to most. However only those galaxies larger than 1.5× the PSF and with measured flexions larger than the reported noise in the measurement are considered. Flexions are decomposed into directions oriented radially and tangentially with respect ot the cluster center. We report both the (meas)ured galaxy shears and flexions and the PSF (corr)ected shears and flexions. These corrected values are what one would measure if one observed from space with an aberration free telescope.

Table 3.17: Lowest noise flexion measurements on the 3 central chips								
(ra, dec), M_r		$\theta_{1/2}$	g_r	g_t	F_r	F_t	G_r	G_t
(13 : 11 : 33.6, −1 : 17 : 51.4) 22.40	meas	0.461	-0.268	-0.154	0.0418	-0.0169	0.0648	-0.0165
	err	0.004	0.008	0.008	0.0153	0.0226	0.0240	0.0240
	corr	0.389	-0.398	-0.213	0.0514	-0.0098	0.0942	-0.0161
	err	0.005	0.012	0.011	0.0279	0.0373	0.0392	0.0392
(13 : 11 : 36.2, −1 : 20 : 22.0) 22.22	meas	0.521	-0.064	-0.051	0.0228	0.0200	0.0825	0.0034
	err	0.006	0.010	0.010	0.0155	0.0189	0.0287	0.0287
	corr	0.458	-0.073	-0.080	0.0410	0.0169	0.0995	0.0080
	err	0.006	0.013	0.014	0.0283	0.0324	0.0444	0.0444
(13 : 11 : 19.3, −1 : 22 : 35.6) 22.27	meas	0.401	-0.100	0.033	-0.0940	-0.1061	-0.1045	0.0603
	err	0.004	0.010	0.010	0.0145	0.0200	0.0302	0.0302
	corr	0.314	-0.188	0.026	-0.1424	-0.0771	-0.1944	0.0215
	err	0.005	0.017	0.017	0.0351	0.0431	0.0580	0.0580
(13 : 11 : 18.5, −1 : 20 : 50.3) 22.26	meas	0.456	-0.089	-0.004	0.1339	-0.0003	-0.0718	0.0101
	err	0.005	0.010	0.010	0.0203	0.0148	0.0303	0.0303
	corr	0.382	-0.116	-0.027	0.1636	0.0045	-0.0108	0.0245
	err	0.006	0.015	0.015	0.0378	0.0304	0.0506	0.0506
(13 : 11 : 41.3, −1 : 23 : 59.4) 22.69	meas	0.509	-0.109	-0.015	-0.1684	-0.0421	0.0474	0.1036
	err	0.006	0.010	0.010	0.0200	0.0157	0.0312	0.0312
	corr	0.444	-0.131	-0.006	-0.1812	-0.0389	0.0121	0.0931
	err	0.007	0.014	0.013	0.0343	0.0288	0.0479	0.0479
(13 : 11 : 26.0, −1 : 18 : 18.7) 22.28	meas	0.420	-0.008	-0.006	0.0295	0.0316	0.0176	-0.0875
	err	0.005	0.012	0.012	0.0183	0.0188	0.0316	0.0316
	corr	0.339	-0.010	0.021	0.0326	0.0236	0.0283	-0.0849
	err	0.007	0.018	0.018	0.0393	0.0400	0.0576	0.0576
(13 : 11 : 26.7, −1 : 24 : 11.2) 22.41	meas	0.434	0.004	0.005	-0.0356	-0.0017	0.0181	0.0467
	err	0.005	0.012	0.012	0.0183	0.0193	0.0318	0.0318
	corr	0.355	-0.019	0.023	-0.0349	0.0011	0.0103	0.0461
	err	0.006	0.018	0.017	0.0383	0.0397	0.0566	0.0566
(13 : 11 : 29.2, −1 : 23 : 07.6) 22.58	meas	0.388	-0.018	0.070	0.0117	0.0283	0.0199	-0.0894
	err	0.005	0.012	0.012	0.0213	0.0161	0.0318	0.0318
	corr	0.297	-0.059	0.152	0.0244	0.0137	0.0319	-0.0999
	err	0.006	0.020	0.020	0.0496	0.0418	0.0652	0.0652
(13 : 11 : 35.4, −1 : 19 : 55.1) 22.41	meas	0.436	-0.099	0.009	-0.0925	-0.0588	-0.1404	-0.0471
	err	0.005	0.011	0.011	0.0165	0.0219	0.0324	0.0324
	corr	0.359	-0.147	-0.015	-0.1981	-0.0555	-0.2740	-0.0945
	err	0.006	0.017	0.017	0.0353	0.0425	0.0570	0.0570

Table 3.17: Lowest noise flexion measurements on the 3 central chips								
(ra, dec), M_r		$\theta_{1/2}$	g_r	g_t	F_r	F_t	G_r	G_t
(13 : 11 : 26.6, −1 : 16 : 51.4) 22.46	meas	0.392	0.078	-0.093	0.0806	0.0142	-0.1052	-0.0444
	err	0.005	0.011	0.012	0.0200	0.0202	0.0330	0.0330
	corr	0.304	0.117	-0.119	0.0731	0.0269	-0.1228	-0.0321
	err	0.006	0.019	0.019	0.0456	0.0458	0.0651	0.0651

Table 3.17: Lowest noise flexion measurements on the background source galaxies in the three chips containing the cluster center. The location of these objects in the cluster center region are shown in figure 3-25. Objects are ordered by total F- plus G-flexion noise, from least to most. However only those galaxies larger than 1.5× the PSF and with measured flexions larger than the reported noise in the measurement are considered. Flexions are decomposed into directions oriented radially and tangentially with respect ot the cluster center. We report both the (meas)ured galaxy shears and flexions and the PSF (corr)ected shears and flexions. These corrected values are what one would measure if one observed from space with an aberration free telescope.

Table 3.18: Flexion measurements for hand-picked lensed galaxies								
(ra, dec), M_r		$\theta_{1/2}$	g_r	g_t	F_r	F_t	G_r	G_t
(13 : 11 : 40.0, −1 : 23 : 37.5) 22.88	meas	0.411	-0.192	-0.143	-0.0323	-0.0300	0.0644	-0.1624
	err	0.007	0.015	0.015	0.0233	0.0402	0.0493	0.0493
	corr	0.326	-0.281	-0.201	-0.0525	-0.0405	0.0536	-0.2182
	err	0.009	0.025	0.025	0.0531	0.0770	0.0902	0.0902
(13 : 11 : 20.2, −1 : 23 : 15.4) 22.22	meas	0.433	-0.346	0.167	-0.0429	-0.0274	-0.0278	0.0451
	err	0.004	0.008	0.008	0.0114	0.0334	0.0270	0.0270
	corr	0.354	-0.545	0.237	-0.0740	-0.0097	-0.1036	0.0697
	err	0.005	0.015	0.012	0.0252	0.0549	0.0463	0.0463
(13 : 11 : 26.4, −1 : 24 : 23.8) 22.62	meas	0.442	-0.221	0.402	-0.0541	0.0160	0.0027	0.0710
	err	0.007	0.011	0.011	0.0609	0.0151	0.0420	0.0420
	corr	0.365	-0.349	0.604	-0.0821	0.0357	-0.0093	0.1706
	err	0.009	0.018	0.022	0.0984	0.0373	0.0732	0.0732
(13 : 11 : 24.7, −1 : 23 : 55.6) 22.68	meas	0.479	-0.206	-0.215	0.0089	0.0162	0.0315	0.0265
	err	0.007	0.013	0.013	0.0160	0.0416	0.0462	0.0462
	corr	0.409	-0.305	-0.290	0.0165	0.0181	0.0388	0.0515
	err	0.009	0.019	0.018	0.0337	0.0662	0.0720	0.0720
(13 : 11 : 27.8, −1 : 24 : 09.0) 22.70	meas	0.529	-0.104	0.400	-0.1113	0.0510	0.0086	0.1135
	err	0.011	0.015	0.015	0.0700	0.0233	0.0539	0.0539
	corr	0.466	-0.147	0.526	-0.1011	0.0447	0.0058	0.1424
	err	0.012	0.020	0.023	0.1007	0.0440	0.0810	0.0810
(13 : 11 : 40.5, −1 : 19 : 32.2) 23.11	meas	0.494	-0.357	0.117	0.0171	-0.0861	-0.0600	-0.0756
	err	0.009	0.014	0.013	0.0496	0.0331	0.0537	0.0537
	corr	0.427	-0.477	0.138	0.0183	-0.0680	-0.0712	-0.1347
	err	0.010	0.021	0.018	0.0748	0.0544	0.0801	0.0801
(13 : 11 : 41.4, −1 : 20 : 42.7) 22.22	meas	0.418	0.049	-0.279	0.0250	0.0426	-0.0164	0.0658
	err	0.005	0.011	0.011	0.0177	0.0342	0.0365	0.0365
	corr	0.337	0.099	-0.451	0.0413	0.0565	-0.0614	0.1018
	err	0.007	0.018	0.021	0.0411	0.0640	0.0671	0.0671
(13 : 11 : 25.7, −1 : 19 : 00.2) 23.27	meas	0.484	-0.425	0.078	-0.0315	-0.0155	0.2813	0.1095
	err	0.015	0.022	0.023	0.0631	0.0998	0.1005	0.1005
	corr	0.417	-0.565	0.124	-0.0437	-0.0117	0.2258	0.1208
	err	0.018	0.037	0.032	0.1021	0.1481	0.1517	0.1517
(13 : 11 : 26.5, −1 : 16 : 39.3) 22.57	meas	0.535	0.269	-0.180	-0.0183	-0.0473	0.0035	0.0332
	err	0.010	0.016	0.016	0.0289	0.0508	0.0540	0.0540
	corr	0.475	0.337	-0.214	-0.0177	-0.0392	0.0191	0.0201
	err	0.011	0.021	0.020	0.0485	0.0747	0.0785	0.0785

Table 3.18: Flexion measurements for hand-picked lensed galaxies								
(ra, dec), M_r		$\theta_{1/2}$	g_r	g_t	F_r	F_t	G_r	G_t
(13 : 11 : 23.7, −1 : 16 : 31.7) 23.00	meas	0.469	-0.316	-0.189	-0.2133	-0.0922	-0.1285	-0.0169
	err	0.026	0.045	0.044	0.1610	0.1110	0.2035	0.2035
	corr	0.399	-0.438	-0.240	-0.2792	-0.1003	-0.3080	-0.1760
	err	0.031	0.070	0.064	0.2561	0.1891	0.3086	0.3086
(13 : 11 : 37.8, −1 : 23 : 40.2) 22.45	meas	0.431	0.306	-0.050	-0.0005	-0.0126	-0.0141	-0.0227
	err	0.005	0.011	0.011	0.0121	0.0363	0.0368	0.0368
	corr	0.351	0.476	-0.049	-0.0013	-0.0217	-0.0211	0.0081
	err	0.007	0.019	0.016	0.0290	0.0619	0.0626	0.0626
(13 : 11 : 33.4, −1 : 16 : 39.4) 22.51	meas	0.409	-0.163	0.260	0.0548	-0.0162	-0.0680	-0.0620
	err	0.005	0.010	0.010	0.0337	0.0115	0.0371	0.0371
	corr	0.326	-0.286	0.421	0.0979	-0.0449	-0.0420	-0.1796
	err	0.006	0.017	0.018	0.0618	0.0306	0.0668	0.0668
(13 : 11 : 33.4, −1 : 18 : 51.6) 22.48	meas	0.443	-0.510	-0.086	0.0354	0.0219	0.0273	0.0214
	err	0.006	0.009	0.009	0.0304	0.0485	0.0384	0.0384
	corr	0.368	-0.764	-0.131	0.0924	0.0210	0.1472	0.0653
	err	0.007	0.019	0.013	0.0501	0.0739	0.0607	0.0607
(13 : 11 : 21.4, −1 : 18 : 40.8) 22.56	meas	0.482	-0.382	0.256	-0.0688	0.0983	0.0104	0.1970
	err	0.009	0.013	0.013	0.0165	0.0714	0.0618	0.0618
	corr	0.414	-0.501	0.358	-0.0866	0.0838	-0.0202	0.3182
	err	0.011	0.021	0.020	0.0353	0.1045	0.0921	0.0921
(13 : 11 : 19.3, −1 : 17 : 45.9) 22.77	meas	0.446	-0.488	0.309	0.1899	-0.0777	0.1210	-0.1745
	err	0.011	0.013	0.013	0.0941	0.0526	0.0676	0.0676
	corr	0.372	-0.686	0.463	0.3512	-0.1222	0.4739	-0.5753
	err	0.013	0.028	0.024	0.1444	0.0880	0.1081	0.1081
(13 : 11 : 22.0, −1 : 16 : 32.1) 22.36	meas	0.425	-0.278	-0.115	0.0888	0.0202	0.1406	-0.2312
	err	0.005	0.011	0.011	0.0360	0.0161	0.0412	0.0412
	corr	0.346	-0.415	-0.145	0.1497	0.0205	0.2645	-0.1650
	err	0.007	0.019	0.017	0.0624	0.0351	0.0699	0.0699

Table 3.18: Flexion measurements for hand-picked lensed galaxies								
(ra, dec), M_r		$\theta_{1/2}$	g_r	g_t	F_r	F_t	G_r	G_t

Table 3.18: Flexion measurements on hand-picked background source galaxies in the three chips containing the cluster center. The location of these objects in the cluster center region are shown in figure 3-25. Objects here are selected visually as likely lensing candidates and must have half light radii that are at least 1.5× the PSF half light radius. Flexions are decomposed into directions oriented radially and tangentially with respect ot the cluster center. We report both the (meas)ured galaxy shears and flexions and the PSF (corr)ected shears and flexions. These corrected are what one would measure if one observed from space with an aberration free telescope.

Table 3.19: Flexion measurements for those objects reported on in Cain et al. [15]								
#, (ra, dec), M_r		$\theta_{1/2}$	g_r	g_t	F_r	F_t	G_r	G_t
# 4	meas	0.489	-0.237	-0.152	0.0015	-0.0031	-0.0094	0.0004
(13 : 11 : 22.2,	err	0.007	0.012	0.012	0.0315	0.0237	0.0377	0.0377
−1 : 21 : 00.2)	corr	0.421	-0.317	-0.225	0.0062	-0.0008	-0.0044	0.0151
22.46	err	0.008	0.017	0.016	0.0512	0.0414	0.0589	0.0589
# 5	meas	0.390	-0.377	-0.120	0.1220	0.0268	0.1523	0.0262
(13 : 11 : 31.5,	err	0.015	0.029	0.029	0.1246	0.0481	0.1351	0.1351
−1 : 20 : 36.7)	corr	0.301	-0.597	-0.213	-0.0305	-0.0006	-0.0262	-0.0136
23.46	err	0.019	0.064	0.052	0.2314	0.1152	0.2499	0.2499
# 13	meas	0.518	0.100	0.111	-0.0489	-0.0068	-0.0314	0.0077
(13 : 11 : 22.5,	err	0.007	0.012	0.012	0.0159	0.0272	0.0361	0.0361
−1 : 20 : 20.4)	corr	0.455	0.142	0.132	-0.0699	-0.0009	-0.0439	0.0106
22.43	err	0.008	0.016	0.016	0.0306	0.0444	0.0552	0.0552
# 19	meas	0.472	0.022	-0.052	-0.3300	-0.1367	0.0963	-0.1150
(13 : 11 : 26.6,	err	0.021	0.040	0.036	0.0707	0.0508	0.1183	0.1183
−1 : 20 : 08.4)	corr	0.401	0.052	-0.073	1.2134	-0.0694	1.4696	-0.0772
23.92	err	0.025	0.056	0.050	0.1316	0.1026	0.1885	0.1885
# 24	meas	0.458	-0.058	0.034	-0.0136	-0.0235	0.0339	0.0486
(13 : 11 : 28.8,	err	0.012	0.024	0.025	0.0441	0.0380	0.0688	0.0688
−1 : 20 : 06.5)	corr	0.384	-0.076	0.071	0.0038	0.0038	-0.0124	0.0016
22.84	err	0.014	0.035	0.036	0.0843	0.0763	0.1164	0.1164
# 25	meas	0.403	0.075	-0.041	0.0385	-0.0268	0.0344	-0.0154
(13 : 11 : 21.9,	err	0.010	0.022	0.022	0.0392	0.0351	0.0625	0.0625
−1 : 21 : 09.3)	corr	0.317	0.121	-0.102	0.0451	-0.0174	0.0356	-0.0020
23.35	err	0.012	0.037	0.037	0.0866	0.0807	0.1200	0.1200
# 26	meas	0.389	-0.334	-0.252	0.3334	0.0421	0.3903	0.0231
(13 : 11 : 30.5,	err	0.015	0.030	0.029	0.1473	0.0364	0.1386	0.1386
−1 : 22 : 10.8)	corr	0.298	-0.584	-0.391	-0.8583	-0.3188	-0.9884	-1.6083
23.45	err	0.019	0.067	0.056	0.2963	0.1022	0.2909	0.2909
# 33	meas	0.551	0.050	-0.167	0.0189	0.0781	-0.0774	0.0204
(13 : 11 : 25.4,	err	0.019	0.031	0.031	0.0396	0.0739	0.0948	0.0948
−1 : 21 : 16.1)	corr	0.492	0.054	-0.222	0.0010	0.0637	-0.0876	0.0543
23.32	err	0.021	0.039	0.040	0.0744	0.1153	0.1402	0.1402
# 46	meas	0.407	0.034	0.005	-0.0335	0.0045	0.0977	0.0163
(13 : 11 : 30.3,	err	0.010	0.024	0.024	0.0359	0.0401	0.0655	0.0655
−1 : 18 : 37.0)	corr	0.324	0.027	0.028	-0.0357	0.0072	0.0937	0.0226
23.21	err	0.013	0.038	0.038	0.0816	0.0874	0.1242	0.1242

Table 3.19: Flexion measurements for those objects reported on in Cain et al. [15]								
#, (ra, dec), M_r		$\theta_{1/2}$	g_r	g_t	F_r	F_t	G_r	G_t
# 47	meas	0.445	0.057	-0.034	-0.1600	-0.0387	-0.0664	0.1059
(13 : 11 : 26.2,	err	0.014	0.029	0.030	0.0488	0.0502	0.0905	0.0905
-1 : 21 : 19.7)	corr	0.369	0.062	-0.064	-0.2938	-0.0270	-0.1954	0.0601
23.88	err	0.016	0.043	0.043	0.0987	0.0995	0.1531	0.1531

Table 3.19: Flexion measurements for objects reported on in Cain et al. [15] that are also larger than 1.5× the PSF in this work. Object numbers correspond to those in table 3 of that work. Flexions are decomposed into directions oriented radially and tangentially with respect ot the cluster center. We report both the (meas)ured galaxy shears and flexions and the PSF (corr)ected shears and flexions. These corrected values are what one would measure if one observed from space with an aberration free telescope.